Universidade do Minho
Escola de Engenharia

Mohammadali Rezazadeh

Innovative Methodologies for the Enhancement of the Flexural Strengthening Performance of NSM CFRP Technique for RC Beams

March 2015

UMinho | 2015

Mohammadali Rezazadeh

Innovative Methodologies for the Enhancement of the Flexural Strengthening Performance of NSM CFRP Technique for RC Beams

Universidade do Minho
Escola de Engenharia

Mohammadali Rezazadeh

Innovative Methodologies for the Enhancement of the Flexural Strengthening Performance of NSM CFRP Technique for RC Beams

Tese de Doutoramento
Engenharia Civil

Trabalho efectuado sob a orientação do
Professor Doutor Joaquim António Oliveira de Barros

March 2015

STATEMENT OF INTEGRITY

I hereby declare having conducted my thesis with integrity. I confirm that I have not used plagiarism or any form of falsification of results in the process of the thesis elaboration.
I further declare that I have fully acknowledged the Code of Ethical Conduct of the University of Minho.

University of Minho, ______________________________

Full name: ____

Signature: ____

Acknowledgements

First and above all, I praise God for supporting me all the way until now…

The research reported in this thesis has been carried out at the Civil Engineering Department of University of Minho, Portugal, under the supervision of Prof. Joaquim Barros. This work was funded by the project “PreLami - Performance of reinforced concrete structures strengthened in flexural with an innovative system using prestressed NSM CFRP laminates”, with the reference PTDC/ECM/114945/2009.

I would never have been able to finish this thesis without the guidance and continuous support of my kind supervisor Prof. Joaquim Barros who honestly gives his deep scientific knowledge to the students. Hence, I would like to express my deepest gratitude to Prof. Barros for his constructive comments and suggestions, and patience along these years for developing the present research.

Also, I would like to thank to Prof. Salvador Dias for his care and great support during all these years. I would like to thank to Prof. Jose Sena-Cruz for his scientific guidance during this research project.

I would also like to thank to the technicians of the laboratory of the Civil Engineering department of University of Minho (LEST), engineers Marco, Matos, and Carlos for the extreme efforts and assistance during my experimental tests. I would like to acknowledge the support provided by S&P, for supplying the adhesives and the laminates, and Casais and CiviTest for the preparation of the specimens of the experimental program.

I am also grateful to all my friends in University of Minho for their supports, sharing thoughts, and all loving memories during all these years.

I would like to express my gratitude to my family, in particular to my parents and my brother for their unconditional support and continuous encouragement. At the end, my special thanks go to my wife for her help, patience, and endless love.

Abstract

Carbon fiber reinforced polymer (CFRP) materials have been extensively adopted for the flexural and shear strengthening of RC structures due to their several advantages, like a low mass density, a high strength and stiffness to weight ratios, excellent fatigue behavior, non-susceptible to corrosion, and high durability in typical environment conditions of civil engineering constructions. These CFRP composite materials can be applied to RC structures to be strengthened by using either externally bonded reinforcing (EBR) or near surface mounted (NSM) techniques.

The main purpose of the current study is to experimentally evaluate the efficiency of two flexural strengthening methodologies using the NSM CFRP technique for the enhancement not only the load carrying capacity at concrete cracking and steel yielding initiations, serviceability limit state, and ultimate condition, but also the ultimate deflection capacity when compared to the use of non-prestressed NSM CFRP technique. The investigated strengthening methodologies include NSM prestressing and NSM hybrid techniques. In the NSM prestressing technique, an appropriate prestress level is applied on the CFRP reinforcement, while the NSM hybrid technique combines non-prestressed and prestressed CFRP reinforcements in the same application. Moreover, the distribution of tensile strain and bond shear stress along the prestressed NSM CFRP reinforcement is experimentally evaluated after the release of prestress force.

On the other hand, the experimental tests are simulated using a nonlinear finite element (FE) model, which considers the nonlinear behavior of the constituent materials, the behavior of CFRP-epoxy adhesive-concrete interfaces, and modeling the prestress process of the CFRP elements adopted in the experimental tests. Besides, simplified analytical approaches, with a design framework, are developed to predict the flexural behavior of RC beams flexurally strengthened with prestressed CFRP reinforcement applied according to either EBR or NSM techniques. Moreover, this study offers an analytical formulation based on a closed form solution for the prediction of the distribution of CFRP tensile strain and bond shear stress and, additionally, the prestress transfer length immediately after the release of the prestress force.

Key-words: NSM technique, composite materials, prestressing, hybrid system, numerical analysis, analytical approach, prestress transmission zone.

Resumo

Materiais compósitos de matriz polimérica reforçados com fibras de carbono (CFRP) podem ser aplicados no reforço de estruturas de BA por intermédio de colagem exterior de sistemas prefabricados (laminados) ou curados in sito (manta ou tecido) na superfície dos elementos a reforçar (EBR -Externally Bonded Reinforcement) ou por utilização da técnica NSM (Near Surface Mounted).

O principal objetivo do presente estudo é avaliar, experimentalmente, a eficiência de duas novas metodologias de reforço à flexão utilizando a técnica NSM com laminados de CFRP, em que numa das metodologias todos os laminados de são aplicados sob determinada pré-tensão, e na outra combinam-se laminados passivos (sem pré-tensão) com laminados pré-tensionados. Quando aplicadas a elementos de BA que desenvolvem rotura por flexão, estas novas técnicas pretendem aumentar a sua capacidade de carga para início da fendilhação do betão, estados limites último e de serviço, bem como melhorar a sua capacidade de deformação última, quando se toma por base de comparação os resultados possíveis de obter com a utilização da técnica NSM com laminados passivos de CFRP. Além disso, a distribuição da deformação por tração e da tensão de corte ao longo do laminado pré-tensionado é experimentalmente avaliada após a libertação da força de pré-esforço.

Os ensaios experimentais foram simulados numericamente utilizando modelos constitutivos capazes de modelar o comportamento não-linear dos materiais constituintes, das interfaces CFRP-adesivo e adesivo-betão, bem como o processo de aplicação do pré-esforço nos laminados de CFRP e transferência deste para o betão do substrato das vigas a reforçado, em similitude com o realizado experimentalmente. Além disso, foram desenvolvidas formulações analíticas simplificadas, para prever o comportamento à flexão de vigas de BA reforçadas à flexão com laminados de CFRP pré-tensionados (e/ou passivos), os quais podem ser aplicados segundo as técnicas EBR ou NSM. A formulação analítica integrada permite prever a relação momento-curvatura de dada secção, e força-flecha de vigas reforçadas segundo as técnicas de reforço desenvolvidas, bem como o campo de extensões e tensões de corte nas zonas críticas dos laminados de CFRP, e o comprimento de transmissão do pré-esforço, recorrendo-se para tal a metodologias aplicáveis no quadro do projeto de estruturas de BA.

Palavras-chave: Técnica NSM, materiais compósitos, pré-esforço, sistema híbrido, análise numérica, formulações analíticas, zona de transmissão do pré-esforço.

Contents

List of Figures

List of Tables

Notations

A_f = area of CFRP reinforcement, mm^2.

A_{groove} = area of groove for NSM technique, mm^2.

A_s = area of tensile steel bars, mm^2.

$A_s^'$ = area of compressive steel bars, mm^2.

a_g = width of groove, mm.

a_L = loading span, mm.

b = width of beam, mm.

b_s = shear span, mm.

b_g = depth of groove, mm.

c = depth of neutral axis from top fiber of concrete at critical point, mm.

c_c = concrete cover for the bottom face of the beam, mm.

c^{cri} = depth of neutral axis from top fiber of concrete at critical CFRP reinforcement ratio, mm.

$c^{(ci)}$ = depth of neutral axis from top fiber of concrete at initial condition, mm.

C_1, C_2 = parameters in solution of differential equation.

d_s = distance from centroid of tensile steel bars to top fiber of concrete, mm.

$d_s^'$ = distance from centroid of compressive steel bars to top fiber of concrete, mm.

d_f = distance from centroid of CFRP reinforcement to top fiber of concrete, mm.

e = eccentricity of prestress force to centroidal axis of cross section, mm.

E_a = elasticity modulus of epoxy adhesive, MPa.

E_c = elasticity modulus of concrete, MPa.

E_f = elasticity modulus of CFRP, MPa.

E_s = elasticity modulus of longitudinal steel bars, MPa.

$f_c^{'}$ = specified compressive strength of concrete, MPa.

f_{ct} = splitting tensile strength of concrete, MPa.

f_r = flexural tensile strength of concrete, MPa.

F_{cf} = resistance of the concrete fracture surface for each CFRP laminate, N.

F_{fu} = tensile strength of CFRP, N.

F_{pre} = prestress force applied to CFRP reinforcement, N.

F_{rb} = maximum value of the force transferable through the resisting bond length, N.

f_{sy} = yield strength of longitudinal tensile steel bar, MPa.

G_a = shear modulus of adhesive, MPa.

G_c = shear modulus of concrete, MPa.

G_e = effective shear modulus of bond, MPa.

h = height of beam, mm.

I_{ucr} = moment of inertia of uncracked section of beam, mm^4.

k_a = shear stiffness of adhesive layer, MPa/mm.

k_c = shear stiffness of concrete, MPa/mm.

k_e = effective bond stiffness, MPa/mm.

L = beam span, mm.

L_b = bonded length of CFRP reinforcement, mm.

L_{rb} = resisting bond length, mm.

L_{ub} = unbonded length of CFRP reinforcement, mm.

M_{epre} = effective negative bending moment due to prestress force, N-mm.

M = flexural moment of beam, N-mm.

N = number of the longitudinal CFRP laminates.

$N.A.$ = neutral axis of beam.

n_f = modular ratio of CFRP laminate to concrete, E_f/E_c.

n_s = modular ratio of steel reinforcement to concrete, E_s/E_c.

P = external load of beam at critical point, N.

s_f = spacing of the two adjacent CFRP laminates, mm.

s'_f = distance between the laminate and the nearest beam edge, mm.

t_a = thickness of adhesive layer, mm.

t_c = thickness of concrete layer, mm.

t_e = thickness of effective shear modulus, mm.

$TL_{(95\%AMS)}$ = prestress transfer length based on 95%AMS method, mm.

$TL_{(ITM)}$ = prestress transfer length based on ITM method, mm.

u_c = longitudinal displacement of concrete, mm.

u_f = longitudinal displacement of CFRP reinforcement, mm.

y_i = distance between top fiber of concrete to centroidal axis of uncracked cross section, mm.

α (Sec. 5.1) = angle between axis and generatrices of the concrete fracture surface (semi-pyramid).

α (Sec. 5.2) = reaction time parameters.

α_1 = multiplier on f'_c to determine intensity of an equivalent rectangular stress distribution.

β_1 = ratio of depth of equivalent rectangular stress block to the depth of neutral axis.

$\delta_{\max}$ = maximum slip of local bond stress-slip relationship, mm.

ε_c = strain level in concrete, mm/mm.

ε'_c = strain of unconfined concrete corresponding to f'_c, mm/mm.

ε_{cc} = strain at top extreme fiber of concrete at critical point, mm/mm.

ε_{ct} = strain at bottom extreme fiber of concrete at critical point, mm/mm.

ε_{cu} = maximum compressive strain in concrete.

ε_{ef} = effective tensile strain of CFRP reinforcement at critical point, mm/mm.

ε_{fu} = ultimate tensile strain of CFRP reinforcement, mm/mm.

ε_{lf} = short-term prestrain loss in CFRP reinforcement, mm/mm.

ε_{f} = tensile strain in CFRP reinforcement, mm/mm.

ε_{fp} = prestrain in CFRP reinforcement, mm/mm.

ε_{s} = strain in longitudinal tensile steel bar at critical point, mm/mm.

$\varepsilon_{s}^{'}$ = strain in longitudinal compressive steel bar at critical point, mm/mm.

ε_{sy} = strain in longitudinal tensile steel bars corresponding to its yield strength, mm/mm.

ρ_{f}^{cri} = critical percentage of CFRP reinforcement, mm^2/mm.mm.

σ_{f} = tensile stress in CFRP reinforcement, MPa.

τ = bond shear stress, MPa.

$\tau_{\max}$ = maximum shear stress of local bond stress-slip relationship, MPa.

υ_{a} = Poisson's ratio of adhesive.

υ_{c} = Poisson's ratio of concrete.

ω = reaction shape parameter.

γ = shear strain.

χ = curvature of beam at critical point.

Chapter 1: Introduction

1.1 General

Concrete structures may become vulnerable during their lifetime due to several reasons such as: degradation of their material properties; design or construction errors; and environmental damage due to earthquake. These structures should be repaired or strengthened to ensure proper performance for the current service load demands.

Several methods have been investigated and applied for the strengthening of reinforced concrete (RC) structures using various materials. Fiber reinforced polymer (FRP) reinforcement is one of the most recent type of material for the strengthening purpose of RC structures. Carbon fiber reinforced polymer (CFRP) is the most used for structural strengthening of RC structures due to its low mass density, high strength and stiffness to weight ratios, excellent fatigue behavior, non-susceptibility to corrosion, and high durability in environment conditions.

CFRP composite materials can be applied to RC structures to be strengthened by using either externally bonded reinforcement (EBR) or near surface mounted (NSM) techniques, as represented in Figure 1-1 (ACI-440.2R. 2008). Studies have shown that the NSM CFRP strengthening technique assures higher shear and flexural strengthening effectiveness than the EBR technique (El-Hacha and Rizkalla 2004, Barros et al. 2007). Moreover, this NSM technique, in addition of decreasing the possibility of debonding failure, provides better resistance against fire (ACI-440.2R. 2008). The NSM technique is based on the insertion of FRP reinforcement into the groove opened on the concrete tensile surface of RC structures to be strengthened.

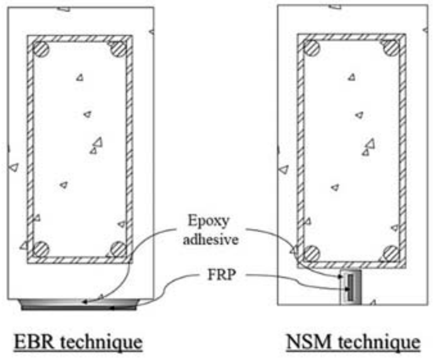

Figure 1-1: FRP reinforcement applied according to EBR and NSM techniques

In different strengthening situations, although, the ultimate load carrying capacity of beams strengthened with NSM CFRP reinforcement is significantly increased when compared to the capacity of the corresponding unstrengthened beam, the increase of load capacity at concrete cracking and at steel yielding initiation stages is in general moderate, not enough in some cases (Figure 1-2) (Barros and Fortes 2005). To increase the load capacity corresponding to these stages, the CFRP reinforcement must be applied with a certain prestress level (Nordin and Taljsten 2006, Badawi and Soudki 2009, El-Hacha and Gaafar 2011, Hosseini et al. 2013). In fact, by using prestressed CFRPs, the load carrying capacity at serviceability limit state conditions, and at yield initiation of flexural reinforcement can increase significantly, but the maximum load is almost not affected (Figure 1-2).

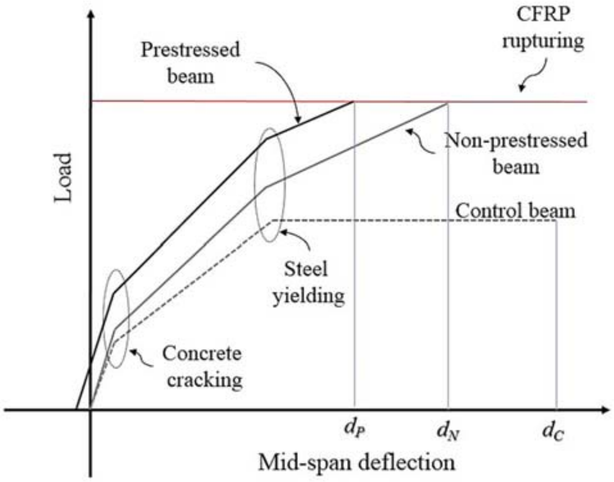

Figure 1-2: Influence of prestressing system on NSM CFRP technique

Many studies have been carried out to investigate the effectiveness of non-prestressed NSM CFRPs for the flexural strengthening of RC structures, while there are still different issues in terms of use of the prestressed NSM CFRPs for the flexural strengthening purpose that need to be addressed in detail to be confidently implemented in practical projects. Some of these issues include: energy absorption; ultimate deflection capacity; effect of the CFRP bonded length; load capacity for deflection levels corresponding to the serviceability limit state (SLS); crack width and cracked zone length; crack spacing; and finally, behavior of the prestressed NSM CFRP beams immediately after the release of the prestress force in terms of such short-term prestress losses, initial negative camber (upward deflection), and initial strain profile of the cross section.

The benefits provided by NSM prestressing technique are as higher as larger is the prestress level applied to the NSM CFRP reinforcement, as long as the initial prestress strain is limited in order to do not promote a premature failure of the CFRP. On the other hand, in spite of these benefits, the experimental research has shown that the deflection capacity at the failure of RC beams flexurally strengthened with prestressed CFRPs decreases with the increase of the prestress level (Badawi and Soudki 2009, Hajihashemi et al. 2011). The reduction of ultimate deflection capacity of the prestressed NSM CFRP beams with the increase of the prestress level is caused by the rupture of the CFRP reinforcement at smaller deflections, as a consequence of the initial tensile strain due to the prestress imposed to these composite materials (Figure 1-2). Moreover, this lack of deflection capacity becomes even more unfavorable by occurring the premature failure modes such as CFRP debonding and concrete cover delamination, before the rupture of CFRP reinforcement.

The improvement of ultimate deflection capacity in the NSM prestressing strengthening technique is a critical aspect to provide an ample warning of failure. Therefore, not only the improvement of load carrying capacity, but also the enhancement in terms of ultimate deflection capacity should be considered to flexurally strengthen RC structures using the NSM prestressing technique. In this context, few studies have been dedicated to propose a technique for the enhancement of the ultimate deflection capacity of RC structures strengthened with prestressed NSM CFRP reinforcement (Choi et al. 2011b).

On the other side, numerical analysis of FRP strengthened beams has been correspondingly carried out for simulating the experimental results. Many researchers simulated the behavior of NSM CFRP strengthened structures using 2D or 3D numerical models considering perfect bond conditions (no-slip occurrence) due to observing no debonding failure between CFRP-epoxy-concrete connections in the experimental tests (Barros et al. 2008b, Oudah and El-Hacha 2011b, Hosseini et al. 2013). Finite element (FE) modeling of NSM CFRP strengthened beams considering debonding effects is, however, very limited (Hawileh 2011). Moreover, FE analysis of RC structures strengthened with prestressed NSM CFRP reinforcement is rarely carried out by taking into account the debonding effects (Omran and El-Hacha 2011). Besides, the numerical simulation of prestress procedure according to the adopted system in the experimental programs to prestress NSM CFRP elements has never been considered in the FE analyses.

Therefore, developing a 3D FE model of RC structures strengthened using prestressed NSM CFRP reinforcement considering the nonlinear behavior of constituent materials, CFRP-epoxy-concrete interfaces, modeling the prestress process of CFRP elements adopted in experimental program, seems necessary on the computational mechanical domain to be used as a numerical strategy to design this type of strengthened structures.

Furthermore, simplified analytical approaches, with a design framework, need to be developed to predict the flexural behavior of RC structures strengthened with either non-prestressed or prestressed CFRP reinforcement applied according to NSM technique, when failed by conventional flexural failure modes (concrete crushing and rupture of CFRP reinforcement) or premature failure modes (such as concrete cover delamination). The model should, also, be capable of simulating the initial effects of prestress force applied by NSM FRP reinforcement, as well as the prestress transmission zone, after the release of prestress force.

1.2 Research Objective

This research study mainly focuses on the aforementioned investigating issues. Therefore, the research is conducted with three main parts: experimental, numerical, and analytical investigations with the following objectives:

1.2.1 Experimental Investigation

- To evaluate the influence of prestress level on the flexural behavior of RC beams strengthened with NSM CFRP laminates;
- To investigate the short-term behavior of the prestressed NSM CFRP strengthened beams immediately after the release of prestress force;
- To evaluate the transmission zone of prestressed CFRP laminate at different levels of prestressing;
- To assess the effectiveness of prestress level on the ultimate deflection capacity of NSM CFRP flexurally strengthened beams;
- To assess the potentialities of a new hybrid strengthening methodology (combining non-prestressed and prestressed CFRP laminates in the same application) in order to provide a good balance in terms of load carrying and ultimate deflection capacity to the strengthened beams.

1.2.2 Numerical Investigation

- To develop a nonlinear 3D FE model with CFRP-epoxy-concrete interfaces that can simulate the behavior of prestressed NSM CFRP flexurally strengthened RC beams;
- To develop a numerical strategy to simulate the experimental prestress procedure;
- To assess the influence of NSM CFRP bonded length on the flexural performance of NSM CFRP strengthened beams;
- To evaluate different configurations of the NSM hybrid technique for the flexural strengthening of RC beams.

1.2.3 Analytical Investigation

- To develop a simplified analytical approach to predict the behavior of RC beams flexurally strengthened with prestressed CFRP reinforcements applied according to either EBR or NSM techniques considering the initial effects of prestress force;
- To develop a methodology to determine the ultimate flexural capacity of NSM CFRP strengthened beams when concrete cover delamination is the governing failure mode;
- To propose an upper limit for the prestress level applied to the CFRP reinforcement in order to optimize the ductility performance of NSM prestressing technique;
- To develop an analytical formulation, with a design framework, for the prediction of the tensile strain and bond shear stress fields along the CFRP, as well as the prestress transfer length;
- To carry out a series of parametric studies to evaluate the influence of the relevant parameters of the analytical model on the prestress transmission zone.

1.3 Thesis Layout

This thesis consists of six chapters as shown in Figure 1-3. Chapter 1 provides the introduction in terms of a summary of the research performed on the behavior of RC structures strengthened with FRP reinforcement, relevant problem statement, and objectives of this thesis. Literature review on flexural strengthening of RC structures with non-prestressed and prestressed CFRP reinforcements is described in Chapter 2. Chapter 3 introduces three experimental programs to evaluate the prestress transmission zone, the effectiveness of the flexural strengthening technique with prestressed NSM CFRP laminates, and the potentialities of a hybrid flexural strengthening methodology for RC structures. In Chapter 4, a 3D nonlinear FE model is developed to simulate the experimental tests and also, to evaluate the influence of CFRP bonded length and different configurations of the NSM hybrid technique on the flexural performance of strengthened beams. Analytical approaches are developed in Chapter 5 to predict, firstly, the flexural behavior of RC beams strengthened with prestressed CFRP reinforcement applied according to either EBR or NSM technique, and then, the prestress transmission zone of CFRP reinforcement after the release of prestress force. Finally, conclusions are summarized in Chapter 6, which finalizes with recommendations for future developments that require specific and deeper research.

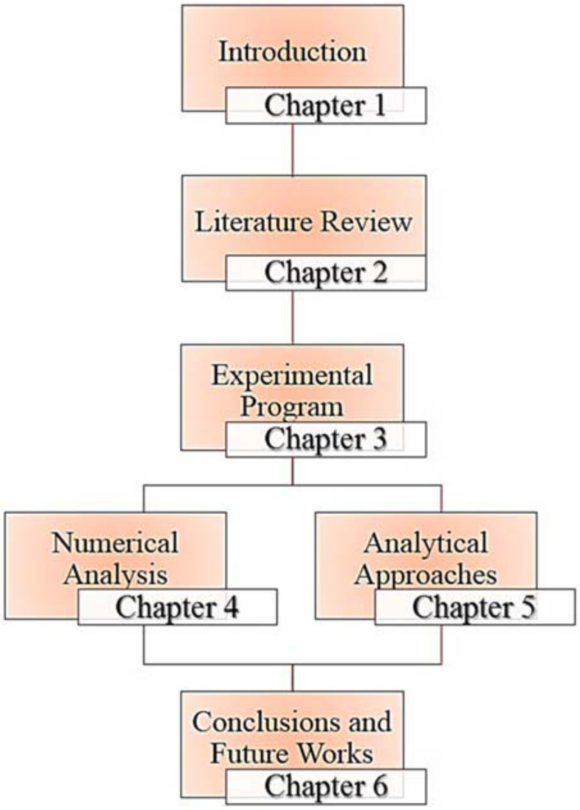

Figure 1-3: Thesis layout

Chapter 2: Literature Review

In the last decades, composite material systems made of fibers embedded in a polymeric resin (FRP) have been developed as an alternative to steel for the strengthening of RC structures (ACI-440.1R. 2001, ACI-440.1R. 2006, ACI-440.2R. 2008). FRP composites are commercially classified into three types according to available fibers: aramid (AFRP), carbon (CFRP), and glass (GFRP) (ACI-440.2R. 2008, Choi 2008). CFRP systems have been extensively investigated for the flexural and shear strengthening of RC structures due to their advantages, such as high durability in environment conditions where conventional materials have serious concerns due to the degradation of their properties (Barros et al. 2008b, Dias and Barros 2009, Perrone et al. 2009, Dias and Barros 2010, Dalfre and Barros 2011, Jayaprakash et al. 2011, Dias and Barros 2012a, Dias and Barros 2012b). These CFRP composite materials can be applied to RC structures to be strengthened by using either externally bonded reinforcing (EBR) or near surface mounted (NSM) techniques (El-Hacha and Rizkalla 2004, ACI-440.2R. 2008, Jayaprakash et al. 2011).

2.1 Experimental Investigations

2.1.1 Strengthening of RC Beams with Non-prestressed CFRP

Experimental research has demonstrated that the NSM technique, based on the insertion of CFRP reinforcement into grooves opened on the concrete cover of the RC elements to be strengthened, assures higher shear and flexural strengthening effectiveness than EBR technique (Barros et al. 2007). This higher effectiveness of the NSM technique can be attributed to the largest ratio of bond area to cross sectional area of the CFRP bar, and higher confinement provided by the surrounding concrete to this reinforcement when using this technique (El-Hacha and Rizkalla 2004, Barros and Fortes 2005, Barros et al. 2007, ACI-440.2R. 2008). However, a hybrid technique combining NSM CFRP reinforcement for the flexural strengthening, with CFRP strips applied according to EBR technique, was experimentally evaluated by Barros et al. (2008) to increase the flexural resistance of RC structures (Figure 2-1). This hybrid technique showed an enhancement in terms of energy dissipation capacity of the strengthened structures due to the higher confinement to the concrete provided by these EBR CFRP strips when compared to the use of NSM technique (Barros et al. 2008a, Perrone et al. 2009).

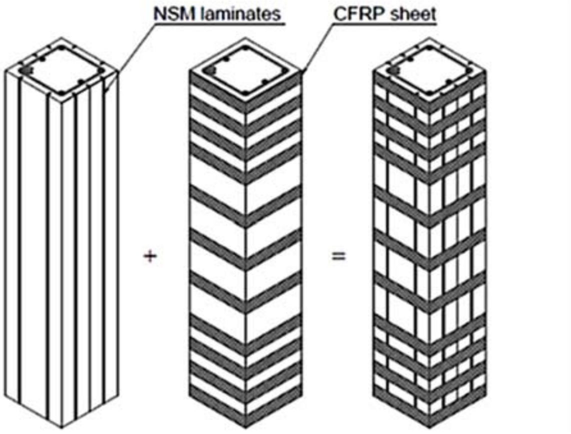

Figure 2-1: Hybrid strengthening technique (Barros et al. 2008a)

Barros et al. (2007) investigated the influence of the longitudinal equivalent reinforcement ratio ($\rho_{l,eq}$,CFRP reinforcements were converted to equivalent steel) on the strengthening effectiveness of both NSM and EBR techniques. The results showed that, although, NSM technique is more effective than EBR technique for the flexural strengthening of RC beams, the difference between the efficacy of NSM and EBR techniques decreases with the increase of the longitudinal equivalent reinforcement ratio.

In RC beams, due to concrete casting condition, a higher percentage of voids exists below the longitudinal tensile steel bars, which can cause the formation of a weak plane in the concrete microstructure just below these bars (Barros and Kotynia 2008, Barros et al. 2011). Besides, when these beams are strengthened with NSM CFRP technique, an in-plane shear crack can be initiated at the extremities of the NSM CFRP reinforcement due to high stress gradient caused by the abrupt termination of the CFRP (ACI-440.2R. 2008). This crack is propagated along the depth of the concrete cover of the beam up to the weak plane level, and then, horizontally progresses along this level, causing concrete cover delamination failure (also, designated by rip-off represented in Figure 2-2a), which is a premature failure of the NSM CFRP strengthened beams. The susceptibility to the formation of a concrete weak plane decreases with the reinforcement ratio of existing longitudinal steel bars and number of CFRP reinforcements (Barros and Kotynia 2008, Barros et al. 2011). On the other side, in order to provide a certain CFRP reinforcement ratio for the flexural strengthening, the use of CFRP strips of larger cross section depth is limited by the thickness of the concrete cover of the tensile steel bars. For exceeding this thickness the bottom arm of the steel stirrups needs to be cut. In this context, Costa and Barros (2009b) experimentally investigated the influence, in terms of the beam's load carrying capacity, of cutting the bottom arm of steel stirrups for the installation of CFRP strips according to NSM technique (Figure 2-2b). The experimental results showed that cutting the bottom arm of steel stirrups in flexurally strengthened RC beams, which have a percentage of steel stirrups that avoids the shear failure, has a marginal impact in terms of the flexural strengthening effectiveness of the NSM technique for monotonic loading conditions, mainly when wet layup CFRP strips of U configuration are applied for providing some shear resistance, and to avoid the occurrence of rip-off failure mode.

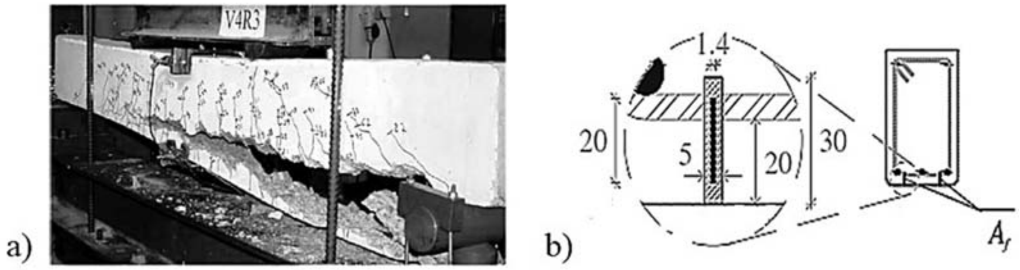

Figure 2-2: a) Concrete cover delamination failure (Barros et al. 2007), b) cutting the bottom arm of the steel stirrups (Costa and Barros 2009b)

The efficiency of NSM CFRP technique for the flexural strengthening of cantilever RC beams (with special focus on the specific problem of cantilever beams in terms of strengthening outward pressure) was experimentally evaluated by Al-Mahmoud et al. (2010) by investigating the efficiency of this technique for the flexural strengthening of simply supported beams (as represented Figure 2-3). The results showed that the prevailing failure mode at the maximum capacity of the cantilever strengthened beams was influenced by the adopted CFRP bonded length. In other words, by increasing the CFRP bonded length applied on the tensile surface of these cantilever strengthened beams, the possibility of occurrence of the pull-out of CFRP bars increases in comparison with the occurrence of concrete cover delamination failure at the ultimate stage. Moreover, both cantilever and simply supported beams strengthened with similar NSM CFRP configuration revealed the same prevailing failure modes at the maximum capacity, implying no effect in terms of strengthening outward pressure of the cantilever beams at the ultimate stage.

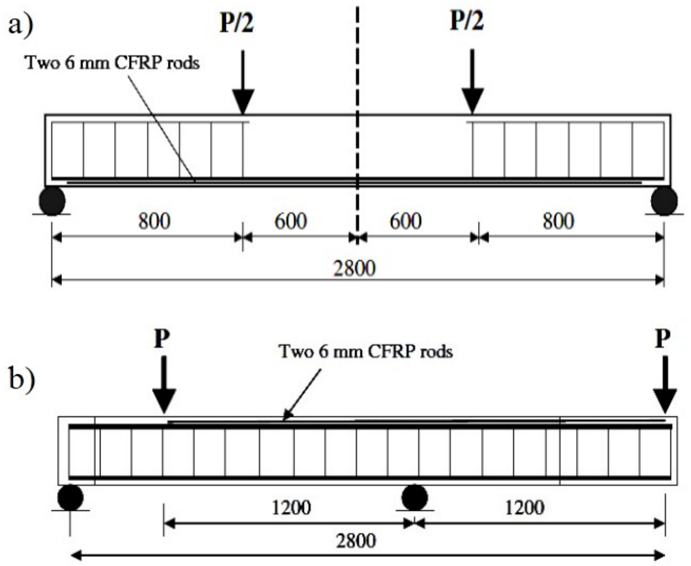

Figure 2-3: Tested beams by Al-Mahmoud et al. (2010), a) four point-loaded beams, b) cantilever beams (dimensions in mm)

In order to improve the ultimate deflection capacity of RC beams strengthened with NSM CFRP bars, a partially bonded strengthening approach was experimentally investigated by Choi et al. in 2011a. The partially bonded system is similar to the fully bonded system except an intentional unbonded length of the CFRP bar within middle portion of RC beams (Figure 2-4). An experimental program was carried out on RC T-beams strengthened with fully bonded and partially bonded CFRP reinforcements. The results revealed that increasing the unbonded length decreased the stiffness of the beams at the postyielding phase resulting in an increase in terms of the ultimate deflection capacity when compared with the fully bonded beams. In terms of ultimate load carrying capacity, the partially bonded beams was slightly smaller due to the prevailing concrete crushing failure mode, since fully bonded beams failed by CFRP rupturing (Choi et al. 2011a).

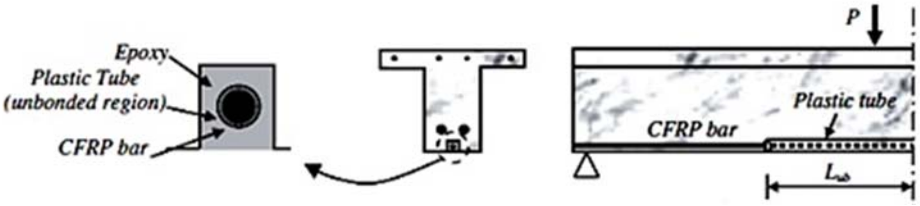

Figure 2-4: Configuration of partially bonded beams (Choi et al. 2011a)

The most common CFRP bar types used in the NSM strengthening technique have cross sections of rectangular, square and circular shape (Figure 2-5). El-Hacha and Rizkalla (2004) conducted a study on the flexural strengthening of RC beams using either NSM CFRP circular or rectangular cross sections, and they found that CFRP of rectangular cross section with high width to thickness ratio exhibits better bond behavior than other types due to the higher contact perimeter to cross sectional area ratio. On the other hand, the influence of filling material of the groove (with either resin or mortar) for NSM technique using the CFRP bars on the flexural performance of the strengthened beams was investigated by Al-Mahmoud et al. (2009). The results evidenced that the prevailing failure mode of the strengthened beams at the ultimate stage is influenced by the type of the used filling material. In other words, the CFRP bar embedded in the resin showed a better bond behavior with the concrete than the one embedded in the mortar.

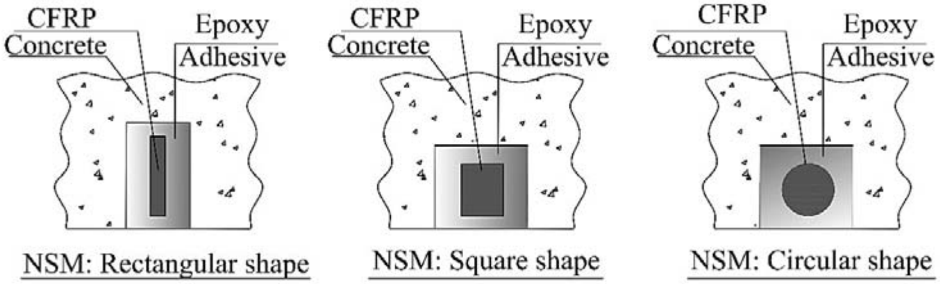

Figure 2-5: NSM CFRP cross sections

The possible flexural failure modes for the RC beams strengthened with CFRP reinforcement using NSM technique can be classified into distinct categories, namely: tension failure of CFRP, concrete compression failure, delamination of concrete cover, and CFRP debonding (ACI-440.2R. 2008, Xue et al. 2009).

In this context, De Lorenzis and Teng (2007) provided a review of existing research on the structural aspects of NSM FRP strengthening of RC structures. They identified different possible bond failure modes of NSM FRP systems, which are briefly described in the following:

a) *Bond failure at the FRP bar-epoxy interface*: this failure may occur as either pure interfacial failure (BE-I) or cohesive shear failure in the groove filler (BE-C), as represented in Figure 2-6a and Figure 2-6b, respectively.

b) *Bond failure at the epoxy-concrete interface*: this bond failure can occur as pure interfacial failure (EC-I) or as cohesive shear failure in the surrounding concrete (EC-C), as represented in Figure 2-6c and Figure 2-6d, respectively.

c) *Splitting of the epoxy cover*: this failure occurs due to longitudinal cracking of the groove filler and/or fracture of the surrounding concrete along inclined planes. When this failure is limited to the epoxy cover, it is designated by SP-E failure in Figure 2-6e. Besides, this failure can involve a combination of the longitudinal cracking in the epoxy cover and fracture of the surrounding concrete along inclined planes (SP-C1 failure in Figure 2-6f). These inclined planes in the concrete have been observed to form an angle (θ) of approximately 30° with horizontal. Moreover, facture of the concrete may occur before cracking of the epoxy cover (SP-C2 in Figure 2-6g). On the other side, when a NSM bar is applied close to the edge of concrete element, the failure involves the splitting of the concrete edge (SP-ED failure in Figure 2-6h) with the angle θ ranging between 45 and 70°.

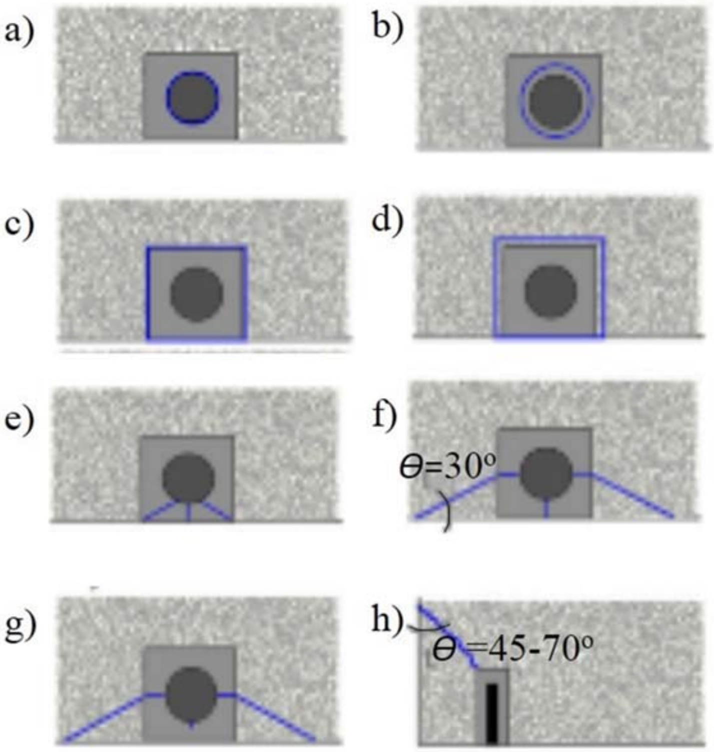

Figure 2-6: Bond failure modes of NSM systems: a) BE-I, b) BE-C, c) EC-I, d) EC-C, e) SP-E, f) SP-C1, g) SP-C2, h) SP-ED failure (De Lorenzis and Teng 2007)

2.1.2 Strengthening of RC Beams with Prestressed CFRP

The strengthening potentialities of high tensile strength CFRP reinforcements can be mobilized by using composite material applied with a certain prestress level. Nordin and Taljsten (2006) applied a prestress force to the NSM CFRP reinforcement for the flexural strengthening of RC beams resulting a better utilization of these high tensile strength materials. The results evidenced that applying an appropriate prestress level on the CFRP reinforcement can significantly increase the load carrying capacity corresponding to concrete cracking and steel yielding initiations compared to the use of non-prestressed CFRP reinforcement (Nordin and Taljsten 2006, El-Hacha and Gaafar 2011).

In fact, this increase of load carrying capacity in terms of concrete cracking and steel yielding initiations can be important for a construction’s lifetime in terms of fatigue behavior and durability benefits. In this regards, Oudah and El-Hacha (2011a) investigated the influence of the prestress level on the fatigue performance of RC beams strengthened with NSM CFRP bars. The obtained fatigue results showed that prestressing the CFRP bars enhanced the debonding resistance at the epoxy-concrete interface, as well as reduced significantly the maximum strain increase of the longitudinal tensile steel bars leading an increase in terms of fatigue life.

On the other side, Hajihashemi et al. (2011) evaluated experimentally the flexural behavior of RC beams strengthened with prestressed CFRP reinforcement in terms of deflection and crack width. They reported that prestressed CFRPs can decrease the deflection and crack width when compared to the corresponding results obtained with non-prestressed CFRPs. In fact, this benefit of NSM prestressing technique can reduce the probability of corrosion in steel reinforcement, which is a remarkable benefit in terms of the durability of RC strengthened structures.

Moreover, by applying an appropriate prestress level on the CFRP, in addition of decreasing the crack width, existing cracks in damaged RC structures to be strengthened can even close. In this regards, an experimental program, consisting of pre-damaged RC I-girders strengthened with either CFRP sheets or prestressed NSM CFRP bars, was executed by Casadei et al. (2006). The test results showed that the NSM prestressing technique provided an initial flexural stiffness for the pre-damaged beam close to the undamaged unstrengthened beam (as control beam), as well as a more ductile behavior when compared to the use of externally bonded CFRP sheet technique.

The experimental studies conducted by Badawi and Soudki (2009), and El-Hacha and Gaafar (2011), evidenced that the maximum load carrying capacity of the strengthened beams is, however, not influenced by the applied prestress level, while the prestressed CFRPs provide an increase of load carrying capacity for deflection levels corresponding to the serviceability limit state (SLS). Moreover, El-Hacha and Gaafar (2011) developed an anchorage system for prestressing NSM CFRP bars by jacking and reacting against the concrete members itself as represented in Figure 2-7a. In this context, Barros (2009) also developed a prestressing system for the flexural strengthening with NSM prestressed CFRP laminates for job site conditions, represented in Figure 2-7b, and a more detailed description of this system can be found in section 3.1.

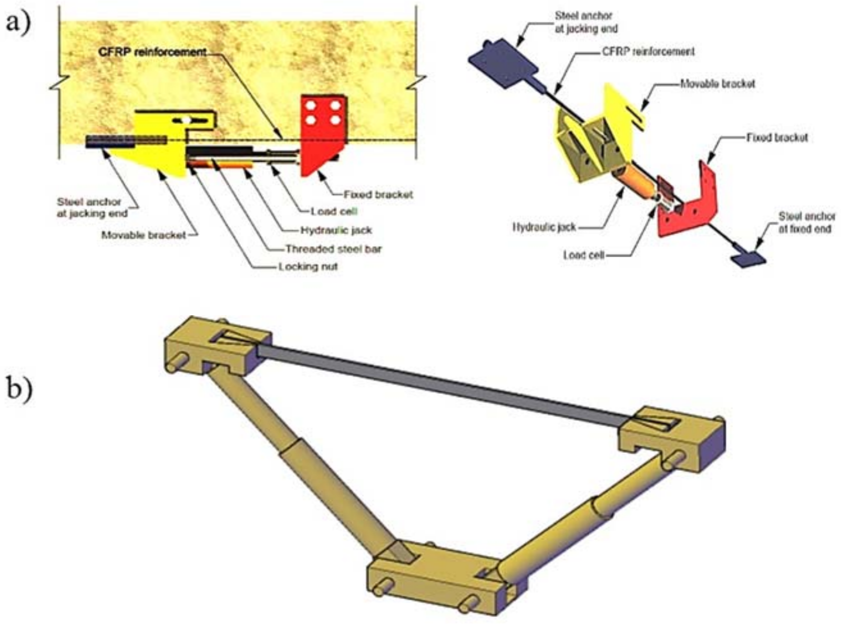

Figure 2-7: Prestressing systems for real applications developed by: a) El-Hacha and Gaafar (2011), b) Barros (2009)

In spite of the mentioned benefits of prestressing system, the experimental results have indicated a decrease in terms of energy absorption and deflection performance up to failure of the strengthened beams, when the prestress level applied to the NSM CFRP reinforcement increases (Nordin and Taljsten 2006, Hajihashemi et al. 2011). The energy absorption (E_d) is determined by integrating the area under the force-deflection curve up to the deflection at ultimate strength (d_u), while the deflection performance is evaluated through a ductility index (μ) that is defined as ratio between the deflection corresponding to the ultimate strength (d_u) and to the steel yield initiation (d_y) of the beams ($\mu = d_u / d_y$). This ductility criterion evaluates the ability of a structure to sustain plastic deformation without significant loss of load carrying capacity prior to collapse.

On the other hand, beams flexurally strengthened with FRP systems applied according to EBR or NSM technique do not present an almost perfectly plastic behavior after yielding of the longitudinal tensile steel bars, as is the case of conventionally RC beams, since the FRP reinforcement has linear elastic behavior up to its brittle failure (Jo et al. 2004, Oudah and El-Hacha 2012). Hence, in order to evaluate the ductility performance of FRP strengthened RC beams, Mufti et al. (1996) and Choi. (2008) proposed deformability criterion to evaluate the capacity of FRP strengthened beams to present, timely, signals of attaining collapse. Deformability index (μ_d) is defined as the ratio between the deflection corresponding to the failure (d_u) and to the SLS conditions (d_{SLS}) of the FRP strengthened beams ($\mu_d = d_u / d_{SLS}$).

To improve the deflection capacity of prestressed NSM CFRP strengthened RC beams, partially bonded prestressing system (similar to fully bonded system except an unbonded portion of CFRP length at mid-span) was applied by Choi et al. (2011b) (as represented in Figure 2-4). Although the partially bonded strengthening has provided an improvement of the deformability compared to the fully bonded strengthening system, a slight decrease (4%-11%) was observed in terms of load carrying capacity at the steel yield initiation and at the failure when the corresponding values for the fully bonded system with similar prestress level were considered for comparison purpose.

The distribution of tensile strain and bond shear stress at the extremity zones of NSM CFRP reinforcement applied on the tensile surface of the RC beams after the total release of the prestress force was experimentally evaluated by Badawi et al. (2010). The experimental program was consisted of twenty-two RC beams strengthened with either prestressed spirally wound or sand blasted CFRP rods. The test results showed that, regardless the prestress level, the length of transmission zone of the prestress force (also known as prestress transfer length) at both extremities of the NSM CFRP rods can be estimated as 35 times the diameter of the CFRP rod.

2.2 Numerical Analyses

Although NSM FRP systems have been extensively used for the flexural and shear strengthening of RC structures, still further numerical analyses are necessary to evaluate the influence of the several parameters on the flexural performance of the NSM CFRP strengthened structures.

In this context, a 3D FE model, capable of simulating the nonlinear behavior of the constituent materials, and the bond behavior between filling materials and concrete, was developed by Hawileh (2011) to simulate RC beams strengthened with FRP rods. This FE model was validated by comparing with the experimental results in terms of flexural response and prevailing failure mode at the ultimate stage, and a good predictive performance was achieved.

Oudah and El-Hacha (2011b) simulated RC beams strengthened with either prestressed NSM CFRP strips or rods using a 2D FE model. In this FE model, the steel and CFRP reinforcements were embedded in the concrete elements. The prestressing force was also applied to the CFRP reinforcement using uniform stress value over the elements as an initial condition. After the assessment of the predictive performance of the FE model, they proposed an optimum prestress level of 25% and 23% of the ultimate CFRP tensile strength for the beams strengthened using NSM CFRP strips and rods, respectively. The optimum prestress level is the one that maintains the ductility index of the prestressed beam equal to the one corresponding to the unstrengthened beam.

Moreover, a 3D nonlinear FE analysis of RC beams strengthened with prestressed NSM CFRP strips was carried out by Omran and El-Hacha (2011) with the aim of determining an optimum prestress level for the NSM CFRP reinforcement that enhances the beam performance under service and ultimate loads by maintaining the energy absorption value of the prestressed beams equal to the unstrengthened control beam. In this FE model, debonding effect at the epoxy-concrete interface was considered using a mixed-mode debonding model (normal tensile stress-separation and shear stress-slip models). Moreover, the prestress force was applied to the CFRP reinforcement adopting an equivalent temperature method. To reduce the computer computational time of numerical analysis, only one quarter of the beam was modeled due to the symmetry in geometry and loading conditions as represented in Figure 2-8a.

This numerical analysis evidenced that increasing the prestress level results in the decrease of energy absorption index (E_d). Therefore, an optimum prestress level of 30% was numerically found for the NSM CFRP reinforcement applied for the flexural strengthening purpose. On the other hand, the numerical results showed that the debonding propagation at ultimate stage, mainly caused by high deflection and crack opening, is less for the prestressed beam compared to the passive beam (Omran and El-Hacha 2011). Figure 2-8b and Figure 2-8c represent debonding parameter (d_m) at ultimate stage for the passive and 30% prestressed strengthened beams, where d_m varies from 0 (debond initiation) to 1 (full debond). These figures evidence that debonding occurrence at ultimate stage for the 30% prestressed beam was much less than the corresponding term of the passive beam.

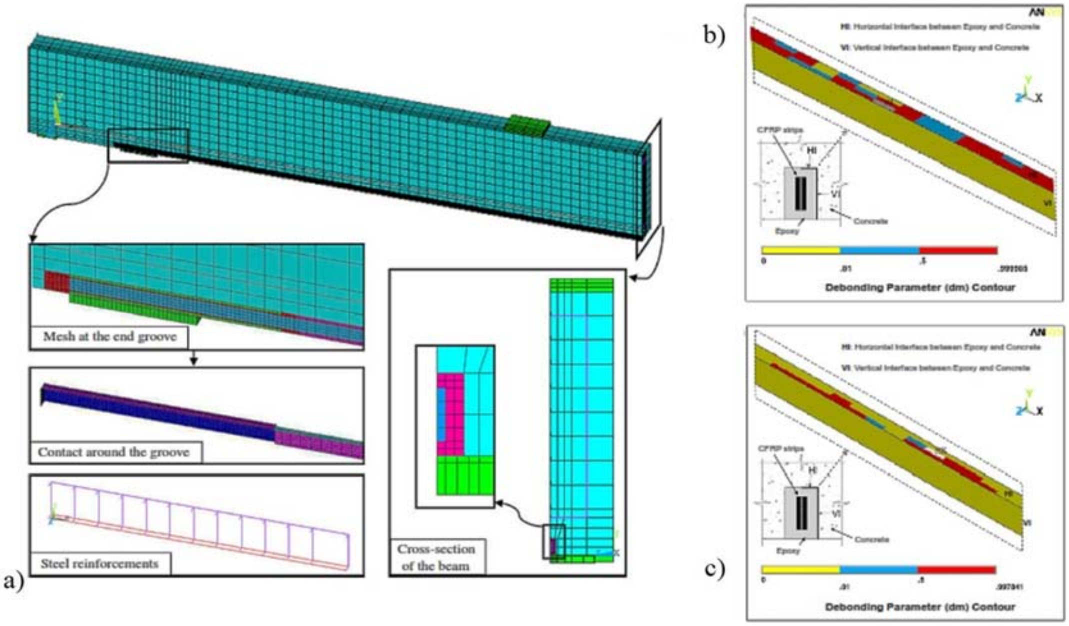

Figure 2-8: a) FE model of the prestressed NSM CFRP beams; debonding parameter d_m at ultimate: b) passive beam, c) 30% prestressed beam (Omran and El-Hacha 2011)

Radfar et al. (2012) developed a 3D numerical strategy to predict the behavior and ultimate load carrying capacity of the RC beams flexurally strengthened with FRP sheet failed by concrete cover delamination (peeling-off failure). In this FE model, full bond is assumed between FRP and concrete without considering the adhesive layer. A fine mesh refinement was applied in the area susceptible to concrete cover delamination failure (at the end of FRP bonded length) as represented in Figure 2-9a (only one quarter of the beam was modeled due to symmetry conditions). Furthermore, in order to numerically simulate the crack initiation at the end section of the FRP bonded length due to the concrete cover delamination failure, an energy-based criterion considering the tensile fracture energy of concrete was defined above a little zone along the beam's width at this section (Figure 2-9b), where relatively high stress gradients are expected to occur due to delamination failure. Moreover, to simulate the tensile behavior of concrete, the Drucker-Prager model was combined with the fracture mechanics in order to detect failure in concrete tensile zone.

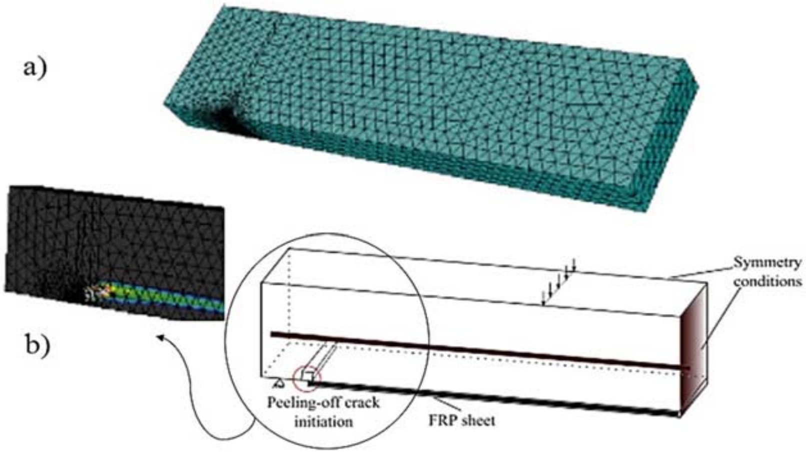

Figure 2-9: a) FE mesh of the model, b) criterion for crack initiation (Radfar et al. 2012)

A 3D FE model was developed by Abdelatif et al. (2014) to simulate the transmission zone of the prestress force from steel to concrete in pre-tensioned concrete elements (Figure 2-10a). The bond between steel and concrete surfaces was modeled using surface-based contact interfaces. Moreover, the coulomb friction law was used to define the friction behavior of these interfaces with a tangent of friction angle of 0.4 and zero cohesion. In this FE model, numerical simulation of the prestressing procedure includes three steps: prestressing the steel tendon; casting of concrete simulated by introducing the interfaces; release of the prestress force. The numerical analysis showed that the release of the prestress force causes radial cracks in the concrete surrounding the steel tendon due to expansion of the tendon. Figure 2-10b shows the crack pattern in the surrounding concrete along the prestress transmission length by plotting the maximum principle plastic tensile strain in the concrete elements.

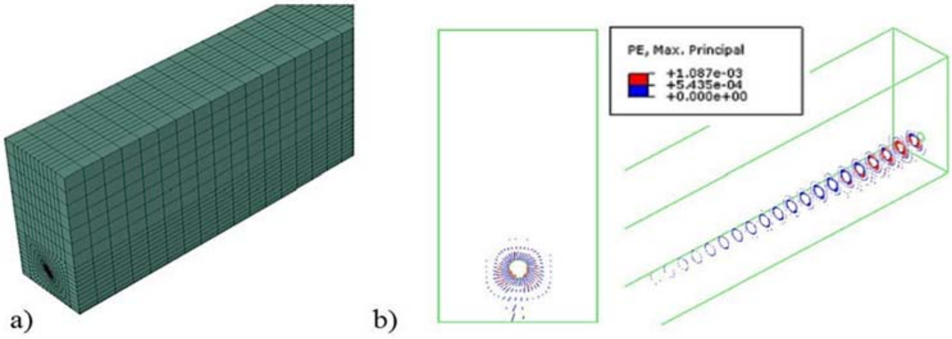

Figure 2-10: a) Meshing of the FE model, b) radial cracks in the concrete surrounding the prestressed steel tendon (Abdelatif et al. 2014)

2.3 Analytical Approaches

In the current section, a review of analytical approaches to predict the behavior of RC structures strengthened with FRP reinforcement applied according to either NSM or EBR techniques, in terms of moment-curvature and force-deflection relationships, is briefly presented.

The moment-curvature relationship of the cross section of RC beams was idealized by Alwis (1990) as a trilinear diagram representing the uncracked concrete, cracked concrete with reinforcement in elastic behavior, and cracked concrete with reinforcement in yielded stages of a RC beam. A trilinear moment-curvature response was also considered by Saqan and Rasheed (2010) for rectangular cross section beams reinforced with prestressed steel strands in order to compute the neutral axis depth with a simple hand calculation instead of an iterative numerical procedure for the cracked section.

On the other hand, the flexural capacity and the deformational behavior of FRP strengthened beams can analytically be predicted by using a trilinear moment-curvature relationship based on the strain compatibility and principles of static equilibrium. In this context, El-Mihilmy and Tedesco (2000), and Rasheed et al. (2004) adopted a trilinear relationship with precracking, postcracking, and postyielding stages to predict the flexural response of RC beams flexurally strengthened with FRP plates (represented in Figure 2-11). The first stage of this trilinear response extends to the onset point of concrete crack initiation, while the second one follows until the steel yield initiation point in tension. The third stage continues up to the maximum flexural capacity, limited by either concrete crushing or rupture of the FRP reinforcement. According to these proposed models, the design procedure of FRP strengthened beams is, however, lengthy to carry out by hand calculation, since the neutral axis depth is determined using the iterative methods for the cracked concrete sections, and accordingly, some programming is needed to expedite the iterations. On the other side, engineers with limited exposure to FRP design need a guidance to design this type of strengthened structures by hand calculation without any programming help.

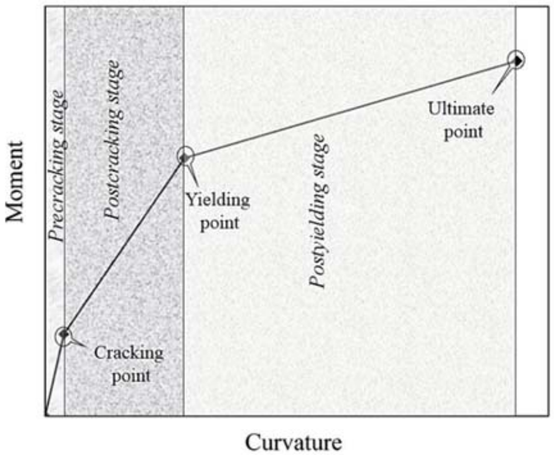

Figure 2-11: Trilinear moment-curvature response of FRP strengthened beam

Although the ultimate flexural capacity of RC beams can be increased significantly by using FRP reinforcement, its efficiency for the flexural strengthening may be limited by the occurrence of premature failure modes, such as: concrete cover delamination, and debonding of FRP from the concrete substrate.

Concrete cover delamination can occur due to the formation and propagation of a fracture surface in the concrete cover at the free extremity of the FRP reinforcement (Xiong et al. 2007). To analytically predict the load carrying capacity of RC beams strengthened with EBR FRP strips when concrete cover delamination takes place, Gao et al. (2004) developed a design methodology considering the stress concentration in concrete just below the longitudinal steel bars in tension at the end section of the FRP bonded length. This methodology was implemented in two stages: (I) prediction the strains of constituent materials along the depth of the cross section assuming a full composite action; (II) determination of the local stresses just below the steel reinforcement and comparison with the concrete strength. Moreover, the model assumes linear elastic and isotropic behavior for concrete, FRP, epoxy, and steel reinforcement, as well as perfect bonding between FRP and concrete.

Debonding of FRP reinforcement from the concrete substrate can be classified in two types: (a) the one induced by a flexural or flexural-shear crack away from the end section of FRP bonded length; (b) the one associated with high interfacial stresses near the end section of the bonded FRP (Teng et al. 2003).

The first failure type, which is referred to as intermediate crack-induced debonding (IC debonding), can be analytically predicted using the design model proposed by Teng et al. (2003). This design model was obtained through a simple modification of the bond strength model for steel and FRP plate-to-concrete bonded joints proposed by Chen and Teng (2001). In this regards, first they discovered the similarity between IC debonding failures and debonding failure in simple shear tests (FRP plate-to-concrete bonded joints), and then, developed the design model to predict IC failures.

The second failure type is caused by shear and normal stress concentrations at the end section of the bonded length of FRP plate (cut-off point). In this context, Malek et al. (1998) proposed a closed form solution to analytically determine these stress consecrations at the FRP cut-off point. They, moreover, defined two equations as maximum stress criteria for the shear and normal stresses at the FRP cut-off section to analytically predict the occurrence of the FRP debonding failure.

On the other side, the proposed model by Malek et al. was modified by Hassan and Rizkalla (2003) to account for the double bonded area of FRP strips flexurally applied according to NSM technique. In this model, debonding of NSM strips is assumed to occur as a result of high shear stress concentration at the NSM FRP cut-off point accounting only for cases in which FRP debonding failure is initiated from this cut-off zone. They, also, proposed a maximum sustainable interface shear stress, as a stress criterion in concrete (at cut-off section) in order to analytically predict this type of FRP debonding failure. This failure criterion was defined using the compressive and tensile strength of concrete considering the Mohr-Coulomb line, which is tangential to both Mohr's circles for pure tension and pure compression, as represented in Figure 2-12.

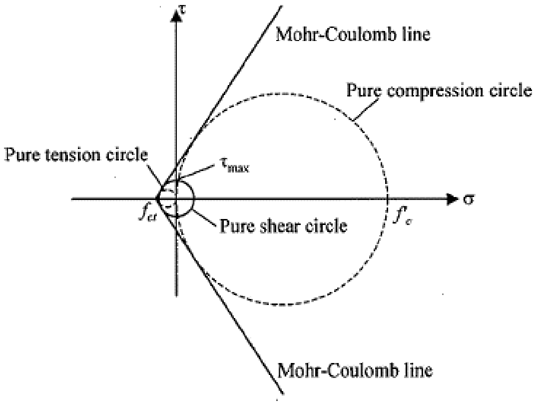

Figure 2-12: Mohr-Coulomb failure criterion (Hassan and Rizkalla 2003)

After analytical prediction of the trilinear moment-curvature relationship of FRP strengthened RC beams, Rasheed et al. (2004) determined the force-deflection response, considering this trilinear relationship, by integrating the curvature along the beam length. On the other hand, El-Mihilmy and

Tedesco (2000) proposed a method for calculating the deflection using the developed effective moment of inertia for FRP strengthened RC beams. In fact, this effective moment of inertia considers the effect of stiffness variation caused by nonuniform cracking of the concrete along the beam length. In this regards, the studies have shown that the performance of the proposed analytical model to predict the force-deflection response of FRP strengthened beam using the effective moment of inertia is dependent on the accuracy of the used method to determine the concrete cracking moment, maximum moment, and uncracked and cracked moment of inertias (Xue et al. 2009, Kalkan 2010, Akmaluddin. 2012).

Barros and Dalfré (2013) proposed an analytical approach to calculate the deflection of RC structures strengthened according to NSM or EBR technique based on the force method, also known as flexibility method, consisting on establishing a set of displacement compatibility equations whose number is equal to the unknown redundant supports and generalized displacements (or forces) to be determined. The proposed model is capable of predicting the force-deflection response up to the collapse of statically indeterminate RC structures whose reactions and internal forces cannot be determined from direct application of the static equilibrium equations.

The deflection of the strengthened beams was also estimated by Badawi and Soudki (2009) based on dividing the beam into a number of elements (sections). According to the concept of this model, the beam span falls into the uncracked and cracked regions (Figure 2-13). The cracked region is discretized in a certain number of elements with the length equal to average crack spacing. This average crack spacing was calculated based on the recommendation of Eurocode accounting for the modular ratio of the reinforcement (steel and CFRP) and the location of the neutral axis for the composite section. Finally, the maximum mid-deflection of the RC beam is estimated based on the integration of curvature in the uncracked and cracked zones along one half of the beam length.

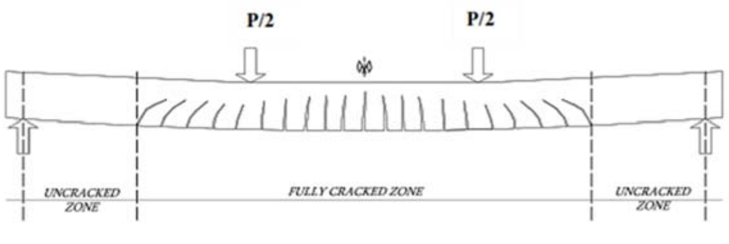

Figure 2-13: Beam divided into uncracked and cracked zones (Badawi and Soudki 2009)

For the beams strengthened with FRP reinforcement partially bonded to concrete applied according to either EBR or NSM techniques, Choi et al. (2008 and 2011a) developed an analytical model based on the curvature approach to predict the flexural behavior of the strengthened beams. This model assumes that a constant tensile strain exists in the unbonded FRP reinforcement located at the mid-span of the beam. This constant FRP tensile strain was estimated using the average compressive strain value at the concrete top fiber located in this region adopting the proportional strain distribution to the distance from the neutral axis depth along the beam's cross section, while this issue reduces the predictive performance of the model, since unbonded conditions exist for the FRP reinforcement within this region. According to this model, the beam is divided into the several sections including the loading point section, bond transition section, and the sections corresponding to the flexural moment of concrete cracking and steel yielding initiation stages (Figure 2-14). Choi et al. (2011b), moreover, adopted this proposed model to predict the flexural behavior of the RC beams partially strengthened with prestressed NSM CFRP reinforcement.

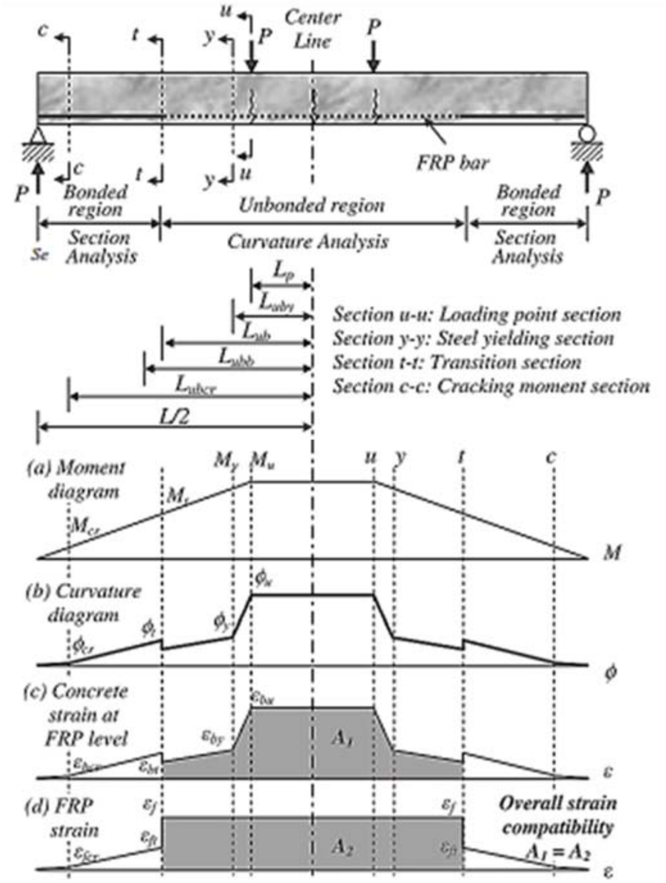

Figure 2-14: Moment, curvature, and strain distribution of a partially FRP strengthened beam (Choi et al. 2011a)

After the total release of prestress force, this force is transferred from FRP reinforcement to concrete over a length in both extremities of the FRP through interfacial bond between FRP-epoxy adhesive and concrete-epoxy adhesive connections. This length is known as transmission length, or transfer length, which is one of the critical aspect that should be taken into account for designing the prestressed RC beams (Abdelatif et al. 2014). In this context, Mahmoud et al. (1999) and Badawi et al. (2010) proposed empirical equations based on the experimental data to predict the prestress transfer length of the RC beams strengthened with prestressed FRP reinforcement.

Chapter 3: Experimental Program

In the context of the flexural strengthening of RC beams with NSM CFRP laminates, the current chapter mainly aims to experimentally assess first, the influence of the prestress level applied to the laminates on the strengthening performance and then, the potentialities of a new NSM hybrid methodology combining non-prestressed and prestressed CFRP laminates in the same application. Moreover, the tensile strain and bond shear stress fields developed along the prestressed NSM CFRP reinforcement just after the release of the prestress force are experimentally evaluated in this chapter. On the other side, a detailed description of the prestressing system adopted in the present experimental program (for the laboratory conditions) and a prestressing system for the flexural strengthening of RC beams with prestressed NSM CFRP laminates capable of being used in job site conditions are introduced in the current chapter.

3.1 Prestressing System

3.1.1 Laboratory Conditions

The prestressing system represented in Figure 3-1 was designed to apply the prestress force to the CFRP reinforcement by taking advantage of an existing high stiff reaction steel frame in the laboratory of Minho University (Costa and Barros 2012). The prestress force was applied to the laminate at the sliding extremity of the prestressing system (Figure 3-1) using a hollow hydraulic cylinder with maximum capacity of 200 kN. This hydraulic cylinder was connected to a through-hole load cell of same capacity to control the process of applying and releasing of the prestress force. To simultaneously release the prestress force in both extremities of the RC beams, two steel rollers were placed under the beams. Additionally, to ensure the simultaneity of this release process, an electrical strain gauge was installed on the CFRP laminate at the fixed extremity (outside the bonded length of the CFRP reinforcement) to monitor the release rate of the prestress force at this extremity. Moreover, a LVDT was installed at the mid-span of the beam to record the vertical deflection of the beam during the prestress releasing.

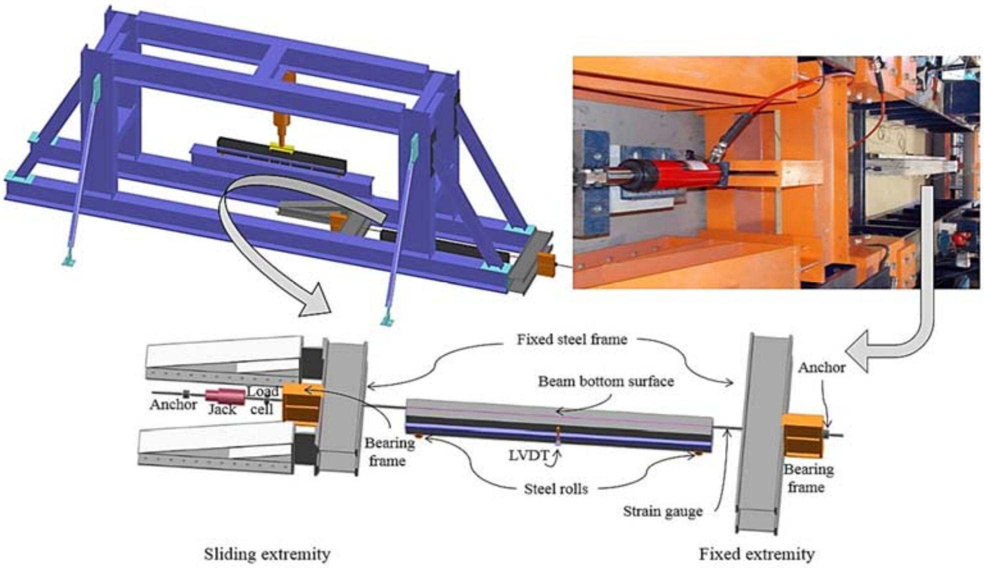

Figure 3-1: Prestressing system adopted in laboratory

The NSM CFRP prestressing procedure adopted for the current experimental programs consists of the following steps: 1) opening a groove on the concrete cover of the tensile surface of beam using a diamond cutter (Figure 3-2a); 2) cleaning the groove using a compressed air; 3) placing the laminate into the center position of the groove and applying the prestress force to the CFRP reinforcement (Figure 3-2b); 4) filling the groove with epoxy adhesive (with the trademark of S&P Resin 220 epoxy adhesive) (Figure 3-2c); 5) releasing the prestress force (Figure 3-2d).

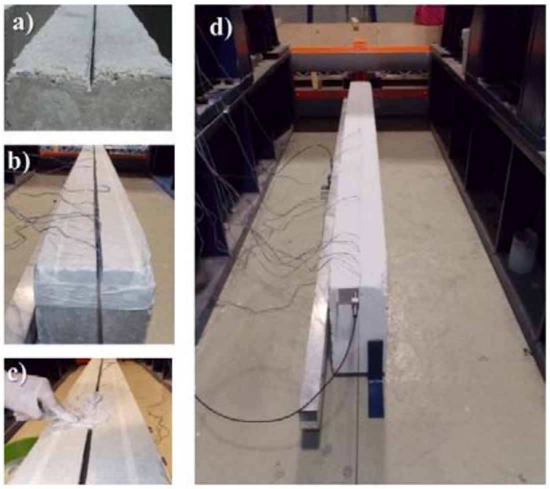

Figure 3-2: NSM CFRP prestressing procedure: a) opening the groove, b) placing laminate into groove and prestressing, c) filling the groove with epoxy, d) releasing the prestress force

In fact, in case of applying prestressed CFRPs according to NSM technique, this procedure has a difficulty in terms of covering the CFRP reinforcement with epoxy adhesive due to the thin thickness of groove, causing an uncertainty to guarantee a completely covered CFRP.

The prestress force was totally removed after the recommended curing time for epoxy adhesive (72 hours at room temperature) adopting a relatively low releasing rate of 0.3 kN/min, in order to avoid damage in the CFRP-adhesive-concrete connections.

3.1.2 Job Site Application

3.1.2.1 Discription of System

The prestressing system used in laboratory conditions is a simplification of the method proposed by Barros (2009) for real conditions on the flexural strengthening with prestressed NSM CFRP laminates, which is schematically represented in Figure 3-3. To apply a certain prestress level on the CFRP laminates using this prestressing system, after removing the concrete cover near the zones where the laminate will be anchored at the extremities of the beams, the prestress force is applied by an actuator through the telescopic steel tubes to the anchorage pieces (Figure 3-3). The detailed description and the design of this system can be found elsewhere (Costa and Barros 2009a). It is worth to note that the prestressing system implemented in the laboratory was designed to take advantage of an existing high stiff reaction frame composed of steel profiles, and aiming a relatively ease, fast and safe application of prestress to the CFRP laminates in laboratory conditions.

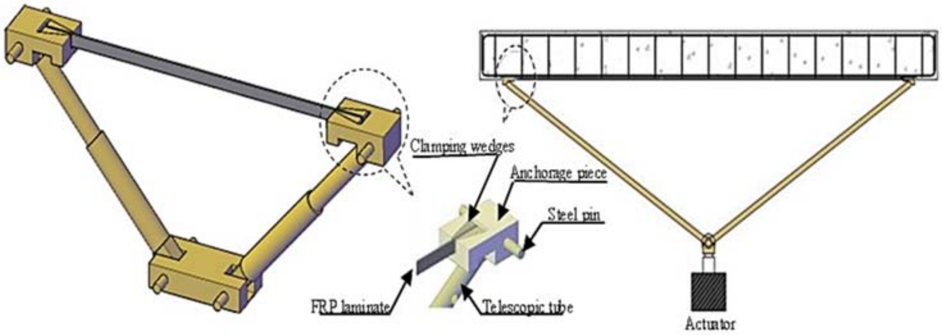

Figure 3-3: Prestressing system for real applications developed by Barros (2009)

3.1.2.2 Design Improvement

The present section aims to optimize and design the components of the proposed prestressing system for real applications (represented in Figure 3-3) to apply a certain prestress level to the CFRP laminates, performing a numerical analysis using finite element (FE) software.

3.1.2.2.1 Description of FE Model

A 3D FE model using ABAQUS software was used to simulate the components of the prestressing system, including anchorage piece, clamping wedges, steel pine, telescopic tube, tube wedge, and CFRP laminate (as represented in Figure 3-3).

Constitutive Material Model

A linear isotropic elasticity model was adopted to simulate the behavior of the steel components of the prestressing system. The elasticity modulus and Poisson ratio of the steel material were considered as 200 GPa and 0.3, respectively.

Interfacial Bond Model

To simulate the bond behavior between the surfaces of the components of the prestressing system, two surface-based interactions (hard-contact and tie constraint) were defined. Tie constraint was applied at the CFRP laminate-clamping wedges (tie1), anchorage piece-clamping wedges (tie2), and telescopic tube-tube wedge (tie3) surfaces (Figure 3-4a), while the hard-contact was used at the tube wedge-steel pin (hard-contact1) and anchorage piece-steel pin (hard-contact2) surfaces (Figure 3-4b).

The surface-based hard-contact does not allow the transference of tensile stress across the interface and minimizes the penetration of two surfaces, resulting to transmit any contact pressure between the surfaces once they are in contact. In other words, the surfaces will be separated when the contact pressure reduces to zero, and these separated surfaces come into contact when the clearance between them reduces to zero.

Surface-based tie constraint provides a perfect bond condition (no-slip occurrence) between two surfaces during the numerical analysis. In other words, it can be used to make the translational and rotational motions, as well as all other active degrees of freedom equal for a pair of surfaces (ABAQUS. 2011).

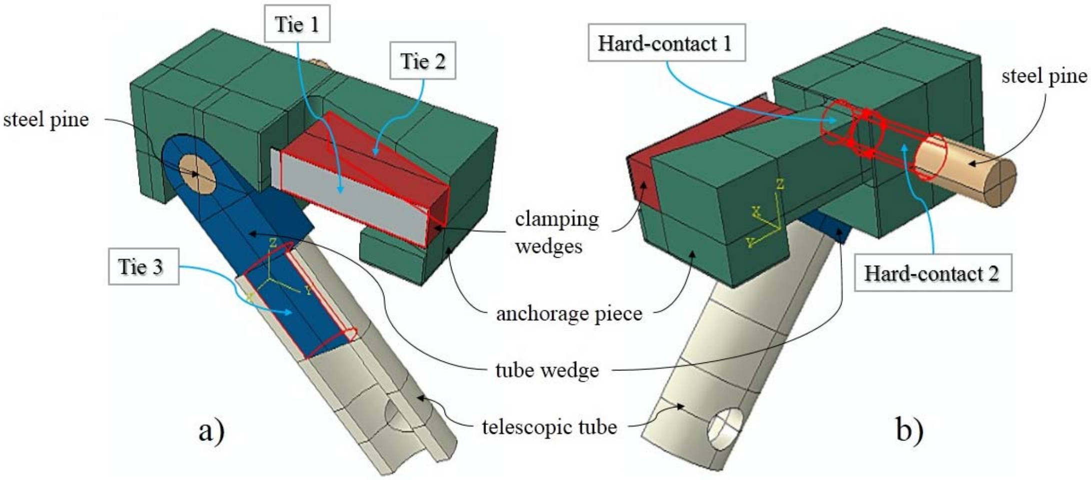

Figure 3-4: Surface-based interactions in FE model: a) tie constraint, b) hard-contact

<u>Boundary Conditions, Element Types and Meshing</u>

3D eight-node solid element was used to model the anchorage piece, clamping wedges, steel pine, telescopic tube, tube wedge and CFRP laminate. Figure 3-5a represents the FE mesh of the numerical model, where a fined mesh refinement was applied in the zones where relatively high stress gradients are expected to develop.

To reduce the computational time of the numerical analysis, one-half of the prestressing system was modeled, taking advantage of the symmetry plane of the prestressing system. The loading and boundary conditions of the model were applied according to the configuration of the prestressing system in real application (Figure 3-5b).

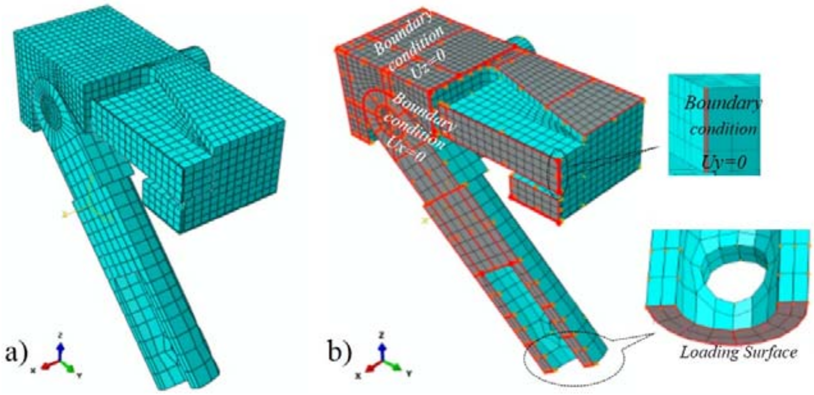

Figure 3-5: a) Finite element mesh of numerical model, b) loading and boundary conditions

3.1.2.2.2 Results of Numerical Analysis

A 60% prestress level of CFRP nominal tensile strength (considering elasticity modulus of 150 GPa and nominal tensile strength of 2000 MPa) was numerically applied through loading of the telescopic tube to the laminate in order to design the components of the prestressing system. This prestress level was adopted as an upper limit of allowable prestress level that can be applied to CFRP reinforcement according to the recommendation of (CAN/CSA-S6-00. 2000). For this prestress level, the stress field according to Von-Mises stress criteria is represented in Figure 3-6 for the components of the prestressing system, where it is verified that the steel's yield stress (355 MPa) is not exceeded.

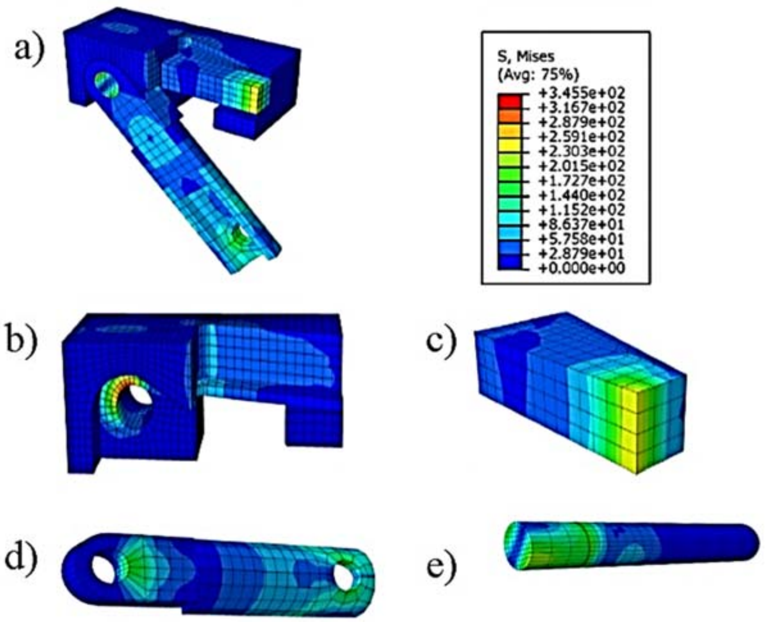

Figure 3-6: Distribution of the Von-Mises stress field in: a) analyzed system of the device , b) anchorage piece, c) clamping wedge, d) telescopic tube and tube wedge, e) steel pin

The dimension of the components of the prestressing system was optimized using a back analysis of these dimensions considering the results of the numerical analysis in order to find relatively small and lightweight components. Hence, according to the results of the numerical analysis (represented in Figure 3-6), Figure 3-7 indicates the finalized dimension of the components of the prestressing system.

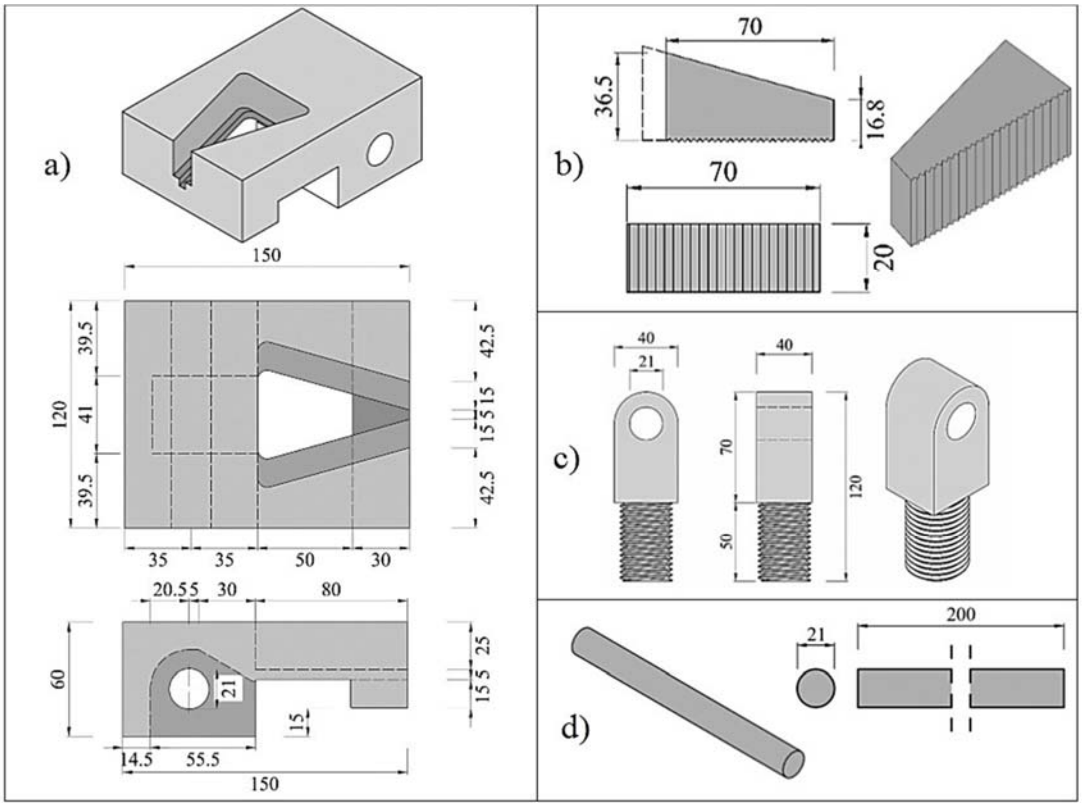

Figure 3-7: Geometry of the components of the prestressing system: a) anchorage piece, b) clamping wedge, c) tube wedge, d) steel pin (dimensions in mm)

3.2 Prestress Transmission Zone

This section presents an experimental program to assess the distribution of the tensile strain and bond shear stress after the release of the prestress force along the prestressed CFRP laminates flexurally applied on the tensile surface of RC beams according to NSM technique.

3.2.1 Specimens

The experimental program reported in this section was composed of four rectangular cross-section RC beams flexurally strengthened with a CFRP laminate prestressed up to approximately 15%, 20%, 30%, and 40% of its nominal tensile strength, by adopting the NSM technique. The geometry, steel and CFRP reinforcement details of the strengthened beams are schematically represented in Figure 3-8 (dimensions are in mm).

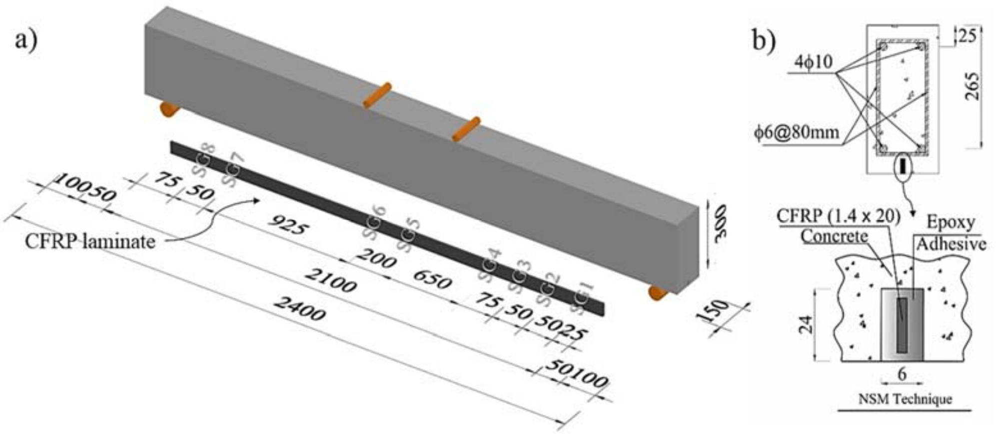

Figure 3-8: The beams of the experimental program: a) geometry and position of strain gauges (SG) installed on the CFRP laminate; b) steel and CFRP reinforcements (dimensions in mm)

For the flexural strengthening of the RC beams according to NSM technique, a CFRP laminate of 1.4 × 20 mm^2 cross sectional area was installed into a groove of 6 × 24 mm^2 cross section pre-executed on the concrete cover along the total beam length (Figure 3-8b). The CFRP laminate was bonded to the surrounding concrete using epoxy adhesive, and its extremities become at 50 mm before the supports in order to simulate a real strengthening application for the NSM technique. To monitor the distribution of tensile strains, and assess the short-term prestress losses in the CFRP reinforcement after the release of the prestress force, eight strain gauges were installed on the laminate, placed at the distances from the extremities of the CFRP bonded length indicated in Figure 3-8a (SG 1-8).

3.2.2 Prestressing Procedure

The applied prestress level was controlled by monitoring the average strain values of the strain gauges installed on the prestressed CFRP laminate (represented in Figure 3-8a), by considering the material properties reported by manufacturer (elasticity modulus of 150 GPa and nominal tensile strength of 2000 MPa).

3.2.3 Material Properties

The average values of the main properties for the concrete, steel bars, CFRP laminate and epoxy adhesive are indicated in Table 3-1. In this table, $f_{cm}^{'}$ and E_c represent the average values of the compressive strength and young's modulus of concrete at the beam testing age (153 days), respectively. f_{sym} , f_{sum} and E_s are the average values of the stress at yield initiation, tensile strength and elasticity modulus of steel bars, respectively. Table 3-1 also reports the average values of the tensile strength, f_{fum}, ultimate tensile strain, ε_{fum}, and elasticity modulus, E_f, for the CFRP laminate. Finally, in this table, f_{aum} and E_a are the average values of the tensile strength and elasticity modulus of the epoxy adhesive, respectively.

Table 3-1: Average values of the main properties of the constituent materials

Concrete (at testing age)	Compressive strength		Young's modulus	
	$f'_{cm} = 32\,\mathrm{MPa}$		$E_c = 27\,\mathrm{GPa}$	
Steel bars	Diameter	Yield strength	Tensile strength	Elasticity modulus
	6 mm	$f_{sym} = 613\,\mathrm{MPa}$	$f_{sum} = 696\,\mathrm{MPa}$	$E_s = 218\,\mathrm{GPa}$
	12 mm	$f_{sym} = 585\,\mathrm{MPa}$	$f_{sum} = 656\,\mathrm{MPa}$	$E_s = 208\,\mathrm{GPa}$
CFRP laminate	Tensile strength	Ultimate tensile strain	Elasticity modulus	
	$f_{fum} = 1922\,\mathrm{MPa}$	$\varepsilon_{fum} = 11.7\,(‰)$	$E_f = 164\,\mathrm{GPa}$	
Epoxy adhesive	Tensile strength		Elasticity modulus	
	$f_{aum} = 20\,\mathrm{MPa}$		$E_a = 7\,\mathrm{GPa}$	

3.2.4 Results

3.2.4.1 Release of the Prestress Force

To evaluate a simultaneous release of the prestress force in both extremities of the bonded CFRP laminate, a comparison is represented in Figure 3-9 of the 40% prestress force versus time recorded at the sliding extremity using the through-hole load cell, and at the fixed extremity using the installed strain gauge outside the bonded length of the CFRP reinforcement (shown in Figure 3-1). This figure evidences that the decrease of the prestress force at the fixed extremity occurred immediately after removing the corresponding force at the sliding extremity resulting in a simultaneous release of the prestress force in both extremities of the strengthened beam.

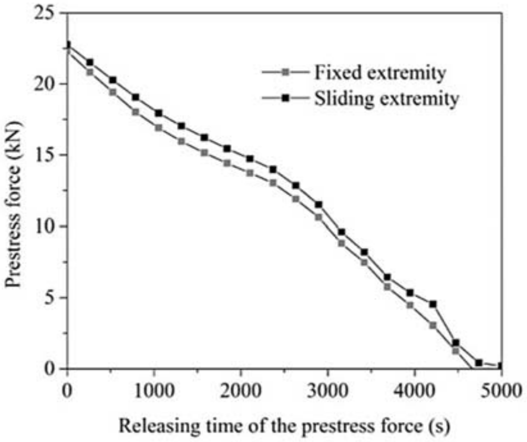

Figure 3-9: Release of the 40% prestress force at sliding and fixed extremities

3.2.4.2 Distribution of CFRP Tensile Strain

The relationship between the normalized tensile strains in the CFRP laminate after the total release of the prestress force and the distance from the end of the CFRP length bonded to the surrounding concrete is depicted in Figure 3-10 for all the prestressed beams. The normalized strain means that the registered CFRP tensile strain is divided by the corresponding initial prestrain applied to the laminate (ε_{fp}). This figure shows that the distribution of the tensile strain in the extremity region of the CFRP bonded length varies from zero (at its end section) to the effective tensile strain ($\varepsilon_{ef}^{(ci)}$, a concept to be treated in Chapter 5) and then, reaches a plateau along the CFRP length up to the mid-span of the beam. Furthermore, this figure evidences an insignificant influence of the prestress level on the transmission zone of the prestressed CFRP. Hence, in Figure 3-10, the best fit curve for the distribution of the CFRP tensile strain is represented by considering the values of the normalized strains for all the tested beams, regardless the applied prestress level.

It worth to note that the prestress force was totally removed after the recommended curing time for epoxy adhesive (72 hours at room temperature) and the reported values of the CFRP tensile strain were monitored immediately after prestress releasing.

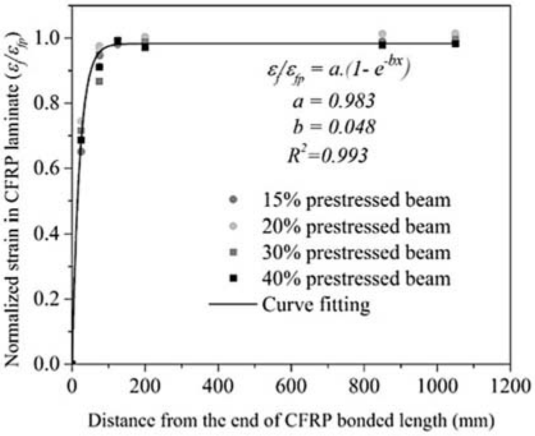

Figure 3-10: Tensile strain distribution along the CFRP bonded length

3.2.4.3 Bond Shear Stress

After the release of the prestress force, the variation of the tensile strains in the extremity regions of the CFRP bonded laminate (transmission zones) imposes a shear stress field on the CFRP-adhesive-concrete bonds. In fact, this bond shear stress, τ_{bm}^{RL}, was determined considering the evolution of the CFRP tensile strain ($\Delta\varepsilon^{RL}$) between two consecutive strain gauges installed on the CFRP laminate (SG^L and SG^R) using Eq. (3.1) (Figure 3-11).

$$\tau_{bm}^{RL} = \frac{E_f \cdot A_f \cdot \Delta\varepsilon^{RL}}{2 \cdot b_f \cdot L^{RL}}$$ Equation Chapter 3 Section 3(3.1)

where E_f, A_f, and b_f are the elasticity modulus, cross sectional area, and width of CFRP reinforcement, respectively. L^{RL} is distance between two consecutive strain gauges.

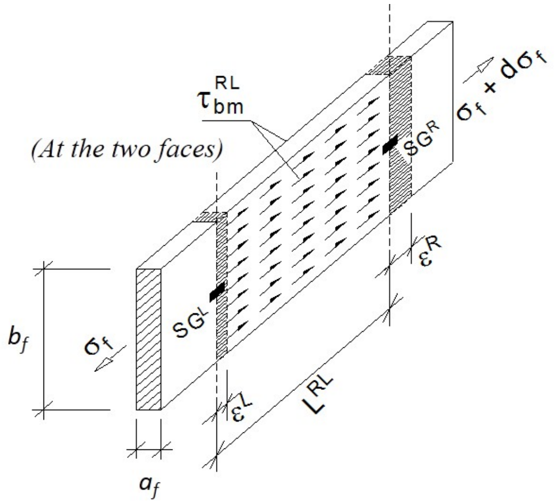

Figure 3-11: Average bond stress (τ_{bm}^{RL}) in-between two consecutive strain gauges installed to the CFRP laminate (Bonaldo et al. 2008)

The relationship between the bond shear stress and distance from the end of CFRP bonded length is represented in Figure 3-12 for all the prestressed strengthened beams after the release of the prestress force, which occurred three days after adhesive has been applied. According to this figure, the bond shear stress increases with the level of the prestress force applied to the CFRP laminate. The bond shear stress decreases exponentially from the end of the CFRP bonded length, and becomes null at the end of the transmission zone (of about 150 mm).

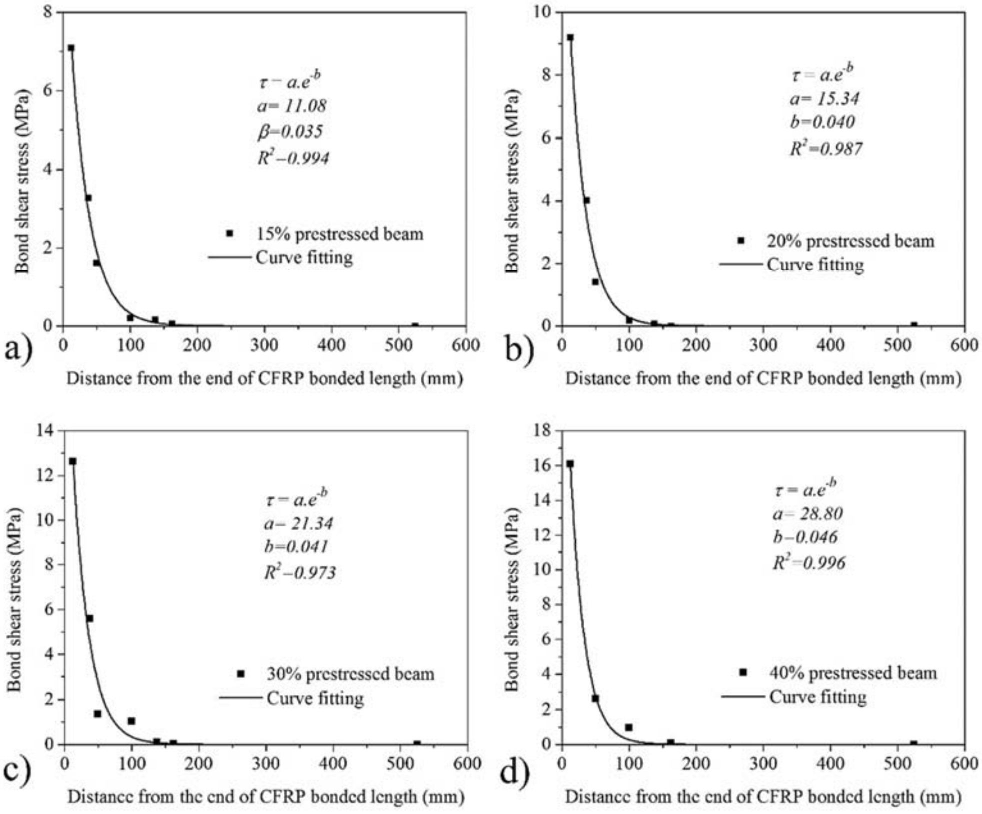

Figure 3-12: Bond shear stress distribution after the release of the prestress force for the prestress level of: a) 15%, b) 20%, c) 30%, d) 40%

3.3 Series of Beams Strengthened According to NSM Prestressing Technique

The present section aims to experimentally evaluate the effectiveness of prestressed CFRP laminates applied according to the NSM technique (designated as NSM prestressing technique) for the flexural strengthening of beams flexurally reinforced with relatively small percentage of longitudinal bars. These RC beams do not respect the deflection limit at serviceability limit state (SLS) imposed by Eurocode (EN 1992-1-1. 2004), which is a recurrent issue in buildings constructed in the 60's until the 80's. Moreover, the influence of the prestress level on the prevailing failure mode and short-term behavior immediately after the release of prestress force was experimentally evaluated.

3.3.1 Specimens and Test Setup

The experimental program reported in this section was composed of five RC beams. One of the RC beams was kept unstrengthened, while another one was flexurally strengthened with a non-prestressed CFRP laminate applied according to the NSM technique, consisting in a passive strengthened beam. The remaining three beams were flexurally strengthened with NSM CFRP laminate prestressed up to approximately 20%, 30% and 40% of its nominal tensile strength.

The geometry, support and loading conditions are schematically represented in Figure 3-13a, and the arrangement of the tensile and compressive longitudinal steel reinforcements of the beams is depicted in Figure 3-13b. To evaluate the tensile strains on the longitudinal steel bars, three strain gauges were installed on the bottom steel bars as represented in Figure 3-13c (SG 2,3 and 5). One strain gauge was installed on the top fiber of the concrete at mid-section of the beams to monitor the concrete strain (SG1 in Figure 3-13c). The shear reinforcement ratio was designed to avoid shear failure, following the recommendations of (EN 1992-1-1. 2004) ($\rho_{sw} = A_{sw} / b.s = 0.47\%$, where A_{sw} is the cross sectional area of a steel stirrup, b is the width of beam's cross section, and $s = 80\,\text{mm}$ is the spacing of the steel stirrups). For the flexural strengthening of the RC beams, a CFRP laminate of $1.4 \times 20\ \text{mm}^2$ cross sectional area was installed into a groove of $6 \times 24\ \text{mm}^2$ cross section opened on the concrete cover along the total length of the beam (Figure 3-13b). The tensile strains of the CFRP reinforcement were recorded by installing two strain gauges on the laminate (SG 4 and 6 in Figure 3-13c), while in the case of the prestressed CFRPs, one more strain gauge was placed at 200 mm far from the end of the CFRP bonded length (SG7 shown in Figure 3-13c). This extra SG was applied for a better assessment of the prestress losses. However, in order to simulate, as much as possible, the restrictions found in a real strengthening application in terms of anchorage conditions for the NSM technique (such as the anchorage pieces represented in Figure 3-3), a length of 150 mm of the CFRP laminates at each extremity of the beams was not bonded with epoxy adhesive to the concrete (see Figure 3-13a).

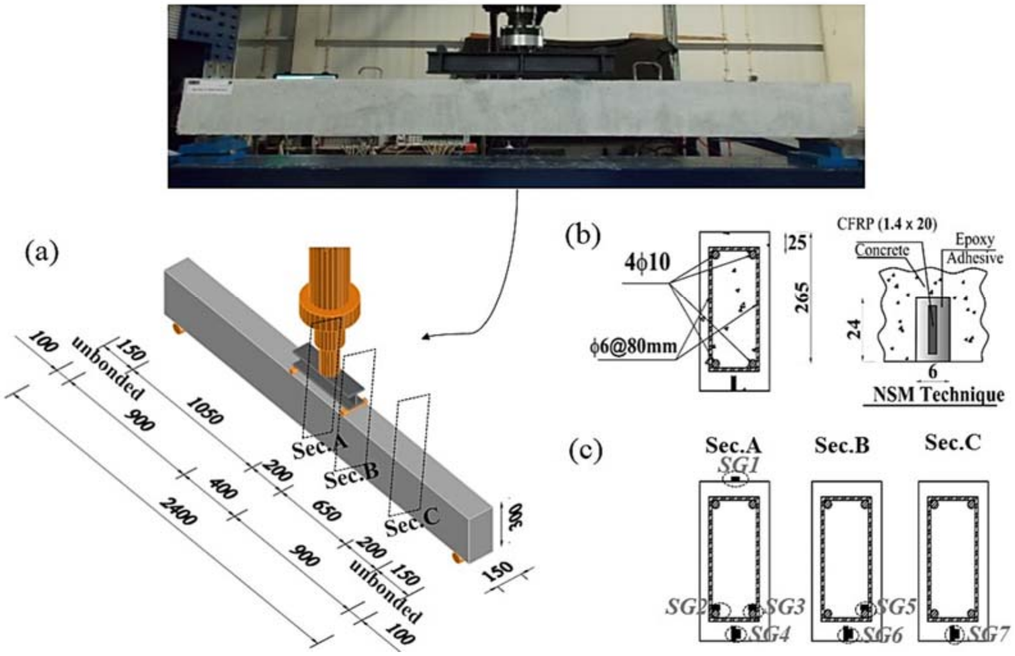

Figure 3-13: Characteristics of the tested type of beams: a) geometry, support and loading conditions, b) steel and CFRP reinforcements, c) positioning of the strain gauges (dimensions in mm)

These simply supported beams were monotonically loaded up to failure under four-point loading, by imposing a deflection rate of 1.2 mm/min controlled by a servo-actuator that applied the load (Figure 3-13a). Furthermore, five LVDTs were used to record vertical displacement of the tested beams during the flexural loading, as represented in Figure 3-14. The LVDTs were supported on an aluminum bar in order to exclude the register of parasitic deformations.

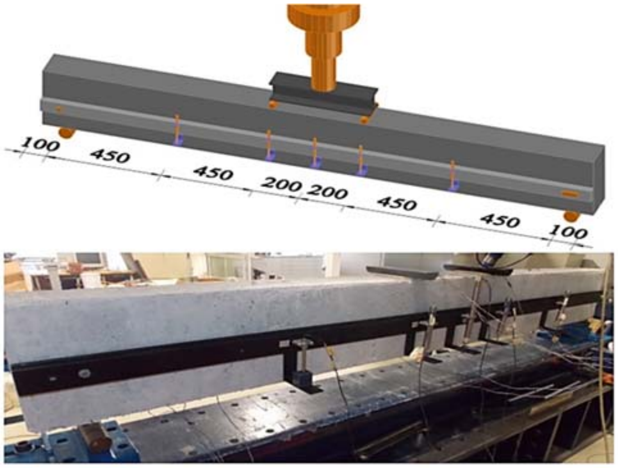

Figure 3-14: Position of LVDTs (dimensions in mm)

3.3.2 Prestressing Procedure

The applied prestress level was controlled by the average strain value recorded by the strain gauges installed on the CFRP laminate (shown in Figure 3-13c) and considering the material properties supplied by manufacturer (elasticity modulus of 150 GPa and nominal tensile strength of 2000 MPa).

3.3.3 Material Properties

The average values of the main properties for the concrete, steel bars, CFRP laminate and epoxy adhesive are indicated in Table 3-1, where the average compressive strength and young's modulus of the concrete were evaluated from uniaxial compression tests on cylinders of 150 mm diameter and 300 mm height at the age of the beam testing (153 days).

3.3.4 Results

3.3.4.1 Short-term Prestress Losses and Initial Camber

Due to the eccentricity of the prestress force in relation to the centroidal axis of the beam cross section, a negative bending moment is created after the release of the prestress force, causing a negative camber (upward deflection) in the beam, as well as a loss of strain in the CFRP laminate. In these prestressed RC beams, the short-term prestress losses were defined as the losses of strain immediately after removing the totality of the prestress load. These prestress losses and initial camber were determined by monitoring the strain variation in the CFRP laminate (using SG 4 and 6 represented in Figure 3-13) and the deflection at mid-span (using the LVDT represented in Figure 3-1) during the release of the prestress force. In fact, a decrease of the tensile strain in the CFRP laminate was observed in consequence of the negative camber caused by the effect of the prestress release. The main relevant results of the prestress losses and initial camber of the prestressed beams are indicated in Table 3-2. As expected, the instantaneous prestress losses increased with the prestress level, but the maximum value was limited to approximately 2%.

Table 3-2: Main results after prestress releasing

Beam with prestress level	Strain before prestress releasing ($\mu\varepsilon$)	Strain after prestress releasing ($\mu\varepsilon$)	Prestress losses (%)	Negative camber at mid-section (mm)
20%	2626	2616	0.4	0.08
30%	4115	4062	1.3	0.18
40%	5117	5020	1.9	*
*Data was missed due to deficient functioning of the LVDT				

3.3.4.2 Load-deflection Curves

The force versus mid-span deflection relationships of all the tested beams are depicted in Figure 3-15, where all the strengthened beams, regardless the prestress level, presented an increase of more than 50% in terms of the ultimate load carrying capacity when compared to the control beam by using only one laminate ($\rho_f = A_f / b.d_f = 0.065\%$, where A_f and d_f are the cross sectional area of the laminate and its internal arm).

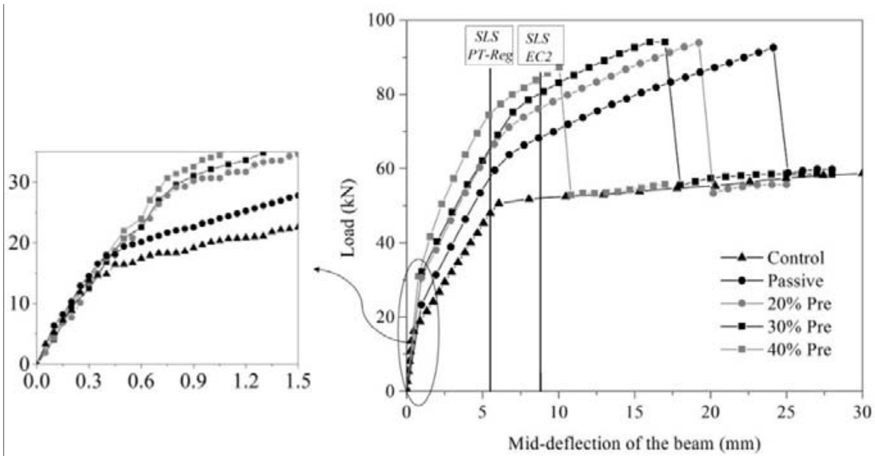

Figure 3-15: Load versus mid-span deflection of the tested beams

As already indicated, a relatively low steel reinforcement ratio ($\rho_s = A_s / b.d_s = 0.39\%$, where A_s is the cross sectional area of tensile steel reinforcement and d_s is the internal arm of this reinforcement) and concrete strength were adopted for the beams of this experimental program in order to evaluate the efficiency of the prestressed NSM CFRP technique on the flexural behavior of RC elements susceptible of developing abnormally high deflections. Assuming these RC beams as representative of constructions built in the 60's to 80's according to the Portuguese (PT) design regulations (also typical of buildings of several European countries), the flexural reinforcement did not yield at SLS, since the deflection limit was $L/400 = 5.5\,\text{mm}$. However, the safety margin between the load at yield initiation and the load at SLS is quite small (6%). Furthermore, these beams do not accomplish the requirements of the actual European design recommendations (EN 1992-1-1. 2004), since for the deflection limit at SLS ($d_{SLS} = L/250 = 8.8\,\text{mm}$) their load carrying capacity was already attained. As Figure 3-15 shows, the proposed strengthening methodology is, however, capable of increasing the load at SLS according to the Eurocode exigencies.

Table 3-3 presents the most relevant results of the flexural response of the tested beams, where it can be verified that, by increasing the level of the prestress force applied to the CFRP laminate, the load carrying capacity corresponding to concrete cracking and steel yielding initiation stages increase, as well as the corresponding deflection (except in the case of the 40% prestressed beam). At the deflection limit corresponding to the SLS requirements, the increase of the load carrying capacity with the prestress level was also quite significant. In fact, for prestress levels of 0%, 20%, 30% and 40%, the increase of load carrying capacity at SLS ($d_{SLS} = L/250$) was 32%, 47%, 55% and 63%, respectively, when compared to the control beam.

Table 3-3: Relevant results obtained in the tested beams

RC beams	P_{cr} (*kN*)	d_{cr} (*mm*)	P_y (*kN*)	d_y (*mm*)	P_u (*kN*)	d_u (*mm*)	P_{SLS} (*kN*)	$\frac{P_{SLS} - P_{SLS}^{control}}{P_{SLS}^{control}}$ (%)
Control	13.81	0.30	49.7	5.87	61.46	45.7	51.86	0.00
Passive	17.01	0.35	60.32	5.93	92.97	24.46	68.32	31.74
20% Prestressed	22.14	0.46	68.69	6.14	94.00	19.36	76.38	47.28
30% Prestressed	23.04	0.55	72.52	6.52	95.16	16.92	80.35	54.94
40% Prestressed	25.08	0.47	74.16	5.34	87.45	10.15	84.56	63.05

- P_{cr} is the load at cracking initiation and d_{cr} its corresponding deflection;
- P_y is the load at yield initiation of the longitudinal tensile bars and d_y its corresponding deflection;
- P_u is the ultimate load and d_u its corresponding deflection;
- P_{SLS} is the load at SLS conditions according to the Eurocode;
- $P_{SLS}^{control}$ is the load at SLS of control beam.

According to Figure 3-15, the beams prestressed with 20% and 30% exhibited similar force-deflection response in the phase between concrete cracking and steel yielding initiations due to the equal reinforcement and strengthening ratios that assures an almost equal elasto-cracked flexural stiffness for the strengthened beams. However, the cracking load was expected to increase with the prestress level, which indicates that the concrete tensile strength of the beam strengthened with 30% prestress would have been a little bit smaller than of the other beams. This smaller concrete tensile strength mainly in the concrete cover can be achieved due to the occurrence of some micro-cracks induced by handling and transportation of the beams. Similar justification can be also pointed out to the beam strengthened with a prestressed laminate at 40%, although in this beam the stiffness in the elasto-cracked phase was slightly larger than the stiffness observed in the other beams, which may be justified by the smaller cracked region in consequence of the higher prestress level. The rupture of the prestressed laminate in this beam, however, occurred for a smaller load, leading to a deflection smaller than the expected one. The higher flexural stiffness during the elasto-cracked stage in this beam, conjugated with the higher initial tensile strain introduced in the CFRP, may have contributed to a higher gradient of tensile stress in the flexural failure cracks, promoting the rupture of the laminate at a smaller deflection of the beam, when compared to what occurred in the other strengthened beams. The expected decrease of the deflection at failure caused by the increase of applied prestress level is visible in the beams strengthened with a laminate prestressed at 20% and

30%. However, in these beams the maximum load capacity of the beam was not influenced by the applied prestress level, since they attained the same capacity of the non-prestressed beam.

Serviceability limit state (SLS) conditions should be respected by controlling the maximum crack width and deflection, as well as limiting the stress level in the longitudinal tensile steel bars, in order to ensure that this level is kept below the yield strain (ACI-440.1R. 2006). By increasing the prestress level in the CFRP laminates, the stress level in the longitudinal tensile steel reinforcement is decreased, as well as the crack width and crack propagation along the depth of the cross section of the beam and beam's span length, resulting in significant benefits in terms of durability due to the smaller probability of corrosion of the steel reinforcement. The results obtained in this experimental program also confirmed that by increasing the prestress level in the CFRP laminate, the load at steel yield initiation increases, as well as the corresponding deflection. This effect is caused by the increase of cracking load and almost constant load amplitude between crack initiation and yield initiation.

In spite of the benefits resulting from the application of prestressed CFRP laminates, Figure 3-15 evidences that the failure of the beams occurs for smaller deflections as the prestress level increases, which might be a concern from the point of view of ductility requirements. To analyze this issue on the tested beams, a ductility index (μ) was evaluated, assumed as capable of indicating the ability of a structural element to withstand plastic deformation without a decrease in the load carry capacity. Therefore, μ is defined as the ratio between the ultimate mid-deflection (d_u) and the deflection corresponding to the steel yield initiation (d_y) of the beams ($\mu = d_u / d_y$). The relationship between the normalized ductility index (μ^{pre} / μ^{pas}) and the applied prestress level is represented in Figure 3-16, where μ^{pre} and μ^{pas} are the ductility indexes of the prestressed beams and passive beam, respectively. More available experimental data, including RC beams strengthened with NSM CFRP elements prestressed at different levels, reported by (Badawi and Soudki 2009, El-Hacha and Gaafar 2011, Hajihashemi et al. 2011), were considered to evaluate the efficiency of prestress level on the normalized ductility index represented in Figure 3-16. This figure shows that the normalized ductility index has a tendency to decrease almost linearly with the increase of the prestress level applied to the CFRP elements up to the maximum level considered in these experimental programs. Therefore, it is suggested that for design purposes this aspect should be taken into account by limiting the level of prestress to be applied in order to do not compromise the ductility behavior of the strengthened beam. A recommendation should be also imposed for the ductility index, $d_u / d_y > C$, a subject that will be treated in Chapter 5.

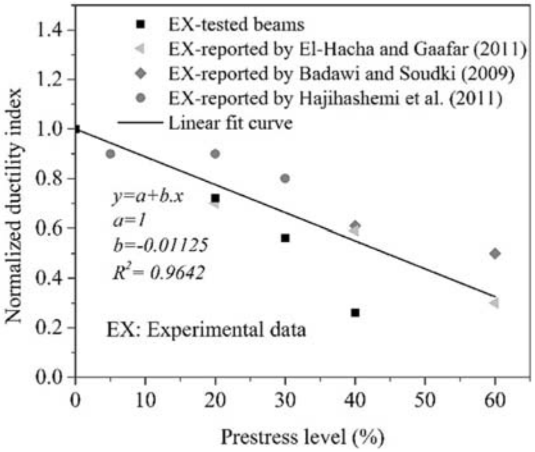

Figure 3-16: Ductility index of the prestressed beams normalized to passive strengthened beam

The influence of laminate's prestress level in terms of the evolution of stiffness during the loading process of the beams was also investigated. The stiffness was calculated as the tangent to the load-deflection curve, and the relationship between the load and normalized stiffness of the tested beams is represented in Figure 3-17, where normalized means that the stiffness is divided by the initial uncracked stiffness of the beam. Just after crack initiation, an abrupt decrease of the stiffness was observed in all the tested beams, and an almost constant variation of the normalized stiffness was determined in the cracking phase up to yield initiation. As expected, the prestress has delayed the abrupt decay of the stiffness due to the increase of the cracking load. The evolution of the normalized stiffness in the post-yielding phase was similar in all the strengthened beams, as Figure 3-15 had already suggested.

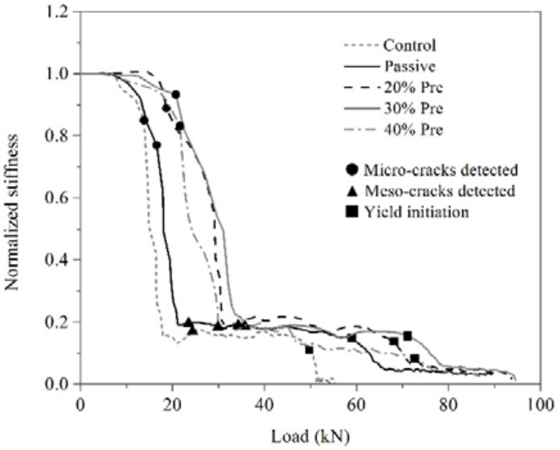

Figure 3-17: Load versus normalized stiffness of the beams

3.3.4.3 Internal Strain Distribution

The load versus CFRP tensile strain at mid-section (monitoring by SG 4 represented in Figure 3-13) is depicted in Figure 3-18, where the initial strain corresponds to the strain after prestress release, which was already reported in Table 3-2. Regardless the prestress level, the CFRP laminates have behaved similarly in three phases composing a load-strain response of the tested beams. In fact, after the yielding of the tensile steel reinforcement, the increase of the load carrying capacity of the prestressed beam is practically assured by the CFRP laminate, since the contribution of the longitudinal steel bars due to its hardening effect is relatively small up to the rupture of the laminate.

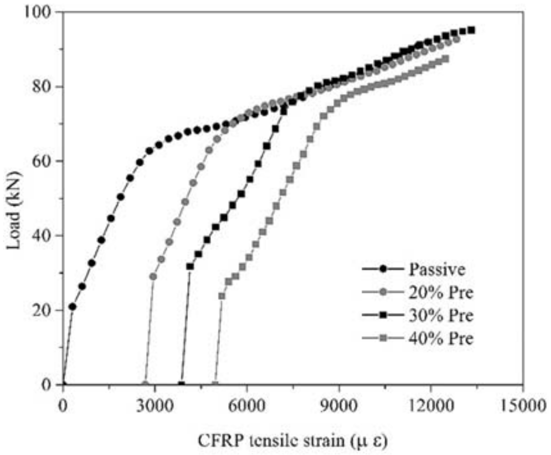

Figure 3-18: Load versus tensile strain in the CFRP laminate

In the some cases of the strengthened beams, the ultimate tensile strain of the CFRP laminate recorded by the strain gauge at mid-section (Figure 3-18) was higher than the ultimate strain reported in the Table 3-1 corresponding to the characterization of the properties of this composite. The strains recorded in the SGs installed on the laminate applied in the strengthened beams can be affected by the local curvature of the laminate, leading to higher strains compared to the situation of direct tensile tests, as reported by Barros et al. (2011).

Figure 3-19a presents the load versus strain in the longitudinal tensile steel reinforcements at mid-span, where a strain value is the average of the values recorded in the two strain gauges installed at mid-section on the steel bars (SG 2 and 3 in Figure 3-13c). The prestress force has introduced an initial compressive strain on the longitudinal steel reinforcement. During the bending test, and before crack initiation, the longitudinal steel reinforcement has started presenting tensile strains. The instant of transition from compressive to tensile strain, defined as steel decompression point for the prestressed beams, is represented in Figure 3-19a. As expected the load corresponding to this point has tended to increase with the prestress level, and, consequently, the load at yield initiation of the longitudinal steel bars has also increased. The increase of load at the steel decompression and yield initiation, provided by the prestress level, and when the corresponding values in the non-prestressed beam are considered for comparison purposes, is depicted in Figure 3-19b. It is verified that up to a prestress level of 40% this load increase has an almost linear increase trend with the prestress level.

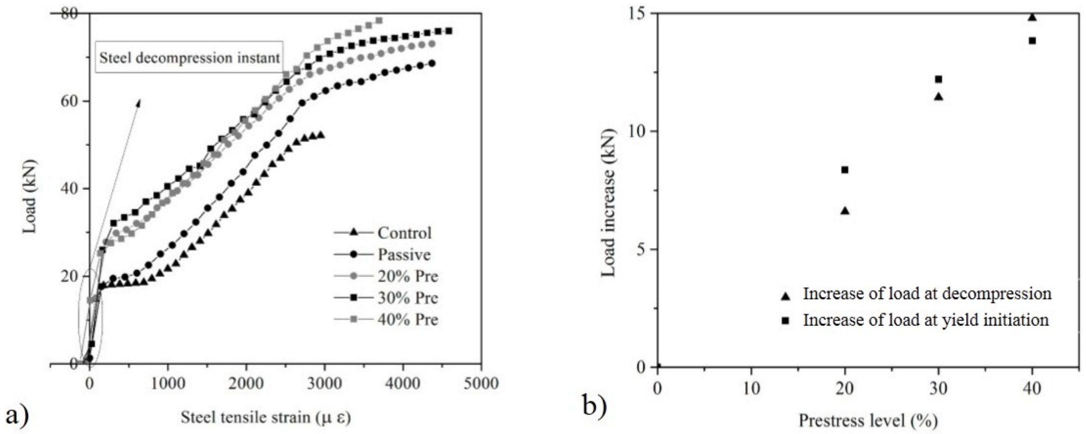

Figure 3-19: a) Load versus strain in the tensile steel reinforcement, b) prestress level versus load increase at steel decompression and at steel yield initiation by considering the corresponding values of the non-prestressed strengthened beam

The relationship between load and concrete strain at the top fiber of mid-span cross section is represented in Figure 3-20, where it is shown that the prestressed beams exhibited an initial small tensile strain on the concrete top fiber (less than 30 microstrain; due to deficient functioning of the strain gauge in the 40% prestressed beam, this data is not available for this beam). The prestressed beams presented a lower concrete compressive strain at failure when compared to the non-prestressed beam, which indicates that the probability of concrete crushing as prevailing failure mode is decreased by the application of prestress. This lower concrete strain at failure can be attributed to the initial strain profile introduced when releasing the prestressed laminates, causing an initial compression field in the steel bars and surrounding concrete, and a downward on the position of the neutral axis.

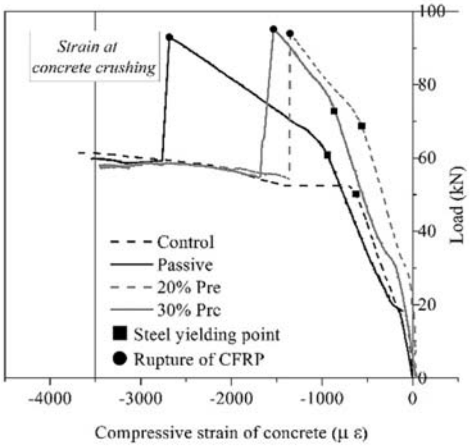

Figure 3-20: Load-concrete strain of the tested RC beams

3.3.4.4 Failure Modes and Crack Patterns

Concrete crushing is assumed to occur in RC beams when the compressive strain on the concrete top fiber of the cross section reaches its maximum usable strain ($\varepsilon_{cu} = 0.0035$ according to the Eurocode (EN 1992-1-1. 2004)). In the control beam, crushing of the concrete in the compression zone after yielding of the tensile steel bars was observed, as represented in Figure 3-20 and Figure 3-21. On the other hand, all beams strengthened with CFRP only experienced concrete crushing after CFRP rupture (see Figure 3-20 and Figure 3-21). The adhesive provided adequate bond conditions since no debonding of the CFRP laminate from the concrete substrate was observed.

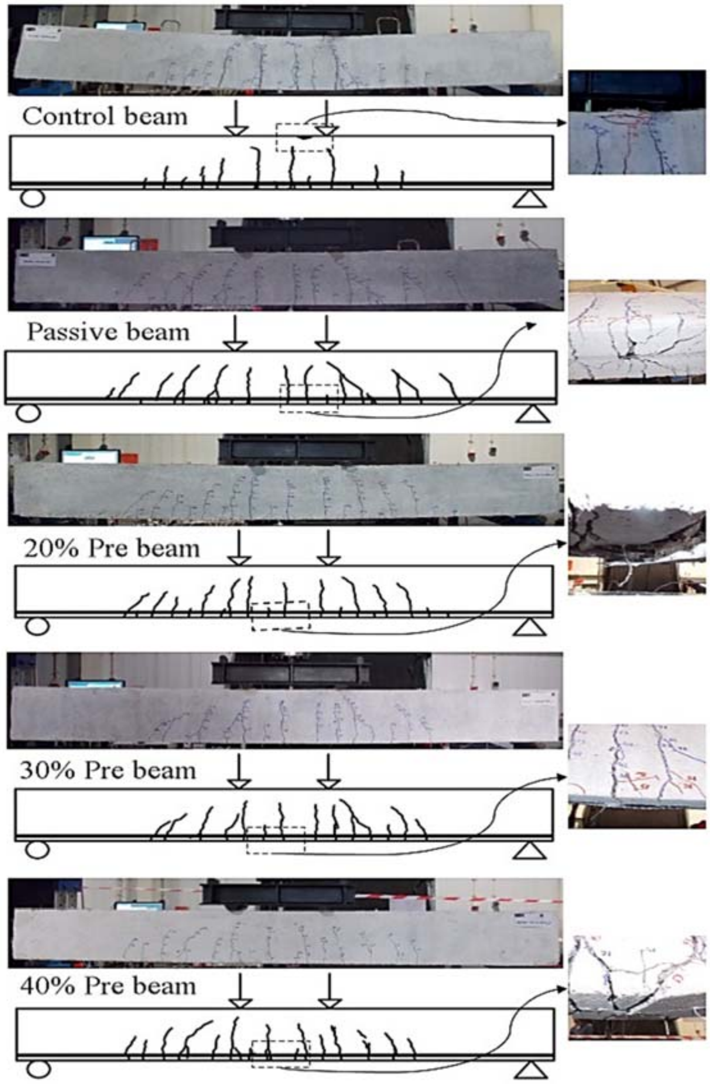

Figure 3-21: Crack pattern at the ultimate stage of the tested beams

The crack pattern of all beams consisted predominantly of flexural cracks, as it can be observed in Figure 3-21, where the crack patterns at ultimate stage are represented. Based on these crack patterns, the average crack spacing was determined by considering all the cracks crossing the tensile steel reinforcement. A better distribution of the cracks was observed in the beams strengthened with NSM CFRP laminates, since, according to Figure 3-22a, a decrease of about 17% on the average crack spacing was noticed in the strengthened beams when compared to the average crack spacing of the control beam.

The experimental results demonstrate that the non-prestressed laminate has increased the cracked zone length in about 35% in relation to the control beam, which is justified by the increase of load carrying capacity provided by the CFRP reinforcement. However, the increase of the prestress level has decreased the cracked zone length due to the initial compressive strain field introduced by the prestress. In fact, for prestress level of 20%, 30% and 40%, the cracked zone length was 25%, 8% and 11% longer than the cracked zone registered in the control beam, respectively (as represented in Figure 3-22b).

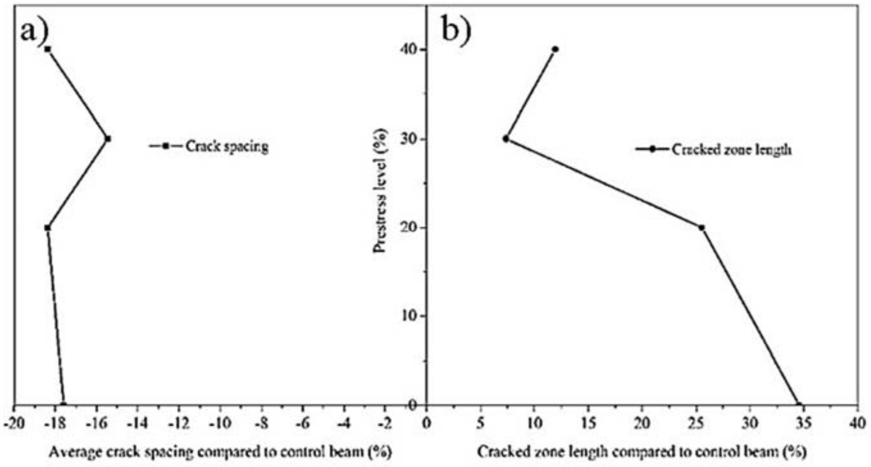

Figure 3-22: a) Average crack spacing of the strengthened beams, b) cracked zone length of the strengthened beams

3.4 Series of Beams Strengthened According to NSM Hybrid Technique

The purpose of the current section is to assess experimentally the potentialities of a new NSM hybrid strengthening methodology (designated as NSM hybrid technique) to enhance not only the load carrying capacity at SLS and ultimate conditions, but also the deflection and energy absorption capacity, when compared to the use of NSM prestressing technique. The proposed NSM hybrid technique combines non-prestressed and prestressed CFRP laminates in the same application for the flexural strengthening of RC beams. In this context an experimental program composed of RC beams strengthened according to the NSM prestressing and NSM hybrid techniques, using CFRP laminates, was carried out.

3.4.1 Specimens and Test Setup

The experimental program was composed of six rectangular cross-section RC beams. One of the RC beams was kept unstrengthened as a control beam, while three RC beams were strengthened with a CFRP laminate prestressed at 0% (serving as a passive strengthened beam), 20%, and 40% of its nominal tensile strength, by adopting the NSM technique (designated as Pre-beams). The remaining two RC beams were strengthened by applying a NSM hybrid technique using non-prestressed and prestressed (20% and 40%) CFRP laminates in the same application (designated as HPre-beams).

Characteristics of the tested beams (geometry, loading configuration, support conditions and reinforcement details) are schematically represented in Figure 3-23. The shear reinforcement ratio was designed to avoid shear failure for the RC beams ($\rho_{sw} = A_{sw}/b.s = 0.38\%$, where A_{sw} is the cross sectional area of a steel stirrup, b is the width of beam's cross section, and s is the spacing of the stirrups). The shear capacity of these beams, calculated according to the recommendations of (EN 1992-1-1. 2004) and (ACI-318-05. 2005), varies between 211 kN and 228 kN, which is slightly higher than the expected maximum flexural capacity for the strengthened beams ($\rho_s = A_s/b.d_s = 0.87\%$, where A_s is the cross sectional area of the tensile steel reinforcement, and d_s is its effective depth from top fiber of beam's cross section).

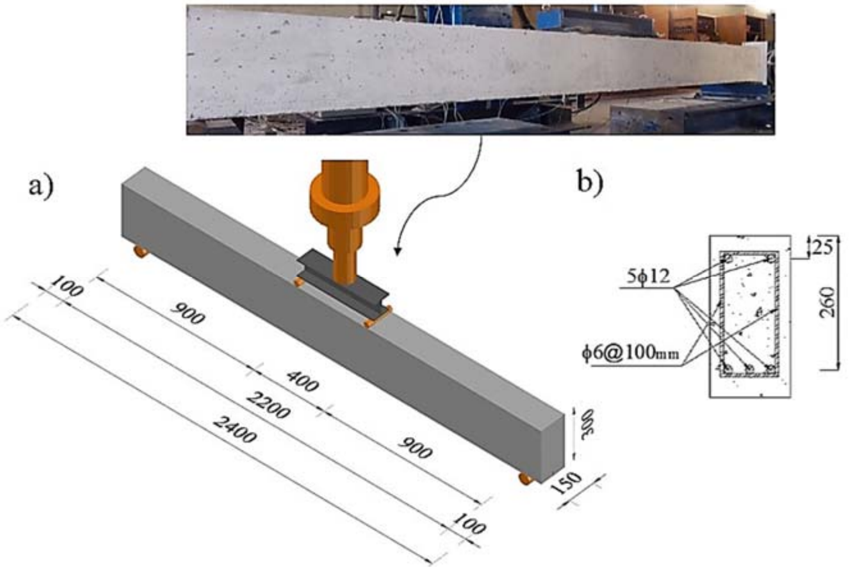

Figure 3-23: The beams of the experimental program: a) geometry and loading configuration; b) steel reinforcement (dimensions in mm)

These simply supported beams were monotonically loaded up to failure under four-point loading configuration by imposing a deflection rate of 1.2 mm/min. Five LVDTs were used to record vertical displacement of the tested beams during the flexural loading, as represented in Figure 3-24.

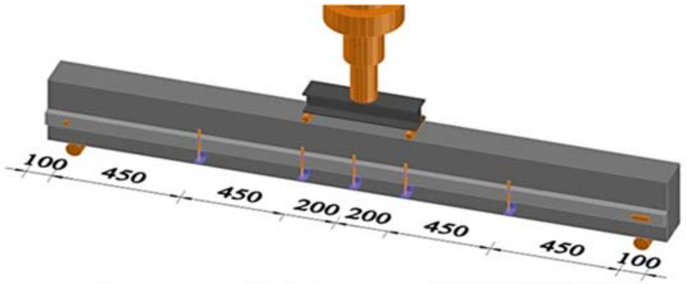

Figure 3-24: Position of LVDTs (dimensions in mm)

For the flexural strengthening of the RC beams according to the NSM prestressing technique, a CFRP laminate of 1.4 × 20 mm^2 cross sectional area was introduced into a groove (6 × 25 mm^2 cross section) pre-executed on the concrete tensile surface along the total beam length (sec.(A) in Figure 3-25) ($\rho_{f(Pre)} = A_f / b.d_f = 0.065\%$, where A_f is the cross sectional area of the CFRP reinforcement, and d_f is its effective depth from top fiber of beam's cross section). The CFRP laminate was bonded to the surrounding concrete with epoxy adhesive, and its extremities become at 50 mm before the supports (150 mm from the extremities of the beam) in order to simulate the anchorage conditions in a real applications. The tensile strains of the CFRP reinforcement in the passive strengthened beam were recorded by installing two strain gauges on the laminate (SG 1 and 2 shown in Figure 3-26), while for the prestressed strengthened beams, in addition of these two strain gauges, one more was installed on the prestressed laminate to better assess of the prestress losses (SG3 in Figure 3-26).

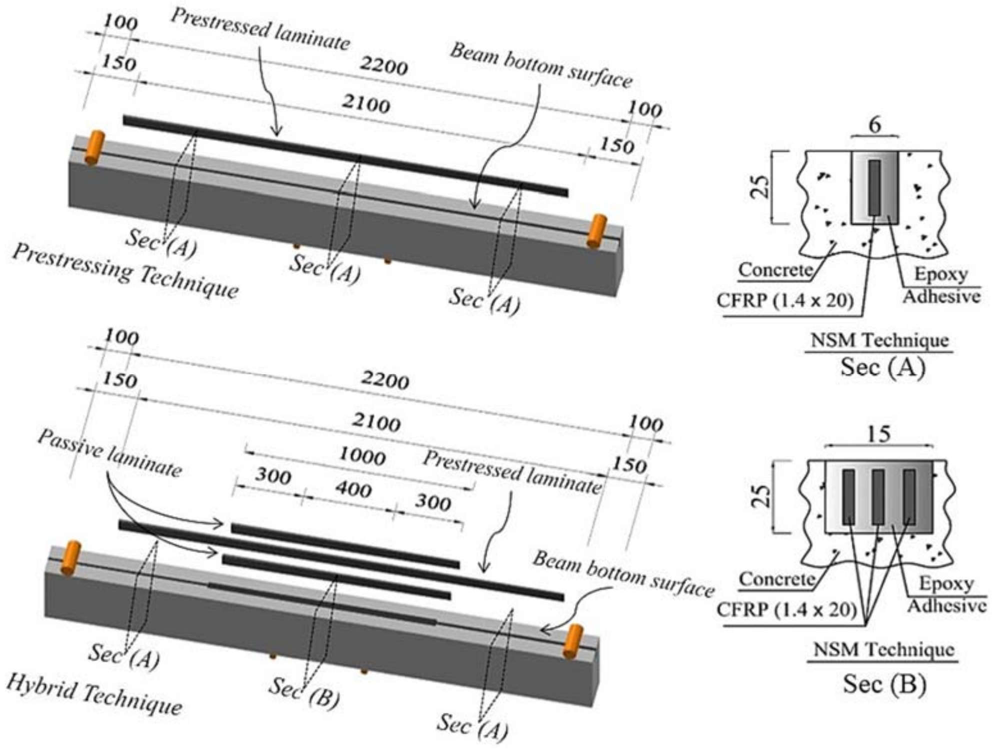

Figure 3-25: CFRP reinforcement details of hybrid and prestressing NSM techniques (dimensions in mm)

In the case of the hybrid strengthened beams, one passive CFRP laminate of 1.4 × 20 mm^2 cross sectional area was placed at both sides of a prestressed CFRP laminate (1.4 × 20 mm^2 cross section) into the same groove (Figure 3-25 and Figure 3-26) to provide an attempt of avoiding rupture of the prestressed CFRP laminate in the maximum bending moment region ($\rho_{f(\text{HPre})} = A_f / b.d_f = 0.195\%$, where A_f is the cross sectional area of the CFRP reinforcement, and d_f is its effective depth from top fiber of beam's cross section). At the location of the passive laminates, the groove size was increased to 15 × 25 mm^2 cross section (sec.(B) in Figure 3-25). The length of the passive laminates was extended at both extremities of the maximum bending moment region, as development length represented in Figure 3-25. The development length was determined according to the recommendation of (ACI-440.2R. 2008), $l_{db} \geq (a_f . b_f . f_{fu}) / (2.(a_f + b_f).\tau_b)$, where a_f and b_f are the thickness and height of the laminate's cross section, f_{fu} and τ_b are the tensile strength of CFRP and the average bond strength, respectively. By considering for a_f, b_f, f_{fu} and τ_b the values of 1.4 mm, 20 mm, 2000 MPa, and 6.9 MPa, respectively, it was obtained $l_{db} \geq 190\,\text{mm}$, and a value of 300 mm was adopted due to the uncertainty in terms of the τ_b values. The tensile strain developed in the passive laminates was assessed by installing one strain gauge on the laminate (SG 1 in Figure 3-26), while four strain gauges were installed on the prestressed laminate (SG 2, 3, 4 and 5 in Figure 3-26). To evaluate an eventual occurrence of a strain gradient in the prestressed laminate in the zone of the extremities of the passive laminates, SG 3 and 4 were installed at 50 mm before and after this section on the prestressed laminate, respectively. Moreover, one strain gauge was installed on the top fiber of the concrete at the mid-section of all the tested beams to monitor the concrete compressive strain ("Concrete SG" in Figure 3-26).

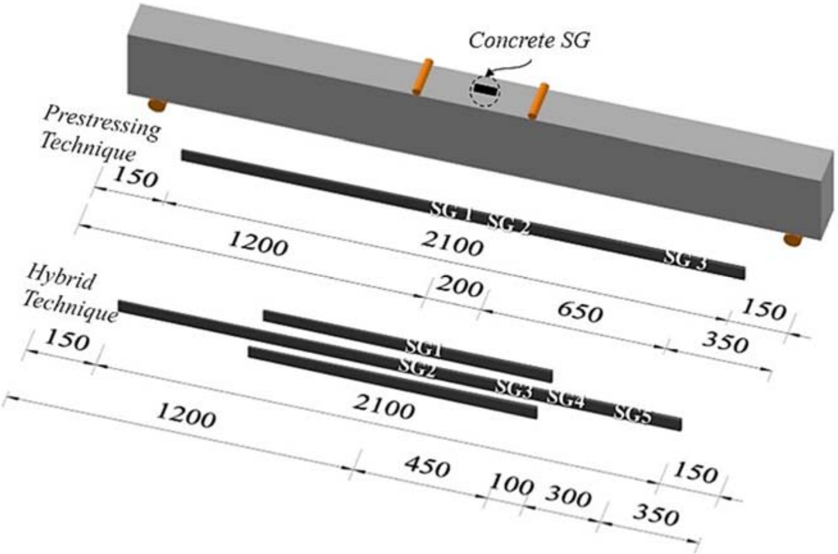

Figure 3-26: Position of the strain gauges (SG) installed on the CFRP laminates and concrete (dimensions in mm)

3.4.2 Prestressing Procedure

The applied prestress level was controlled by monitoring the average strain values of the strain gauges installed on the prestressed CFRP laminate (represented in Figure 3-26), considering the material properties reported by the manufacturer (elasticity modulus of 150 GPa and nominal tensile strength of 2000 MPa).

3.4.3 Material Properties

The average values of the main properties for concrete, steel bars, CFRP laminate, and epoxy adhesive are indicated in Table 3-4, where the average compressive strength and young's modulus of the concrete were evaluated from uniaxial compression tests on cylinders of 150 mm diameter and 300 mm height at the age of the beam testing (165 days).

Table 3-4: Average values of the main material properties of the constituent materials

Concrete (at testing age)	Compressive strength		Young's modulus	
	$f'_{cm} = 24.5$ MPa		$E_c = 20\,\text{GPa}$	
Steel bars	Diameter	Yield strength	Tensile strength	Elasticity modulus
	6 mm	$f_{sym} = 613\,\text{MPa}$	$f_{sum} = 696\,\text{MPa}$	$E_s = 218\,\text{GPa}$
	12 mm	$f_{sym} = 563\,\text{MPa}$	$f_{sum} = 656\,\text{MPa}$	$E_s = 203\,\text{GPa}$
CFRP laminate	Tensile strength	Ultimate tensile strain	Elasticity modulus	
	$f_{fum} = 1922\,\text{MPa}$	$\varepsilon_{fum} = 11.7\,(‰)$	$E_f = 164\,\text{GPa}$	
Epoxy adhesive	Tensile strength		Elasticity modulus	
	$f_{aum} = 20\,\text{MPa}$		$E_a = 7\,\text{GPa}$	

3.4.4 Results

3.4.4.1 Load-deflection Curves

The relationship between the applied load and the deflection at the mid-span for all the tested beams is depicted in Figure 3-27a. Regardless the prestress level, Figure 3-27a and Table 3-6 show an average increase of about 30% in terms of the maximum load carrying capacity for the beams strengthened with the NSM prestressing technique when compared to the control beam, while the average increase for the HPre-beams was about 44% when the same comparison is done. Figure 3-27b represents the strengthening efficiency in terms of load carrying capacity at concrete cracking, SLS conditions, steel yield initiation, and ultimate stage for all the strengthened beams, where the load capacities were normalized to the corresponding ones of the control beam. The SLS conditions for this experimental program were adopted according to the requirements of the actual European design recommendations ($d_{SLS} = L/250 = 8.8\,\text{mm}$, where L is the beam's span) (EN 1992-1-1. 2004).

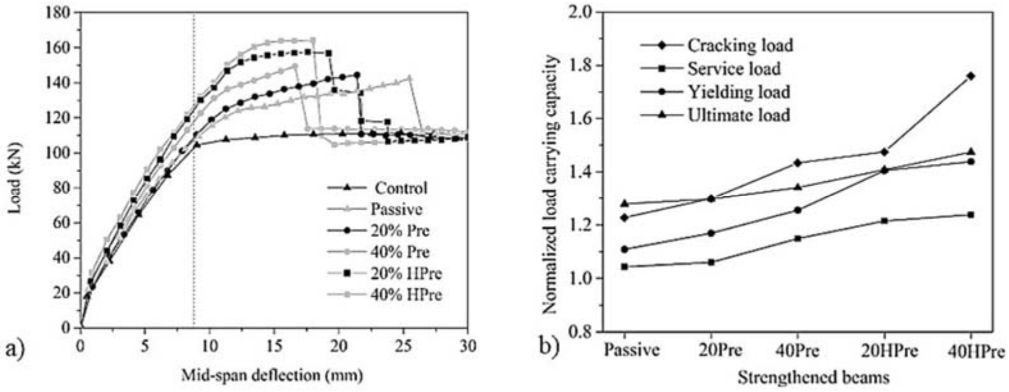

Figure 3-27: a) Load versus mid-span deflection of the tested beams, b) load capacities at concrete cracking, SLS deflection, steel yielding, and ultimate point normalized to the control beam

Table 3-5 shows the main relevant results of the flexural response of the tested beams, where it can be confirmed that both strengthening techniques (Pre and HPre) have assured an increase in terms of load carrying capacity at concrete cracking (P_{cr}), SLS deflection conditions (P_{SLS}), and steel yield initiation (P_y), when the corresponding values of the passive strengthened beam are considered for comparison purposes, since an initial compression field in the tensile steel bars and surrounding concrete is introduced after the release of the prestress force. The increase of these force indicators is relatively small because only one prestressed laminate was applied in the Pre and HPre beams, which corresponds to a strengthening ratio of only 0.065%. However, the HPre-beams presented a higher increase in terms of the aforementioned force indicators and maximum load (P_u) without compromising the ultimate deflection capacity. This higher increase of the force indicators for the HPre-beams can be justified by the higher CFRP reinforcement ratio in the maximum bending moment region ($\rho_{f\,(\mathrm{HPre})} = 0.195\%$).

Table 3-5: Relevant results obtained in the tested beams

RC beams	ρ_f $(\%)$	P_{cr} (kN)	d_{cr} (mm)	P_y (kN)	d_y (mm)	P_u (kN)	d_u (mm)	P_{SLS} (kN)	E_d $(kN-mm)$	μ_d (d_u/d_{SLS})
Control	0	18.00	0.51	104.50	9.01	111.39	24.79	102.68	2284	2.82
Passive	0.065	22.10	0.60	115.84	10.17	142.48	25.43	107.10	2721	2.89
20% Pre	0.065	23.39	0.85	122.18	10.45	144.52	21.40	108.88	2226	2.43
40% Pre	0.065	25.81	0.90	131.17	10.59	149.40	16.60	117.95	1688	1.89
20% HPre	0.195	26.55	0.80	146.83	11.28	156.80	19.20	124.75	2203	2.18
40% HPre	0.195	31.68	0.90	150.31	11.41	164.20	18.00	127.17	2099	2.04

- ρ_f is the CFRP reinforcement ratio at mid-section of the beams;
- P_{cr} is the load at cracking initiation, and d_{cr} its corresponding deflection;
- P_y is the load at yielding of tensile bars, and d_y its corresponding deflection;
- P_u is the ultimate load, and d_u its corresponding deflection;
- P_{SLS} is the load at SLS conditions according to the Eurocode;
- E_d is energy absorption index;
- μ_d is deformability index.

As previously mentioned, all strengthened beams presented higher P_y than the control beam, which results in a higher safely margin at SLS conditions ($(P_y - P_{SLS}^{control})/P_{SLS}^{control}$, where $P_{SLS}^{control}$ is the load corresponding to the SLS deflection of the control beam) based on the requirements of (EN 1992-1-1. 2004) (keeping the stress level in the longitudinal tensile steel bars below its yield strength) (Table 3-6). This increase of the safety margin was 13%, 19%, and 28% for the beams strengthened with the CFRP laminate prestressed at 0%, 20%, and 40% level, respectively, while the HPre-beams prestressed at 20% and 40% level presented an enhancement of 43% and 46% in terms of this safety margin, respectively. On the other hand, at the deflection limit corresponding to the SLS requirement, the NSM prestressing technique provided an increase of 4%, 6%, and 15% in terms of the load carrying capacity for prestress level of 0%, 20%, and 40%, respectively, when the control beam is considered for comparison purposes, while for the HPre-beams, the increase of the service load was 21% and 24%, for 20% and 40% prestress levels, respectively (Table 3-6).

Table 3-6: Relevant results obtained in the tested beams

RC beams	$\frac{P_{SLS}-P_{SLS}^{control}}{P_{SLS}^{control}}$ (%)	$\frac{P_y-P_{SLS}^{control}}{P_{SLS}^{control}}$ (%)	$\frac{P_u-P_u^{control}}{P_u^{control}}$ (%)	$\frac{P_u-P_u^{pas}}{P_u^{pas}}$ (%)	$\frac{d_u-d_u^{control}}{d_u^{control}}$ (%)	$\frac{d_u-d_u^{pas}}{d_u^{pas}}$ (%)
Control	-	1.77	-	-	-	-
Passive	4.30	12.81	27.91	-	2.58	-
20% Pre	6.04	18.99	29.74	1.43	-13.67	-15.84
40% Pre	14.87	27.74	34.12	4.85	-33.03	-34.72
20% HPre	21.49	42.99	40.76	10.05	-22.54	-24.49
40% HPre	23.85	46.38	47.41	15.24	-27.39	-29.21

- $P_{SLS}^{control}$ is the load of the control beam at SLS conditions;
- $P_u^{control}$ is maximum load of the control beam, and $d_u^{control}$ its corresponding deflection;
- P_u^{pas} is the maximum load of the passive beam, and d_u^{pas} its corresponding deflection;

According to Table 3-5, the energy absorption (E_d) and deformability (μ_d) indexes tended to decrease with the increase of the prestress force applied to the CFRP reinforcement, where E_d is determined by integrating the area under the force-deflection curve up to the deflection at ultimate load carrying capacity (d_u), and μ_d is defined as the ratio between the deflection corresponding to the ultimate strength (d_u) and to the SLS conditions (d_{SLS}) of the beams ($\mu_d = d_u / d_{SLS}$). In fact, by increasing the prestress level in the laminate, the rupture of the CFRP, when is the prevailing failure mode, occurs at a smaller deflection, resulting a decrease of the nonlinear response of the prestressed beams after steel yielding. Figure 3-28 shows the normalized indexes of energy absorption (E_d / E_d^{pas}) and deformability (μ_d / μ_d^{pas}) for the strengthened beams, where the E_d^{pas} and μ_d^{pas} are the energy absorption and deformability indexes of the passive strengthened beam.

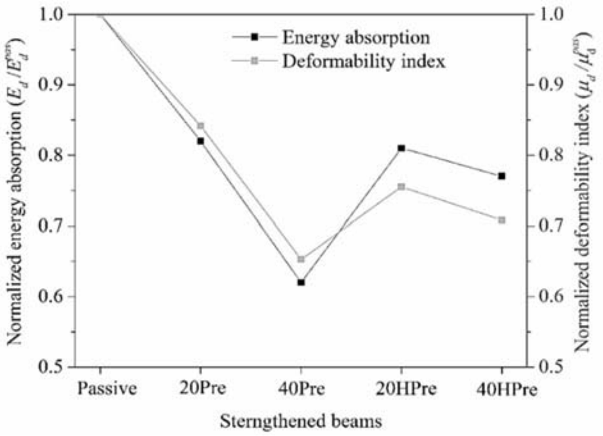

Figure 3-28: Energy absorption and deformability indexes normalized to the passive strengthened beam

Figure 3-28 evidenced that for 40% prestress level, the HPre-beam showed an enhancement of 24% and 9% in terms of energy absorption and deformability indexes, respectively, compared to the beam strengthened according to the NSM prestressing technique. For 20% prestress level, the HPre-beam developed an energy absorption similar to the beam strengthened with prestressed CFRP laminate (Pre-beam), while the NSM hybrid technique showed a decrease of 12% in terms of deformability index when compared to the use of NSM prestressing technique for the flexural strengthening of the beam. This fact can be justified by an unexpected premature failure of the 20% HPre-beam before the rupture of the prestressed laminate, which will be discussed in section 3.4.4.3.

3.4.4.2 Internal Strain Distribution

At the maximum flexural capacity of the strengthened beams, the tensile strains recorded by the strain gauges installed on the laminates (see Figure 3-26) are depicted in Figure 3-29, where the prestrain value represents the initial tensile strain of the laminate after the release of the prestress force. Figure 3-29 evidences that the maximum tensile strain in the laminate of the beams strengthened with the NSM prestressing technique, has occurred in the maximum bending moment region, while in the case of the HPre-beams, due to the strengthening contribution of the passive laminates, the location of the maximum tensile strain in the prestressed laminate was transferred to just after the extremity of the passive laminates (SG4), which can postpone the failure of the prestressed laminate.

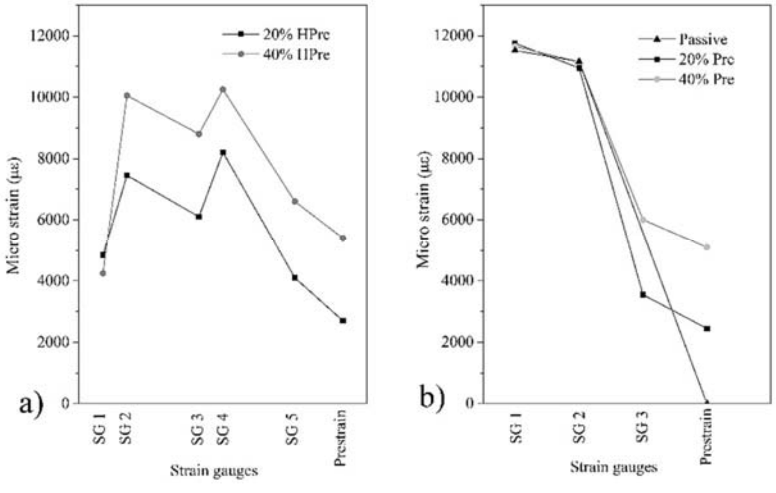

Figure 3-29: Tensile strains of the CFRP laminate at maximum load: a) hybrid strengthened beams; b) beams strengthened with NSM prestressing technique

The relationship between the applied load and concrete compressive strain at the top fiber of the mid-section is represented in Figure 3-30 (data of the strain gauge in the control beam has not been reported due to the deficient functioning of this SG). This figure evidences that by increasing the level of the prestress force applied to the CFRP laminate, the Pre-beams exhibited a lower concrete compressive strain at the failure (as also observed in section 3.3.4.3). On the other side, the concrete compressive strains at the top fiber of the HPre-beams were, at the maximum beam's capacity, significantly lower than the compressive strains of the beams strengthened with the NSM prestressing technique. This is justified by a downward of the position of the neutral axis, as well as a lower tensile strain in the laminates due to the higher flexural strengthening ratio in the region of highest bending moment in the HPre-beams.

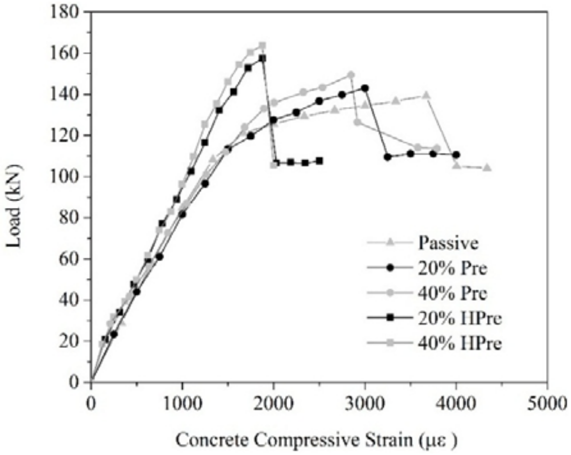

Figure 3-30: Load versus concrete compressive strain for strengthened beams

3.4.4.3 Failure Modes and Crack Patterns

The ultimate flexural capacity of all the tested beams was controlled by three types of failure modes after yielding of the tensile steel bars, namely: crushing of the concrete in the compression zone (CC); rupture of the laminate (CR); and concrete cover delamination (CD), as represented in Figure 3-31. In the control and passive strengthened beams, the concrete has crushed at the top zone of the central region of these beams (a maximum compressive strain of 0.0035 was recorded in the passive strengthened beam before the rupture of the laminate). In the passive strengthened beam, the laminate has ruptured immediately after concrete crushing. The beams strengthened with prestressed CFRP laminate failed by the rupture of the laminate due to the attainment of the ultimate tensile strength of the CFRP in a cracked section.

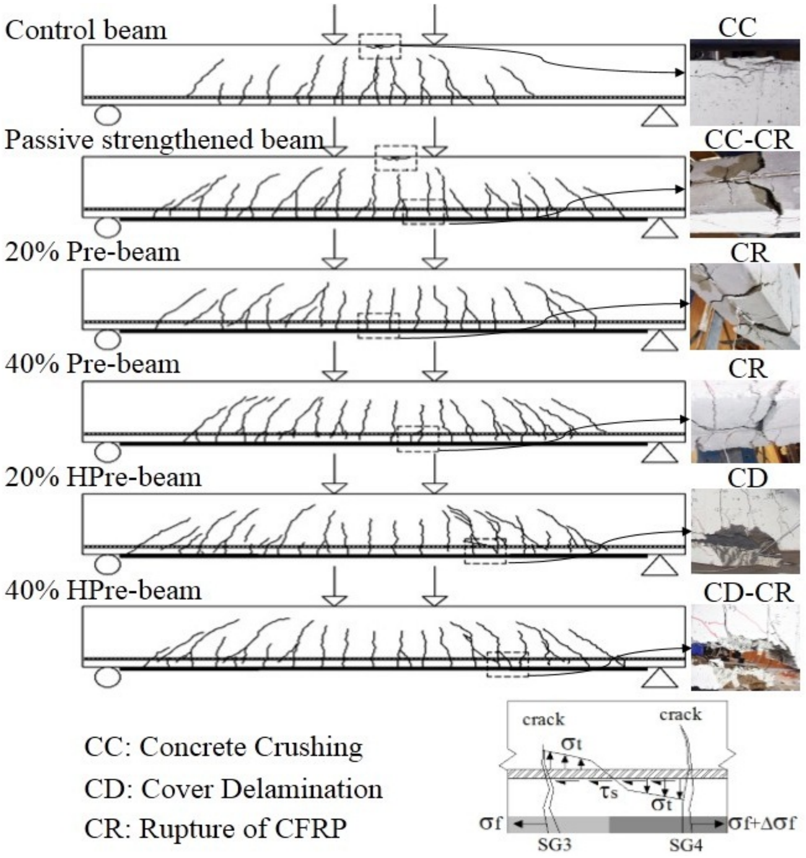

Figure 3-31: Crack pattern and prevailing failure modes at the ultimate capacity of the tested beams

After yielding of the tensile steel bars, the HPre-beams experienced different failure modes, located at the end section of the passive laminates, as represented in Figure 3-31, while the failure modes of all other beams were located within the maximum bending moment region. Investigation of the crack widths in the HPre-beams evidenced that the cracks in the concrete surrounding the laminates in the region where the SG4 is located (Figure 3-26 and Figure 3-31) were wider than the cracks at the SG3 section (Figure 3-26 and Figure 3-31). This is supported by the higher tensile strain value recorded by the SG4 compared to the corresponding value of SG3 in the prestressed laminate of the HPre-beams, as shown in Figure 3-29. According to the principle of static equilibrium applied to the concrete placed between these two cracked sections, the shear (τ_s) and tensile (σ_t) stresses can be developed along the concrete section of weakest strength (as shown in Figure 3-31), which is localized just below the tensile steel bars due to a higher percentage of the voids formed during the concrete casting process (as previously confirmed by (Xiong et al. 2007, Barros et al. 2011)). At this weak plane's level, the tensile stress (normal to the plane), conjugated with the shear stress, can contribute to separate the concrete cover below the tensile steel bars by horizontally extending the cracks at the SG4 section. On the other side, the prestressed laminate (continuously passing from both SG3 and SG4 cracked sections) attempts to prevent this concrete cover separation.

During the bending loading process, by increasing the aforementioned stresses in the weak plane, the 20% HPre-beam showed a staircase pattern of load decay after the maximum flexural capacity (Figure 3-27a) due to the gradually separation of the concrete cover (cover delamination), while the 40% HPre-beam failed by rupturing of the prestressed CFRP laminate at a tensile strain less than its ultimate tensile strength (see Figure 3-29 and Figure 3-31), since tendency for the separation of concrete cover, conjugated with the higher initial tensile strain introduced in the CFRP, may have contributed to a higher gradient of tensile stress in the flexural failure cracks , promoting the rupture of the laminate at a lower tensile strain. However, the 40% HPre-beam provided a higher maximum load carrying capacity when compared to the corresponding value of the 20% HPre-beam (Table 3-5). In fact, by increasing the prestress level, a higher compressive strain field is created in the concrete cover and longitudinal steel bars in tension providing an increase of load carrying capacity in terms of concrete cracking and steel yielding initiations, which may provide more resistance in terms of opening and extending the cracks at the section of SG4, resulting in a higher load carrying capacity for the strengthened beam when failing by concrete cover delamination.

The crack pattern of all the tested beams at the ultimate stage is shown in Figure 3-31, where most cracks consisted of flexural nature. In the shear spans (defined between the point loading and the nearest support) flexural-shear cracks have formed. Due to the higher load carrying capacity of the HPre-beams, a more diffuse crack pattern with a predominance of shear cracks has formed in the shear spans of these beams, when compared to the other beams, since the shear capacity of all the beams is equal. Additionally, Figure 3-31 evidenced that by increasing the prestress level applied to the CFRP laminate, a decrease in terms of cracked zone length was observed in the Pre-beams due to an initial compressive strain field introduced by the prestress force. However, the HPre-beams showed longer cracked zone length compared to the Pre-beams due to a higher load carrying capacity provided by the hybrid strengthening system. The comparison between the cracked zone lengths for all the strengthened beams is indicated in Figure 3-32b, where the cracked zone lengths were normalized to the corresponding length of the control beam.

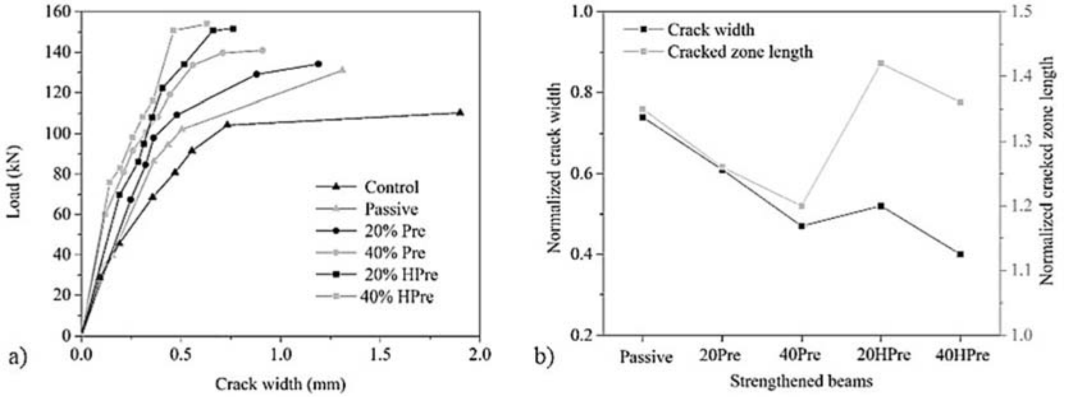

Figure 3-32: a) Load versus crack width of the tested beams, b) cracked zone length and crack width at SLS deflection normalized to the corresponding values of the control beam

The relationship between the average crack width and applied load for the tested beams is represented in Figure 3-32a, where the average crack width was calculated by averaging the widths of the cracks located in the maximum bending moment region at the level of the tensile steel reinforcement. To evaluate the efficiency of the presented strengthening techniques in terms of limiting the crack width of the beams at SLS conditions, Figure 3-32b compares the average crack width of the strengthened beams at the SLS deflection limit (8.8 mm) normalized to the one registered in the control beam. Both prestressing and hybrid strengthening techniques showed a smaller average crack width when the prestress level applied to the CFRP laminate increases. This reduction of the average crack width was more noticeable in the HPre-beams when compared to the Pre-beams with similar prestress level, which can be attributed to the higher flexural stiffness provided by the hybrid technique due to the contribution of the passive laminates.

3.5 Conclusions

The current chapter aimed to experimentally investigate the distribution of CFRP tensile strain and bond shear stress, immediately after the release of the prestress force, in the context of using NSM CFRP reinforcement for the flexural strengthening of RC beams. Moreover, the efficiency of the NSM prestressing and NSM hybrid techniques for the flexural strengthening of RC beams was experimentally evaluated by performing two experimental programs. According to the observed results, the following conclusions can be drawn:

- The experimental results showed that the distribution of tensile strains in the extremity region of the CFRP bonded length varies from zero (at its end section) to its effective tensile strain during the prestress transmission zone, and reaches a plateau beyond this zone. Moreover, the results evidenced that the prestress level applied to the CFRP reinforcement has a negligible influence on the transmission zone of the prestressed CFRP.
- The experimental investigation demonstrated that the bond shear stress starts from high value at the end of the CFRP bonded length and continues decreasing along the prestress transmission zone, and becomes approximately null after that. This bond shear stress increases with the prestress force applied to the NSM CFRP reinforcement.
- After releasing the prestress force, a negative camber is generated due to the negative bending moment caused by the eccentricity of this force in relation to the centroidal axis of the beam's cross section. This negative camber resulted in a decrease of tensile strain in the prestressed CFRP laminate, which represents the short-term prestress loss immediately after release.
- The prestress force created an initial compressive strain in the tensile steel reinforcement and surrounding concrete, which led to an increase of the load carrying capacity at concrete cracking and steel yielding initiations.
- The load carrying capacity at serviceability limit conditions increased significantly with the prestress level, when compared to the load carrying capacity of the beam strengthened with a non-prestressed CFRP laminate. However, the ultimate deflection of the beams strengthened with NSM prestressing technique decreased with the increase of applied prestress level. These results, which imply a decrease of the ductility index with the prestress level, suggest the adoption of an upper limit of the prestress level to be applied to the CFRP laminates in order do not compromise the ductility performance of the RC beams strengthened according to the NSM prestressing technique.
- All the beams strengthened with NSM prestressing technique provided an increase in terms of ultimate load carrying capacity, regardless the prestress level applied to the CFRP laminate, when compared to the control beam.
- The cracked zone length of the beam strengthened with a non-prestressed NSM CFRP laminate increased when compared to the control beam, while the increase of the prestress level inverted this tendency, by decreasing the cracked zone length in comparison to the passive strengthened beam. The NSM CFRP system, regardless the prestress level, has also provided a decrease of average crack spacing when compared to the control beam.

- The hybrid strengthened beams provided an average increase in terms of ultimate load carrying capacity higher than the ones obtained for the beams strengthened with NSM prestressing technique, when compared to the results obtained for the control beam. This ultimate load carrying capacity of the hybrid beams was influenced by the prestress level applied to the CFRP laminate, due to the different prevailing failure modes.
- The ultimate flexural capacity of all the tested beams was controlled by three types of failure modes after yielding of the tensile steel bars, namely: concrete crushing (CC); rupture of the CFRP laminate (CR); and concrete cover delamination (CD). The failure modes of the control and prestressed strengthened beams (CC and CR) were located within the maximum bending moment region, while the hybrid strengthened beams failed (by CR and CD) at the end section of the passive laminates. Moreover, the results showed that both prestressing and hybrid techniques decrease the possibility of the CC as prevailing failure mode of the strengthened beams, while this reduction was more evident when hybrid technique was adopted for strengthening application.
- Both prestressing and hybrid strengthening techniques showed a smaller average crack width when the prestress level applied to the CFRP laminate increases. This reduction of the average crack width was more noticeable in the hybrid beams when compared to the prestressed beams with similar prestress level.
- Reduction of the ultimate deflection capacity of the beams strengthened with NSM prestressing technique was observed with the increase of the prestress level, resulting a decrease in terms of energy absorption and deformability indexes, while the aforementioned indicators for the hybrid NSM CFRP beams were influenced by the type of prevailing failure mode at the maximum capacity (CR or CD). The hybrid strengthened beam, failed by the CR failure mode at the maximum capacity, showed a higher energy absorption and deformability indexes compared to the beams strengthened with NSM prestressing technique with similar prestress level.

Chapter 4: Numerical Analysis

A reliable simulation of the behavior of RC beams strengthened with such NSM prestressing and NSM hybrid techniques requires advanced numerical modeling based on the finite element method (FEM), which is still a challenge on the computational mechanical domain. Hence, in the current study, a nonlinear FE model is developed to simulate the experimental tests. This numerical analysis can be summarized as follows:

- Development of a 3D FE model including concrete, steel bars, CFRP reinforcement, and epoxy adhesive;
- Numerical simulation of the beams strengthened with either NSM prestressing or NSM hybrid techniques and evaluation of the predictive performance of the FE model;
- Executing a series of parametric studies in order to numerically assess the influence of the relevant parameters of the strengthening techniques on the flexural performance of the RC structures to be strengthened.

4.1 Simulation of Experimental Tests

4.1.1 Description of FE Model

A 3D FE model using ABAQUS software, including all the constitutive material models of the tested beams, was used to simulate the experimental tests, and to complement the analysis of this research program. The used material models, prestress procedure and implemented solution algorithms are discussed in the following sections.

4.1.1.1 Constitutive Material Models

4.1.1.1.1 Concrete

The concrete constitutive model used in the numerical analysis of the current study is the nonlinear concrete damage plasticity (CDP) model in ABAQUS. The CDP model considers the stiffness degradation of materials and stiffness recovery effects under cycling loading, essential aspects to simulate the behavior of RC structures subjected to either monotonic or cyclic loading conditions up to their collapse. In this CDP model, the concepts of linear isotropic elasticity in combination with isotropic tensile and compressive plasticity are used to simulate the inelastic behavior of concrete. In other words, the elastic stiffness of concrete is assumed to be the same under tension and compression. The CDP model considers two main damage mechanisms of the concrete, namely: cracking formation and propagation in tension; and elasto-plasticity in compression. In this model, the Drucker-Prager hyperbolic function is used to assess the flow potential, G , as follows (ABAQUS. 2011):

$$G = \sqrt{(e\sigma_{t0}\tan\psi)^2 + \bar{q}^2} - \bar{p}\tan\psi$$ Equation Section 4(4.1)

where σ_{t0} is the uniaxial tensile stress at failure, and e is flow potential eccentricity that adjusts the shape of meridional plane (herein assumed as a hyperbola) at which the function approaches the asymptote, meaning that the flow potential tends to a straight line in the meridional plane as the eccentricity tends to zero (see Figure 4-1a) (ABAQUS. 2011, Kmiecik and Kaminski 2011). The default flow potential eccentricity, recommended by CDP model, is $e = 0.1$, which implies that the material has almost the same dilation angle (ψ) over a wide range of confining pressure stress values (ABAQUS. 2011).

Dilation angle (ψ) is the inclination of the failure surface towards the hydrostatic axis at high confining pressure measured in the meridional plane ($p-q$). The CDP model is non-associated potential plastic flow in the $p-q$ plane (resulting in a non-symmetric stiffness matrix) when the dilation angle and the material friction angle (β) are different (ABAQUS. 2011). On the other side, this hyperbolic model provides associated potential plastic flow in the $p-q$ plane only when $\psi = \beta$ (see Figure 4-1).

For normal concrete materials, dilation angle (ψ) and flow potential eccentricity (e) can be physically estimated equal to concrete internal friction angle ($\beta = \psi : (36-40^o)$) and ratio between tensile and compressive strength of concrete, respectively (Kmiecik and Kaminski 2011). However, in this regards, Jankowiak and Lodigowski (2005) recommended to identify the material parameters of CDP model by considering the proposed ranges for $\psi : (34-43^o)$ and $e : (1-1.5)$.

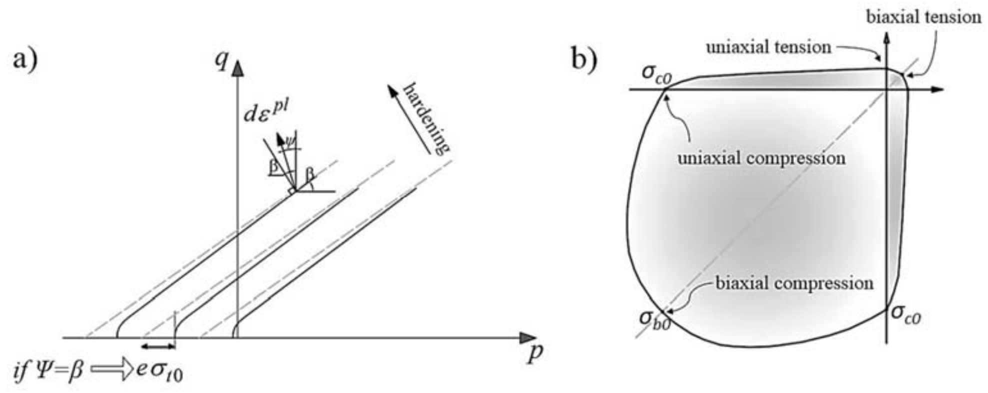

Figure 4-1: a) Hyperbolic flow potentials in the *p*-*q* plane, b) yield surface in plane stress

The proposed yield function (F) by Lee and Fenves (1998), which is a modification of the plastic damage model of Lubliner et al. (1989), is used in the CDP model to consider the different evolution of concrete strength under tension and compression controlled by the hardening variables, $\tilde{\varepsilon}_t^{pl}$ and $\tilde{\varepsilon}_c^{pl}$, which are referred to equivalent plastic strain in tension and compression (Figure 4-2), respectively, as follows (ABAQUS. 2011, Abdelatif et al. 2014):

$$F = \frac{1}{1-\alpha}\left(\bar{q} - 3\alpha\,\bar{p} + \beta(\tilde{\varepsilon}^{pl})\left\langle \hat{\bar{\sigma}}_{\max} \right\rangle - \gamma\left\langle -\hat{\bar{\sigma}}_{\max} \right\rangle - \bar{\sigma}_c(\tilde{\varepsilon}_c^{pl})\right) = 0 \qquad \text{(4.2)-a}$$

with

$$\alpha = \frac{(\sigma_{b0}/\sigma_{c0}) - 1}{2(\sigma_{b0}/\sigma_{c0}) - 1}\ ;\ 0 \le \alpha \le 0.5 \qquad \text{(4.2)-b}$$

$$\beta = \frac{\bar{\sigma}_c(\tilde{\varepsilon}_c^{pl})}{\bar{\sigma}_t(\tilde{\varepsilon}_t^{pl})}(1-\alpha) - (1+\alpha) \qquad \text{(4.2)-c}$$

$$\gamma = \frac{3(1-K_c)}{2K_c - 1} \rightarrow 0.5 < K_c < 1 \qquad \text{(4.2)-d}$$

$$\bar{\sigma}_c(\tilde{\varepsilon}_c^{pl}) = E_0(\varepsilon_c - \tilde{\varepsilon}_c^{pl}) \qquad \text{(4.2)-e}$$

$$\bar{\sigma}_t(\tilde{\varepsilon}_t^{pl}) = E_0(\varepsilon_t - \tilde{\varepsilon}_t^{pl}) \qquad \text{(4.2)-f}$$

$$\tilde{\varepsilon}_c^{pl} = \tilde{\varepsilon}_c^{in} - \frac{d_c}{(1-d_c)}\frac{\sigma_c}{E_c} \qquad \text{(4.2)-g}$$

$$\tilde{\varepsilon}_t^{pl} = \tilde{\varepsilon}_t^{ck} - \frac{d_t}{(1-d_t)}\frac{\sigma_t}{E_c} \qquad \text{(4.2)-h}$$

where the Macaulay bracket symbol, $\langle \ \rangle$, is defined by $\langle x \rangle = (|x| + x)/2$. Moreover, $\hat{\bar{\sigma}}_{\max}$ is the maximum principal effective stress which is algebraically the maximum eigenvalue of the effective stress tensor ($\bar{\sigma}$), and $\bar{\sigma}_t(\tilde{\varepsilon}_t^{pl})$ and $\bar{\sigma}_c(\tilde{\varepsilon}_c^{pl})$ are effective tensile and compressive cohesion stress (Eqs. (4.2)-f and (4.2)-e), respectively. σ_{b0}/σ_{c0} (known also as f_{b0}/f_{c0}) is the ratio of initial biaxial compressive yield stress to initial uniaxial compressive yield stress that is taken as 1.16 in this study, as recommended by CDP model (Figure 4-1b) (ABAQUS. 2011). $\tilde{\varepsilon}_c^{in}$ and $\tilde{\varepsilon}_t^{ck}$ are the crushing strain and the cracking strain, respectively (Figure 4-2). Furthermore, d_c and d_t are the scalar stiffness degradation variable in a compression zone and in a tension zone, respectively (see Figure 4-2). In the formulation, this stiffness degradation variable is a function of $\bar{\sigma}$ and $\tilde{\varepsilon}^{pl}$ ($\tilde{\varepsilon}_c^{pl}$ or $\tilde{\varepsilon}_t^{pl}$).

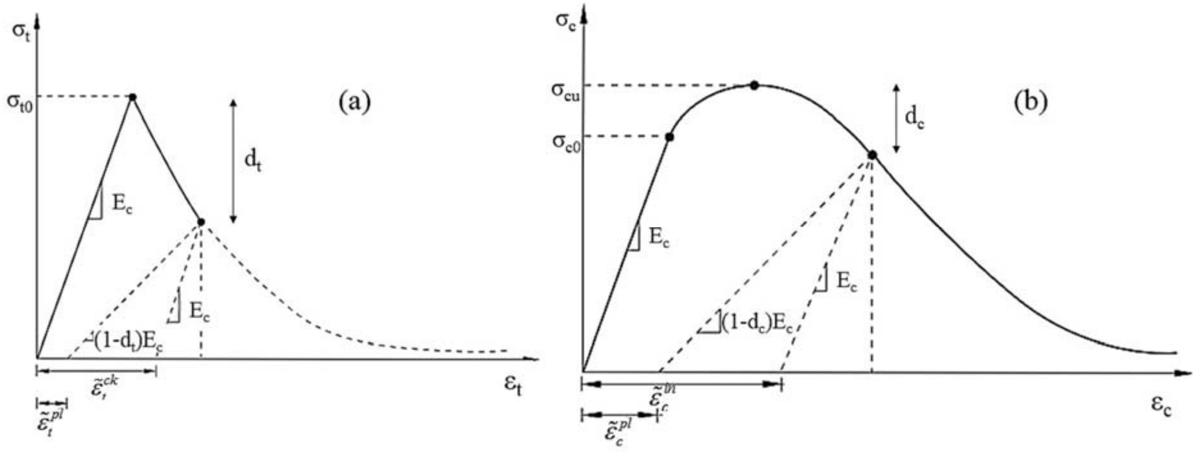

Figure 4-2: Response of concrete to uniaxial loading in: a) tension, b) compression (ABAQUS. 2011)

K_c describes the ratio of the distance between the hydrostatic axis and respectively the compression meridian and the tension meridian in the deviatoric cross section (Kmiecik and Kaminski 2011). In fact, according to the modified model of Lee and Fenves, the yield function in the deviatoric cross section needs not to be a circle and it is governed by K_c designated as shape of the loading surface parameter. In other words, the assumption of $K_c = 1$ results in a circle deviatoric cross section for the yield function (as in the classic Drucker-Prager model), and moreover, this K_c ratio is always higher than 0.5. Consequently, K_c ranges between 0.5 and 1, and the CDP model recommends to assume $K_c = 2/3$ (Figure 4-3) (ABAQUS. 2011).

On the other hand, CDP model uses the viscosity parameter, V , for considering the visco-plastic regularization to improve the rate of convergence of the model in softening phase, without compromising results, but in the current numerical analysis, this parameter was assumed to be zero.

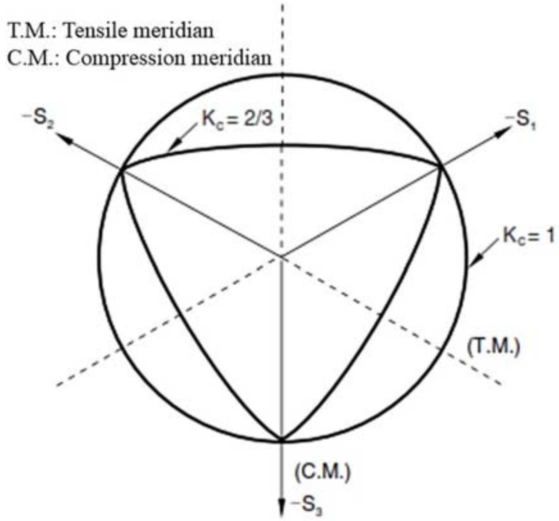

Figure 4-3: Yield surfaces in the deviatoric plane, corresponding to different values of K_c (ABAQUS. 2011)

In the present research, the uniaxial behavior of the uncracked concrete in tension and compression was assumed to be linear up to f_{ct} (concrete tensile strength) and $0.45f_c^{'}$ (concrete compressive strength), respectively (Figure 4-4a) (ACI-318-08 2008, CEB-FIP. 2011). The concrete nonlinear stress-strain relation for uniaxial compression was obtained according to the recommendations of CEB-FIP model code. Moreover, to describe the concrete tensile post-cracking behavior, a stress-crack opening relation according to CEB-FIP model code, represented in Figure 4-4b, was used for the cracked concrete (using concrete tensile fracture energy, G_f, recommended by (ABAQUS. 2011)). In this regards, the CDP model uses the concept of concrete crack bandwidth considering a characteristic length related to the element size (associated with an integration point).

4.1.1.1.2 Steel and CFRP reinforcements and epoxy adhesive

Elasto-plastic models with associated plastic flow were used to simulate the behavior of epoxy adhesive and steel bars (ABAQUS. 2011). An idealized isotropic hardening plasticity model was considered to simulate the behavior of steel bars up to its ultimate tensile strength based on the simplified model recommended by CEB-FIP code (Figure 4-4c). On the other hand, the perfect plasticity model, with no hardening, was used to simulate the epoxy adhesive behavior, as represented in Figure 4-4c. A linear elastic stress-strain relation up to the ultimate tensile strength was adopted to simulate the tensile behavior of the CFRP laminates (Figure 4-4d). After CFRP ultimate tensile strain, ε_{fu} , the contribution of the laminates was neglected.

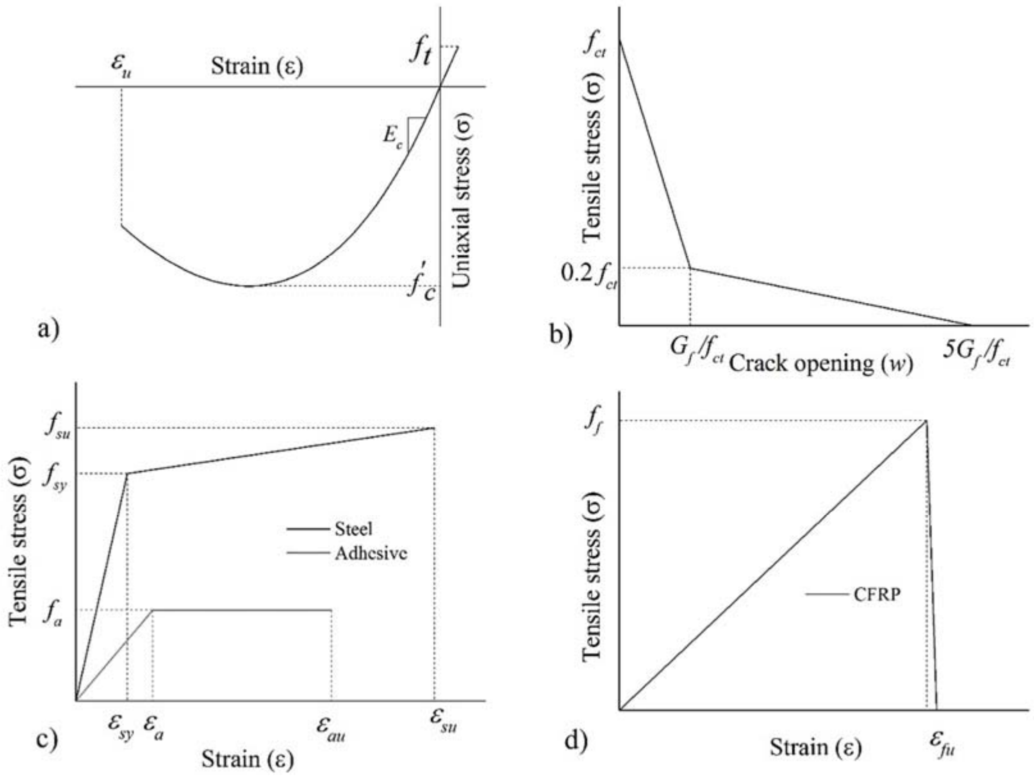

Figure 4-4: Uniaxial constitutive laws of materials: a) concrete in compression and in tension up to crack initiation; b) concrete tensile post-cracking; c) steel reinforcement and epoxy adhesive; d) CFRP reinforcement

4.1.1.2 Interfacial Bond Model

In the current study, to simulate the bond behavior of the CFRP laminate-adhesive-concrete connections, two surface-based contact interfaces were defined. One was used at the laminate-epoxy adhesive interface, while the other was applied at the concrete-epoxy adhesive interface (Figure 4-5). A mixed mode of debonding including stress-separation (in the normal direction of the interface element plane) and shear stress-slip (on both directions of the interface element plane) was used to simulate the concrete-epoxy interface, while for the laminate-epoxy interface only the shear stress-slip, in both directions of the plane, was considered.

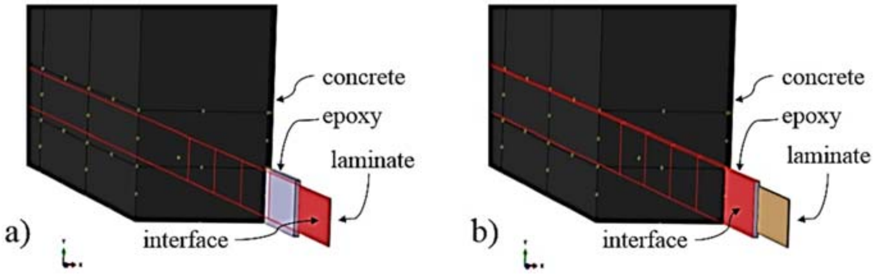

Figure 4-5: Surface-based contact interfaces: a) between laminate and epoxy adhesive; b) between concrete and epoxy adhesive

Cohesive behavior was defined for a pair of surfaces for these contact interfaces, where the first surface was treated as a slave surface and the second surface as its corresponding master surface. Cohesive forces potentially act on the all nodes of the slave surface. Moreover, separations and slips of the contact interface are measured along this surface. In other words, contact separations and slips are the relative displacement between the nodes on the salve surface and the nodes on the master surface that are initially in contact at the beginning of the analysis (ABAQUS. 2011).

The governed laws for the surface-based cohesive behavior were defined according to the following steps: 1st linear elastic stress-separation and shear stress-slip relationships (St.1); 2nd damage initiation criteria (St.2); and 3rd damage evolution laws (St.3), as represented in Figure 4-6. This figure, moreover, shows that a linear softening branch is assumed as damage evolution law for the contact interfaces in this numerical analysis considering the fracture energy of the interfaces in normal direction (G_n) and in both directions ($G_{s,t}$) of the interface element plane.

The normal and tangential stiffness components of contact interfaces were assumed to be uncoupled, meaning that pure normal separation does not influence the cohesive forces in the shear direction, and pure shear slip with zero normal separation does not cause any cohesive forces in the normal direction.

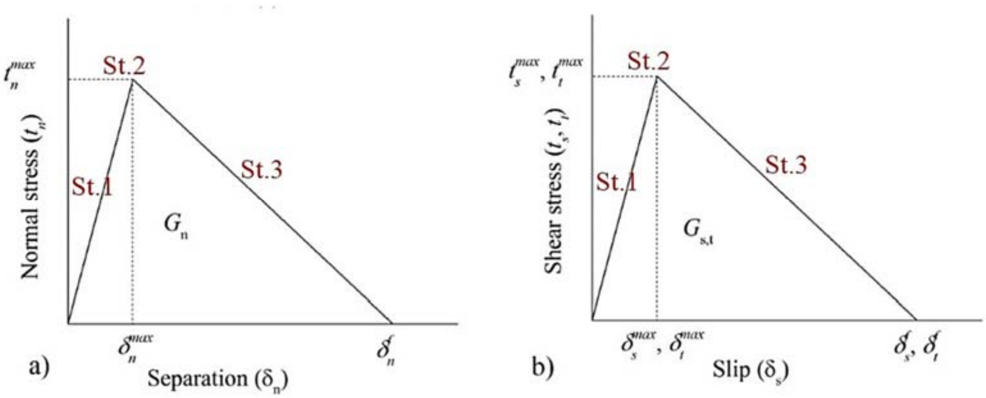

Figure 4-6: Governed laws for surface-based cohesive behavior: a) normal direction; b) both shear directions

Initial linear response of the contact interfaces (St.1 in Figure 4-6) is limited by the damage initiation criteria (St.2 in Figure 4-6) corresponding to the beginning of degradation of the cohesive response at a contact point. The process of this degradation begins when a quadratic interaction function considering the contact stresses reaches a value of one. This criterion can be represented as:

$$\left(\frac{\langle t_n \rangle}{t_n^{\max}}\right)^2 + \left(\frac{t_s}{t_s^{\max}}\right)^2 + \left(\frac{t_t}{t_t^{\max}}\right)^2 = 1 \tag{4.3}$$

where t_n is normal contact stress in the pure normal mode, and t_s and t_t are shear contact stress along the first and second directions, respectively. $t_n^{\max}$, $t_s^{\max}$, and $t_t^{\max}$ are the peak values of the contact stress when the separation is either purely normal to the interface or purely in the first or the second shear directions, respectively (Figure 4-6). The Macaulay bracket symbol, $\langle\ \rangle$, is used to signify that the contact interfaces in normal direction potentially act only for tensile stress and a purely compressive stress does not cause any cohesive forces in the normal direction.

In the present work, the maximum tensile stress of the concrete-epoxy interface in the normal direction is limited to the concrete tensile strength, resulting in the failure of the surrounding concrete when the tensile stress exceeds the concrete tensile strength (f_{ct}) (Omran and El-Hacha 2011). Accordingly, the tensile fracture energy of concrete can be considered to specify the damage evaluation of this interface ($G_f = G_n$ in Figure 4-6).

To simulate both directions of the shear stress-slip interface between the epoxy adhesive and concrete, interface properties, including the maximum shear stress ($t_s^{\max}, t_t^{\max}$) and shear fracture energy (G_s, G_t), are obtained from Eqs. (4.4) and (4.6), recommended by (Seracino et al. 2007).

$$t_s^{\max} = t_t^{\max} = \left(0.802 + 0.078\ .\ \varphi\right)\ .f_{cm}^{0.6} \tag{4.4}$$

$$\delta_s^f = \delta_t^f = \left(0.976\ .\ \varphi^{0.526}\right)\ /\ \left(0.802 + 0.078\ .\ \varphi\right) \tag{4.5}$$

$$G_s = (t_s^{\max}.\delta_s^f)/2\,,\ G_t = (t_t^{\max}.\delta_t^f)/2 \tag{4.6}$$

where φ is the aspect ratio of the interface failure plane, defined as (groove depth + t_d)/(groove width + $2.t_b$) with $t_d = t_b = 1\text{mm}$, δ_s^f and δ_t^f are maximum shear slip, and f_{cm} is the concrete average compressive strength.

The following shear stress-slip law, recommended by (Sena-cruz and Barros 2004), was adopted to simulate the behavior of shear-slip interface between the epoxy adhesive and CFRP laminate in both directions:

$$t_s(\delta) = \begin{cases} t_s^{\max}\left(\dfrac{\delta}{\delta_s^{\max}}\right)^{\alpha} & \delta \le \delta_s^{\max} \\ t_s^{\max}\left(\dfrac{\delta}{\delta_s^{\max}}\right)^{-\alpha'} & \delta > \delta_s^{\max} \end{cases}\ ,\ t_t(\delta) = \begin{cases} t_t^{\max}\left(\dfrac{\delta}{\delta_t^{\max}}\right)^{\alpha} & \delta \le \delta_t^{\max} \\ t_t^{\max}\left(\dfrac{\delta}{\delta_t^{\max}}\right)^{-\alpha'} & \delta > \delta_t^{\max} \end{cases} \tag{4.7}$$

where $t_s^{\max}, t_t^{\max}$ and $\delta_s^{\max}, \delta_t^{\max}$ are the maximum shear stress and its corresponding slip, respectively, and α and α' are parameters defining the shape of the pre- and post-peak shear stress-slip curves. The values of these parameters were found in literature (Sena-cruz and Barros 2004) for concrete with similar strength to the one of the tested beams. The shear fracture energy (G_s, G_t) of this interface was estimated to be equal to the area under the shear stress-slip curve considering a maximum shear slip equal to the corresponding one for the concrete-epoxy interface obtained by Eq. (4.5).

These equations were selected due to their simplicity and ability to simulate appropriately the bond behavior between epoxy adhesive and both CFRP laminate and concrete.

4.1.1.3 Simulation of Experimental Test Setup

In order to reduce the computational time of the numerical analysis, only one quarter of the full size beam was modeled taking the advantage of the double symmetry of the beams ($U_x = 0, U_z = 0$ as represented in Figure 4-7). The loading and boundary conditions of the model were applied according to the particularities of the test setup (Figure 4-7).

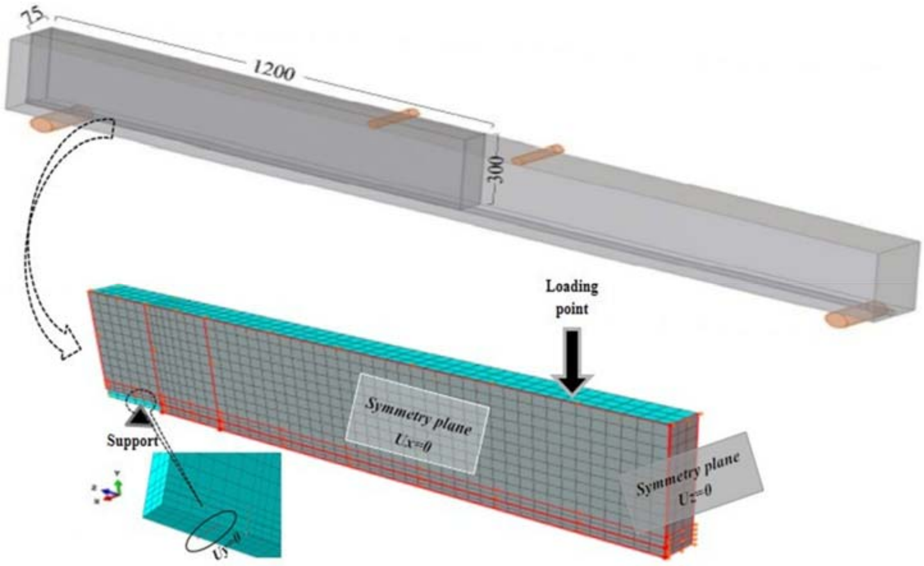

Figure 4-7: Boundary condition of the FE model (dimensions in mm)

To reproduce, as much as possible, the real test conditions for the prestressed beams, four steps of analysis were numerically adopted to simulate the experimental prestress procedure:

Step 1: Prestressing: applying tensile stress corresponding to the prestress level at the extremities of CFRP laminate (St.(1) in Figure 4-8);

Step 2: Injecting and curing of epoxy adhesive: activating the interfaces between concrete-epoxy adhesive and CFRP laminate-epoxy adhesive, assuming that the properties of the interfaces correspond to a hardened stage of the epoxy (St.(2) in Figure 4-8);

Step 3: Prestress releasing: releasing the prestress force from the extremities of CFRP laminate (St.(3) in Figure 4-8);

Step 4: Flexural loading: applying the monotonic load up to the collapse of the beam.

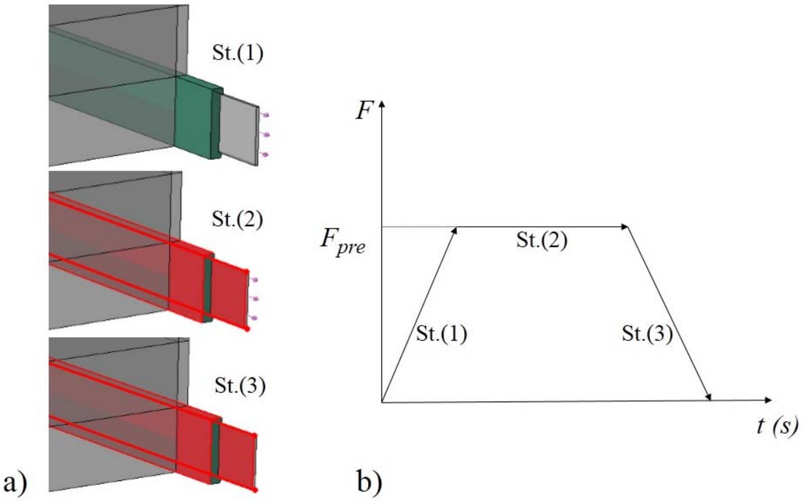

Figure 4-8: a) Numerical prestressing procedure; b) numerical procedure adopted to simulate the application and release of the prestress force

On the other side, in the current study, explicit solver (using ABAQUS/Explicit-dynamic) was used for the numerical analysis, since this solver is more efficient than implicit solver (in ABAQUS/Standard-static) for three-dimensional nonlinear FE models involving contact and large deformations (ABAQUS. 2011). In fact, the explicit dynamics procedure was originally developed to model high-speed impact events and solving the state of dynamic equilibrium where inertia can play a dominant role in the solution (ABAQUS. 2011, Tasnimi and Rezazadeh 2012).

Applying the explicit dynamic procedure to quasi-static situation requires some special considerations. Since a static solution is fundamentally a long-time solution, it is often computationally impractical to simulate an event in its natural time scale, which would require an excessive number of small time increments. Hence, to obtain an economic solution, the numerical analysis must be accelerated. One way to accelerate the numerical analysis is increasing the loading rate, resulting in decreasing the time analysis. On the other hand, when the numerical analysis is accelerated, the state of static equilibrium evolves into the dynamic equilibrium at which inertial forces become more dominant. Hence, the economic solution to model quasi-static situations using explicit dynamics for the analysis can be obtained considering the shortest time period of analysis, at which inertial forces remain insignificant (Tasnimi and Rezazadeh 2012).

4.1.1.4 Element Types and Meshing

Eight-node 3D solid hexahedral elements (C3D8R element) were adopted to model the concrete, CFRP laminate and epoxy adhesive (Figure 4-9), and these C3D8R elements are linear with one reduced-integration point in order to reduce running time. 3D two-node truss elements (T3D2 element) were embedded into the concrete elements to simulate the behavior of steel reinforcements (Figure 4-9). T3D2 elements have linear displacement and can carry only tensile or compressive load and have no resistance to bending (ABAQUS. 2011).

The numerical studies showed that the formulation of the CDP model, when the used material exhibits strain-softening behavior, results in a strong mesh dependency, since the model is dependent on the concrete crack bandwidth (ABAQUS. 2011, Abdelatif et al. 2014). In order to alleviate mesh dependency during the material softening, ABAQUS introduces a characteristic length related to the element size (associated with an integration point) into the formulation, so that the constitutive law is expressed as a stress-displacement relation. Hence, in the present work, the stress-crack opening concept for the softening part of the concrete tensile behavior was adopted in the CDP model to alleviate mesh dependency of the FE model (see section 4.1.1.1). Furthermore, a fine mesh refinement was applied in the zones where relatively high stress gradients are expected to occur (Figure 4-9).

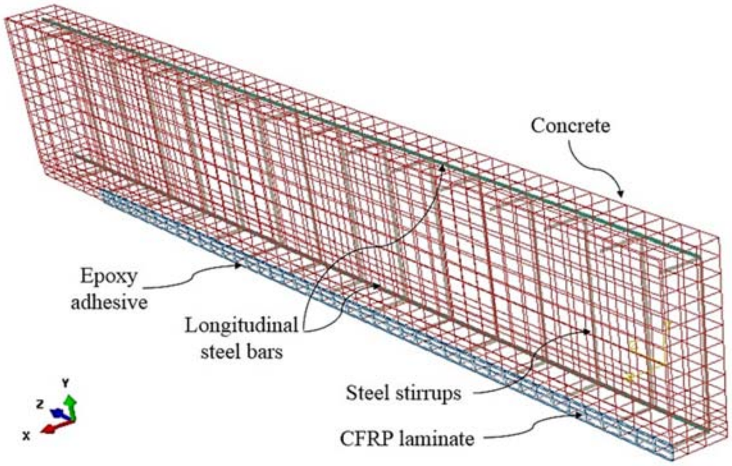

Figure 4-9: Meshing of the tested beams

4.1.2 Numerical Simulation of NSM Prestressed Beams

The proposed numerical approach was used to simulate the experimental tests of the beams strengthened with NSM prestressing technique (represented in section 3.3). Figure 4-10 represents the FE mesh, steel and CFRP reinforcements of this numerical model.

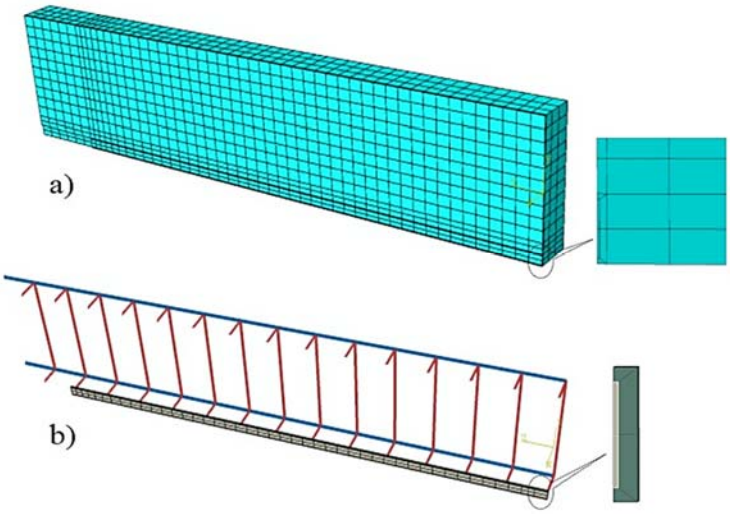

Figure 4-10: a) Mesh of FE model; b) steel and CFRP reinforcements

For this numerical simulation, the constitutive parameters of the CDP model are indicated in Table 4-1 and the main material properties reported in Table 3-1 were assigned to the used constituent materials. The normal tensile stress and tensile fracture energy of the concrete-epoxy interface were limited to the tensile strength and fracture energy of the concrete ($t_n^{\max} = f_{ct} = 2.51$ MPa, $G_n = G_f = 0.08\,\mathrm{N/mm}$), while the maximum shear stress and shear fracture energy of this bond were obtained using Eqs. (4.4) and (4.6) ($t_s^{\max} = t_t^{\max} = 8.4\,\mathrm{MPa}$, $G_s = G_t = 7.1\,\mathrm{N/mm}$). The maximum shear stress and shear fracture energy of the laminate-epoxy interface were found using Eq. (4.7) ($t_s^{\max} = t_t^{\max} = 20\,\mathrm{MPa}$, $G_s = G_t = 23.56\,\mathrm{N/mm}$).

Table 4-1: Constitutive parameters of CDP model

CDP Parameters	dilation angle ψ	plastic eccentricity e	stress ratio f_{b0}/f_{c0}	shape of loading surface K_c	viscosity parameter V
	38°	0.1	1.16	0.67	0

4.1.2.1 Assessment of the Numerical Model

To assess the predictive performance of the described numerical model, the obtained load versus mid-deflection response is compared in Figure 4-11 with the ones registered experimentally. The prevailing failure modes of the beams at the maximum load carrying capacity were numerically predicted similar to the ones experienced experimentally, but some deviation was obtained on the prediction of the deflection corresponding to the maximum capacity. It worth to note that the smaller predictive performance on the numerical simulation of the 40% prestressed beam can be related to the unexpected behavior of this beam, as explained in section 3.3.

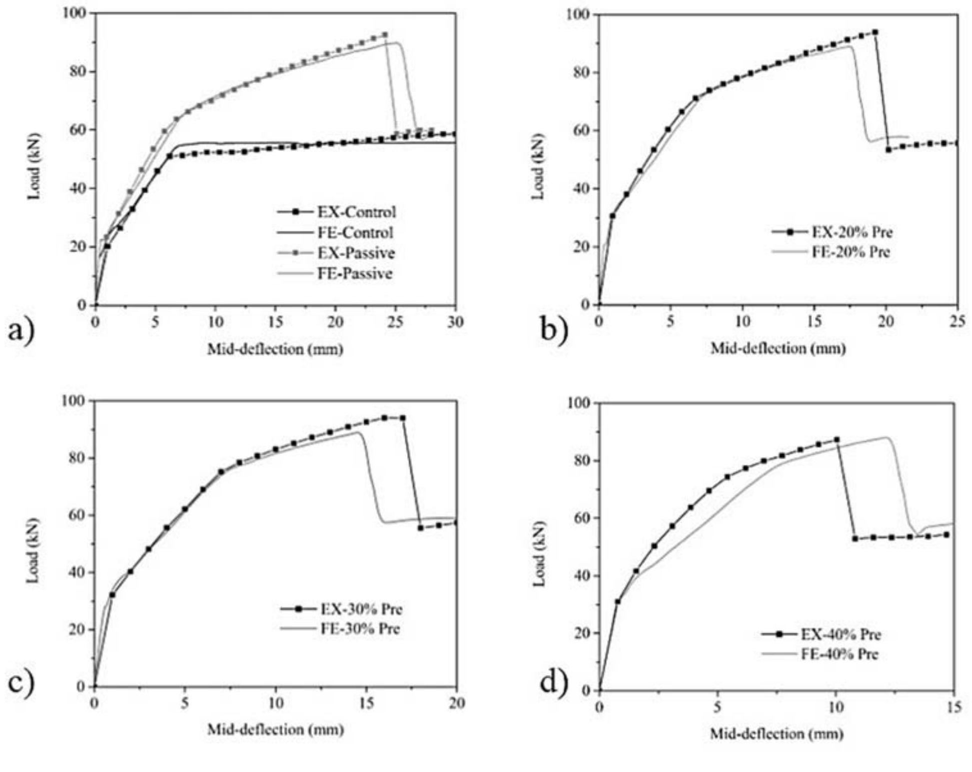

Figure 4-11: Numerical simulation of the experimental results: a) control and passive beams, b) 20% prestressed beam, c) 30% prestressed beam, and d) 40% prestressed beam

The numerical model has also confirmed that by increasing the prestress level in the laminate, the failure of the strengthened beams occurs at smaller deflection. The relationship between the applied prestress level and the normalized ductility index to the passive beam, obtained experimentally and numerically, is compared in Figure 4-12a, where, a part the beam prestressed at 40%, a very good prediction is shown. A good predictive performance in terms of tensile strains recorded in the laminate and steel reinforcement, as well as, compressive strain monitored at the concrete top surface of mid-span cross section, is also evidenced in Figure 4-12b, Figure 4-12c, and Figure 4-12d, respectively, where the corresponding values for the passive beam in comparison with the either or both of 20% and 30% prestressed beams are considered in order to obtain a better representation of the figures.

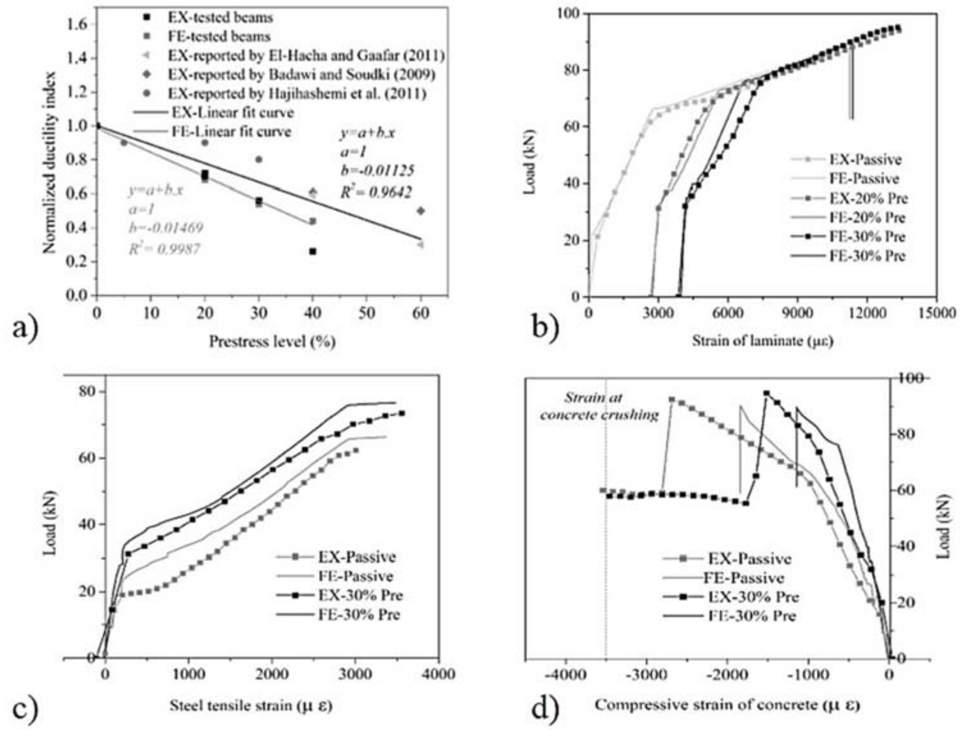

Figure 4-12: Numerical simulation: a) normalized ductility index to the passive beam, b) strain of CFRP laminate at mid-span, c) strain of tensile steel reinforcement at mid-span, d) strain at concrete top fiber at mid-span

4.1.2.2 Influence of NSM CFRP Bonded Length on Flexural Strengthening Performance

The proposed prestressing system, represented in Figure 3-3, is capable of introducing the prestressed CFRP laminates with different bonded lengths to strengthen RC beams in real applications. This bonded length should be extended up to a certain distance from the loading section in shear span of the strengthened beam to avoid the premature failure modes (such as concrete cover delamination and debonding of the CFRP laminate from the concrete substrate) before the CFRP rupture. In order to avoid the debonding failure of NSM CFRP reinforcement from the surrounding concrete, the CFRP bonded length should be extended at its both extremities of the maximum bending moment region as a required development length (l_{db}) according to the recommendation of (ACI-440.2R. 2008). This development length is obtained $l_{db} \geq 190\,\text{mm}$ for the current experimental beams, and a value of 300 mm can be adopted due to the uncertainty in terms of the average bond strength, τ_b, values (detailed description of l_{db} can be found in section 3.4).

On the other hand, in real strengthening applications, the anchorage conditions of the NSM prestressing system (Figure 3-3) and the restrictions imposed by supports (column-beam joints) cause a constraint to fulfill the total length of groove with epoxy adhesive up to the support (on the beam tensile surface). Hence, this section aims to numerically assess the influence of the prestressed CFRP bonded length on the flexural behavior of the strengthened beams. Accordingly, the 20% prestressed NSM CFRP strengthened beam was numerically modeled considering the CFRP development length (l_{db}) of 300 mm, 450 mm, 600 mm, 800 mm (adopted for the experimental program), and 900 mm (fulfilling the groove up to the support) (Figure 4-13).

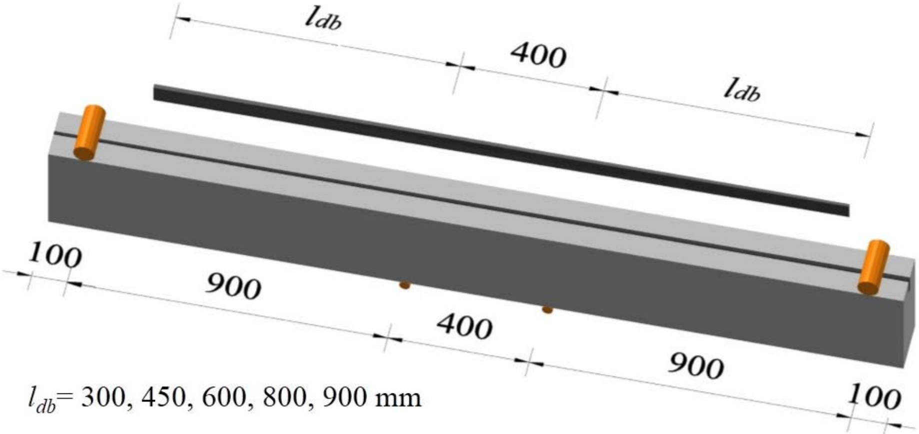

Figure 4-13: Prestressed CFRP laminate with different development length (l_{db})

The relationship between the force and mid-span deflection of the 20% prestressed beams with different CFRP development lengths (l_{db}) is shown in Figure 4-14. This figure evidences that for the 20% prestressed beams with l_{db} of 600 mm, 800 mm, and 900 mm, the maximum load capacity was not influenced by the applied development length (l_{db}), while the prestressed beams with l_{db} of 300 mm and 450 mm showed a smaller maximum load capacity when the development length (l_{db}) decreases.

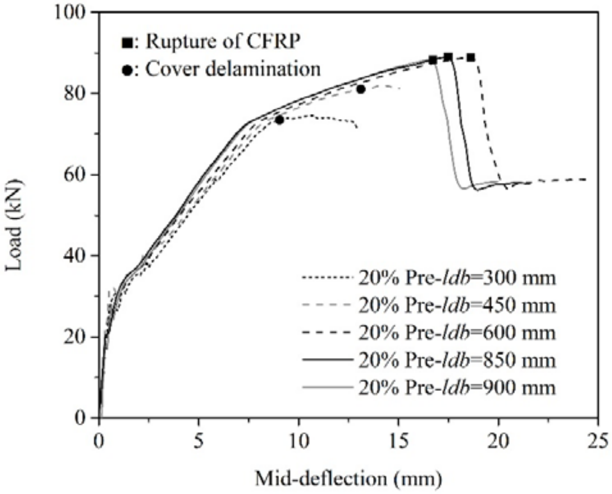

Figure 4-14: 20% prestressed beam with different CFRP bonded lengths

The ultimate flexural capacity of the 20% prestressed beams with l_{db} of 600 mm, 800 mm, and 900 mm was numerically controlled by the rupture of the CFRP laminate (as pointed in Figure 4-14), while the two 20% prestressed beams with l_{db} of 300 mm and 450 mm experienced the separation of the concrete cover (cover delamination) from the end section of the CFRP bonded length at the ultimate stage. Moreover, for these two beams, the instant of the development of a concrete tensile strain higher than the strain corresponding to the end of tensile strain softening of concrete (assuming about 10 times the strain corresponding to the tensile strength of concrete according to the recommendation of ABAQUS (2011)) was pointed on the corresponding numerical flexural responses in Figure 4-14, as a stage when concrete cover delamination can occur.

The concrete tensile strain field based on the PEEQT output (equivalent plastic strain in uniaxial tension ($\tilde{\varepsilon}_t^{pl}$) obtained using Eq. (4.2)-h) and based on the PE22 output (plastic strain in Y direction) of the FE software is represented in Figure 4-15 for the 20% prestressed beams with l_{db} of 300 mm, 450 mm, and 600 mm, at the maximum capacity.

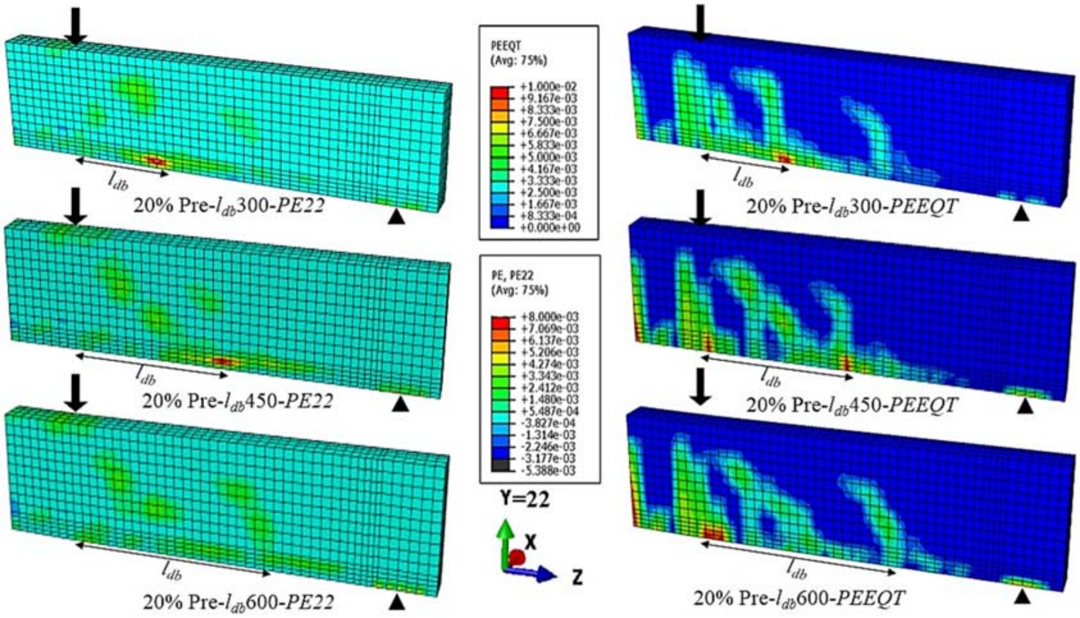

Figure 4-15: Distribution of concrete tensile strain based on the PEEQT and PE outputs

Finally, from the current parametric studies, it can be concluded that by increasing the NSM CFRP development length in shear span of the strengthened beams, the possibility of occurrence of the concrete cover delamination (as a premature failure model before the rupture of the CFRP) decreases. Accordingly, in real applications, for design purpose of strengthening of RC beams using NSM CFRP reinforcement, the CFRP bonded length should be extended as much as possible close to the support to decrease the susceptibility to the concrete cover delamination failure.

4.1.3 Numerical Simulation of NSM Hybrid Beams

The numerical approach was also used to simulate the experimental tests of the beams strengthened with NSM hybrid technique (represented in section 3.4). Figure 4-16 indicates the FE mesh, steel and CFRP reinforcements of this numerical model.

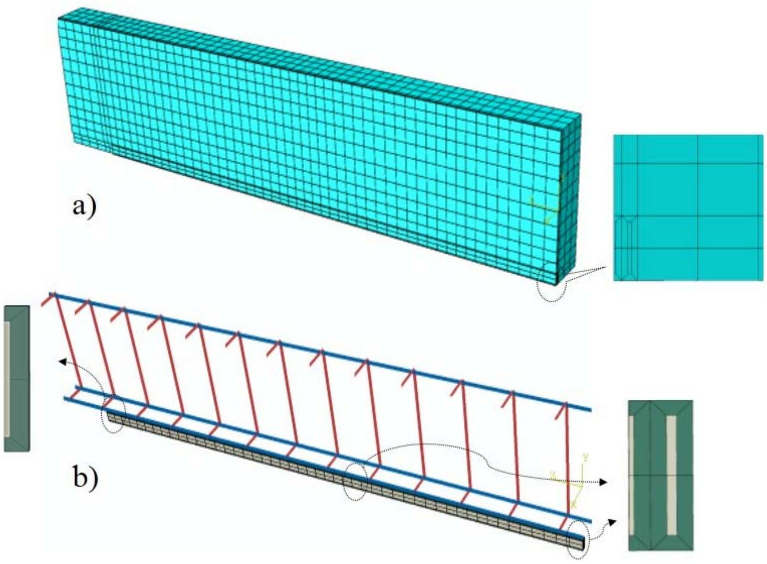

Figure 4-16: a) Mesh of FE model; b) steel and CFRP reinforcements

For the present numerical simulation, the constitutive parameters of the CDP model are represented in Table 4-2 and the main material properties reported in Table 3-4 were assigned to the used constituent materials. The normal tensile stress and tensile fracture energy of the concrete-epoxy interface were limited to the tensile strength and fracture energy of the concrete ($t_n^{\max} = f_{ct} = 1.8\,\text{MPa}$, $G_n = G_f = 0.07\,\text{N/mm}$), while the maximum shear stress and shear fracture energy of this bond were obtained using Eqs. (4.4) and (4.6) ($t_s^{\max} = t_t^{\max} = 7.1\,\text{MPa}$, $G_s = G_t = 6.4\,\text{N/mm}$). The maximum shear stress and shear fracture energy of the laminate-epoxy interface were found using Eq. (4.7) ($t_s^{\max} = t_t^{\max} = 20\,\text{MPa}$, $G_s = G_t = 23.56\,\text{N/mm}$).

Table 4-2: Constitutive parameters of CDP model

CDP Parameters	dilation angle ψ	plastic eccentricity e	stress ratio f_{b0}/f_{c0}	shape of loading surface K_c	viscosity parameter V
	40°	1	1.16	0.67	0

4.1.3.1 Assessment of the Numerical Model

The predictive performance of the described numerical model was assessed by simulating all the tested beams, and the comparison of the applied load versus mid-deflection response obtained numerically and experimentally is depicted in Figure 4-17. This figure indicates a good predictive performance of the numerical strategy in terms of the flexural response of the tested beams. Moreover, in the cases of the control beam and beams strengthened with prestressed laminate at 0%, 20%, and 40% level, the numerical model predicted with good accuracy the deflection level when the concrete crushing and the rupture of the CFRP have occurred experimentally.

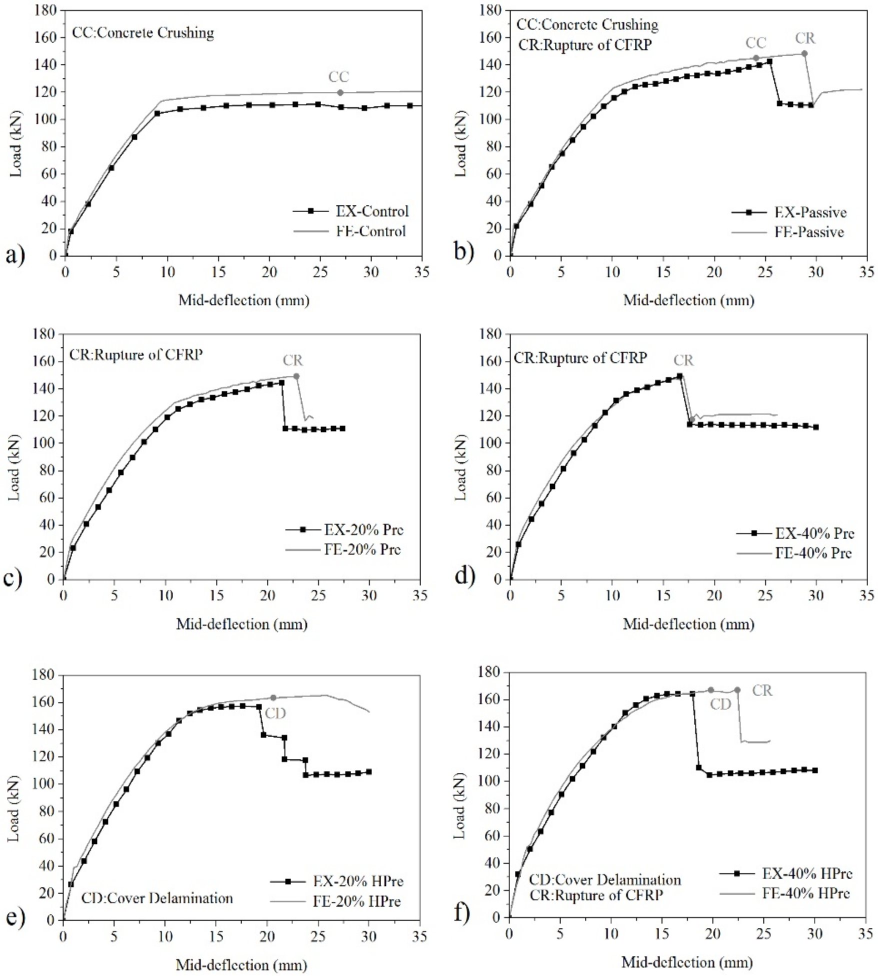

Figure 4-17: Numerical simulation of the experimental tests: a) control beam, b) passive strengthened beam, c) 20% Pre-beam, d) 40% Pre-beam, e) 20% HPre-beam, f) 40% HPre-beam

For the flexural response of the hybrid strengthened beams, the numerical model estimates an almost constant load carrying capacity after the development of high stress gradient in the zone where experimentally an intense damage evolution was observed (Figure 3-31). The instant of the development of concrete tensile strain in this zone higher than the strain corresponding to the end of tensile strain softening of concrete (assuming about 10 times the strain corresponding to the tensile strength of concrete according to the recommendation of ABAQUS (2011)) was pointed on the numerical flexural response of the HPre-beams in Figure 4-17, as a stage when the concrete cover below the tensile steel bars cannot sustain the created stress concentration, and concrete cover delamination can occur. Finally, the failure modes registered experimentally were captured numerically, but for deflection levels higher than the ones observed experimentally. This fact can be attributed to the use of embedded truss elements within the concrete elements to model the longitudinal tensile steel bars, preventing to create the weak plane just below the tensile steel bars in the concrete. The concrete tensile strain field based on the PEEQT output (equivalent plastic strain in uniaxial tension) of the FE software is represented in Figure 4-18 for the prestressed and hybrid strengthened beams at the maximum capacity.

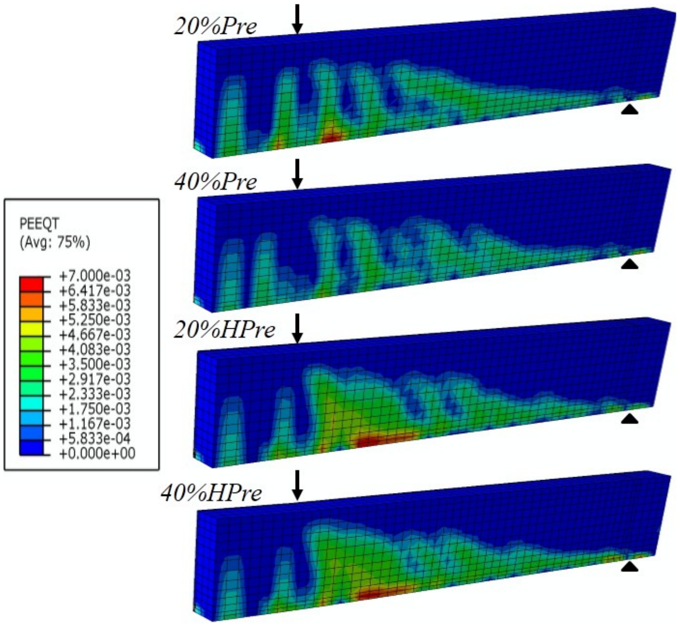

Figure 4-18: Distribution of the concrete tensile strain based on the PEEQT output

4.1.3.2 Evaluation of another Configuration of the NSM Hybrid Technique

This section aims to numerically evaluate the efficiency of passive CFRP reinforcement ratio of the NSM hybrid technique (lower than the one adopted in the experimental program), on the prevailing failure mode and deflection capacity of the strengthened beams. For this purpose, another configuration for combining passive and prestressed CFRP laminates based on the NSM hybrid technique was adopted for the flexural strengthening of the RC beams. This configuration was composed of two prestressed CFRP laminates of 1.4 × 10 mm^2 cross sectional area and one passive CFRP laminate of either 1.4 × 10 mm^2 (designated as HPre-L10, sec. (A1) in Figure 4-19) or 1.4 × 20 mm^2 (designated as HPre-L20, sec. (A2) in Figure 4-19) cross sectional area, introduced in separate grooves. The ratio of the prestressed CFRP reinforcement of this configuration was adopted similar to the corresponding ones in the experimental program ($\rho_{f(pre)} = 0.065\%$), and was also prestressed at 20% and 40% of its nominal tensile strength (Figure 4-19). The total length of the passive laminates was determined for fulfilling the development length adopted in the experimental tests (Figure 3-25).

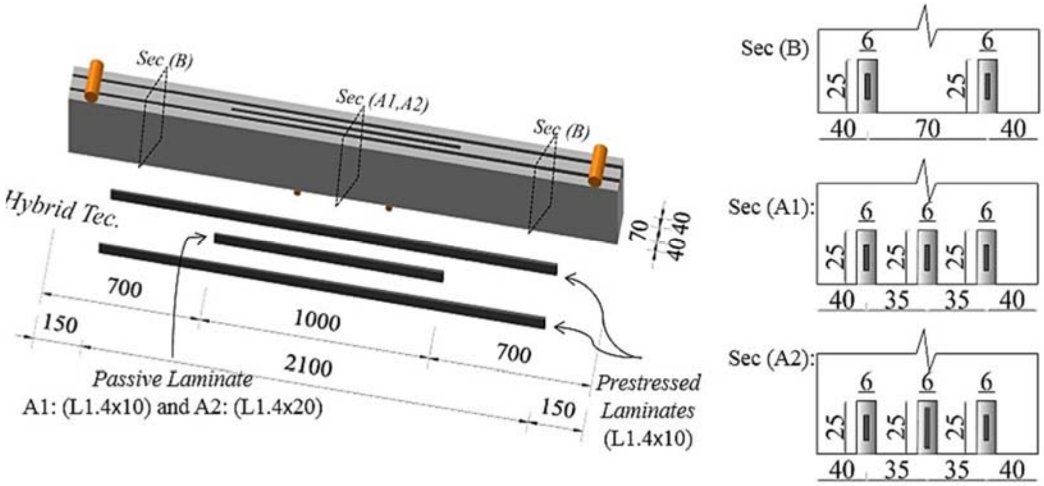

Figure 4-19: Characteristics of another configuration for the hybrid technique (dimensions in mm)

The RC beams strengthened with the proposed hybrid configuration (represented in Figure 4-19) were simulated using the described FE model, and the applied load versus mid-span deflection responses are represented in Figure 4-20a and Figure 4-20b for 20% and 40% prestress levels, respectively. This figure also numerically compares the flexural response of HPre-L10 and

HPre-L20 beams with the Pre and HPre beams adopted in the experimental tests (designated as Pre-FE and HPre-FE, respectively) with similar prestress level.

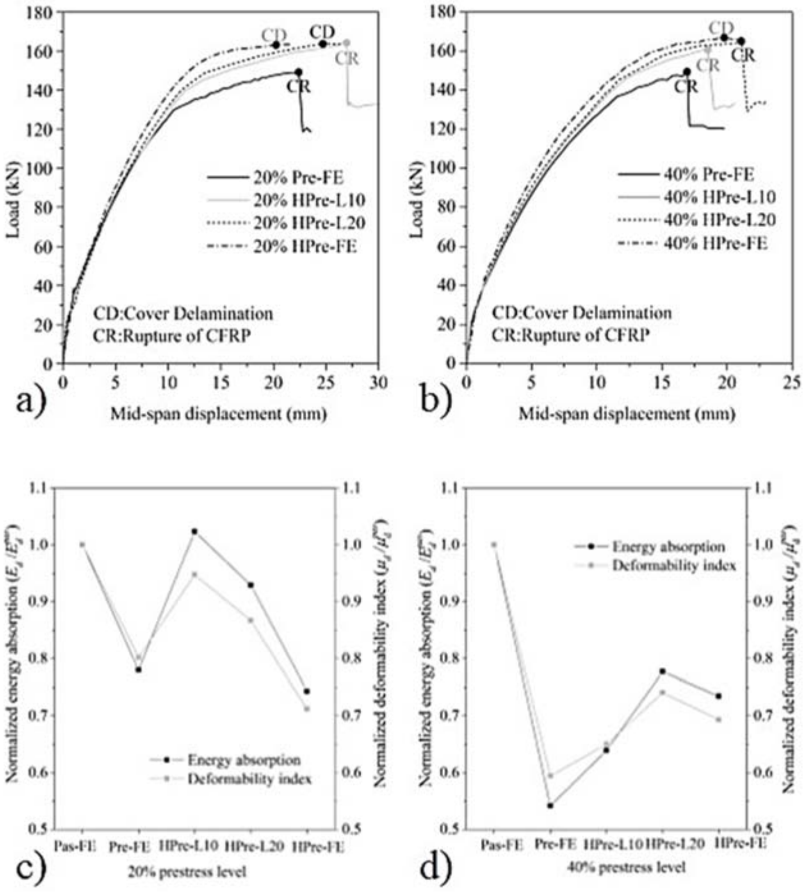

Figure 4-20: a) Load versus mid-span deflection of 20% hybrid beams, b) load versus mid-span deflection of 40% hybrid beams, c) normalized energy absorption and deformability indexes for 20% prestress level, d) normalized energy absorption and deformability indexes for 40% prestress level

Figure 4-20a and Figure 4-20b evidence that, regardless the prestress level, both HPre-L10 beams (prestressed at 20% and 40% level) failed by yielding of the tensile steel bars followed by the rupture of the prestressed CFRP laminates due to the attainment of its ultimate tensile strength at the end section of the passive laminate, while the HPre-L20 beams prestressed at 20% and 40% level experienced different failure modes after yielding of the tensile steel bars at the end section of the passive laminate. For 20% prestress level, the HPre-L20 beam failed by concrete cover delamination, while rupture of the prestressed laminates occurred in the 40% HPre-L20 beam. In fact, as previously mentioned (section 3.4), by increasing the prestress level, due to the higher compressive strain field in the concrete cover below the tensile steel bars, a higher resistance to the susceptibility of concrete cover delamination can be provided for the hybrid strengthened beams. This higher resistance when conjugated with the higher initial tensile strain introduced in the CFRP, can result to increase the possibility of occurrence of the rupture of the prestressed laminates before the concrete cover delamination.

Table 4-3 presents the most relevant results of the flexural response of the beams simulated in this section. It can be confirmed that, regardless the prestress level, by increasing the passive CFRP reinforcement ratio ($\rho_{f(pas)}$) of the hybrid beams, the load carrying capacity corresponding to the steel yield initiation stage has increased, as well as the corresponding deflection. On the other hand, increasing the passive CFRP reinforcement ratio has provided a higher ultimate deflection capacity (deflection corresponding to the ultimate strength (d_u)) and energy absorption index when the hybrid beams have failed by rupture of the prestressed laminates. In fact, the ultimate deflection capacity of the hybrid beams can significantly be affected by the prevailing failure mode at this stage.

Table 4-3: Relevant results obtained in the numerical investigation

Prestress level (%)	Specimens	$\rho_{f(pas)}$ $(\%)$	$\rho_{f(pre)}$ (%)	P_y (kN)	d_y (mm)	P_u (kN)	d_u (mm)	μ_d (δ_u/δ_{SLS})	E_d $(kN-mm)$
0%	Pas-FE	0.065	-	123.29	10.12	148.17	28.42	3.23	3306.22
20%	Pre-FE	-	0.065	129.64	10.84	149.12	22.82	2.59	2578.87
	HPre-L10	0.032	0.065	139.64	11.61	164.22	26.96	3.06	3383.21
	HPre-L20	0.065	0.065	144.23	12.26	163.75	24.71	2.80	3071.48
	HPre-FE	0.129	0.065	154.41	13.07	163.07	20.25	2.30	2456.89
40%	Pre-FE	-	0.065	136.70	11.57	149.30	16.95	1.92	1790.97
	HPre-L10	0.032	0.065	144.34	11.97	162.02	18.52	2.10	2113.53
	HPre-L20	0.065	0.065	146.99	12.21	165.02	21.10	2.393	2568.86
	HPre-FE	0.129	0.065	159.20	14.16	166.89	19.79	2.24	2428.90

- $\rho_{f(pas)}$ is the passive CFRP reinforcement ratio at mid-section of the beams;
- $\rho_{f(pre)}$ is the prestressed CFRP reinforcement ratio at mid-section of the beams.

Figure 4-20c and Figure 4-20d show the normalized indexes of energy absorption (E_d/E_d^{pas}) and deformability (μ_d/μ_d^{pas}) for the simulated beams prestressed at 20% and 40% level, respectively, where the (E_d^{pas}) and (μ_d^{pas}) are the energy absorption and deformability indexes of the numerical response of the passive strengthened beam. These figures show that, for 20% prestress level, the HPre-L10 beam (with $\rho_{f(pas)} = 0.032\%$) presented the highest energy absorption and deformability indexes amongst the beams strengthened according to the NSM hybrid technique, while for 40%

prestress level, the HPre-L20 beam (with $\rho_{f(pas)} = 0.065\%$) provided the highest values for these indexes. Hence, it can be concluded that, regardless the prestress level, the increase of the passive CFRP reinforcement ratio ($\rho_{f(pas)}$) of the hybrid strengthened beams provides a higher energy absorption and deformability indexes when the rupture of the prestressed laminates (located at the end section of the passive laminate) is observed at the maximum capacity as governing failure mode.

4.2 Conclusions

- A 3D nonlinear FE approach simulating both concrete-epoxy adhesive and laminate-epoxy adhesive interfaces, as well as, the relevant nonlinear behavior of the intervening materials, and the prestress process adopted in the test setup, was developed.
- The good predictive performance of this proposed numerical strategy was demonstrated by simulating the experimental tests of the beams strengthened with either NSM prestressing or NSM hybrid techniques. This modeling strategy can be used to design the type of structures investigated in the present work.
- The numerical parametric studies evidenced that by increasing the NSM CFRP development length in shear span of the strengthened beam, the possibility of occurrence of the concrete cover delamination (as a premature failure model before the rupture of the CFRP) decreases. Accordingly, in real applications, for design purpose of strengthening of RC beams using NSM CFRP reinforcement, the CFRP bonded length should be extended as much as possible close to the support to decrease the susceptibility to the concrete cover delamination failure.
- The efficiency of another configuration for the proposed NSM hybrid technique was numerically assessed for the flexural strengthening of RC beams. The results of this numerical analysis showed that, by increasing the passive CFRP reinforcement ratio in the hybrid system, a higher energy absorption and deformability indexes, when the rupture of the prestressed CFRPs occurs before the concrete cover delamination failure at the maximum capacity, can be achieved for the hybrid strengthened beams. The highest energy absorption and deformability indexes for the simulated hybrid beams were numerically obtained with an average increase of 21% and 37%, respectively, when the corresponding values of the prestressed NSM CFRP beam with similar prestress level are considered for comparison purpose.

Chapter 5: Analytical Approaches

The objective of this chapter is to propose a simplified analytical approach to predict the flexural behavior of simply supported RC beams flexurally strengthened with prestressed CFRP reinforcements using either EBR or NSM techniques. Besides the current failure modes that are considered for the evaluation of the ultimate flexural capacity of NSM CFRP strengthened beams, the proposed design methodology also accounts for the possibility of occurring concrete cover delamination, as a governing failure mode. The good predictive performance of the analytical model is appraised by simulating the force-deflection response registered in the experimental programs composed of RC beams strengthened with prestressed NSM CFRP reinforcements. Additionally, an upper limit for the prestress level is proposed in order to optimize the ductility performance of the NSM prestressing technique.

This chapter, moreover, aims to develop an analytical formulation, with a design framework, for the prediction of the distribution of CFRP tensile strain and bond shear stress and, additionally, the prestress transfer length. After demonstration the good predictive performance of the proposed analytical approach, parametric studies are carried out to analytically evaluate the influence of the main material properties, and CFRP and groove cross section on the distribution of the CFRP tensile strain and bond shear stress, and on the prestress transfer length. The proposed analytical approach can also predict the variation of the prestress transfer length during the curing time of the adhesive by considering the increase of its elasticity modulus during this period.

5.1 Flexural Analysis of RC Beams Strengthened with Prestressed CFRP

The current section intends to propose an analytical formulation, with a design framework, based on the strain compatibility and principles of static equilibrium to predict moment-curvature and force-deflection relationships of RC beams flexurally strengthened with prestressed CFRP reinforcement. The moment-curvature response of the prestressed section is simulated by the proposed simplified trilinear diagram (representing the precracking, postcracking, and postyielding stages) consisting on two stages up to concrete crack initiation (precracking stage) in order to simulate the effect of the prestressing. One of these stages refers to concrete decompression, and the other to steel decompression. In fact, according to this analytical approach, the influence of the prestress force on the trilinear moment-curvature response of the non-prestressed section can be considered by adding the strain profile of the cross section at the concrete and steel decompression points to the corresponding strain values in the non-prestressed section at the concrete cracking and steel yielding initiation points, respectively. Furthermore, the analytical equations are proposed to determine the neutral axis depth of the cracked non-prestressed and prestressed strengthened sections at the critical points in order to provide a simple hand calculation and eliminate the iterative numerical procedure. The developed design methodology also considers the possibility of occurring the concrete cover delamination failure mode, since this can limit the ultimate flexural load carrying capacity of RC beams strengthened with NSM CFRP reinforcement. This methodology is developed by considering the influence of the effective parameters on the occurrence of the concrete cover delamination failure mode.

The force versus mid-span deflection of the beam is analytically predicted using the curvature distribution along the beam length. The calculation complexities are simplified by assuming a linear curvature variation between the critical points that decompose the beam in the three regions corresponding to the trilinear flexural behavior.

The developed analytical formulation can be also applied on the design of RC slabs strengthened with FRP systems other than CFRP reinforcements. The predictive performance of the analytical model is assessed by simulating the tests of experimental studies, consisting of RC beams flexurally strengthened with prestressed or non-prestressed NSM CFRP reinforcements. Moreover, an upper limit for the prestress level is analytically proposed in order to optimize the ductility performance of the NSM prestressing technique for the flexural strengthening purpose.

5.1.1 Assumptions

The following assumptions were adopted in the proposed analytical model:

a) Strain in the longitudinal steel bars, CFRP reinforcement and concrete is directly proportional to their distance from the neutral axis of the cross section of the RC element;
b) There is no slip between steel and CFRP reinforcements and surrounding concrete when conventional flexural failure modes are considered as the prevailing ones;
c) The maximum compressive strain in concrete is 0.003.

5.1.2 Analytical Model Description

The moment-curvature ($M-\chi$) relationship of the cross section of a prestressed strengthened RC beam can be idealized by a trilinear diagram representing the precracking, postcracking, and postyielding phases, delimited by the following $M-\chi$ points (Figure 5-1): initial camber (point (ci)); concrete crack initiation (point (cr)); steel yield initiation (point (y)); and ultimate capacity (point (u)). The strain distribution on the beam cross section at each of these points is also schematically represented in Figure 5-1.

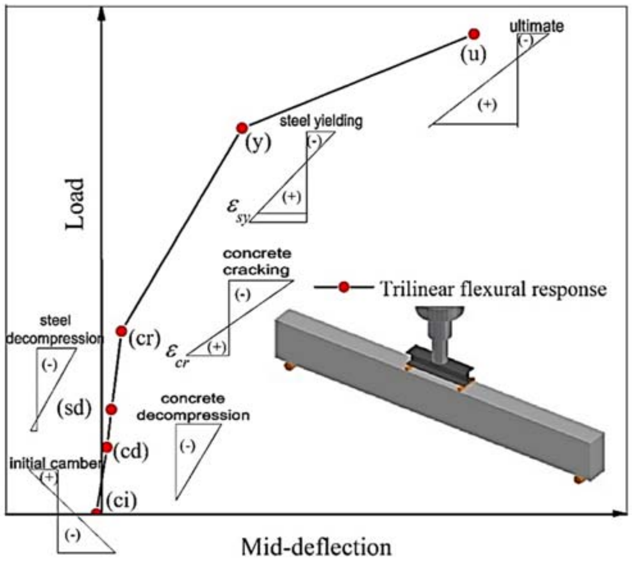

Figure 5-1: Critical points of the trilinear flexural response of the prestressed strengthened beams

When releasing the prestress force, an initial compression field in the longitudinal steel bars and surrounding concrete is introduced (Badawi and Soudki 2009). By applying an increasing external load, these compressive strains are converted in tensile strains. The transition from compressive to tensile strain (null strain) at the bottom fiber of concrete and at the longitudinal steel bars is defined as the concrete decompression point (point (cd) in Figure 5-1) and steel decompression point (point (sd) in Figure 5-1), respectively. As expected, the load carrying capacity corresponding to the concrete cracking and steel yielding initiation increase with the level of prestress due to this initial compressive strain profile. Hence, the strain profile of the cross section at the concrete decompression and steel decompression instants should be added to the corresponding strain values in the non-prestressed strengthened beam at the concrete cracking and steel yielding initiation points, respectively, as represented in Figure 5-2 (see section 5.1.4). It should be mentioned that both decompression points do not exist when non-prestressed FRP reinforcement is applied.

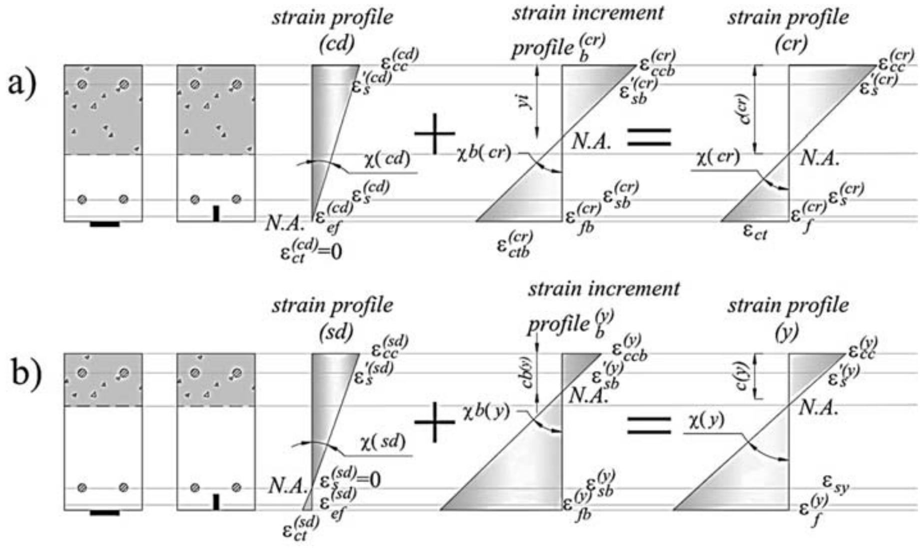

Figure 5-2: Strain profile of the cross section: a) at concrete crack initiation point (cr), b) at steel yield initiation point (y)

The analytical model detects the ultimate flexural capacity of the strengthened beams adopting three types of failure modes, namely: concrete crushing, tensile rupture of the CFRP, and concrete cover delamination. Firstly, the possibility of occurring either concrete crushing or tensile rupture of the CFRP (conventionally known as flexural failure modes) is evaluated by considering a critical percentage of CFRP reinforcement ($\rho_f^{(cri)}$) that assures the simultaneous occurrence of the aforementioned failures. A CFRP reinforcement ratio higher than this critical percentage causes a concrete crushing failure mode, otherwise the tensile rupture of the CFRP reinforcement is the dominant failure mode (see section 5.1.4.3). In the next stage, the ultimate flexural capacity of the strengthened beam when failing by concrete cover delamination is determined. Finally, the ultimate flexural capacity governed by conventional flexural failure modes is compared to the one conditioned by the concrete cover delamination, in order to determine the prevailing failure mode.

Figure 5-3 schematically represents the geometry and reinforcement details of the simply supported strengthened beam adopted for the analytical study. The beam is assumed to be subjected to a four-point loading configuration. The analytical approach can be also applied in case of monotonic three-point bending loading by considering a null loading span ($a_L = 0$).

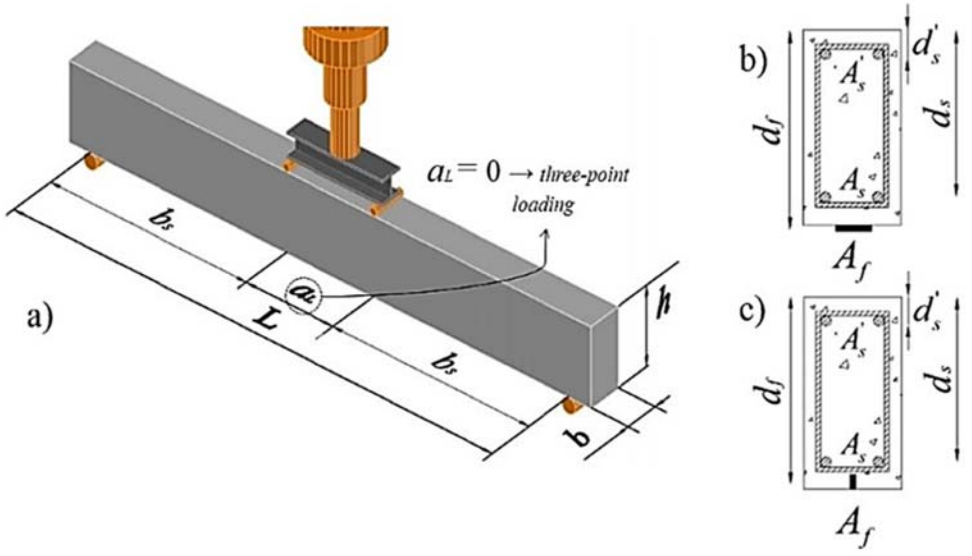

Figure 5-3: Definition of the geometry and reinforcement configuration for the analytical model: a) geometry of strengthened beam, b) reinforcement details in EBR technique, c) reinforcement details in NSM technique

5.1.3 Constitutive Law of the Materials

The compressive behavior of concrete is assumed linear up to the yielding of the longitudinal steel reinforcement in order to simplify the calculation procedure. After steel yielding, the contribution of concrete in compression is simulated by a rectangular compressive stress block, defined by the α_1 and β_1 parameters (Eq. (5.1)) schematically represented in Figure 5-4a (ACI-440.2R. 2008).

$$\beta_1 = \frac{4.\varepsilon_c' - \varepsilon_c}{6.\varepsilon_c' - 2.\varepsilon_c} \qquad \text{Equation Section (Next)} \quad (5.1)\text{-a}$$

$$\alpha_1 = \frac{3.\varepsilon_c'.\varepsilon_c - \varepsilon_c^{2}}{3.\beta_1.\varepsilon_c'^{2}} \qquad (5.1)\text{-b}$$

where ε_c' is the strain corresponding to the specified compressive strength of concrete f_c', which is calculated as:

$$\varepsilon_c' = \frac{1.7 f_c'}{E_c} \qquad (5.2)$$

The tensile behavior of concrete is assumed linear up to the strain at concrete crack initiation (ACI-318-08. 2008). An elasto-perfectly plastic model is used to simulate the behavior of the longitudinal steel bars, as represented in Figure 5-4b, while a linear behavior is adopted for the CFRP up to its ultimate tensile strength (Figure 5-4c).

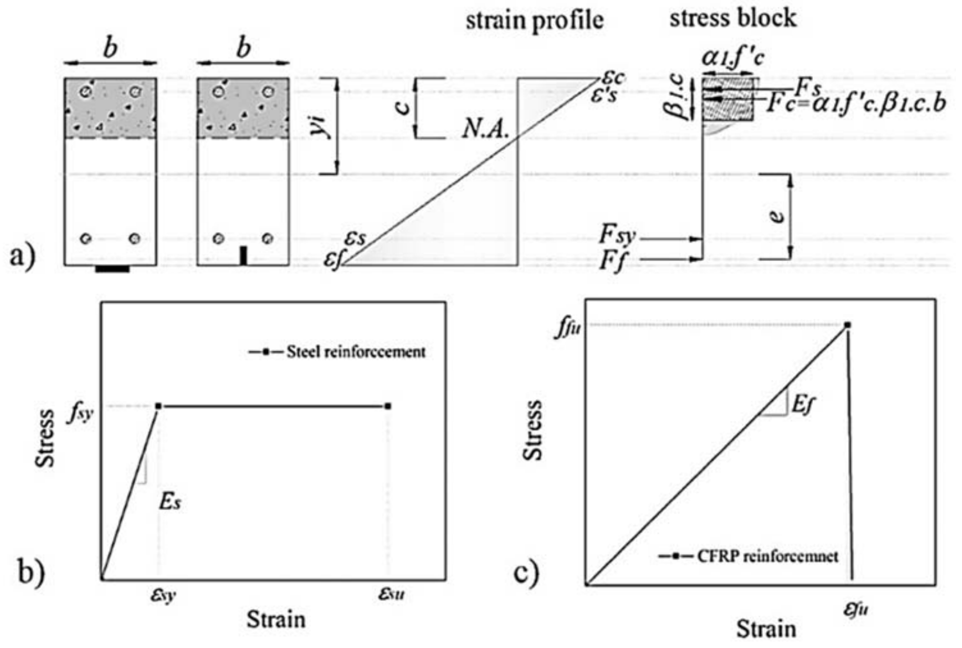

Figure 5-4: a) Compressive stress block for the concrete in compression, b) stress-strain relationship for the steel, c) stress-strain relationship for the CFRP

5.1.4 Moment-curvature Relationship

The analytical approach defines the moment-curvature response of the cross section of a RC element flexurally strengthened with CFRP reinforcements (failing in bending) using sectional analysis based on the strain compatibility and force equilibrium at the governing stages assumed representatives of the behavior of this type of elements.

5.1.4.1 Precracking Stage

When the CFRP reinforcement is applied with a certain prestress level, an initial negative camber (upward deflection) is obtained due to the eccentricity (e) of the prestress force (F_{pre}) in relation to the centroidal axis of the cross section (y_i, Figure 5-4a) at the precracking stage. This negative camber causes a tensile strain at the top fiber ($\varepsilon_{cc}^{(ci)}$) and a compressive strain at the bottom fiber ($\varepsilon_{ct}^{(ci)}$) of concrete, whose equations are provided in Appendix A.

The initial negative curvature of the prestressed strengthened beams ($\chi^{(ci)}$) can be determined by considering the neutral axis depth from the extreme top fiber of concrete ($c^{(ci)}$) as follows:

$$c^{(ci)} = \frac{\varepsilon_{cc}^{(ci)}.h}{\left(\varepsilon_{cc}^{(ci)} + \varepsilon_{ct}^{(ci)}\right)} \rightarrow \chi^{(ci)} = \frac{\varepsilon_{cc}^{(ci)}}{c^{(ci)}} \tag{5.3}$$

A loss of strain in the CFRP reinforcement occurs immediately after the total release of the prestress force due to the initial negative camber. This short-term prestrain loss ($\varepsilon_{lf}^{(ci)}$) and effective tensile strain ($\varepsilon_{ef}^{(ci)}$) in the CFRP reinforcement are determined from the following equations:

$$\varepsilon_{lf}^{(ci)} = \frac{\varepsilon_{cc}^{(ci)}.\left(d_f - c^{(ci)}\right)}{c^{(ci)}} \rightarrow \varepsilon_{ef}^{(ci)} = \varepsilon_{fp} - \varepsilon_{lf}^{(ci)} \tag{5.4}$$

where d_f is the internal arm of the CFRP (Figure 5-3b and Figure 5-3c) and ε_{fp} is the applied prestrain.

The concrete decompression point ((cd) in Figure 5-1) corresponds to the stage where the initial compressive strain in the bottom fiber of concrete ($\varepsilon_{ct}^{(ci)}$) becomes zero, resulting in a neutral axis depth equal to h, while the steel decompression point ((sd) in Figure 5-1) refers to the stage when the initial compressive strain in the bottom longitudinal steel bars ($\varepsilon_{s}^{(ci)}$), due to prestress application, becomes null, at which d_s is the neutral axis depth. The curvature at concrete decompression ($\chi^{(cd)}$) and steel decompression ($\chi^{(sd)}$) points can be assessed by adopting the ratio between the compressive strain installed on the concrete top fiber (ε_{cc}) at each point (Eq. (5.5)) and the corresponding neutral axis depth. Strains in the constituent materials along the depth of the cross section (longitudinal top ($\varepsilon_s^{'}$) and bottom (ε_s) steel bars, and in the CFRP reinforcement (ε_f)) are directly proportional to the distance from the neutral axis depth at each decompression point, while the concept of effective tensile strain should be adopted for the prestressed CFRP reinforcement (see Appendix B and Figure 5-2).

$$\varepsilon_{cc}^{(cd)} = \varepsilon_{cc}^{(ci)} - \frac{\left|\varepsilon_{ct}^{(ci)}\right|.y_i}{\left(h - y_i\right)} \tag{5.5-a}$$

$$\varepsilon_{cc}^{(sd)} = \varepsilon_{cc}^{(ci)} - \frac{\left|\varepsilon_{s}^{(ci)}\right|.y_i}{\left(d_s - y_i\right)} \tag{5.5-b}$$

The flexural bending moment at the concrete decompression ($M^{(cd)}$) and steel decompression ($M^{(sd)}$) points can be derived based on the sum of internal moments with respect to the corresponding neutral axis using the strain distribution of the section:

$$M^{(cd)} = \frac{1}{3}\varepsilon_{cc}^{(cd)}.b.E_c.h^2 + \varepsilon_s^{'(cd)}.E_s.A_s^{'}.\left(h-d_s^{'}\right) + \varepsilon_s^{(cd)}.E_s.A_s.\left(h-d_s\right) + \varepsilon_{ef}^{(cd)}.E_f.A_f.\left(d_f-h\right) \tag{5.6}$$

$$M^{(sd)} = \frac{1}{3}\varepsilon_{cc}^{(sd)}.b.E_c.d_s^2 + \varepsilon_s^{'(sd)}.E_s.A_s^{'}.\left(d_s-d_s^{'}\right) + \frac{1}{3}\varepsilon_{ct}^{(sd)}.b.E_c.\left(h-d_s\right)^2 + \varepsilon_{ef}^{(sd)}.E_f.A_f.\left(d_f-d_s\right) \tag{5.7}$$

The steel decompression point is followed by the concrete crack initiation, where the beam still exhibits linear elastic behavior, but the tensile strain at the extreme bottom fiber of concrete ($\varepsilon_{ctb}^{(cr)}$) reaches its flexural tensile strength ($\varepsilon_{ct} = f_r/E_c \rightarrow f_r = 0.62\sqrt{f_c^{'}}$ (ACI-318-08 2008)) (Figure 5-2a). The strains in the constituent materials along the cross section are proportional to the distance from the centroidal axis of the beam cross section (y_i) (Figure 5-2a). The increment of curvature and flexural capacity corresponding to the bending moment between the concrete decompression and crack initiation points can be obtained from Eqs. (5.8) and (5.9) in relation to the centroidal axis of the beam cross section (y_i).

$$\chi_b^{(cr)} = \frac{\varepsilon_{ccb}^{(cr)}}{y_i} \tag{5.8}$$

$$M_b^{(cr)} = \frac{1}{3}\varepsilon_{ccb}^{(cr)}.b.E_c.y_i^2 + \varepsilon_{sb}^{'(cr)}.E_s.A_s^{'}.\left(y_i-d_s^{'}\right) + \frac{1}{3}\varepsilon_{ctb}^{(cr)}.b.E_c.\left(h-y_i\right)^2 + \varepsilon_{sb}^{(cr)}.E_s.A_s.\left(d_s-y_i\right) + \varepsilon_{fb}^{(cr)}.E_f.A_f.\left(d_f-y_i\right) \tag{5.9}$$

where the equations for the determination of the strain components are provided in Appendix C. Finally, the curvature ($\chi^{(cr)}$) and flexural bending moment ($M^{(cr)}$) of the prestressed strengthened beams at the concrete crack initiation can be determined by using Eqs. (5.10) and (5.11), where the $\chi^{(cd)}$ and $M^{(cd)}$ are considered null for the non-prestressed beam (Figure 5-2a).

$$\chi^{(cr)} = \chi^{(cd)} + \chi_b^{(cr)} \tag{5.10}$$

$$M^{(cr)} = M^{(cd)} + M_b^{(cr)} \tag{5.11}$$

5.1.4.2 Postcracking Stage

The steel yield initiation point corresponds to the stage where the strain in the longitudinal tensile steel reinforcement ($\varepsilon_{sb}^{(y)}$) reaches its yield strength ($\varepsilon_{sy} = f_{sy}/E_s$). The steel decompression point should be introduced as an initial condition for the steel yield initiation instant. Accordingly, to determine the strain distribution of the cross section at the steel yield initiation point, the strain profile of the cross section at the steel decompression instant should be added to the corresponding strain values of the cross section due to the bending moment after this decompression point (Figure 5-2b).

The strain profile of the cross section due to the bending moment between the steel decompression and steel yield initiation points can be obtained adopting the proportional strain distribution to the distance from the neutral axis depth ($c_b^{(y)}$) by considering the strain value in the longitudinal tensile steel bars ($\varepsilon_{sb}^{(y)}$). According to the principles of static equilibrium, a quadratic equation is obtained to calculate the neutral axis depth ($c_b^{(y)}$) at the steel yield initiation stage due to the bending moment after the steel decompression point (Eq. (5.12)) (see Appendix D).

$$a.c_b^{(y)\,2} + b.c_b^{(y)} + c = 0 \tag{5.12)-a}$$

where

$$\begin{aligned} a &= E_c.b \\ b &= 2.\left(E_s.A_s^{'} + E_s.A_s + E_f.A_f\right) \\ c &= -2.\left(E_s.A_s^{'}.d_s^{'} + E_s.A_s.d_s + E_f.A_f.d_f\right) \end{aligned} \tag{5.12)-b}$$

The increment of curvature ($\chi_b^{(y)}$) and flexural capacity ($M_b^{(y)}$) corresponding to the bending moment between the steel decompression and yield initiation points can be determined by Eqs. (5.13) and (5.14), respectively, with regard to the neutral axis depth ($c_b^{(y)}$).

$$\chi_b^{(y)} = \frac{\varepsilon_{ccb}^{(y)}}{c_b^{(y)}} \tag{5.13}$$

$$M_b^{(y)} = \frac{1}{3}\varepsilon_{ccb}^{(y)}.E_c.b.c_b^{(y)\,2} + \varepsilon_{sb}^{'(y)}.E_s.A_s^{'}.\left(c_b^{(y)} - d_s^{'}\right) + \varepsilon_{sb}^{(y)}.E_s.A_s.\left(d_s - c_b^{(y)}\right) + \varepsilon_{fb}^{(y)}.E_f.A_f.\left(d_f - c_b^{(y)}\right) \tag{5.14}$$

Finally, the curvature ($\chi^{(y)}$) and flexural bending moment ($M^{(y)}$) of the prestressed strengthened beams at the steel yield initiation point are determined using Eqs. (5.15) and (5.16), where the $\chi^{(sd)}$ and $M^{(sd)}$ are considered null for the non-prestressed strengthened beam (Figure 5-2b).

$$\chi^{(y)} = \chi^{(sd)} + \chi_b^{(y)} \tag{5.15}$$

$$M^{(y)} = M^{(sd)} + M_b^{(y)} \tag{5.16}$$

5.1.4.3 Postyielding Stage

The ultimate flexural capacity of the strengthened beams is controlled by adopting three types of failure modes, namely, yielding of the steel bars in tension followed by either concrete crushing or rupture of the CFRP reinforcement (known as conventional flexural failure modes), and delamination of the concrete cover.

5.1.4.3.1 Conventional flexural failure modes

The concrete crushing is assumed to occur when the compressive strain on the concrete top fiber of the cross section reaches its maximum usable strain ($\varepsilon_{cu} = 0.003$ according to the ACI-440.2R), while the strengthened beams are assumed to experience the rupture of the CFRP reinforcement when the ultimate tensile strain in the CFRP is achieved (ε_{fu}).

To assess the prevailing failure mode in the strengthened beams at the ultimate stage, a critical percentage of CFRP reinforcement ($\rho_f^{(cri)}$) can be determined assuming simultaneous tension and compression failures to detect the appropriate failure mode (Appendix E). If the CFRP ratio exceeds the critical value, failure will be due to the concrete crushing, otherwise failure will be caused by rupture of the CFRP reinforcement. The critical area ($A_f^{(cri)}$) and the corresponding percentage ($\rho_f^{(cri)}$) for the CFRP reinforcement can be determined from:

$$A_f^{(cri)} = \frac{\alpha_1 . f_c^{'} . \beta_1 . c^{(cri)} . b + A_s^{'} . \varepsilon_s^{'(cri)} . E_s - A_s . f_{sy}}{\varepsilon_{fu} . E_f} \rightarrow \rho_f^{(cri)} = \frac{A_f^{(cri)}}{b . d_f} \tag{5.17}$$

<u>*Concrete Crushing*</u>

Concrete crushing will prevail at ultimate stage when the CFRP ratio exceeds the critical percentage. From the equilibrium of the internal forces results a quadratic equation that determines the neutral axis depth ($c_{cc}^{(u)}$) at failure (Appendix E):

$$a . c_{cc}^{(u)\,2} + b . c_{cc}^{(u)} + c = 0 \tag{5.18-a}$$

where

$$\begin{aligned} a &= f_c^{'} . b . \left(3 . \varepsilon_c^{'} . \varepsilon_{cu} - \varepsilon_{cu}^2\right) \\ b &= 3 . \varepsilon_c^{'2} . \left(\varepsilon_{cu} . \left(E_s . A_s^{'} + E_f . A_f\right) - A_s . f_{sy} - E_f . A_f . \varepsilon_{fp}\right) \\ c &= -3 . \varepsilon_c^{'2} . \varepsilon_{cu} . \left(E_s . A_s^{'} . d_s^{'} + E_f . A_f . d_f\right) \end{aligned} \tag{5.18-b}$$

The curvature ($\chi_{cc}^{(u)}$) and ultimate flexural capacity ($M_{cc}^{(u)}$) are obtained from the following equations (Appendix E):

$$\chi_{cc}^{(u)} = \frac{\varepsilon_{cu}}{c_{\mathrm{cc}}^{(u)}} \tag{5.19}$$

$$M_{cc}^{(u)} = \alpha_1.f_c^{'}.\beta_1.c_{cc}^{(u)\,2}.b.\left(1-\frac{\beta_1}{2}\right)+\varepsilon_{s,cc}^{'(u)}.E_s.A_s^{'}.\left(c_{cc}^{(u)}-d_s^{'}\right)+f_{sy}.A_s.\left(d_s-c_{cc}^{(u)}\right)+E_f.\varepsilon_{f,cc}^{(u)}\,.A_f.\left(d_f-c_{cc}^{(u)}\right) \tag{5.20}$$

Rupture of CFRP Reinforcement

The equilibrium of the internal forces at the cross section, when the rupture of the CFRP reinforcement occurs, can be derived adopting strain compatibility, resulting in a cubic equation, whose solution leads the depth of the neutral axis at ultimate stage ($c_{rc}^{(u)}$) (Appendix E):

$$a.c_{rc}^{(u)\,3}+b.c_{rc}^{(u)\,2}+c.c_{rc}^{(u)}+d=0 \tag{5.21-a}$$

where

$$\begin{aligned}
a &= \varepsilon_{fb,rc}^{(u)}.f_c^{'}.b.\left(3.\varepsilon_c^{'}+\varepsilon_{fb,rc}^{(u)}\right)\\
b &= 3.\varepsilon_c^{'}.\left(\varepsilon_{fb,rc}^{(u)}.(\varepsilon_c^{'}.E_s.A_s^{'}-f_c^{'}.b.d_f)+\varepsilon_c^{'}.\left(A_f.f_{fu}+A_s.f_{sy}\right)\right)\\
c &= -3.\varepsilon_c^{'2}.\left(\varepsilon_{fb,rc}^{(u)}.E_s.A_s^{'}.\left(d_f+d_s^{'}\right)+2.d_f.\left(A_f.f_{fu}+A_s.f_{sy}\right)\right)\\
d &= 3.\varepsilon_c^{'2}.d_f.\left(\varepsilon_{fb,rc}^{(u)}.E_s.A_s^{'}.d_s^{'}+d_f.\left(A_f.f_{fu}+A_s.f_{sy}\right)\right)
\end{aligned} \tag{5.21-b}$$

Accordingly, the curvature ($\chi_{rc}^{(u)}$) and ultimate flexural capacity ($M_{rc}^{(u)}$) regarding the neutral axis depth level ($c_{rc}^{(u)}$) at CFRP failure are determined as follows (Appendix E):

$$\chi_{rc}^{(u)} = \frac{\varepsilon_{cc,rc}^{(u)}}{c_{rc}^{(u)}} \tag{5.22}$$

$$M_{rc}^{(u)} = \alpha_1.f_c^{'}.\beta_1.c_{rc}^{(u)\,2}.b.\left(1-\frac{\beta_1}{2}\right)+\varepsilon_{s,rc}^{'(u)}.E_s.A_s^{'}.\left(c_{rc}^{(u)}-d_s^{'}\right)+f_{sy}.A_s.\left(d_s-c_{rc}^{(u)}\right)+f_{fu}.A_f.\left(d_f-c_{rc}^{(u)}\right) \tag{5.23}$$

5.1.4.3.2 Concrete cover delamination

Concrete cover delamination, also designated by rip-off, is initiated by forming an in-plane shear crack at the extremities of the CFRP reinforcement due to high strain gradient caused by the abrupt termination of the CFRP. This crack is propagated along the depth of the concrete cover of the beam up to attain the tensile steel reinforcement level, and then progresses horizontally along this level due to the resistance offered by this reinforcement to the propagation of the crack through it. The presence of higher percentage of voids just below this reinforcement also helps for the localization of the crack in this plane (Gao et al. 2004). Subsequently, separation of the concrete cover along the longitudinal tensile steel bars occurs in the shear span of the beam, which can compromise the flexural strengthening effectiveness of this technique if it occurs prematurely. Furthermore, the susceptibility to the concrete cover delamination in the NSM CFRP strengthened beams is influenced by some variables, such as the concrete strength class, reinforcement ratio of existing longitudinal steel bars, number and diameter of the bars composing this reinforcement, the relative position between the longitudinal steel and CFRP reinforcements, number of CFRP reinforcements, and distance between the consecutive CFRPs (Barros and Kotynia 2008).

The present section aims to propose a new methodology to predict the ultimate flexural capacity of a RC beam strengthened with NSM CFRP laminates failing by concrete cover delamination. For this purpose, the concrete cover delamination is assumed to occur when the principal tensile stress transferred to the surrounding concrete at the extremity of the longitudinal CFRP laminate attains the concrete tensile strength ($f_{ct} = 0.56\sqrt{f_c^{'}}$ (ACI-318-08 2008)). The present approach, for the tensile fracture surface of this surrounding concrete, was inspired on the work of Bianco et al. (2014) that proposed a semi-pyramidal shape for modeling the concrete resisting contribution during the pullout process of NSM FRP reinforcement bridging a shear failure crack in the context of the use of these composite materials and technique for the shear strengthening of RC beams. Hence, in the current analytical model, the semi-pyramidal configuration was adopted for the concrete tensile fracture surface at the extremities of each CFRP laminate applied for flexural strengthening, as represented in Figure 5-5a.

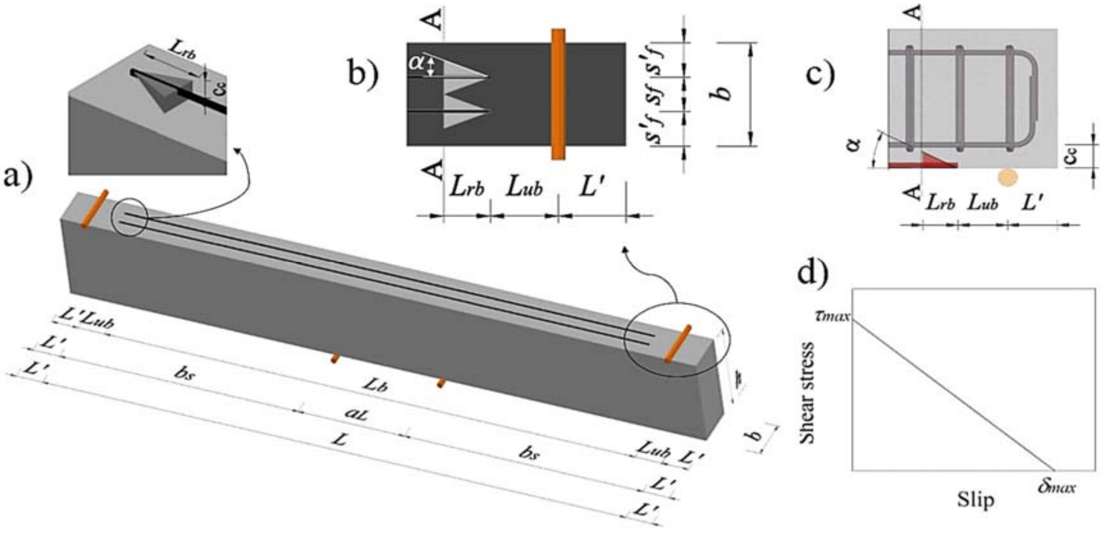

Figure 5-5: a) Characteristics of the bonded CFRP reinforcement, b) position of the CFRP laminates on the beam's tensile surface, c) concrete cover for the beam bottom face and resisting bond length, d) shear stress-slip relationship of local bond

The dimensions of this tensile fracture surface of the surrounding concrete (assumed by simplification as having a semi-pyramid format) are supposed to be limited by some restrictions to consider the influence of the aforementioned variables on the susceptibility of concrete cover delamination, and also simplify the model. These restrictions of the semi-pyramid on the beam's tensile surface aim to avoid interaction between the concrete fracture surfaces of consecutive CFRP laminates. On the other hand, due to the possibility of occurring a weak plan just beneath the tensile steel bars, the thickness of the semi-pyramid is limited to the concrete cover thickness (c_c) (Figure 5-5c).

Accordingly, the semi-pyramidal concrete fracture surface is assumed to be extended until the base area of the semi-pyramid (rectangular shape) reaches a boundary limit. This boundary limit is defined when the short side of the rectangular base achieves the length of c_c (Figure 5-5c), while the long side of this rectangle should be limited to the $\min(s_f\ ; 2s'_f)$ for the CFRP laminates near the beam edge (side-laminates) and s_f for the mid-laminates (Figure 5-5b). However, considering that s_f is in general higher than 40 mm (Barros and Kotynia 2008) and the angle α formed by the principal generatrices of the semi-pyramid with the CFRP longitudinal axis (Figure 5-5b and Figure 5-5c) is presumed to be in the interval of 10 to 35 degrees (Bianco et al. 2014), the above boundary limit on the beam's tensile surface seems to be experimentally supported.

According to the base area and α of the semi-pyramid of the concrete fracture surface (Figure 5-5a and Figure 5-5c), the height of the semi-pyramid can be defined as the resisting bond length (L_{rb}), where the slip between the CFRP laminate and surrounding concrete is neglected along this length to calculate the resistance of the concrete fracture surface. The resistance of the concrete fracture surface for each CFRP laminate (F_{cf}) can be determined by considering the concrete tensile strength (f_{ct}). Accordingly, the ultimate flexural capacity of a strengthened beam developing a concrete cover delamination failure mode ($M_{ccd}^{(u)}$) can be determined using the maximum applicable force to all the CFRP laminates at the end section of L_{rb} (section A-A in Figure 5-5b and Figure 5-5c).

The implementation of the proposed methodology to predict the concrete cover delamination as prevailing failure mode comprises the following steps (Figure 5-6): 1) providing the input parameters; 2) determination of the resisting bond length (L_{rb}); 3) evaluation of the tensile strength of CFRP (F_{fu}), maximum value of the force transferable through the resisting bond length (F_{rb}), and concrete tensile fracture capacity (F_{cf}) for each CFRP laminate; 4) assessment the possibility of the concrete tensile fracture at the end of the CFRP laminate considering the characteristics of bond conditions and the CFRP tensile strength; 5) determination of ultimate flexural capacity of the strengthened beam adopting concrete cover delamination failure; and 6) evaluation the possibility of occurrence of the concrete cover delamination in comparison to the conventional prevailing failure modes including concrete crushing and rupture of the CFRP far from its extremities.

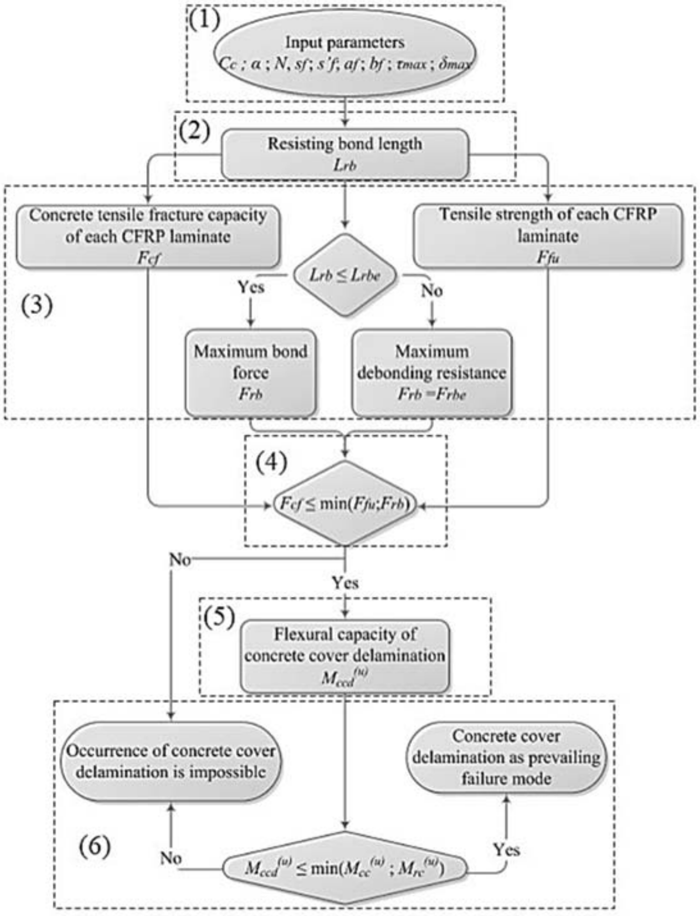

Figure 5-6: Calculation procedure for concrete cover delamination failure mode

1) Input parameter

The input parameters include: concrete cover thickness c_c, angle α between principal generatrices of the semi-pyramidal fracture surface and the CFRP longitudinal axis, number of the longitudinal CFRP laminates N, distance between two adjacent CFRP laminates s_f, distance between the beam edge and the nearest CFRP laminate $s_f^{'}$, thickness a_f and width b_f of laminate’s cross section, and values of local bond stress-slip relationship: maximum shear stress $\tau_{\max}$ and maximum slip $\delta_{\max}$ (Figure 5-5).

2) Resisting bond length L_{rb}

The resisting bond length (L_{rb}) at each extremity of the CFRP laminate can be calculated as follows:

$$L_{rb} = \frac{c_c}{\tan\alpha} \tag{5.24}$$

3) Tensile strength of CFRP F_{fu}, concrete tensile fracture capacity F_{cf}, and resisting bond force F_{rb}

Tensile strength of the CFRP laminate can be determined by Eq. (5.25). It should be noted that in the case of a round CFRP bar, its cross section is converted to an equivalent square cross sectional area.

$$F_{fu} = a_f . b_f . f_{fu} \tag{5.25}$$

The concrete tensile fracture capacity (F_{cf}) of each CFRP laminate, adopting a semi-pyramidal fracture surface, can be determined considering the tensile resistance of concrete on the slant area of the semi-pyramid. It was evidenced that the concrete tensile resistance of the slant area is equivalent to simply multiplying the base area of semi-pyramid times the concrete tensile strength (Bianco 2008). Hence, for the current study, Eq. (5.26) is proposed to determine the concrete tensile fracture capacity (F_{cf}) corresponding to each CFRP laminate.

$$F_{cf} = \min\left(2.L_{rb}.\tan\alpha \; ; \; 2.s'_f \; ; \; s_f\right).c_c.f_{ct} \tag{5.26}$$

The maximum value of the force (F_{rb}) that can be transferable through the resisting bond length (L_{rb}) by the CFRP laminate can be obtained by Eq. (5.27) adopting an idealized local bond-slip relationship with a single softening branch as shown in Figure 5-5d (Bianco et al. 2014).

$$F_{rb}(L_{rb}) = L_p.\frac{1}{J_1}.\lambda.\left\{C_1.\left[\cos\left(\lambda.L_{rb}\right)-1\right] - C_2.\sin\left(\lambda.L_{rb}\right)\right\} \tag{5.27-a}$$

where

$$\begin{gathered} L_p = 2.b_f + a_f \; ; \; J_1 = \frac{L_p}{\left(a_f.b_f\right)}.\left(\frac{1}{E_f} + \frac{\left(a_f.b_f\right)}{\left(A_c.E_c\right)}\right) \\ \frac{1}{\lambda^2} = \frac{\delta_{\max}}{\left(\tau_{\max}.J_1\right)} \; ; \; C_1 = \delta_{\max} - \frac{\left(\tau_{\max}.J_1\right)}{\lambda^2} \; ; \; C_2 = -\frac{\left(\tau_{\max}.J_1\right)}{\lambda^2} \end{gathered} \tag{5.27-b}$$

and A_c is the cross sectional area of the surrounding concrete that provides confinement to each CFRP laminate, and for side-laminates and mid-laminates can be obtained by Eqs. ((5.27)-c) and ((5.27)-d), respectively.

$$A_c = \min\left(2.s_f^{'};s_f\right).c_c \tag{5.27-c}$$

$$A_c = s_f.c_c \tag{5.27-d}$$

The maximum bond force (F_{rb}) for the resisting bond length (L_{rb}) should be limited to the maximum debonding resistance (F_{rbe}) and its corresponding effective resisting bond length (L_{rbe}) given in Eq. (5.28) (Bianco et al. 2014).

$$L_{rbe} = \frac{\pi}{(2.\lambda)}\ ;\ F_{rbe} = \frac{\left(L_p.\lambda.\delta_{\max}\right)}{J_1} \tag{5.28}$$

4) Assessment the possibility of concrete tensile fracture

This step of the algorithm aims to check which of the three types of failure modes occurs, namely, rupture of the CFRP, interfacial debonding failure, or concrete tensile fracture when the tensile force is applied to the CFRP laminate at the end section of resisting bond length (section A-A in Figure 5-5). In fact, the concrete tensile fracture can occur when the concrete tensile fracture capacity (F_{cf}) corresponding to the CFRP laminate is a lower than the minimum of the tensile strength of the CFRP (F_{fu}) and the resisting bond force (F_{rb}). Otherwise, by increasing the applied force to the CFRP laminate at the section A-A represented in Figure 5-5, either the rupture of the CFRP or interfacial debonding failure would occur before the concrete tensile fracture (Figure 5-6).

5) Ultimate flexural capacity of the strengthened beam failed by concrete cover delamination

The effective concrete tensile fracture capacity (F_{cfe}) of the CFRP laminates can be determined by summing the concrete tensile fracture capacity (F_{cf}) of all the CFRP laminates flexurally applied on the tensile face of the beam (Eq. (5.29)).

$$F_{cfe} = \sum_{i=1}^{N} F_{cfi} \tag{5.29}$$

The flexural capacity ($M_{ccd}^{(Lrb)}$) of the strengthened beam at the end section of resisting bond length (section A-A in Figure 5-5) can be obtained by Eq. (5.30) using the effective concrete tensile fracture capacity (F_{cfe}) of the CFRP laminates, where the beam's cross section is supposed to be located between the concrete cracking and steel yield initiation phases (postcracking stage). Otherwise, for the section located in the postyielding stage, the contribution of concrete in compression should be simulated by a rectangular compressive stress block (Eq. (5.1)), and the compressive and tensile strains in the longitudinal top and bottom steel bars, respectively, should be limited by its yield strength ($\varepsilon_{sy} = f_{sy} / E_s$).

$$M_{ccd}^{(Lrb)} = \frac{1}{3} \varepsilon_{cc,ccd} . E_c . b . c_{ccd}^2 + \varepsilon'_{s,ccd} . E_s . A'_s . \left(c_{(ccd)} - d'_s \right) + \varepsilon_{s,ccd} . E_s . A_s . \left(d_s - c_{ccd} \right) + F_{cfe} . \left(d_f - c_{ccd} \right) \qquad (5.30)$$

where the strains of the components along the cross section can be determined adopting the proportional strain distribution to the distance from the neutral axis depth (c_{ccd}) by considering the average tensile strain in the CFRP laminates ($\varepsilon_{f,ccd} = F_{cfe} / (N.a_f.b_f.E_f)$).

According to the principles of static equilibrium and proportionality of the strain distribution along the cross section, the neutral axis depth (c_{ccd}) can be obtained using a quadratic equation represented in Eq. (5.31).

$$a.{c_{ccd}}^2 + b.c_{ccd} + c = 0 \qquad (5.31)\text{-a}$$

where

$$\begin{aligned} a &= E_c . b \\ b &= 2.\left(E_s . A'_s + E_s . A_s + E_f . N . a_f . b_f \right) \\ c &= -2.\left(E_s . A'_s . d'_s + E_s . A_s . d_s + E_f . N . a_f . b_f . d_f \right) \end{aligned} \qquad (5.31)\text{-b}$$

As a final point, the ultimate flexural capacity ($M_{ccd}^{(u)}$) of the NSM CFRP strengthened beam adopting the concrete cover delamination as prevailing failure mode is determined by Eq. (5.32) according to the bending moment distribution along the beam length (Figure 5-5a).

$$M_{ccd}^{(u)} = \frac{b_s . M_{ccd}^{(Lrb)}}{(L_{rb} + L_{ub})} \qquad (5.32)$$

where b_s is the distance between the support and the point load (shear span) and L_{ub} is the unbonded length of the CFRP at each extremity of the laminate (shown in Figure 5-5).

6) Prevailing failure mode of the NSM CFRP strengthened beam

Occurrence of the concrete cover delamination of the strengthened beam can be expected when the corresponding ultimate flexural capacity ($M_{ccd}^{(u)}$) is lower than the ultimate flexural capacity of the prevailing conventional flexural failure mode obtained from section 5.1.4.3.1 ($M_{ccd}^{(u)} \leq \min(M_{cc}^{(u)};M_{rc}^{(u)})$) (Figure 5-6). On the other hand, the concrete cover delamination failure can occur after yielding of the longitudinal tensile steel bars when $M_{ccd}^{(u)}$ is higher than the flexural capacity of the beam at the steel yield initiation point ($M^{(y)}$, Eq. (5.16)), otherwise, the strengthened beam experiences the concrete cover delamination before the tensile steel yielding.

5.1.5 Force-deflection Relationship

The force-deflection relationship of the beams is predicted by using the moment-curvature response at the governing stages derived from the proposed analytical model. For this purpose, it is assumed a linear curvature variation between the beam's sections corresponding to the governing stages. Accordingly, a simply supported beam is divided in distinct regions along the length corresponding to these governing stages, namely, precracking, postcracking and postyielding regions, as shown in Figure 5-7. The mid-span deflection of the beam is estimated by summing the deflection of each region (δ_i) in one half of the beam length ($L/2$) (Figure 5-8). The deflection of the each region can be determined by integrating the function, $\chi(x)$, that defines the curvature along the length of this region:

$$\delta_{i(L_i-L_{i+1})} = \int_{Li}^{Li+1} \chi_i(x).x.d(x) \tag{5.33}$$

where x is a variable along this region, and L_i and L_{i+1} are the distances of the section boundaries of this region to the support.

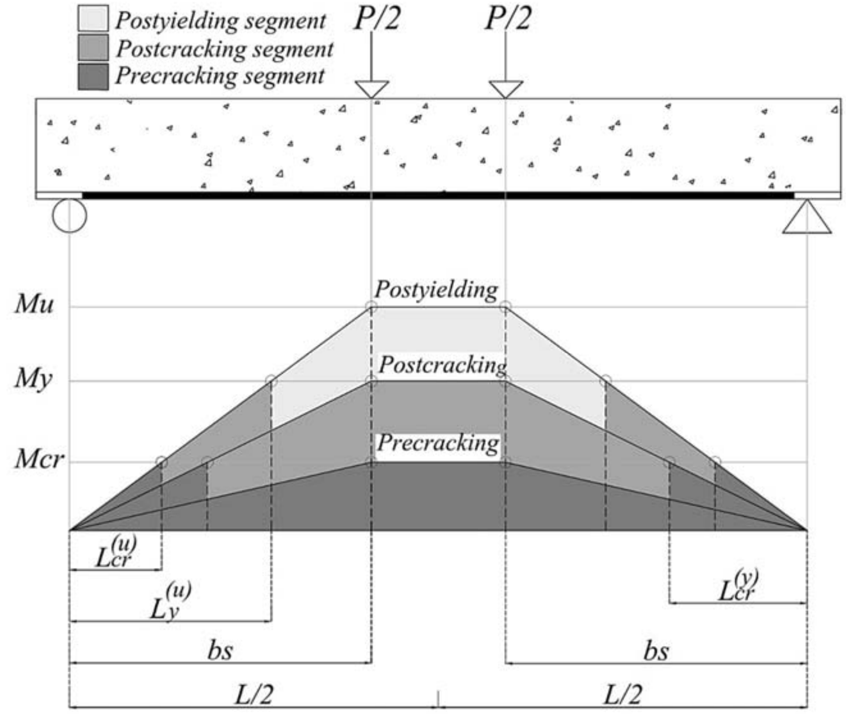

Figure 5-7: Distinct regions of the beam

The negative camber (upward deflection) ($d^{(ci)}$) of the prestressed strengthened beam can be obtained by considering the constant curvature variation due to the effective negative bending moment ($M_{epre} = \varepsilon_{ef}^{(ci)}.E_f.A_f.e$) at both extremities of the bonded length of CFRP reinforcement (L_b), as shown in Figure 5-8a:

$$d^{(ci)} = \int_{L_{ub}}^{L/2} \chi_e^{(ci)}.x.dx = \frac{M_{epre}.L_b(2.L - L_b)}{8.E_c.I_{ucr}} \tag{5.34}$$

where $\chi_e^{(ci)}$ is the effective initial negative curvature by considering the effective negative bending moment, and I_{ucr} is the moment of inertia of the uncracked section (Appendix A).

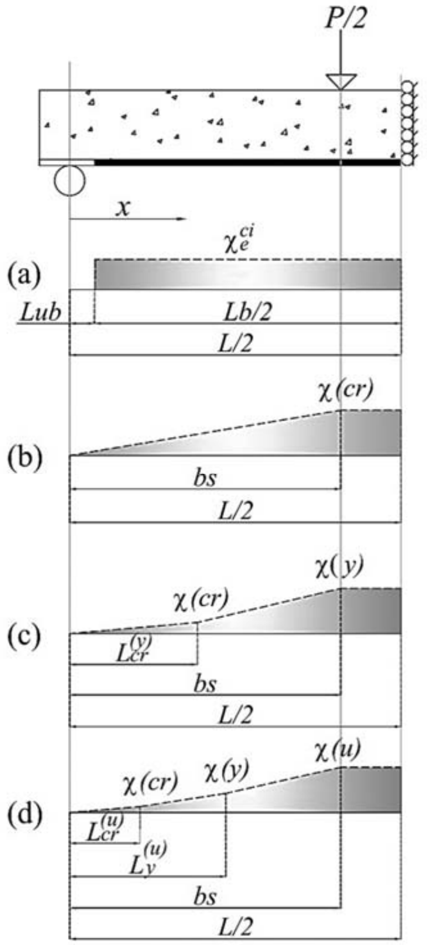

Figure 5-8: Curvature distribution along the beam length at the stages: a) initial camber, b) precracking, c) postcracking, d) postyielding

The mid-span deflection of the beam at the concrete crack initiation is calculated adopting the curvature variation along the length of the beam (see Figure 5-8b) by using Eq. (5.35). The mid-span deflection corresponding to the concrete and steel decompression points can also be obtained by substituting $\chi^{(cd)}$ and $\chi^{(sd)}$ into Eq. (5.35) instead of $\chi^{(cr)}$, respectively.

$$d^{(cr)} = \int_{0}^{b_s} (\frac{\chi^{(cr)}}{b_s}).x^2.dx + \int_{b_s}^{L/2} \chi^{(cr)}.x.dx = \delta^{(cr)}_{(0-b_s)} + \delta^{(cr)}_{(b_s-L/2)} \qquad (5.35)$$

To predict the mid-span deflection at the steel yield initiation stage, the beam length should be divided into the precracking and postcracking regions (Figure 5-7). In the precracking region, the bending moment is less than the crack initiation moment ($M^{(cr)}$), while the bending moment within the postcracking region is limited to the steel yield initiation moment ($M^{(y)}$). The mid-span deflection of the beam can be determined by Eq. (5.36) assuming a linear variation of the curvature between the governing sections, as represented in Figure 5-8c.

$$\begin{aligned} d^{(y)} &= \int_{0}^{L_{cr}^{(y)}} \left(\frac{\chi^{(cr)}}{L_{cr}^{(y)}}\right).x^{2}.dx + \int_{L_{cr}^{(y)}}^{b_s} \left(\left(\frac{\chi^{(y)}-\chi^{(cr)}}{b_s - L_{cr}^{(y)}}\right).(x - L_{cr}^{(y)}) + \chi^{(cr)}\right).x.dx + \int_{b_s}^{L/2} \chi^{(y)}.x.dx \\ &= \delta^{(y)}_{(0-L_{cr}^{(y)})} + \delta^{(y)}_{(L_{cr}^{(y)}-b_s)} + \delta^{(y)}_{(b_s-L/2)} \end{aligned} \tag{5.36}$$

where $L_{cr}^{(y)}$ is the length of the precracking region at the steel yield initiation stage (Figure 5-7 and Figure 5-8c).

The mid-span deflection of the beam at the ultimate stage can be determined by dividing the beam length in three regions (precracking, postcracking, and postyielding), by considering the trilinear moment-curvature relationship represented in Figure 5-7. The maximum bending moment within the precracking and postcracking regions are limited by the crack initiation ($M^{(cr)}$) and steel yield initiation ($M^{(y)}$) bending moments, while the ultimate flexural moment of the beam limits the bending moment in the postyielding region. According to the linear variation of the curvature in the three regions of the governing stages, as shown in Figure 5-8d, Eq. (5.37) can be considered to calculate the mid-span deflection of the beam corresponding to its flexural capacity.

$$\begin{aligned} d^{(u)} &= \int_{0}^{L_{cr}^{(u)}} \left(\frac{\chi^{(cr)}}{L_{cr}^{(u)}}\right).x^{2}.dx + \int_{L_{cr}^{(u)}}^{L_y^{(u)}} \left(\left(\frac{\chi^{(y)}-\chi^{(cr)}}{L_y^{(u)} - L_{cr}^{(u)}}\right).(x - L_{cr}^{(u)}) + \chi^{(cr)}\right).x.dx + \int_{L_y^{(u)}}^{b_s} \left(\left(\frac{\chi^{(u)}-\chi^{(y)}}{b_s - L_y^{(u)}}\right).(x - L_y^{(u)}) + \chi^{(y)}\right).x.dx \\ &\quad + \int_{b_s}^{L/2} \chi^{(u)}.x.dx = \delta^{(u)}_{(0-L_{cr}^{(u)})} + \delta^{(u)}_{(L_{cr}^{(u)}-L_y^{(u)})} + \delta^{(u)}_{(L_y^{(u)}-b_s)} + \delta^{(u)}_{(b_s-L/2)} \end{aligned} \tag{5.37}$$

where $L_{cr}^{(u)}$ is the length of the precracking region, and $L_y^{(u)}$ is the distance of $\chi^{(y)}$ from the support along the beam length at ultimate stage.

It is worth to note that the load (P) corresponding to the flexural bending moment at the governing stages for the simply supported beams under four-point loading configuration can be computed by using Eq. (5.38).

$$P_{(i)} = \frac{4.M_{(i)}}{\left(L - a_L\right)} \tag{5.38}$$

where a_L is the loading span represented in Figure 5-3.

5.1.6 Assessment of Predictive Performance of the Analytical Approaches

5.1.6.1 Conventional Flexural Failure Modes

To assess the predictive performance of the proposed analytical model, it is applied on the prediction of the force-deflection relationship of the beams forming three experimental programs (represented in section 3.3 and conducted by Badawi and Soudki (2009), and El-Hacha and Gaafar (2011)). These experimental programs are composed of RC beams strengthened with prestressed NSM CFRP reinforcement failed by conventional flexural failure modes, and included an unstrengthened RC beam serving as a control beam, as well as a strengthened beam with a non-prestressed NSM CFRP reinforcement. The level of the prestress force applied to the CFRP reinforcement was 20%, 30% and 40% of its nominal tensile strength in series 1 of the tested beams (as represented in section 3.3), 40% and 60% in series 2 (Badawi and Soudki 2009), and 20%, 40% and 60% in series 3 (El-Hacha and Gaafar 2011).

The data defining the geometry and reinforcement details of the three series of the experimental programs is included in Table 5-1. All beams were simply supported, and were monotonically tested under four-point loading. It is worth to note that the shear reinforcement ratio and spacing of the stirrups in all the RC beams were designed to avoid the shear failure. The average values of the main properties for concrete, longitudinal steel bars and CFRP elements are indicated in Table 5-2, where the nominal properties of the CFRP reinforcement were supplied by manufacturer. The used epoxy adhesive provided a proper bond in all cases and, therefore, the analytical formulation previously described is applicable.

Table 5-1: Geometry and reinforcement details of the beam series

Beam series	No.	L (mm)	a_L (mm)	b_s (mm)	b (mm)	h (mm)	d'_s (mm)	d_s (mm)	d_f (mm)	A'_s (mm^2)	A_s (mm^2)	A_f (mm^2)	*groove size* (mm^2)
Series 1	5	2200	400	900	150	300	25	265	288	157.1 (2φ10)	157.1 (2φ10)	28 CFRP laminate (1.4×20)	144 6×24
Series 2 (Badawi and Soudki)	4	3300	1100	1100	152	254	35	220	241.5	197 (2φ11.2)	353.4 (2φ15)	70.9 CFRP bar (1φ9.5)	375 15×25
Series 3 (El-Hacha and Gaafar)	5	5000	1000	2000	200	400	35	343	387.5	200.6 (2φ11.3)	603.2 (3φ16)	63.6 CFRP bar (1φ9)	500 20×25

Table 5-2: Main properties for concrete, steel and CFRP reinforcements

Beam series	*concrete*	*Steel reinforcement*			*CFRP reinforcement*		*nominal CFRP properties*	
	f'_c (MPa)	f_{sy} (MPa)	f_{su} (MPa)	E_s (GPa)	f_{fu} (MPa)	E_f (GPa)	$f_{fu(n)}$ (MPa)	$E_{f(n)}$ (GPa)
Series 1	32	585	656	208	1922	164	2000	150
Series 2 (Badawi and Soudki)	45	440	560	190	1970	136	1970	136
Series 3 (El-Hacha and Gaafar)	40	475	-	200	2167	130	2068	124

Two types of failure modes of the tested beams were experimentally observed: concrete crushing; rupture of the CFRP reinforcement (both after yielding of the tensile steel reinforcement). The prevailing failure modes of the beams at the maximum capacity were analytically predicted similar to the ones experienced experimentally (using the critical percentage of the CFRP reinforcement (Eq. 5.17)), except in the case of the non-prestressed strengthened beam in series 3 (see Table 5-5). This can be attributed to the value of the compressive strain experimentally observed on the top fiber of concrete (0.0039 (El-Hacha and Gaafar 2011)) at the CFRP failure, which is higher than the analytical limit assumed for concrete crushing (0.003). The load versus mid-span deflection relationship obtained analytically and registered experimentally for the all beams of series 1, 2, and 3 is compared in the Figure 5-9, Figure 5-10, and Figure 5-11, respectively. A good predictive performance of the proposed analytical model is achieved for all the tested beams. Table 5-3, Table 5-4, and Table 5-5 compare the values obtained analytically and registered experimentally for the governing stages of the flexural response of the beams, and also include the short-term prestress loss, initial camber, and prevailing conventional failure mode.

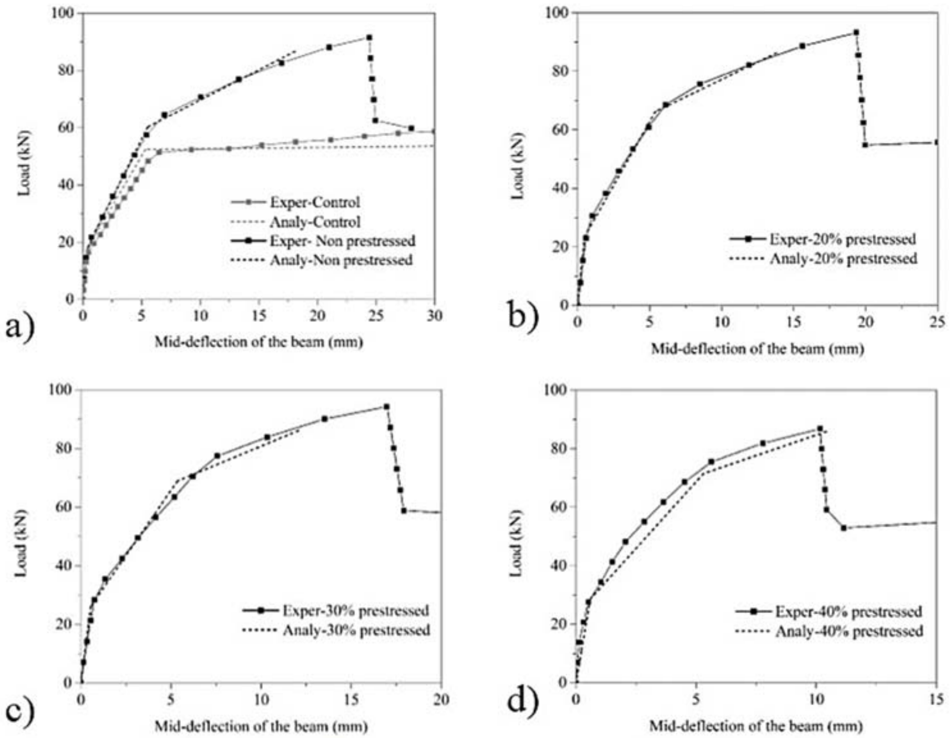

Figure 5-9: Analytical prediction of the tested beams of series 1: a) control and non-prestressed, b) 20% prestressed, c) 30% prestressed, d) 40% prestressed

Table 5-3: Experimental and analytical values of the governing stages of the flexural response for the RC beams of the series 1

RC beams	*Result*	d^{ci}	ε_{lf}^{ci}	P^{cd}	d^{cd}	P^{sd}	d^{sd}	P^{cr}	d^{cr}	P^{y}	d^{y}	P^{u}	d^{u}	*Failue Mode*
		(mm)	*(%)*	*(kN)*	*(mm)*	*(kN)*	*(mm)*	*(kN)*	*(mm)*	*(kN)*	*(mm)*	*(kN)*	*(mm)*	
Control	Exper	-	-	-	-	-	-	13.81	0.30	49.70	5.87	61.46	45.70	CC
	Analy							17.70	0.37	52.40	5.30	53.64	30.43	CC
Non prestressed	Exper	0	0	0	0	0	0	17.01	0.35	60.32	5.93	92.97	24.46	RC
	Analy							17.85	0.37	60.24	5.53	86.60	18.11	RC
20% prestressed	Exper	-0.08	0.40	-	-	7.10	0.17	22.14	0.46	68.69	6.14	94.00	19.36	RC
	Analy	-0.10	1.20	5.71	0.11	6.00	0.13	23.59	0.49	66.37	5.41	86.34	13.80	RC
30% prestressed	Exper	-0.18	1.30	-	-	15.5	0.36	23.04	0.55	72.52	6.52	95.16	16.92	RC
	Analy	-0.15	1.20	8.20	0.17	8.60	0.18	26.08	0.54	68.88	5.35	86.10	12.07	RC
40% prestressed	Exper	-	1.90	-	-	18.10	0.25	25.08	0.47	74.16	5.34	87.45	10.15	RC
	Analy	-0.20	1.20	10.68	0.22	11.21	0.24	28.46	0.59	71.48	5.30	85.82	10.42	RC

- d^{ci} is initial deflection due to prestressing force;
- ε_{lf}^{ci} is the short-term losses of the tensile strain of the prestressed laminate after releasing;
- P^{cd} is the load at concrete decompression point, and d^{cd} its corresponding deflection;
- P^{sd} is the load at steel decompression point, and d^{sd} its corresponding deflection;
- P^{cr} is the load at cracking initiation, and d^{cr} its corresponding deflection;
- P^{y} is the load at yield initiation of the longitudinal tensile bars, and d^{y} its corresponding deflection;
- P^{u} is the ultimate load, and d^{u} its corresponding deflection;
- *CC* is concrete crushing, and *RC* is rupture of CFRP

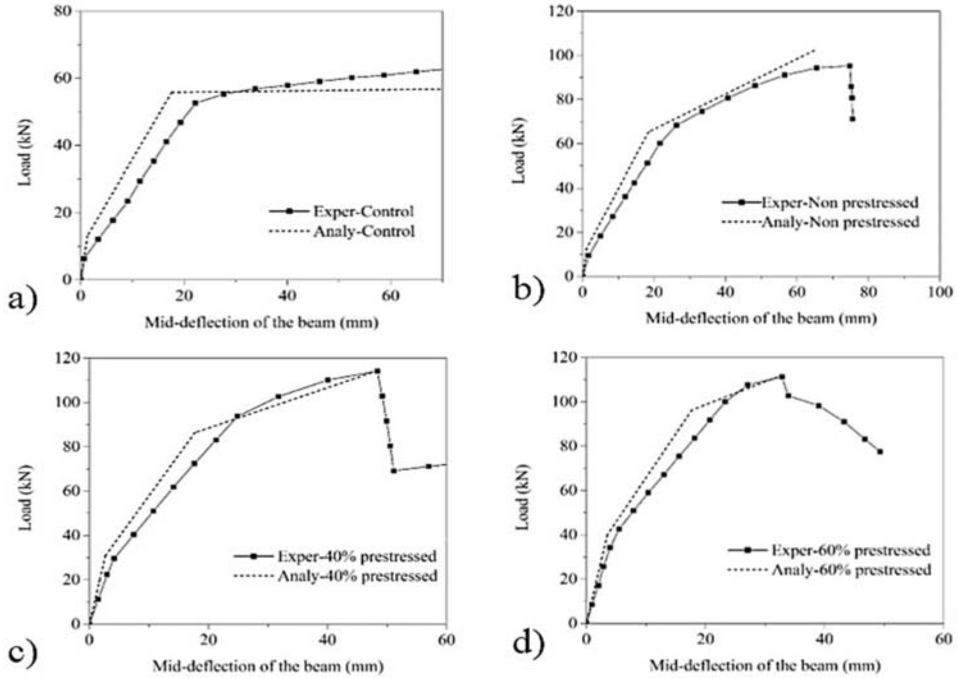

Figure 5-10: Analytical prediction of the tested beams of series 2 (Badawi and Soudki): a) control, b) non-prestressed, c) 40% prestressed, d) 60% prestressed

Table 5-4: Experimental and analytical values of the governing stages of the flexural response for the RC beams of the series 2 (Badawi and Soudki)

RC beams	*Result*	d^{ci} *(mm)*	ε_{lf}^{ci} *(%)*	P^{cd} *(kN)*	d^{cd} *(mm)*	P^{sd} *(kN)*	d^{sd} *(mm)*	P^{cr} *(kN)*	d^{cr} *(mm)*	P^{y} *(kN)*	d^{y} *(mm)*	P^{u} *(kN)*	d^{u} *(mm)*	*Failue Mode*
Control	Exper	-	-	-	-	-	-	10.20	1.86	55.10	23.50	64.30	85.30	CC
	Analy							13.13	1.29	55.80	17.60	57.43	95.00	CC
Non prestressed	Exper	0	0	0	0	0	0	10.92	1.76	69.50	26.03	96.50	65.49	CC
	Analy							12.90	1.14	65.26	18.43	102.23	64.80	CC
40% prestressed	Exper	-	-	-	-	-	-	30.09	4.34	95.00	25.82	115.25	48.34	RC
	Analy	-1.21	2.48	17.8	1.55	19.85	1.73	30.92	2.70	86.38	17.71	113.35	47.13	RC
60% prestressed	Exper	-	-	-	-	-	-	40.00	5.05	105.0	25.72	112.26	32.89	RC
	Analy	-1.81	2.48	26. 8	2.33	29.78	2.61	39.85	3.51	96.31	17.70	112.08	32.96	RC

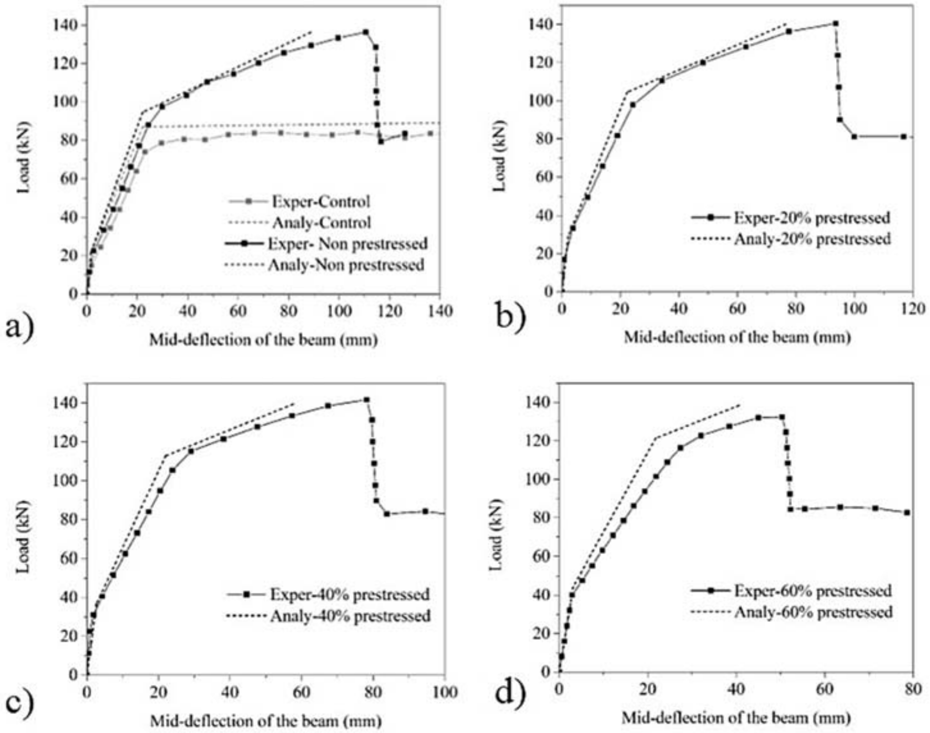

Figure 5-11: Analytical prediction of the tested beams of series 3 (El-Hacha and Gaafar): a) control and non-prestressed, b) 20% prestressed, c) 40% prestressed, d) 60% prestressed

Table 5-5: Experimental and analytical values of the governing stages of the flexural response for the RC beams of the series 3 (El-Hacha and Gaafar)

RC beams	*Result*	d^{ci} *(mm)*	ε_{lf}^{ci} *(%)*	P^{cd} *(kN)*	d^{cd} *(mm)*	P^{sd} *(kN)*	d^{sd} *(mm)*	P^{cr} *(kN)*	d^{cr} *(mm)*	P^{y} *(kN)*	d^{y} *(mm)*	P^{u} *(kN)*	d^{u} *(mm)*	*Failue Mode*
Control	Exper	-	-	-	-	-	-	12.50	1.30	78.90	25.10	83.80	109.9	CC
	Analy							21.54	1.64	86.90	22.20	89.56	143.6	CC
Non prestressed	Exper	0	0	0	0	0	0	18.40	1.60	90.20	25.30	136.40	114.5	RC
	Analy							21.45	1.53	94.49	22.15	136.26	88.8	CC
20% prestressed	Exper	-0.50	6.3	-	-	-	-	22.10	1.50	105.70	27.70	141.00	92.5	RC
	Analy	-0.47	1.2	7.59	0.52	8.35	0.6	29.06	2.07	104.46	22.29	140.13	76.5	RC
40% prestressed	Exper	-0.60	6.0	-	-	-	-	27.90	1.70	114.50	28.60	141.70	79.3	RC
	Analy	-0.94	1.2	15.2	1.10	16.7	1.2	36.65	2.61	112.81	22.02	139.45	57.7	RC
60% prestressed	Exper	-1.30	10.1	-	-	-	-	34.40	2.40	117.70	28.20	134.70	49.7	RC
	Analy	-1.42	1.2	22.9	1.64	25.2	1.8	44.40	3.17	121.33	21.87	138.43	40.2	RC

In order to evaluate the efficiency of the proposed simplified analytical approach (formed by a trilinear response), the moment-curvature relationship ($M-\chi$) of the non-prestressed and 40% prestressed strengthened beams of the series 3 obtained with this approach is compared to the one determined by using a sectional analysis software developed at University of Minho (DOCROS-Design Of CROss Sections). DOCROS assumes that a plane section remains plane after deformation and perfect bond exists between distinct materials. According to DOCROS, a cross section is divided in horizontal layers, and the thickness and width of each layer are user-defined and depend on the cross-section geometry. DOCROS can analyze sections of irregular shape and size, composed of different types of materials subjected to an axial force and variable curvature. Composite layers are used when more than one material exist at same depth of the cross section. Each layer can have an initial non-null stress in order to simulate a prestress effect. DOCROS has a wide database of constitutive laws for the simulation of monotonic and cyclic behavior of cement based materials, polymer based materials and steel bars. More detailed information about DOCROS can be found in (Rajendra 2012).

In the analysis carried out with DOCROS, the cross section of the non-prestressed and 40% prestressed strengthened beams of the series 3 was discretized in horizontal layers of 1 mm thick. Moreover, in the case of the prestressed section, an initial prestrain was applied to the layers corresponding to the CFRP reinforcement in order to simulate the prestress effect.

The behavior of concrete in uniaxial compression was simulated by the stress-strain relationship proposed by CEB-FIP model code (CEB-FIP 1993), while the behavior of concrete in tension was assumed linear up to its tensile strength and the post-cracking residual strength was neglected in order to provide a more realistic comparison with the analytical approach as described by the diagram represented in Figure 5-12a (Barros and Fortes 2005). To simulate both tension and compression behavior of the steel bars, the stress-strain relationship represented in Figure 5-12b was used (Barros and Fortes 2005). The tensile behavior of the CFRP reinforcement was assumed linear up to its ultimate tensile strength.

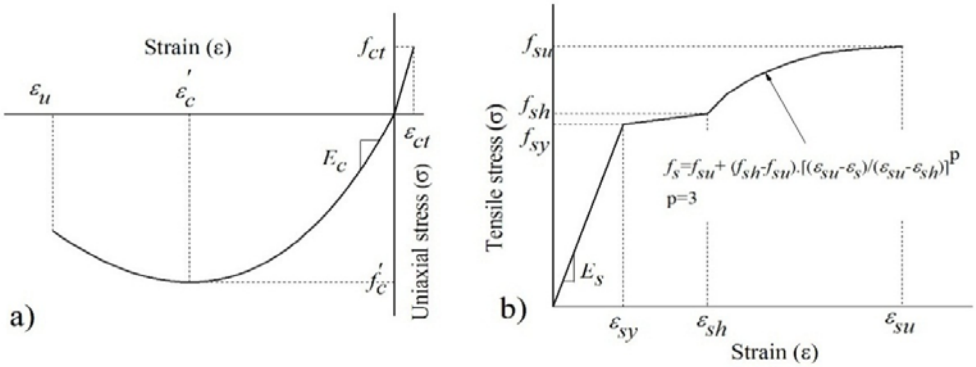

Figure 5-12: Stress-strain relationship used in DOCROS to simulate: a) concrete, b) steel bars (Barros and Fortes 2005)

In Figure 5-13, the predictive performance of the proposed analytical approach in terms of moment-curvature and neutral axis-curvature relationships is assessed by comparing the results obtained experimentally and numerically (DOCROS) for the non-prestressed and 40% prestressed strengthened beams of the series 3. This figure evidences a good predictive performance for the proposed simplified analytical approach. It should be noted that the experimental moment-curvature and neutral axis-curvature relationships of the analyzed beams were determined by using the strains of components along the mid-span cross section of the aforementioned beams reported by (El-Hacha and Gaafar 2011).

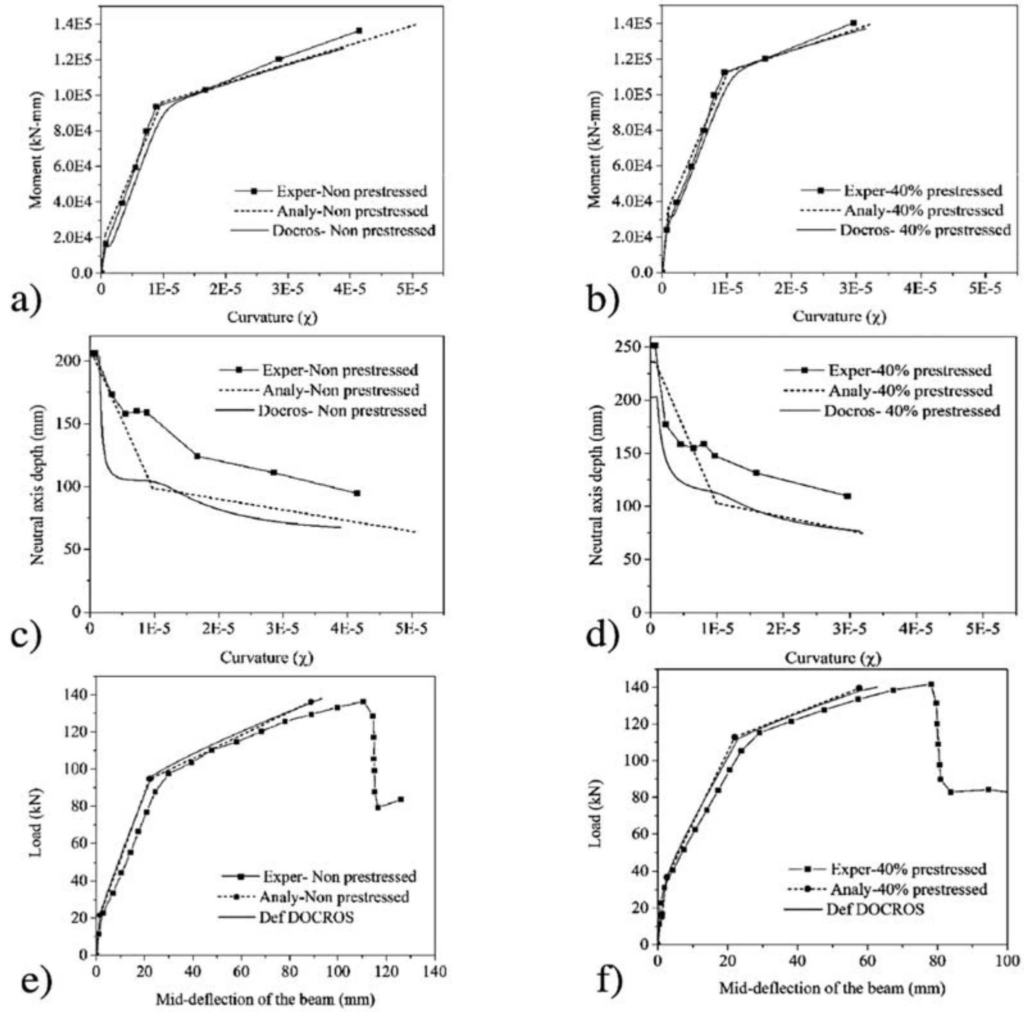

Figure 5-13: Experimental, analytical, and numerical (by DOCROS and Def-DOCROS) predictions of the beams in series 3 in terms of moment-curvature: a) non-prestressed, b) 40% prestressed; and neutral axis depth: c) non-prestressed, d) 40% prestressed; and mid-deflection e) non-prestressed, f) 40% prestressed

To evaluate the level of accuracy of the proposed analytical approach on the prediction of force-deflection using the $M-\chi$ relationship, the mid-span deflection of the non-prestressed and 40% prestressed strengthened beams of the series 3 was analytically and numerically obtained using the proposed analytical approach and Def-DOCROS software. For this purpose, the $M-\chi$ relationship obtained in section 5.1.4 by using the analytical and numerical approaches was used. According to Def-DOCROS software, a statically determinate beam is discretized in Euler-Bernoulli beam elements of 2 nodes. The updated flexural stiffness of each element is determined from the $M-\chi$ relationship of the cross section representative of the element by using a matrix displacement approach described elsewhere (Rajendra 2012). The experimental, analytical, and numerical force-deflection relationships for the aforementioned beams are compared in Figure 5-13e and Figure 5-13f, where it is visible that the proposed analytical approach has high level of predictive performance accuracy.

5.1.6.2 Concrete Cover Delamination Failure Mode

The proposed methodology for the prediction of the ultimate flexural capacity of the NSM CFRP strengthened beams with concrete cover delamination failure, was applied to six NSM CFRP strengthened beams tested by Sharaky et al. (2014), Sharaky (2013), Al-Mahmoud et al. (2009), Barros and Fortes (2005) and Barros et al. (2007). The support and loading configuration of the tested beams are schematically represented in Figure 5-3 and Figure 5-5a. The geometry, steel and CFRP reinforcement details of the strengthened beams are described in Table 5-6. Moreover, the main material properties of the tested beams are represented in Table 5-7. The shear reinforcement ratio and spacing of stirrups were adopted for all the beams in order to avoid the shear failure.

Table 5-6: Geometry, steel and CFRP reinforcement details of the tested beams

Tested beams	L_b (mm)	L_{ub} (mm)	a_L (mm)	b_s (mm)	b (mm)	h (mm)	d'_s (mm)	d_s (mm)	d_f (mm)	A'_s (mm)	A_s (mm)	A_f* (mm)	s_f (mm)	s'_f (mm)
by Sharaky et al.	2000	200	800	800	160	280	40	240	272	2φ8	2φ12	2bφ8	80	40
by Sharaky	2000	200	800	800	160	280	40	240	270	2φ8	2φ12	1bφ8 & 2L:1.4x20	45.5	34.5
by Al-Mahmoud et al.	2100	350	1200	800	150	280	40	240	274	2φ6	2φ12	2bφ6	88	31
by Barros and Fortes -a	1400	50	500	500	100	177	25	152	171	2φ8	3φ6	2L:1.4x10	30	35
by Barros and Fortes -b	1400	50	500	500	100	175	25	152	169	2φ8	2φ6 & 1φ8	2L:1.4x10	30	35
by Barros et al.	800	50	300	300	120	170	21	149	164	2φ6.5	2φ6.5	2L:1.4x10	40	40

* Two types of CFRP reinforcement were used: CFRP round bar (b) and CFRP laminate (L)

Table 5-7: Main properties for the concrete, steel and CFRP reinforcements

Tested beams	concrete	Steel reinforcement			CFRP reinforcement	
	f'_c (MPa)	f_{sy} (MPa)	f_{su} (MPa)	E_s (GPa)	f_{fu} (MPa)	E_f (GPa)
by Sharaky et al. and Sharaky	32	545	624	205	2350	170
by Al-Mahmoud et al.	37	600	-	210	1875	146
by Barros and Fortes	46	730	800	200	2740	159
by Barros et al.	52	627	765	200	2740	159

The parameters of local bond-slip relationship for all the tested beams were adopted similar to the corresponding values considered by (Bianco et al. 2014): $\tau_{\max} = 20.1\,\text{MPa}$ and $\delta_{\max} = 7.12\,\text{mm}$. On the other side, the angle (α) between the CFRP longitudinal axis and generatrices of the concrete fracture surface (semi-pyramid) for all the investigated beams was found equal to 35° by considering the best ultimate flexural capacity for the strengthened beams by using a back analysis of the experimental data. Moreover, this value of α was adopted considering the recommended range by (Bianco et al. 2014) (10°-35°).

The ultimate flexural capacity obtained analytically and registered experimentally for all the tested beams is compared in Table 5-8, where it can be confirmed that the ultimate flexural capacity of the strengthened beams when failing by the concrete cover delamination was analytically predicted less than the one corresponding to the prevailing conventional flexural failure modes ($P_{ccd}^{(u)} \leq \min(P_{cc}^{(u)};P_{rc}^{(u)})$). Table 5-8 also indicates the comparison between the concrete tensile fracture capacity (F_{cf}) with the tensile strength of CFRP (F_{fu}) and resisting bond force (F_{rb}) corresponding to the resisting bond length (L_{rb}) for each CFRP laminate. A good predictive performance of the analytical approach in terms of the ultimate flexural capacity of the strengthened beams when failing by concrete cover delamination is evidenced by considering the ratio between the analytical and experimental flexural capacity of the tested beams ($P_{ccd}^{(u)} / P_{ccd}^{(u)\exp}$), where this ratio was found between [0.83-1.13] for all the tested beams.

Table 5-8: Experimental and analytical values of the ultimate flexural capacity of the tested beams

Tested beams	α (°)	L_{rb} (mm)	F_{cf} (kN)	F_{fu} (kN)	F_{rb} (kN)	F_{cfe} (kN)	$P_{cc}^{(u)}$ (kN)	$P_{rc}^{(u)}$ (kN)	$P_{ccd}^{(u)}$ (kN)	$P_{ccd}^{(u)\exp}$ (kN)	$\frac{P_{ccd}^{(u)}}{P_{ccd}^{(u)\exp}}$
by Sharaky et al.	35	57.12	10.20	117.79	24.28	20.40	164.30	-	118.75	116.01	1.02
by Sharaky	35	57.12	5.80	83.29	21.89	17.40	165.39	-	99.33	118.58	0.83
by Al-Mahmoud et al.	35	55.70	8.20	52.86	17.72	16.40	-	128.29	102.56	108.12	0.94
by Barros and Fortes -a	35	35.70	2.84	36.77	14.67	5.69	88.10	-	84.46	78.50	1.07
by Barros and Fortes -b	35	32.84	2.62	36.77	13.51	5.24	94.25	-	93.09	81.91	1.13
by Barros et al.	35	29.99	3.39	36.77	12.36	6.79	108.80	-	91.47	92.49	0.99

5.1.7 Limit State Criteria for Prestress Level

As already experimentally evidenced in Chapter 3, applying an appropriate prestress level to the NSM CFRP reinforcement offers several benefits for the flexural behavior of the strengthened beams, while the ultimate deflection capacity of the beams strengthened with the NSM prestressing technique decreases with the increase of the applied prestress level, implying a decrease of the ductility index with the prestress level. In this regards, for all the analyzed beams (series 1, 2, and 3) in section 5.1.6.1, the relationship between the normalized ductility index (defined in section 3.3.4.2

(μ^{pre}/μ^{pas})) and the applied prestress level registered experimentally and obtained analytically is represented in Figure 5-14.

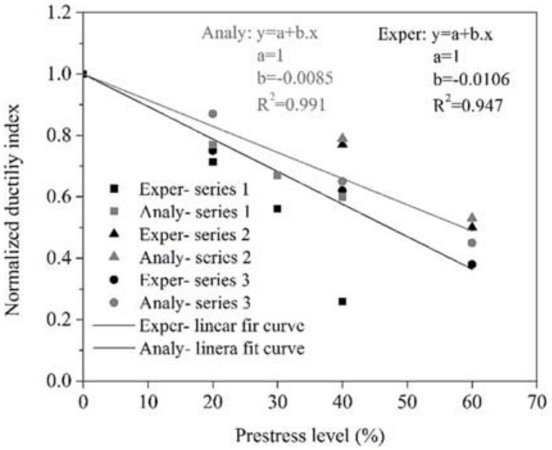

Figure 5-14: Normalized ductility index of the all beam series

According to this figure, a criterion to limit the prestress level that can be applied to the CFRP reinforcement should be considered in order to optimize the ductility performance of the NSM prestressing technique, maintaining a sufficient degree of the ductility. This sufficient ductility index can be achieved by considering the strain in the longitudinal tensile steel bars at the ultimate stage adopting conventional flexural failure modes, calculated according to the following equations:

$$\varepsilon_{s,cc}^{(u)} = \chi_{cc}^{(u)}.(d_s - c_{cc}^{(u)}) \qquad (5.39)\text{-a}$$

$$\varepsilon_{s,rc}^{(u)} = \chi_{rc}^{(u)}.(d_s - c_{rc}^{(u)}) \qquad (5.39)\text{-b}$$

where $\varepsilon_{s,cc}^{(u)}$ and $\varepsilon_{s,rc}^{(u)}$ are the tensile strain in the longitudinal bottom steel bars at the ultimate stage adopting concrete crushing and rupture of CFRP reinforcement failure modes, respectively.

For the reinforced concrete members, ACI-318 proposes to maintain the strain in the tensile steel reinforcement equal to or greater than 0.005 at ultimate limit state for ductile response of the section (or tension-controlled section), resulting in an ample warning of failure. In opposition, when the tensile strain of the steel reinforcement at ultimate stage is less than or equal to the yield strain of the steel (ε_{sy}), a brittle response of the section (or compression-controlled section) with a little warning of impending failure may be expected. Some sections have the steel tensile strain between above limits. These sections provide a transition region between compression- and tension-controlled sections (ACI-318-08 2008, ACI-440.2R. 2008).

The experimental results reported by (Badawi and Soudki 2009, El-Hacha and Gaafar 2011) evidenced that the strain in the longitudinal steel bars in tension decreases at the ultimate stage with the increase of the prestress level due to an initial compressive strain in the tensile steel bars after the release of the prestress force, and a smaller deflection at the rupture of the CFRP reinforcement. Both these reasons lead to a lower strain increment in the longitudinal tensile steel bars. Accordingly, to assure a sufficient degree of the ductility for the prestressed beams, the maximum prestress level that can be applied to the CFRP reinforcement should be limited by the condition of do not reducing the strain in the longitudinal tensile steel bars less than 0.005 at the ultimate stage.

The applied prestress level versus the strain in the longitudinal tensile steel bars at ultimate stage (calculated by Eq. (5.39) for all the beam series) relationship is represented in Figure 5-15, where it can be observed that CFRP reinforcement prestressed at 58% of its nominal tensile strength can be approximately defined as the maximum prestress level that can be applied to these beams. This limit is in good agreement to the maximum prestress level recommended by (CAN/CSA-S6-00. 2000, ISIS-9 2007) (60% of CFRP ultimate capacity).

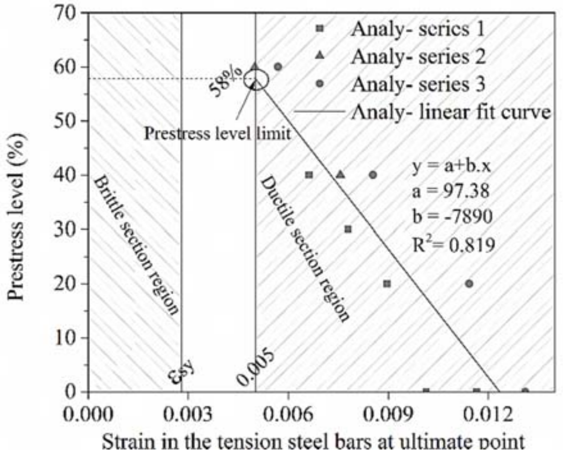

Figure 5-15: Limit for the prestress level applied to the CFRP reinforcement

The ductility index corresponding to this prestress level (58%) was analytically determined for all the beam series, and the obtained values were 1.57, 1.93, and 1.94 for the beams of series 1, 2, and 3, respectively. Therefore, it is suggested that for design purposes the prestress level applied to the CFRP reinforcement should be limited in order to guarantee a sufficient degree of the ductility index for the prestressed strengthened beams, and according to the obtained results, $\mu^{pre} = d_u / d_y > C$, where C varies from 1.5 to 2, seems to be appropriate.

5.2 Transfer Zone of Prestressed CFRP Reinforcement

The objective of this section is to propose an analytical formulation, with a design framework, for the prediction of the distribution of CFRP tensile strain and bond shear stress and, additionally, the prestress transfer length. The analytical approach is developed by considering the influence of the effective parameters on the prestress transfer length, like elasticity modulus of concrete, CFRP, and epoxy adhesive, and their corresponding thickness. Besides, the proposed approach offers a method to identify the transfer length using tensile strain distribution along the CFRP length. Moreover, the analytical equations are proposed to predict the distribution of the CFRP tensile strain and bond shear stress along the CFRP bonded length when the prestress force is released.

After demonstration the good predictive performance of the proposed analytical approach, a series of parametric studies was carried out to analytically evaluate the influence on the prestress transfer length of the different material properties, CFRP and groove cross section, and hardening of epoxy adhesive during its curing time. Subsequently, a formula is proposed to predict the evolution of the prestress transfer length during the curing time of epoxy adhesive.

5.2.1 Analytical Approach

Malek et al. (1998) proposed a combined shear-bending analytical model for the RC beams strengthened with EBR FRP plate to predict interfacial debonding failure at the end of the plate bonded length (cut-off point). This proposed model was modified by Hassan and Rizkalla (2003) to account for the double bonded area of FRP strips flexurally applied according to NSM technique. According to this modification, debonding of NSM strips is assumed to occur as a result of high shear stress concentration at FRP cut-off point.

In the current study, the model proposed by Hassan and Rizkalla (2003) is modified to analytically predict the tensile strain distribution and bond shear stress along the NSM CFRP bonded length immediately after the release of the prestress force. The model takes into account the strain profile of the beam’s cross section due to the negative camber created after the release of the prestress force (using the model proposed in section 5.1.4.1), as an initial condition (designated by superscript symbol of (ci) in the current section) for the strains in the constituent materials.

5.2.2 Assumptions

The following assumptions were adopted in the proposed analytical model:

a) Linear elastic and isotropic behavior is used for concrete, epoxy adhesive, CFRP and steel reinforcements;

b) There is no slip between steel and CFRP reinforcements with surrounding concrete;

c) Strain in the longitudinal steel bars, CFRP reinforcement and concrete is directly proportional to their distance from the neutral axis of the cross section of the RC element.

5.2.3 Analytical Approach Description

The static equilibrium of an infinitesimal portion (dx) of the strengthened RC beam after the release of the prestress force (at the level of section A-A shown in Figure 5-16), results in Eq. (5.40) to determine the bond shear stress (τ) along a length of dx using the variation of the tensile strain in the CFRP reinforcement ($d\sigma_f$) and its thickness (a_f).

$$\tau = \frac{a_f}{2}.\frac{d\sigma_f}{dx} \tag{5.40}$$

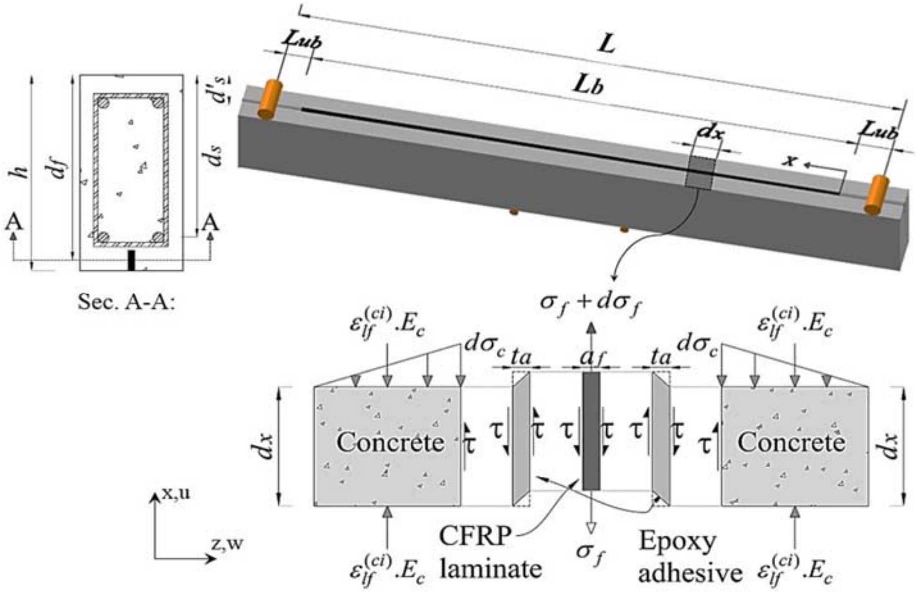

Figure 5-16: Infinitesimal portion of strengthened beam after releasing of prestress force

According to Figure 5-16, tensile stress in the CFRP reinforcement is transferred to the concrete surfaces mainly through shear stresses (τ) in the adhesive layers assuming linear elastic behavior for the adhesive and no-slip conditions for the interfacial connections. In other words, the tensile stress in the CFRP reinforcement is in equilibrium with shear stresses in both adhesive layers and a very thin layer of concrete substrate adjacent to the adhesive (Faella et al. 2003, Dai et al. 2005). Therefore, an effective bond stiffness ($k_e = G_e/t_e$, where G_e and t_e are the effective shear modulus and its thickness, respectively) can be defined to simulate the bond shear stiffness of these materials surrounding the CFRP reinforcement (adhesive and thin concrete layers) applied according to the NSM technique (Figure 5-16 and Figure 5-17a) (Dai et al. 2005):

$$k_e = \frac{G_e}{t_e} = \frac{k_a . k_c}{k_a + k_c} \tag{5.41}$$

where $k_a = G_a/t_a$ is the shear stiffness of adhesive layer (G_a and t_a are the shear modulus and the thickness of adhesive, respectively), and $k_c = G_c/t_c$ is the shear stiffness of the thin layer of concrete adjacent to the adhesive layer (G_c and t_c are the shear modulus and the thickness of concrete layer, respectively).

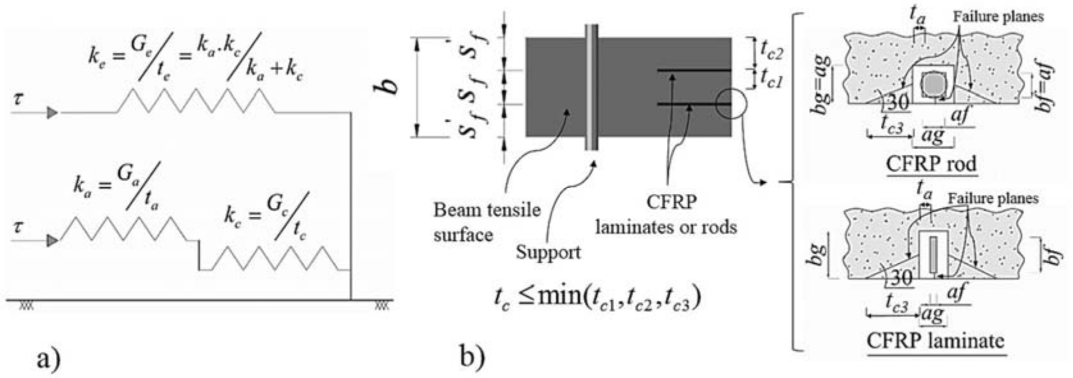

Figure 5-17: a) Schematic spring in series for bond shear stiffness, b) view of the bottom tensile surface of the beam in the zone of the extremities of the CFRP reinforcement

Assuming isotropic linear elastic behavior for concrete and epoxy adhesive, G_c and G_a can be derived using the modulus of elasticity of concrete (E_c) and adhesive (E_a), respectively:

$$G_c = \frac{E_c}{2(1+\upsilon_c)}\ ,\ G_a = \frac{E_a}{2(1+\upsilon_a)} \tag{5.42}$$

where υ_c and υ_a are the Poisson's ratio of concrete and adhesive, respectively. Moreover, t_a and t_c are the thickness of the adhesive layer and a thin layer of concrete that is influenced by the shear stress exerting by the CFRP. For EBR-FRP strengthened beams, t_c is typically adopted as 2.5-3 times the maximum aggregate size, or about 40-50 mm (Dai et al. 2005, Toutanji et al. 2012). However, for FRP strengthened beams according to NSM technique, the following equation is proposed to determine t_c (Figure 5-17b):

$$t_c = \min\left(t_{c1}, t_{c2}, t_{c3}\right) = \min\left(s_f^{'}, \frac{s_f}{2}, \frac{b_g}{2\tan(30^o)}\right) \tag{5.43}$$

where s_f is the distance between two adjacent CFRPs, $s_f^{'}$ is the distance between the lateral face of the beam's cross section and the nearest CFRP (this assumption is inspired on the work represented in section 5.1). The last condition of Eq. (5.43) aims to consider the possibility of occurring a failure mode for NSM FRP system according to concrete fracture propagation through inclined planes with an angle of approximately 30° with the beam's tensile surface ($t_{c3} = b_g / 2\tan(30^o)$, where b_g is the groove's depth), as represented in Figure 5-17b, which was inspired on the work of De Lorenzis and Teng (2007).

Therefore, by assuming linear elastic behavior for the constituent materials, bond shear stress can be obtained by the following equation:

$$\tau = G_e . \gamma \rightarrow \gamma = \frac{du}{dz} + \frac{dw}{dx} \tag{5.44}$$

where γ is the shear strain, u and w are the longitudinal and transversal displacements of t_e (Figure 5-16).

Differentiating Eqs. (5.40) and (5.44) with respect to x, results in:

$$\frac{d^2\sigma_f}{dx^2} = \frac{2.G_e}{a_f}\left(\frac{d^2u}{dx.dz} + \frac{d^2w}{dx^2}\right) \tag{5.45}$$

where d^2w/dx^2 can be neglected due to symmetry conditions, and $d^2u/dx.dz$ can be expressed as:

$$\frac{d^2u}{dx.dz} = \frac{d}{dz}\left(\frac{du}{dx}\right) = \frac{d}{dz}\left(\frac{du_c}{dx} - \frac{du_f}{dx}\right) = \frac{1}{t_e}\left(\varepsilon_c - \varepsilon_{lsf}\right) \tag{5.46}$$

where u_c and u_f are the longitudinal displacement of concrete and CFRP reinforcement, respectively, at the level of section A-A (Figure 5-16). ε_c is the compressive strain in concrete at the level of NSM CFRP reinforcement (section A-A in Figure 5-16). Besides, ε_{lsf} is the reduction of tensile strain in the CFRP reinforcement due to the short-term prestrain loss ($\varepsilon_{lf}^{(ci)}$) and its shortening effect after the prestress releasing that can be obtained by $\varepsilon_{lsf} = \varepsilon_{fp} - \varepsilon_f$ noting that ε_{fp} and ε_f are applied prestrain and tensile strain in the CFRP, respectively (Wu et al. 2005).

In fact, when the prestress force (F_{pre}) is released, the negative camber causes a compressive strain at the section A-A of concrete, which is equal to the short-term prestrain loss ($\varepsilon_c = \varepsilon_{lf}^{(ci)}$) in the CFRP reinforcement assuming proportionality of the strain distribution along the cross section (as represented in section 5.1.4.1). This short-term prestrain loss and effective tensile strain ($\varepsilon_{ef}^{(ci)}$) in the CFRP reinforcement are determined using Eq. (5.4).

Using Eqs. (5.4), (5.41) and (5.46) in Eq. (5.45), results in:

$$\frac{d^2\sigma_f}{dx^2} - \frac{2.G_e}{t_e.a_f.E_f}\sigma_f = -\frac{2.G_e}{t_e.a_f}(\varepsilon_{fp} - \varepsilon_{lf}) \rightarrow \frac{d^2\sigma_f}{dx^2} - \frac{2.k_e}{a_f.E_f}\sigma_f = -\frac{2.k_e}{a_f}(\varepsilon_{ef}^{(ci)}) \qquad (5.47)$$

By rewriting Eq. (5.47):

$$\frac{d^2\sigma_f}{dx^2} - B^2.\sigma_f = -B^2.E_f.\varepsilon_{ef}^{(ci)} \rightarrow B^2 = \frac{2k_e}{a_f.E_f} \qquad (5.48)$$

where B is a stiffness parameter.

The solution for Eq. (5.48) can be expressed as:

$$\sigma_f(x) = C_1e^{Bx} + C_2e^{-Bx} + E_f.\varepsilon_{ef}^{(\mathrm{ci})} \qquad (5.49)$$

The bond shear stress (τ) can also be derived considering Eq. (5.40), as follows:

$$\tau(x) = \frac{a_f}{2}(B.C_1e^{Bx} - B.C_2e^{-Bx}) \qquad (5.50)$$

The following boundary conditions can be adopted to determine the constants C_1 and C_2:

$$\begin{aligned} &\sigma_f = 0 \;\; at \;\; x = 0 \\ &\tau = 0 \;\; at \;\; x = L_b/2 \end{aligned} \qquad (5.51)$$

where L_b is the CFRP bonded length (Figure 5-16). Considering the introduced boundary conditions, the constants C_1 and C_2 can be expressed by:

$$C_1 = \frac{-E_f.\varepsilon_{ef}^{(ci)}}{(1+e^{BL_b})} \qquad (5.52)$$

$$C_2 = \frac{-E_f.\varepsilon_{ef}^{(ci)}.e^{BL_b}}{(1+e^{BL_b})} \qquad (5.53)$$

A parametric study of the variables in Eqs. (5.52) and (5.53) evidenced that e^{BL_b} is always a very large number for the practical values of B and L_b. Hence, C_2 can be simplified to $C_2 = -E_f.\varepsilon_{ef}^{(ci)}$ and C_1 can be ignored. Accordingly, Eqs. (5.49) and (5.50) can be rewritten as:

$$\sigma_f(x) = E_f.\varepsilon_{ef}^{(\mathrm{ci})}(1 - e^{-Bx}) \tag{5.54}$$

$$\tau(x) = \frac{a_f.E_f.B.\varepsilon_{ef}^{(ci)}.e^{-Bx}}{2} \tag{5.55}$$

It should be noted that in the case of a round CFRP bar, for using the proposed analytical model, its cross section is converted to an equivalent square cross sectional area.

5.2.4 Prestress Transfer Length

When the prestress force is removed at both extremities of CFRP reinforcement after hardened stage of the epoxy, this force is transferred gradually from the CFRP to the surrounding concrete through a transmission zone at the extremity of the CFRP bonded length. In other words, the prestress force starts from zero at the end section of the CFRP bonded length and continues increasing along the transmission zone (known as prestress transfer length) and becomes constant beyond this zone. Moreover, variation of the prestress force in the CFRP along the transfer length causes a shear stress in the CFRP-adhesive-concrete bonds.

Russel and Burns (1993) proposed a method to determine transfer length for the prestressed steel strands using the tensile strain distribution along the prestressed element. This method is known as 95% Average Maximum Strain (95%AMS) method and comprises the following steps (Figure 5-18):

1. Plotting the tensile strain distribution along the prestressed element;
2. Determining the average maximum strain by computing the average strain values within the plateau zone of strain distribution after the release of the prestress force;
3. Considering a horizontal line corresponding to 95% of the average maximum strain;
4. Transfer length is determined by the intersection of the 95% line with the strain distribution plot.

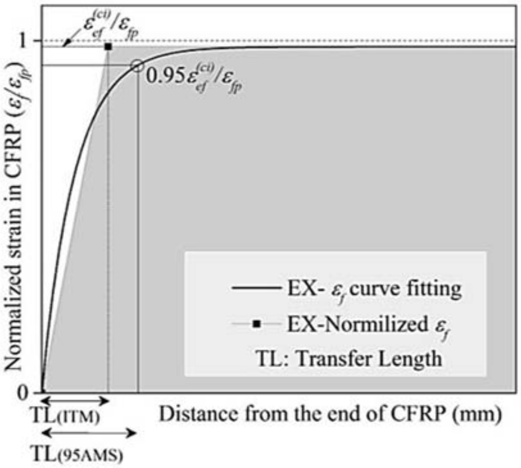

Figure 5-18: Prestress transfer length according to 95%AMS and ITM methods

In the current study, another method is also proposed to determine the prestress transfer length using an idealized trapezoid plot of the normalized tensile strain distribution along the FRP bonded length (designated as ITM method). According to this method, prestress transfer length ($TL_{(ITM)}$) starts from the end section of FRP bonded length up to the beginning of plateau zone (see Figure 5-18). The dimensions of the idealized trapezoid plot are obtained assuming a height equal to $\varepsilon_{ef}^{(ci)}/\varepsilon_{fp}$ and an area equal to the area under the normalized CFRP tensile strain curve obtained by $\int\left(\sigma_f(x)/(E_f.\varepsilon_{fp})\right)d(x)$, as represented in Figure 5-18. Hence:

$$\int_0^{L_b/2} \frac{\sigma_f(x)}{E_f.\varepsilon_{fp}} d(x) = \left(\frac{(L_b/2)+((L_b/2)-TL_{(ITM)})}{2}\right).\left(\frac{\varepsilon_{ef}^{(ci)}}{\varepsilon_{fp}}\right) \tag{5.56}$$

Rewriting Eq. (5.56) using Eq. (5.54) results in:

$$\int_0^{L_b/2} \frac{E_f.\varepsilon_{ef}^{(\mathrm{ci})}(1-e^{-Bx})}{E_f.\varepsilon_{fp}} d(x) = \left(\frac{\varepsilon_{ef}^{(ci)}}{\varepsilon_{fp}}\right).\left[x+\frac{e^{-Bx}}{B}\right]_0^{L_b/2} = \left(\frac{L_b-TL_{(ITM)}}{2}\right).\left(\frac{\varepsilon_{ef}^{(ci)}}{\varepsilon_{fp}}\right) \tag{5.57}$$

Therefore, $TL_{(ITM)}$ can be expressed by:

$$TL_{(ITM)} = \frac{2(1-e^{-BL_b/2})}{B} \tag{5.58}$$

Using practical values for B and L_b, $e^{-BL_b/2}$ is always a very small number when compared to the other terms, and can be ignored. Hence, by rewriting Eq. (5.58), $TL_{(ITM)}$ can be obtained, as follows:

$$TL_{(ITM)} = \frac{2}{B} \rightarrow B = \left(\frac{2k_e}{a_f . E_f} \right)^{0.5} \tag{5.59}$$

This equation evidences that the prestress transfer length is directly related to the stiffness parameter (B). In fact, the B parameter represents physically the relative stiffness of the materials surrounding the CFRP reinforcement and the stiffness of this last one.

5.2.5 Assessment of Predictive Performance of Analytical Approach

The performance of the described analytical approach is assessed by predicting the distribution of the normalized tensile strain in the CFRP reinforcement and the bond shear stress for all the prestressed strengthened beams (represented in section 3.2) immediately after the release of the prestress force. The relationship between the aforementioned terms obtained analytically and experimentally versus distance from the end of CFRP bonded length is depicted in Figure 5-19 and Figure 5-20. These figures indicate a good predictive performance of the analytical approach in terms of distribution of the CFRP tensile strain and bond shear stress along the CFRP bonded length when the prestress force is released. Besides, Figure 5-19 evidences that the analytical model predicts with good accuracy the normalized effective tensile strain in the CFRP laminate ($\varepsilon_{ef}^{(ci)} / \varepsilon_{fp}$) registered experimentally, beyond the transmission zone.

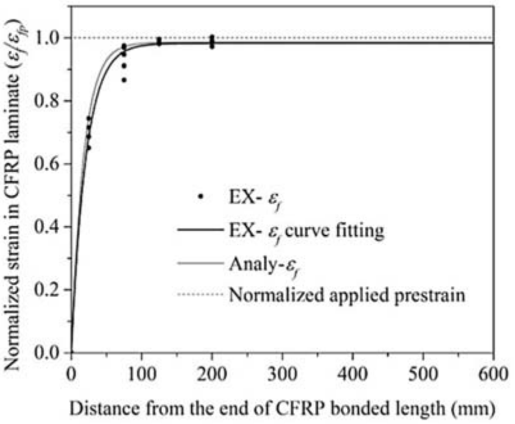

Figure 5-19: Analytical prediction of the tensile strain distribution in the CFRP reinforcement

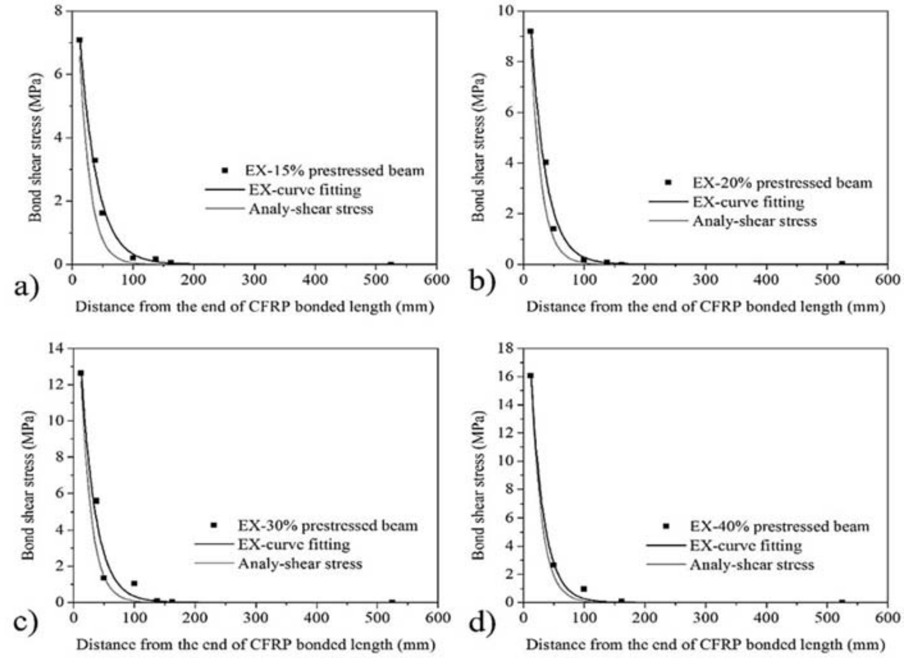

Figure 5-20: Analytical prediction of bond shear stress for the beam prestressed at the level of: a) 15%, b) 20%, c) 30%, d) 40%

The proposed analytical model is, moreover, applied on the prediction of the distribution of the CFRP tensile strain and bond shear stress of the RC beams strengthened with either prestressed spirally wound rod or sand blasted CFRP rod, whose tests were conducted by Badawi et al. (2010). The data defining the geometry and reinforcement details, as well as the main material properties of this experimental program is included in Table 5-9.

Table 5-9: Geometries and main material properties of the tested beams by Badawi et al.

Geometries	L_b (mm)	b (mm)	h (mm)	d_s (mm)	d_f (mm)	A'_s (mm^2)	A_s (mm^2)	A_f *spirally wound* (mm^2)	A_f *sand blasted* (mm^2)	*groove size* (mm^2)
	3300	152	254	209	241.5	200	400	1φ9	1φ9.5	15×25

L_b: CFRP bonded length, b and h: width and height of beam cross section, A'_s: area of compressive steel bar, A_s and d_s: area of tensile steel bar and its depth from top fiber of section, A_f and d_f: area of CFRP reinforcement and its depth from top fiber of section.

Material properties	Concrete	Steel bars		CFRP spirally wound		CFRP sand blasted		Epoxy adhesive	
	f'_{cm} (MPa)	f_{sym} (MPa)	f_{sum} (MPa)	E_f (GPa)	f_{fum} (MPa)	E_f (GPa)	f_{fum} (MPa)	E_a (GPa)	f_{am} (MPa)
	45	440	560	136	1970	130	2166	4.48	24.8

f'_{cm}: concrete compressive strength, f_{sym} and f_{sum}: yield and ultimate tensile strength of steel bars, E_f and f_{fum}: elasticity modulus and tensile strength of CFRP, E_a and f_{am}: elasticity modulus and tensile strength of adhesive.

The distribution of normalized tensile strain in the spirally CFRP rods and in the sand blasted CFRP rods obtained analytically and registered experimentally for these beams is compared in Figure 5-21a and Figure 5-21b, respectively. Furthermore, Figure 5-21c and Figure 5-21d compare the bond shear stress distribution predicted analytically and recorded experimentally in the cases of 45% prestressed spirally CFRP rod and 40% prestressed sand blasted CFRP rod, respectively.

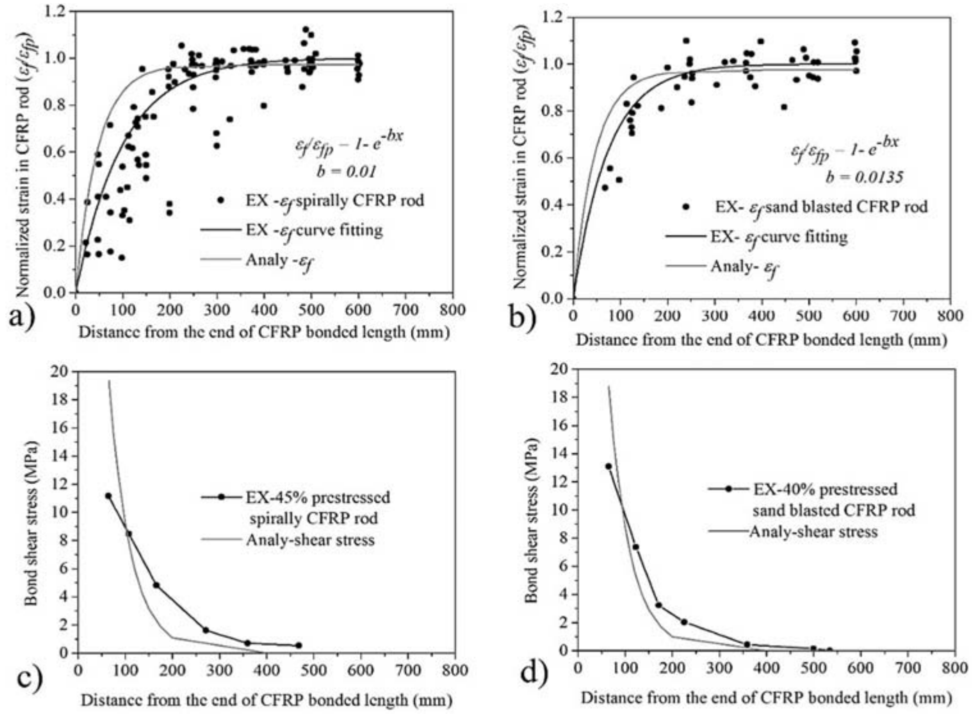

Figure 5-21: Analytical prediction of the tensile strain distribution of the CFRP reinforcement for: a) spirally CFRP, b) sand blasted CFRP; and bond shear stress for: c) 45% prestressed spirally CFRP, d) 40% prestressed sand blasted CFRP

By considering the relationship between $\varepsilon_f / \varepsilon_{fp}$ and the distance from the end of the CFRP bonded length registered experimentally in the program carried out in the present work (Figure 5-19) and in the program executed by Badawi et al. (2010) (Figure 5-21a and Figure 5-21b), the two analytical approaches (95%ASM and ITM) are applied in order to determine the prestress transfer length (*TL*), whose results are presented in Table 5-10.

Table 5-10: Comparison of prestress transfer length (TL) for the tested beams

Beams	$TL_{(95AMS)}^{\exp}$	$TL_{(ITM)}^{\exp}$	$TL_{(95AMS)}^{analy}$	$TL_{(ITM)}^{analy}$	$\frac{TL_{(95AMS)}^{\exp}}{TL_{(95AMS)}^{analy}}$	$\frac{TL_{(ITM)}^{\exp}}{TL_{(ITM)}^{analy}}$
Experimental beams	61	42	50	36	1.20	1.17
Tested by Badawi et al. (spirally wound)	281	200	145	94	1.93	2.13
Tested by Badawi et al. (sand blasted)	208	148	140	92	1.48	1.60

In fact, in the cases of beams reported by (Badawi et al. 2010), experimental distribution of the CFRP tensile strain along the bonded length represented in Figure 5-21a and Figure 5-21b showed more gradually increasing than the corresponding analytical ones during the transfer length, resulting in a lower bond shear stress and higher transfer length for the experimental results. The higher increase rate of the $\varepsilon_f / \varepsilon_{fp}$ predicted analytically than the one registered experimentally may be attributed to the following reasons:

1) Better bond behavior of the equivalent square cross section for the CFRP (used in the analytical model) compared to its round cross section (used in experimental program) due to a higher contact perimeter;
2) Damages in the CFRP-adhesive-concrete bonds within the transmission zone due to a high possible rate of the prestress releasing in the laboratory and/or due to a deficient filling of the groove with the epoxy because of the relatively small thickness of the groove.

It should be noted that Poisson's ratio of the epoxy adhesive (υ_a) used in the analytical approach for the simulation of the experimental tests and the beams tested by (Badawi et al. 2010) was assumed 0.33 and 0.49, respectively, according to the recommendation of (He 2010) considering the corresponding elasticity modulus of adhesive (E_a).

5.2.6 Parametric Study

By using the developed analytical model, parametric studies were carried out to evaluate the influence of the relevant parameters of this model on the distribution of CFRP tensile strain (ε_f) and bond shear stress (τ), as well as on the prestress transfer length (TL). The parameters considered in this parametric study were: the elasticity modulus of concrete, CFRP, and adhesive; the shape of CFRP cross section; the thickness of adhesive layer; and the curing time of the epoxy adhesive. For an easier interpretation of the influence of these parameters on the distribution of ε_f, τ and on the TL values, these results were normalized (divided by) to, respectively, the initial prestrain applied to the laminate (ε_{fpi}), maximum bond shear stress obtained analytically at the end section of CFRP bonded length (τ_i), and prestress transfer length obtained analytically by using the ITM method (TL_i) applied to the experimental beams (Table 5-10).

5.2.6.1 Material Properties

Figure 5-22 shows the influence of the normalized elasticity modulus of concrete (E_c/E_{ci}), CFRP (E_f/E_{fi}), and adhesive (E_a/E_{ai}), on the normalized CFRP tensile strain ($\varepsilon_f/\varepsilon_{fpi}$), normalized bond shear stress (τ/τ_i), and normalized prestress transfer length (TL/TL_i) obtained according to the ITM method, where E_{ci}, E_{fi}, and E_{ai} are the elasticity modulus of concrete, CFRP, and adhesive as reported in Table 3-1. It should be noted that an equal variation ratio (0.5, 1, and 2) was adopted for the aforementioned properties in order to facilitate the comparison of the influence of the variation of different material properties on the investigated terms.

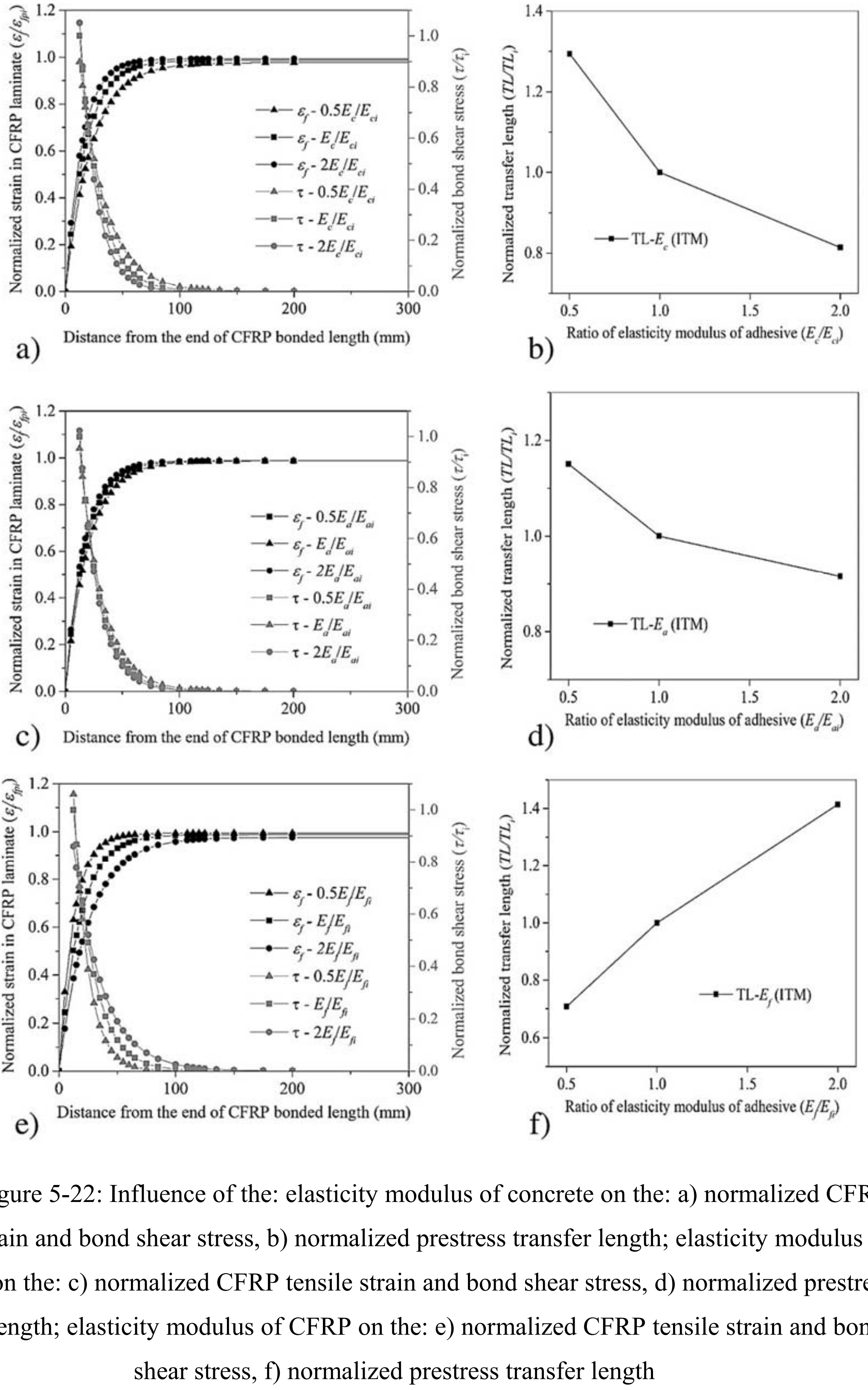

Figure 5-22: Influence of the: elasticity modulus of concrete on the: a) normalized CFRP tensile strain and bond shear stress, b) normalized prestress transfer length; elasticity modulus of adhesive on the: c) normalized CFRP tensile strain and bond shear stress, d) normalized prestress transfer length; elasticity modulus of CFRP on the: e) normalized CFRP tensile strain and bond shear stress, f) normalized prestress transfer length

The results show that the increase of the elasticity modulus of concrete and adhesive reduces the prestress transfer length (Figure 5-22b and Figure 5-22d), but increases the maximum bond shear stress causing a higher possibility of damage in the concrete substrate (Figure 5-22a and Figure 5-22c). In fact, the effective bond stiffness (k_e) increases with the shear stiffness of adhesive layer (k_a) and concrete layer (k_c), causing a higher stiffness parameter (B), resulting a decrease of the prestress transfer length (see Eq. (5.59)) and an increase of the bond shear stress (see Eq. (5.55)).

On the other hand, a higher elasticity modulus of CFRP reinforcement resulted in a longer transfer length and a smaller maximum bond shear stress (Figure 5-22e and Figure 5-22f). In fact, a certain prestress force applied in a stiffer CFRP reinforcement induces a smaller strain in the CFRP causing a lower bond shear stress (τ) (see Eq. (5.40)). According to the principles of static equilibrium, this lower bond shear stress should be in equilibrium with the applied prestress force and consequently, acts in a longer length to transfer the prestress force. In other words, a higher elasticity modulus of CFRP reinforcement decreases the stiffness parameter, B, resulting in a longer prestress transfer length according to the Eq. (5.59).

5.2.6.2 CFRP and Groove Cross Section

The most common CFRP bar types for the flexural strengthening of RC beams according to NSM technique have cross section of rectangular, square or circular shape. The experimental research has evidenced a better bond behavior of the CFRP bar of rectangular cross section when compared to the other types of bars due to the higher ratio of the bond contact area to the cross sectional area (El-Hacha and Rizkalla 2004).

Figure 5-23a shows a comparison between the use of rectangular and square CFRP bars with equal cross sectional area and thickness of the adhesive layer (designated by $C1$ and $C2$, respectively) in terms of the normalized CFRP tensile strain ($\varepsilon_f / \varepsilon_{fpi}$) and bond shear stress (τ / τ_i). According to this figure, the CFRP bar with square shape increased significantly the maximum bond shear stress when compared to the use of rectangular CFRP bar due to the direct influence of a_f on the τ, according to Eq. (5.40).

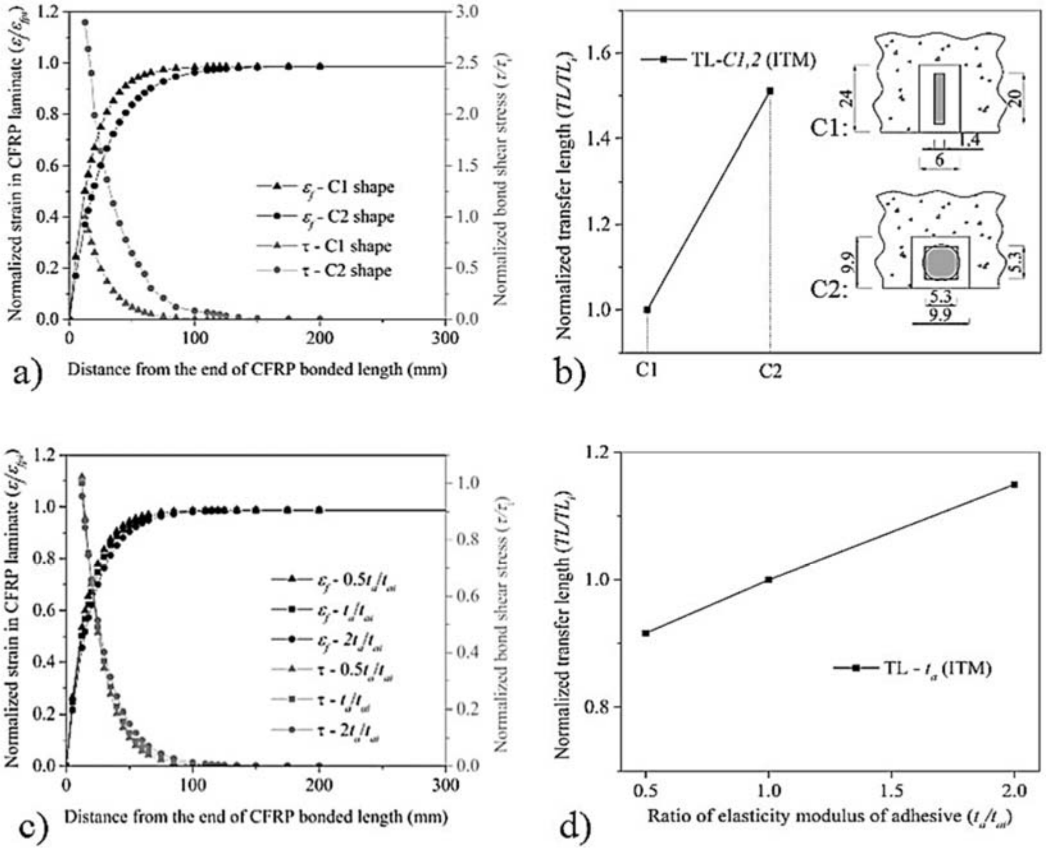

Figure 5-23: Influence of the geometry of the CFRP bar cross section on the: a) normalized CFRP tensile strain and bond shear stress, b) normalized prestress transfer length; influence of the thickness of adhesive layer on the: c) normalized CFRP tensile strain and bond shear stress, d) normalized prestress transfer length

The higher bond contact area of the rectangular CFRP bar, moreover, caused analytically a decrease in terms of prestress transfer length when compared to the use of square CFRP bar, as represented in Figure 5-23b. This figure evidences that the use of square CFRP bar ($a_f/b_f = 1$, where a_f and b_f are width and height of the CFRP cross section) provides an increase of 51% in terms of prestress transfer length according to the ITM method compared to the use of rectangular CFRP bar with $a_f/b_f = 0.07$. In other words, a higher width/height ratio (a_f/b_f) of the CFRP cross section increases the prestress transfer length.

On the other side, Figure 5-23c and Figure 5-23d show the influence of the normalized adhesive layer thickness (t_a/t_{ai}) on the normalized terms of CFRP tensile strain ($\varepsilon_f/\varepsilon_{fpi}$), bond shear stress ($\tau/\tau_i$), and prestress transfer length (TL/TL_i), where t_{ai} is the thickness of adhesive layer adopted for the experimental program (as represented in Figure 3-8). This figures evidence that the prestress transfer length increases with the adhesive layer thickness due to the decrease of the adhesive shear stiffness (k_a), resulting a lower effective bond stiffness (k_e).

5.2.6.3 Transfer Length during the Epoxy Curing Time

This section aims to identify a time at which the epoxy adhesive provides the minimum structural requirements in terms of prestress transfer length to release the prestress force applied to the NSM CFRP reinforcement. For this period of time, the evolution of the elasticity modulus of the type of epoxy adhesive (E_a) adopted in the present experimental program can be obtained using Eq. (5.60) (Fernandes et al. 2015). Accordingly, the evolution of the shear modulus of the epoxy adhesive during this period can be obtained using Eq. (5.42) neglecting the influence of the evolution of the Poisson's ratio of the epoxy adhesive, as follows:

$$E_a(t) = E_a.e^{\left(-\frac{1}{2}\left(\frac{\omega}{t}\right)^{\alpha}\right)} \rightarrow G_a(t) = G_a.e^{\left(-\frac{1}{2}\left(\frac{\omega}{t}\right)^{\alpha}\right)} \tag{5.60}$$

where ω and α are shape parameter ($\omega = 12.926$) and time parameter ($\alpha = 2.779$), respectively. $E_a(t)$ and $G_a(t)$ are elasticity and shear modulus of the epoxy adhesive at a given time, t, from the onset of groove injection with epoxy ($t = 0$).

Hence, the effective bond stiffness ($k_e(t)$) can be derived using shear stiffness of the adhesive layer ($k_a(t)$) (with Eq. (5.41)) during the epoxy curing time, as follows:

$$k_a(t) = \frac{G_a.e^{\left(-\frac{1}{2}\left(\frac{\omega}{t}\right)^{\alpha}\right)}}{t_a} \rightarrow k_e(t) = \left(\frac{k_c}{1 + \frac{k_c}{k_a(t)}}\right) \tag{5.61}$$

Therefore, during the curing time of epoxy adhesive, the evolution of the prestress transfer length can be obtained by:

$$TL_{(ITM)}(t) = \frac{2}{B} \rightarrow B(t) = \left(\frac{2k_e(t)}{a_f.E_f}\right)^{0.5} \tag{5.62}$$

Figure 5-24a represents the evolution of the shear modulus during the hardening process of the epoxy adhesive in its curing time, resulting an increase of the effective bond stiffness during this period. The hardening of the epoxy adhesive during its curing time leads to a decrease of the prestress transfer length, as shown in Figure 5-24b.

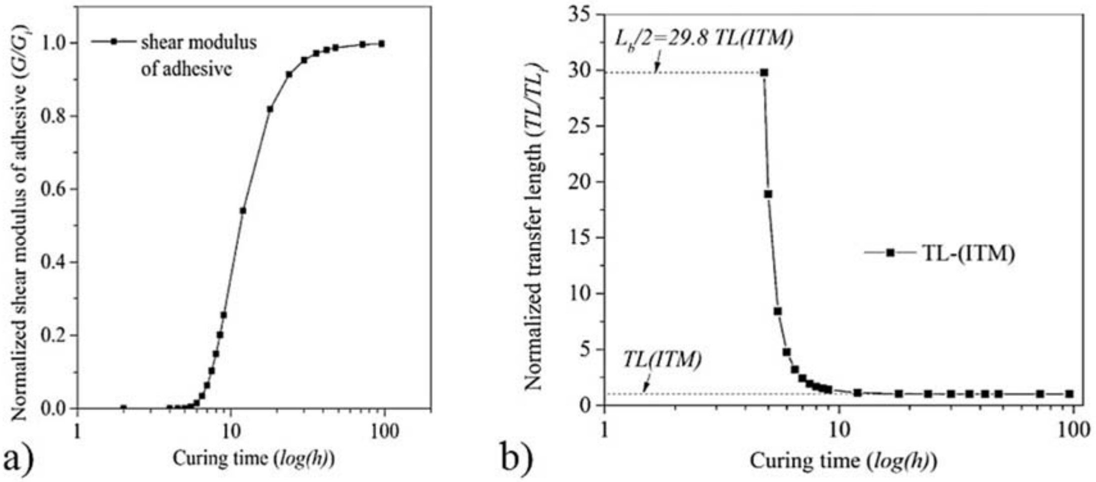

Figure 5-24: a) Shear modulus evolution of the epoxy adhesive during the curing time, b) prestress transfer length during the curing time

5.3 Conclusions

The current chapter aimed to propose analytical approaches, with a design framework, to predict first the flexural behavior of simply supported RC beams flexurally strengthened with prestressed CFRP reinforcements using either EBR or NSM techniques and then, the distribution of CFRP tensile strain and bond shear stress and, additionally, the prestress transfer length. The relevant developments were the following ones:

- An analytical approach was developed based on the strain compatibility and principles of static equilibrium to predict the moment-curvature and load-deflection relationships of simply supported beams strengthened with prestressed CFRP reinforcement that can be applied according to the EBR or NSM techniques. This formulation assumes that the moment-curvature response of a beam’s cross section can be simulated by a trilinear diagram defining precracking, postcracking, and postyielding stages. Two further stages are proposed, namely: concrete and steel decompression stages, to assess the initial effects of the prestress force applied by the CFRP reinforcement. A linear variation is assumed for the curvature along the beam length between the sections corresponding to the governing stages of the beam’s response in order to simplify the calculation of the beam’s deflection. The flexural capacity of the strengthened beams according to either EBR or NSM techniques is predicted adopting two types of failure modes, comprising yielding of the steel bars in tension followed by either concrete crushing or rupture of the CFRP reinforcement.

- For the NSM technique, a design framework methodology is proposed to obtain the ultimate flexural capacity of the NSM CFRP strengthened beams when failing by concrete cover delamination. Concrete cover delamination is predicted by assessing the possibility of occurring the concrete tensile fracture at the extremities of the CFRP reinforcement in comparison with debonding and rupture of the CFRP failure modes. Finally, the concrete cover delamination is adopted as prevailing failure of the strengthened beams when its ultimate flexural capacity is less than the one corresponding to the occurrence of the conventional flexural failure modes (concrete crushing or rupture of the CFRP reinforcement).
- The results of three experimental programs composed of RC beams strengthened with prestressed NSM CFRP reinforcement, failed by conventional flexural failure modes, were compared with the ones obtained by the proposed analytical approach, and a good predictive performance was determined. Moreover, the results in terms of moment-curvature and force-deflection relationships obtained with the proposed model and by using a computer package (DOCROS and Def-DOCROS software) based on a cross section layer model were compared. The results showed that the proposed analytical approach can accurately simulate the effect of the prestress force on the flexural behavior of the NSM CFRP strengthened beam (by introducing the concrete and steel decompression points as an initial condition to the concrete cracking and steel yielding initiation points of the non-prestressed strengthened beam) compared to the use of a cross section layer model.
- A methodology to obtain an upper limit of the prestress level that can be applied to the CFRP reinforcement is proposed in order to maintain a sufficient degree of the ductility for the prestressed strengthened beams, and a limit of 60% was determined.
- The predictive performance of the proposed methodology for concrete cover delamination failure was evaluated by considering the ultimate load carrying capacity of six NSM CFRP strengthened beams failed according to this failure mode. The proposed formulation provided a good estimate of the ultimate load carrying capacity for concrete cover delamination as prevailing failure mode, resulting the ratio of the analytical and experimental flexural capacity of the tested beams of a mean value and a standard deviation of 0.99 and 0.10, respectively. According to this proposed methodology, by increasing the unbonded length of the CFRP reinforcement at its extremities, the resistance to the occurrence of concrete cover delamination can decrease, while a higher concrete tensile strength and also, a higher concrete cover depth below the tensile steel bars can

increase this resistance. On the other side, this resistance is influenced by the distance between the two adjacent CFRPs, as well as distance between the lateral face of the beam's cross section and the nearest CFRP. Accordingly, by adopting a strengthening configuration for consecutive NSM CFRPs according to minimizing the interaction of the concrete tensile fracture of the adjacent CFRPs, can provide the maximum resistance to the occurrence of concrete cover delamination.

- Simple analytical equations are proposed to predict the distribution of CFRP tensile stress and bond shear stress along the NSM CFRP bonded length when the prestress force is released.
- An analytical formulation, with a design framework, is developed based on the closed form solution for the prediction of prestress transfer length by considering the influence of the effective parameters on this length.
- The results of two experimental programs composed of RC beams strengthened with prestressed NSM CFRP reinforcement, in terms of distribution of CFRP tensile strain and bond shear stress, and prestress transfer length, were compared with the ones obtained by the proposed analytical approach, and a good predictive performance was determined.
- From the analytical parametric studies, it was verified that by increasing the elasticity modulus of the concrete and epoxy adhesive, the prestress transfer length decreases and the bond shear stress increases, while the opposite occurs with the increase of the CFRP elasticity modulus. Moreover, by increasing the thickness of epoxy adhesive layer, the prestress transfer length increases. On the other side, the CFRP reinforcement with rectangular cross section requires a lower transfer length compared to the use of square cross section with equal cross sectional area. In other words, a higher width/height ratio (a_f / b_f) of the CFRP cross section increases the prestress transfer length.
- A formula is analytically proposed to predict the evolution of the prestress transfer length during the curing time of epoxy adhesive by inspired on the evolution of the elasticity modulus of epoxy adhesive during this period.

Chapter 6: Conclusions and Future Works

The current research mainly aimed to study the efficiency of NSM prestressing and NSM hybrid (combining non-prestressed and prestressed reinforcements in the same application) techniques using CFRP laminates for the flexural strengthening of RC beams. Moreover, the prestress transmission zone of NSM CFRP reinforcement after the total release of prestress force was determined. To attain comprehensive and complementary achievements in these fields, experimental, numerical, and analytical research was carried out. In this chapter, the main conclusions of this work and the recommendations for future research are presented.

6.1 Conclusions

6.1.1 Experimental Research

After the release of prestress force applied to the NSM CFRP laminate, the distribution of tensile strain in the extremity region of the CFRP bonded length varies from zero (at its end section) to its effective tensile strain during the prestress transmission zone, and reaches a plateau beyond this zone, while the bond shear stress starts from high value at the end of the CFRP bonded length and continues decreasing along the prestress transmission zone, and becomes approximately null after that. Moreover, although this bond shear stress increases with the prestress level applied to the NSM CFRP reinforcement, this prestress level has a negligible influence on the distribution of CFRP normalized tensile strain (divided by the applied prestrain).

After releasing the prestress force a negative camber is generated due to the negative bending moment caused by the eccentricity of this force in relation to the centroidal axis of the beam's cross section. This negative camber led to a decrease of tensile strain in the prestressed CFRP laminate, which represents the short-term prestress loss immediately after release. Furthermore, this prestress force created an initial compressive strain in the tensile steel reinforcement and surrounding concrete, which led to an increase of the load carrying capacity at concrete cracking and steel yielding initiations, as well as an enhancement in terms of load carrying capacity at serviceability limit state conditions. However, the ultimate deflection of the beams strengthened with NSM prestressing technique decreased with the increase of applied prestress level. These results, which imply a decrease of the ductility index with the prestress level, suggest the adoption of an upper limit of the prestress level to be applied to the CFRP laminates in order do not compromise the ductility performance of the RC beams strengthened according to the NSM prestressing technique. On the other side, by increasing the prestress level, the cracked zone length and average crack width decrease compared to the passive strengthened beam.

The higher strengthening ratio adopted in the NSM hybrid technique led to an increase of load carrying capacity at concrete cracking, SLS conditions, steel yield initiation, and ultimate stage, as well as a decrease of average crack width when compared to the use of NSM prestressing technique for the flexural strengthening of RC beams. Moreover, the results showed that both prestressing and hybrid techniques decrease the possibility of the concrete crushing as prevailing failure mode of the strengthened beams. On the other hand, reduction of the ultimate deflection capacity of the beams strengthened with NSM prestressing technique was observed with the increase of the prestress level, resulting a decrease in terms of energy absorption and deformability indexes, while the aforementioned indicators for the hybrid NSM CFRP beams were influenced by the type of prevailing failure mode at the maximum capacity. The hybrid strengthened beam, failed by the rupture of the prestressed CFRP at the maximum capacity, showed a higher energy absorption and deformability indexes compared to the beams strengthened with NSM prestressing technique with similar prestress level.

6.1.2 Numerical Analysis

A 3D nonlinear FE approach simulating both concrete-epoxy adhesive and laminate-epoxy adhesive interfaces, as well as, the relevant nonlinear behavior of the intervening materials, and the prestress process adopted in the test setup, was developed, and its good predictive performance was demonstrated. This modelling strategy can be used to design the type of structures investigated in the present work.

The numerical analysis evidenced that the possibility of occurring the concrete cover delamination (as a premature failure model before the rupture of the CFRP) is highly dependent to the NSM CFRP development length in shear span of the strengthened beam. Accordingly, to decrease the susceptibility to the concrete cover delamination failure, the CFRP bonded length should be extended as much as possible close to the support.

Moreover, this analysis showed that by increasing the passive CFRP strengthening ratio in the hybrid system, a higher energy absorption and deformability indexes can be achieved for the hybrid strengthened beams when the rupture of the prestressed CFRPs occurs before the premature failure modes at the maximum capacity.

6.1.3 Analytical Approaches

An analytical approach was developed based on the strain compatibility and principles of static equilibrium to predict the moment-curvature and load-deflection relationships of RC beams strengthened with prestressed CFRP reinforcement that can be applied according to the EBR or NSM techniques. This approach considers two types of failure modes, comprising yielding of the steel bars in tension followed by either concrete crushing or rupture of the CFRP reinforcement. The developed formulation assumes that the moment-curvature response of a beam's cross section can be simulated by a trilinear diagram defining precracking, postcracking, and postyielding stages. Two further stages are proposed, namely: concrete and steel decompression stages, in order to assess the initial effects of the prestress force applied by the CFRP reinforcement. A good predictive performance of the model was demonstrated by simulating the tests executed in the experimental programs. The predictive performance was also assessed by comparing the moment-curvature and force-deflection relationships obtained with the developed model and using a computer package based on a cross section layer model. Moreover, a methodology to obtain an upper limit of the prestress level that can be applied to the CFRP reinforcement is proposed in order to maintain a sufficient degree of ductility for the prestressed strengthened beams, and a limit of 60% was determined.

In the case of the NSM technique, a design framework methodology is proposed to obtain the ultimate flexural capacity of the NSM CFRP strengthened beams when failing by concrete cover delamination, and its good predictive performance was determined. Concrete cover delamination is predicted by assessing the possibility of occurring the concrete tensile fracture at the extremities of the CFRP reinforcement in comparison with debonding and rupture of the CFRP failure modes. Finally, the concrete cover delamination is adopted as prevailing failure of the strengthened beams when its ultimate flexural capacity is less than the one corresponding to the occurrence of the conventional flexural failure modes (concrete crushing or rupture of the CFRP reinforcement). According to this proposed methodology, by decreasing the bonded length of the CFRP reinforcement, the resistance to the occurrence of concrete cover delamination can decrease, while a higher concrete tensile strength, and also a higher concrete cover depth below the tensile steel bars can increase this resistance. On the other side, this resistance is influenced by the distance between the two adjacent CFRPs, as well as the distance between the lateral face of the beam's cross section and the nearest CFRP. Accordingly, by adopting a strengthening configuration for consecutive NSM CFRPs according to minimizing the interaction of the concrete tensile fracture of the adjacent CFRPs, can provide the maximum resistance to the occurrence of concrete cover delamination.

Closed form analytical formulations were developed to predict the distribution of CFRP tensile stress and bond shear stress along the NSM CFRP bonded length, as well as the prestress transfer length when the prestress force is released, and a good predictive performance of these analytical formulations was determined. The analytical parametric studies showed that by increasing the elasticity modulus of the concrete and epoxy adhesive, the prestress transfer length decreases and the bond shear stress increases, while the opposite occurs with the increase of the CFRP elasticity modulus. Moreover, by increasing the thickness of epoxy adhesive layer, the prestress transfer length increases. On the other side, the CFRP reinforcement with rectangular cross section requires a lower transfer length compared to the use of square cross section with equal cross sectional area. In other words, a higher width/height ratio of the CFRP cross section increases the prestress transfer length. Besides, the analytical model offers a formula to predict the evolution of the prestress transfer length during the curing time of epoxy adhesive.

6.2 Recommendations for Future Works

In the following, some recommendations are proposed for a deeper knowledge on the areas treated in this document, as well as to use and extend the developed scientific patrimony to other areas where its seems possible to apply with technical and economic advantages:

- Evaluation of the influence of prestress level on the flexural performance of continuous RC beams and slabs strengthened with NSM CFRP reinforcement applied not only in the intermediate support (hogging region), but also in the positive bending moment zones (sagging regions), is an interesting issue that needs to be investigated experimentally and numerically.
- Influence of the prestress level on the bond behavior of CFRP-epoxy-concrete connections of NSM CFRP technique needs to be experimentally and numerically investigated.
- The effectiveness of prestress level applied to the NSM CFRP reinforcement on the possibility of occurring concrete cover delamination as a prevailing failure mode of NSM CFRP strengthened beams should be evaluated.
- In order to provide a higher resistance to the susceptibility of concrete cover delamination for the NSM hybrid strengthened beams, the efficiency of applying vertical CFRP sheets at the extremity zones of non-prestressed CFRP laminates (where the concrete cover delamination failure was observed in the tested hybrid beams) for the NSM hybrid technique should be experimentally investigated.
- The potentialities of the proposed NSM hybrid technique for the flexural strengthening of RC slabs should be experimentally evaluated.
- Flexural performance of RC structures strengthened with EBR hybrid technique combining non-prestressed and prestressed CFRP sheets in the same application should be experimentally assessed.

- For the NSM hybrid technique, the bond behavior of a set of non-prestressed and prestressed CFRP reinforcements in the same groove should be assessed and compared to the bond behavior of only one laminate per groove.
- The influence of the bonded length of non-prestressed CFRP laminate in the NSM hybrid technique on the flexural performance of the strengthened beam needs to be studied.
- A 3D nonlinear FE model capable of simulating the release rate of the prestress force needs to be developed to evaluate the influence of this release rate on the transmission zone of the prestressed CFRP reinforcement.
- An analytical approach capable of considering the shear stress-slip relationships of the bond between CFRP and concrete can be developed to predict the prestress transfer length.

Appendix

Appendix A

Distance from the centroidal axis of beam cross section (y_i) and moment of inertia of uncracked section (I_{ucr}) can be obtained using the concept of transformed cross section as follows (Figure A-1):

$$y_i = \frac{\sum_{i=1}^{n} A_i.d_i}{\sum_{i=1}^{n} A_i} = \frac{b.h^2/2 - A_{groove}.d_f + A_s^{'}.(n_s-1).d_s^{'} + A_s.(n_s-1).d_s + A_f.n_f.d_f}{b.h - A_{groove} + A_s^{'}.(n_s-1) + A_s.(n_s-1) + A_f.n_f} \tag*{(A1)-a}$$

$$\begin{aligned} I_{ucr} = \frac{1}{12}.b.h^3 + b.h.\left(y_i - \frac{h}{2}\right)^2 - A_{groove}.\left(d_f - y_i\right)^2 + A_s^{'}.(n_s-1).\left(y_i - d_s^{'}\right)^2 \\ + A_s.(n_s-1).\left(d_s - y_i\right)^2 + A_f.n_f.\left(d_f - y_i\right)^2 \end{aligned} \tag*{(A1)-b}$$

where A_{groove} is area of the groove for NSM technique, n_s and n_f are the modular ratio of steel ($n_s = E_s/E_c$) and CFRP ($n_f = E_f/E_c$) reinforcements to concrete, respectively.

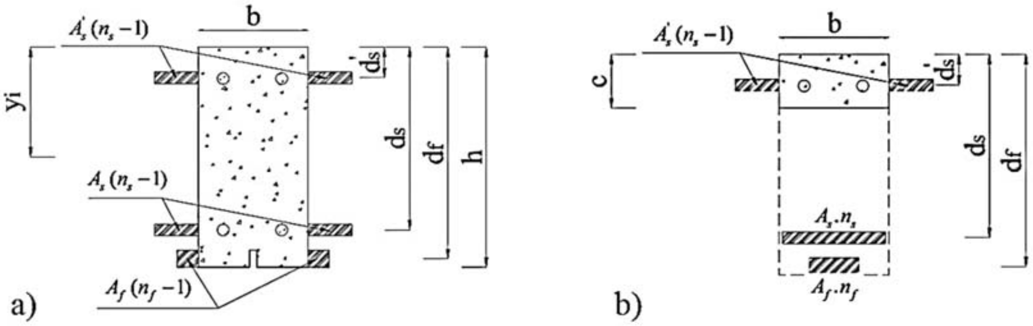

Figure A-1: Transformed cross section for: a) uncracked section, b) cracked section

Tensile strain at the top fiber ($\varepsilon_{cc}^{(ci)}$) and compressive strain at the bottom fiber ($\varepsilon_{ct}^{(ci)}$) of concrete are:

$$\varepsilon_{cc}^{(ci)} = \frac{\left(\left(\frac{F_{pre}.e.y_i}{I_{ucr}}\right) - \left(\frac{F_{pre}}{b.h}\right)\right)}{E_c} \tag*{(A1)-c}$$

$$\varepsilon_{ct}^{(ci)} = \frac{\left(\left(\frac{F_{pre}.e.(h-y_i)}{I_{ucr}}\right)+\left(\frac{F_{pre}}{b.h}\right)\right)}{E_c} \tag{A1-d}$$

In fact, due to the short-term prestrain loss in the CFRP reinforcement ($\varepsilon_{ef}^{(ci)}$ obtained from Eq. (5.4)) after the release of the prestress force, effective prestress force ($F_{epre} = E_f.\varepsilon_{ef}^{(ci)}.A_f$) should be used in Eqs. (A1)-c and (A1)-d instead of the applied prestress force ($F_{pre} = E_f.\varepsilon_{fp}.A_f$), while the effect of this short-term prestrain loss was neglected to determine the tensile strain at the top fiber and compressive strain at the bottom fiber of concrete in order to simplify the calculation procedure.

Strains in the compressive and tensile steel bars can be obtained by:

$$\varepsilon_s^{'(ci)} = \frac{\varepsilon_{cc}^{(ci)}.\left(c^{(ci)} - d_s^{'}\right)}{c^{(ci)}} \tag{A2-a}$$

$$\varepsilon_s^{(ci)} = \frac{\varepsilon_{cc}^{(ci)}.\left(d_s - c^{(ci)}\right)}{c^{(ci)}} \tag{A2-b}$$

It should also be noted that Eqs. (A1)-c to (A2)-b are derived by assuming no cracking occurs after the release of the prestress force (Figure 5-3 and Figure A-2).

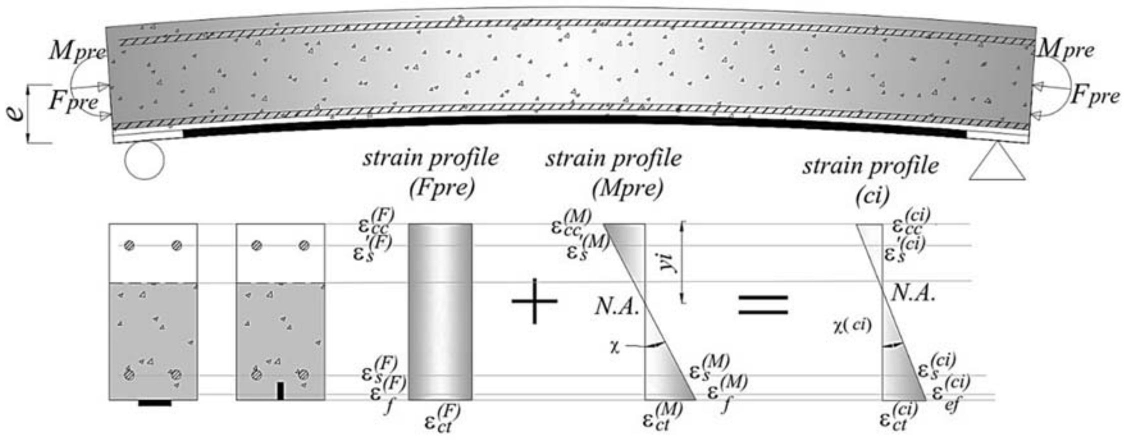

Figure A-2: Strain profile of the prestressed section at initial curvature (ci)

Appendix B

Strains in the constituent materials along the depth of the cross section (longitudinal top ($\varepsilon_s^{'}$) and bottom (ε_s) steel bars, CFRP reinforcement (ε_f), and bottom fiber of concrete (ε_{ct})) at concrete decompression (cd) and steel decompression (sd) points are:

$$\varepsilon_s^{'(cd)} = \frac{\varepsilon_{cc}^{(cd)}.\left(h-d_s^{'}\right)}{h} \tag{A3)-a}$$

$$\varepsilon_s^{(cd)} = \frac{\varepsilon_{cc}^{(cd)}.\left(h-d_s\right)}{h} \tag{A3)-b}$$

$$\varepsilon_f^{(cd)} = \frac{\varepsilon_{cc}^{(cd)}.\left(h-d_f\right)}{h} \tag{A3)-c}$$

$$\varepsilon_s^{'(sd)} = \frac{\varepsilon_{cc}^{(sd)}.\left(d_s-d_s^{'}\right)}{d_s} \tag{A4)-a}$$

$$\varepsilon_{ct}^{(sd)} = \frac{\varepsilon_{cc}^{(sd)}.\left(h-d_s\right)}{d_s} \tag{A4)-b}$$

$$\varepsilon_f^{(sd)} = \frac{\varepsilon_{cc}^{(sd)}.\left(d_f-d_s\right)}{d_s} \tag{A4)-c}$$

Effective tensile strains for the prestressed CFRP reinforcements are as follows:

$$\varepsilon_{ef}^{(cd)} = \varepsilon_{fp} + \varepsilon_f^{(cd)} \tag{A5)-a}$$

$$\varepsilon_{ef}^{(sd)} = \varepsilon_{fp} + \varepsilon_f^{(sd)} \tag{A5)-b}$$

Both concrete and steel decompression points are assumed to occur before the concrete crack initiation point by considering an uncracked section (Figure 5-3 and Figure A-3).

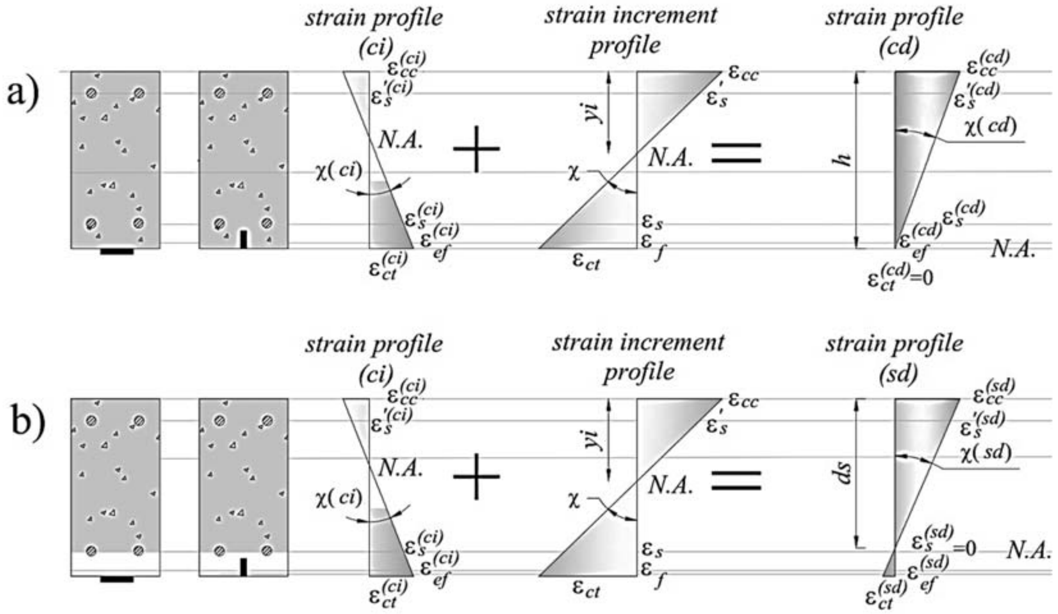

Figure A-3: Strain profile of the cross section: a) at concrete decompression point (cd), b) at steel decompression point (sd)

Appendix C

$$\varepsilon_{ctb}^{(cr)} = \varepsilon_{ct} = \frac{f_r}{E_c} \rightarrow \varepsilon_{ccb}^{(cr)} = \frac{\varepsilon_{ctb}^{(cr)}.y_i}{(h - y_i)} \tag{A6-a}$$

Strain components of the longitudinal steel bars in compression ($\varepsilon_{sb}^{'(cr)}$) and in tension ($\varepsilon_{sb}^{(cr)}$), and CFRP reinforcement ($\varepsilon_{fb}^{(cr)}$) can be obtained by:

$$\varepsilon_{sb}^{'(cr)} = \frac{\varepsilon_{ccb}^{(cr)}.(y_i - d_s^{'})}{y_i} \tag{A6-b}$$

$$\varepsilon_{sb}^{(cr)} = \frac{\varepsilon_{ccb}^{(cr)}.(d_s - y_i)}{y_i} \tag{A6-c}$$

$$\varepsilon_{fb}^{(cr)} = \frac{\varepsilon_{ccb}^{(cr)}.(d_f - y_i)}{y_i} \tag{A6-d}$$

Uncracked section was assumed to determine Eqs. (A6)-a to (A6)-d (Figure 5-2a and Figure 5-3).

Appendix D

By adopting the principles of static equilibrium at the steel yield initiation point (Figure 5-2b):

$$\frac{1}{2}\varepsilon_{ccb}^{(y)}.E_c.c_b^{(y)}.b+A_s^{'}.\varepsilon_{sb}^{'(y)}.E_s-A_s.\varepsilon_{sb}^{(y)}.E_s-A_f.\varepsilon_{fb}^{(y)}.E_f=0 \qquad \text{(A7)}$$

where compressive strains at the top fiber of concrete ($\varepsilon_{ccb}^{(y)}$) and longitudinal top steel bars ($\varepsilon_{sb}^{'(y)}$), and tensile strain in the CFRP reinforcement ($\varepsilon_{fb}^{(y)}$) can be obtained by:

$$\varepsilon_{ccb}^{(y)}=\frac{\varepsilon_{sb}^{(y)}.c_b^{(y)}}{\left(d_s-c_b^{(y)}\right)} \qquad \text{(A8)-a}$$

$$\varepsilon_{sb}^{'(y)}=\frac{\varepsilon_{sb}^{(y)}.\left(c_b^{(y)}-d_s^{'}\right)}{\left(d_s-c_b^{(y)}\right)}\leq\varepsilon_{sy} \qquad \text{(A8)-b}$$

$$\varepsilon_{fb}^{(y)}=\frac{\varepsilon_{sb}^{(y)}.\left(d_f-c_b^{(y)}\right)}{\left(d_s-c_b^{(y)}\right)} \qquad \text{(A8)-c}$$

By substituting Eqs. (A8-a) to (A8-c) into Eq. (A7) yields:

$$\frac{1}{2}.\left(\frac{\varepsilon_{sb}^{(y)}.c_b^{(y)}}{\left(d_s-c_b^{(y)}\right)}\right).E_c.c_b^{(y)}.b+A_s^{'}.\left(\frac{\varepsilon_{sb}^{(y)}.\left(c_b^{(y)}-d_s^{'}\right)}{\left(d_s-c_b^{(y)}\right)}\right).E_s-A_s.\varepsilon_{sb}^{(y)}.E_s-A_f.\left(\frac{\varepsilon_{sb}^{(y)}.\left(d_f-c_b^{(y)}\right)}{\left(d_s-c_b^{(y)}\right)}\right).E_f=0 \qquad \text{(A9)-a}$$

By rewiring Eq. (A9-a), Eq. (A9-b) is obtained to calculate the neutral axis depth ($c_b^{(y)}$) at the steel yield initiation stage:

$$\frac{\varepsilon_{sb}^{(y)}.\left((E_c.c_b^{(y)2}.b+2.A_s^{'}.E_s.\left(c_b^{(y)}-d_s^{'}\right)-2.A_f.E_f.\left(d_f-c_b^{(y)}\right)\right)}{2.\left(d_s-c_b^{(y)}\right)}=A_s.\varepsilon_{sb}^{(y)}.E_s \qquad \text{(A9)-b}$$

$$\rightarrow\ (E_c.b).c_b^{(y)2}+2.(A_s^{'}.E_s+A_s.E_s+A_f.E_f)c_b^{(y)}-2(A_s^{'}.E_s.d_s^{'}+A_s.E_s.d_s+A_f.E_f.d_f)=0$$

The equations represented in this section are determined by assuming a cracked section, and also the resistance of concrete in tension is neglected (Figure 5-2b and Figure 5-3).

Appendix E

The critical percentage of CFRP reinforcement ($\rho_f^{(cri)}$) can be determined assuming simultaneous tension and compression failures (Figure A-4a):

$$\alpha_1.f_c^{'}.\beta_1.c^{(cri)}.b+A_s^{'}.\varepsilon_s^{'(cri)}.E_s-A_s.f_{sy}-A_f^{(cri)}.\varepsilon_{fu}.E_f=0 \tag{A10}$$

where the neural axis depth ($c^{(cri)}$) and strain components in the longitudinal top ($\varepsilon_s^{'(cri)}$) and bottom ($\varepsilon_s^{(cri)}$) steel bars at simultaneous tension and compression failures are:

$$c^{(cri)}=\frac{d_f.\varepsilon_{cu}}{((\varepsilon_{fu}-\varepsilon_{fp})+\varepsilon_{cu})} \tag{A11}$$

$$\varepsilon_s^{'(cri)}=\frac{\varepsilon_{cu}.\left(c^{(cri)}-d_s^{'}\right)}{c^{(cri)}}\leq\varepsilon_{sy}\quad if\ not\ \rightarrow\varepsilon_s^{'(cri)}.E_s=f_{sy} \tag{A12)-a}$$

$$\varepsilon_s^{(cri)}=\frac{\varepsilon_{cu}\left(d_s-c^{(cri)}\right)}{c^{(cri)}}\geq\varepsilon_{sy}\rightarrow\varepsilon_s^{(cri)}.E_s=f_{sy} \tag{A12)-b}$$

The equations of this section are derived by assuming a cracked section, and also the resistance of concrete in tension is neglected (Figure 5-3 and Figure A-4a).

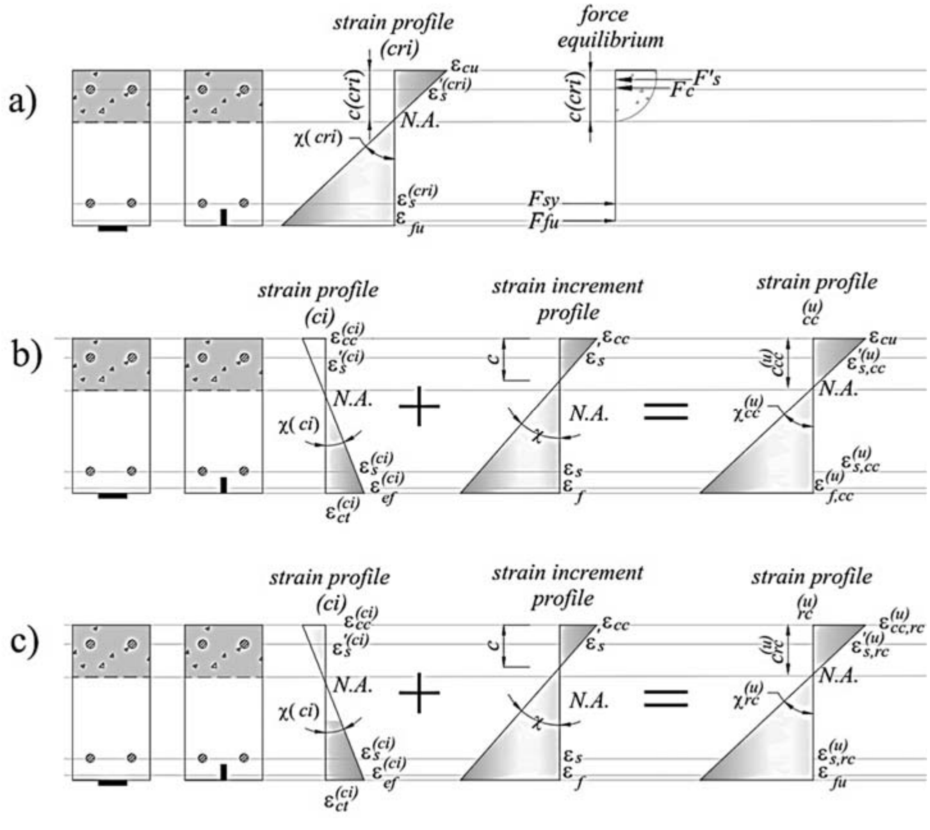

Figure A-4: Strain profile of the cross section, a) simultaneous tension and compression failures (cri), b) compression failure (cc), c) tension failure (rc)

Concrete Crushing

From the strain profile of the cross section when the concrete crushing occurs (Figure A-4b):

$$\alpha_1 . f_c^{'} . \beta_1 . c_{\mathrm{cc}}^{(u)} . b + A_s^{'} . \varepsilon_{s,cc}^{'(u)} . E_s - A_s . f_{sy} - A_f . E_f . \varepsilon_{f,cc}^{(u)} = 0 \qquad \text{(A13)}$$

where compressive strains in the longitudinal top steel bars ($\varepsilon_{s,cc}^{'(u)}$), and tensile strain in the CFRP reinforcement ($\varepsilon_{fb,cc}^{(u)}$) can be obtained from the following equations:

$$\varepsilon_{s,cc}^{'(u)} = \frac{\varepsilon_{cu} . \left(c_{\mathrm{cc}}^{(u)} - d_s^{'} \right)}{c_{\mathrm{cc}}^{(u)}} \le \varepsilon_{sy} \quad \textit{if not} \rightarrow \varepsilon_{s,cc}^{'(u)} . E_s = f_{sy} \qquad \text{(A14)-a}$$

$$\varepsilon_{fb,cc}^{(u)} = \frac{\left(d_f - c_{\mathrm{cc}}^{(u)} \right) . \varepsilon_{cu}}{c_{\mathrm{cc}}^{(u)}} \rightarrow \varepsilon_{f,cc}^{(u)} = \varepsilon_{fb,cc}^{(u)} + \varepsilon_{fp} \le \varepsilon_{fu} \qquad \text{(A14)-b}$$

Substituting Eqs. (A14-a) and (A14-b) and Eqs. (5.1-a) and (5.1-b) into Eq. (A13) results:

$$\left(\frac{3.\varepsilon_c^{'} . \varepsilon_{cu} - \varepsilon_{cu}^{\ 2}}{3.\beta_1 \varepsilon_c^{'2}} \right) . f_c^{'} . \left(\frac{4.\varepsilon_c^{'} - \varepsilon_{cu}}{6.\varepsilon_c^{'} - 2.\varepsilon_{cu}} \right) . c_{\mathrm{cc}}^{(u)} . b + A_s^{'} . \left(\frac{\varepsilon_{cu} . \left(c_{\mathrm{cc}}^{(u)} - d_s^{'} \right)}{c_{\mathrm{cc}}^{(u)}} \right) . E_s - A_s . f_{sy} - A_f . E_f . \left(\frac{\left(d_f - c_{\mathrm{cc}}^{(u)} \right) . \varepsilon_{cu}}{c_{\mathrm{cc}}^{(u)}} + \varepsilon_{fp} \right) = 0 \qquad \text{(A15)-a}$$

Rewiring Eq. (A15-a), Eq. (A15-b) is obtained to determine the neutral axis depth ($c_{cc}^{(u)}$) at failure:

$$\left(\frac{3.\varepsilon_c^{'} . \varepsilon_{cu} - \varepsilon_{cu}^{\ 2}}{3.\varepsilon_c^{'2}} \right) . f_c^{'} . c_{\mathrm{cc}}^{(u)} . b + A_s^{'} . \left(\frac{\varepsilon_{cu} . \left(c_{\mathrm{cc}}^{(u)} - d_s^{'} \right)}{c_{\mathrm{cc}}^{(u)}} \right) . E_s - A_f . E_f . \left(\frac{\left(d_f - c_{\mathrm{cc}}^{(u)} \right) . \varepsilon_{cu}}{c_{\mathrm{cc}}^{(u)}} + \varepsilon_{fp} \right) = A_s . f_{sy}$$

$$\rightarrow \left(\frac{3.\varepsilon_c^{'} . \varepsilon_{cu} - \varepsilon_{cu}^{\ 2}}{3.\varepsilon_c^{'2}} \right) . f_c^{'} . c_{\mathrm{cc}}^{(u)} . b + A_s^{'} . \left(\frac{\varepsilon_{cu} . \left(c_{\mathrm{cc}}^{(u)} - d_s^{'} \right)}{c_{\mathrm{cc}}^{(u)}} \right) . E_s - A_f . E_f . \left(\frac{\left(d_f - c_{\mathrm{cc}}^{(u)} \right) . \varepsilon_{cu}}{c_{\mathrm{cc}}^{(u)}} \right) = A_s . f_{sy} + A_f . E_f . \varepsilon_{fp}$$

$$\rightarrow \frac{f_c^{'} . c_{\mathrm{cc}}^{(u)2} . b . (3.\varepsilon_c^{'} . \varepsilon_{cu} - \varepsilon_{cu}^{\ 2}) + A_s^{'} . E_s . 3.\varepsilon_c^{'2} . \varepsilon_{cu} . \left(c_{\mathrm{cc}}^{(u)} - d_s^{'} \right) - A_f . E_f . 3.\varepsilon_c^{'2} . \varepsilon_{cu} . \left(d_f - c_{\mathrm{cc}}^{(u)} \right)}{3.\varepsilon_c^{'2} . c_{\mathrm{cc}}^{(u)}} = A_s . f_{sy} + A_f . E_f . \varepsilon_{fp} \qquad \text{(A15)-b}$$

$$\rightarrow \left(f_c^{'} . b . \left(3.\varepsilon_c^{'} . \varepsilon_{cu} - \varepsilon_{cu}^{2} \right) \right) . c_{\mathrm{cc}}^{(u)2} + \left(3.\varepsilon_c^{'2} . \left(\varepsilon_{cu} . \left(E_s . A_s^{'} + E_f . A_f \right) - A_s . f_{sy} - E_f . A_f . \varepsilon_{fp} \right) \right) . c_{\mathrm{cc}}^{(u)}$$

$$- \left(3.\varepsilon_c^{'2} . \varepsilon_{cu} . \left(E_s . A_s^{'} . d_s^{'} + E_f . A_f . d_f \right) \right) = 0$$

Rupture of CFRP Reinforcement

The equilibrium of the internal forces, when the rupture of the CFRP reinforcement occurs, results in the following equation (Figure A-4c):

$$\alpha_1.f_c^{'}.\beta_1.c_{rc}^{(u)}.b+A_s^{'}.\varepsilon_{s,rc}^{'(u)}.E_s-A_s.f_{sy}-A_f.f_{fu}=0 \tag{A16}$$

where compressive strains at the top fiber of concrete ($\varepsilon_{cc,rc}^{(u)}$) and in the longitudinal top steel bars ($\varepsilon_{s,rc}^{'(u)}$), and tensile strain in the CFRP reinforcement ($\varepsilon_{fb,rc}^{(u)}$) can be obtained by:

$$\varepsilon_{cc,rc}^{(u)}=\frac{\varepsilon_{fb,rc}^{(u)}.c_{rc}^{(u)}}{\left(d_f-c_{rc}^{(u)}\right)} \tag{A17)-a}$$

$$\varepsilon_{fb,rc}^{(u)}=\varepsilon_{fu}-\varepsilon_{fp} \tag{A17)-b}$$

$$\varepsilon_{s,rc}^{'(u)}=\frac{\varepsilon_{fb,rc}^{(u)}.\left(c_{rc}^{(u)}-d_s^{'}\right)}{\left(d_f-c_{rc}^{(u)}\right)}\leq\varepsilon_{sy}\quad if\ not\rightarrow\varepsilon_{s,rc}^{'(u)}.E_s=f_{sy} \tag{A18}$$

Substituting Eqs. (A17-a) to (A18) and Eqs. (5.1-a) and (5.1-b) into Eq. (A16) yields:

$$\left(\frac{3.\varepsilon_c^{'}.\varepsilon_{cc,rc}^{(u)}-\varepsilon_{cc,rc}^{(u)2}}{3.\beta_1\varepsilon_c^{'2}}\right).f_c^{'}.\left(\frac{4.\varepsilon_c^{'}-\varepsilon_{cc,rc}^{(u)}}{6.\varepsilon_c^{'}-2.\varepsilon_{cc,rc}^{(u)}}\right).c_{rc}^{(u)}.b+A_s^{'}.\left(\frac{\varepsilon_{fb,rc}^{(u)}.\left(c_{rc}^{(u)}-d_s^{'}\right)}{\left(d_f-c_{rc}^{(u)}\right)}\right).E_s-A_s.f_{sy}-A_f.f_{fu}=0 \tag{A19)-a}$$

Rewiring Eq. (A19-a), Eq. (A19-b) leads the depth of the neutral axis at ultimate stage ($c_{rc}^{(u)}$):

$$\left(\frac{3.\varepsilon_c^{'}.\varepsilon_{cc,rc}^{(u)}-\varepsilon_{cc,rc}^{(u)2}}{3.\varepsilon_c^{'2}}\right).f_c^{'}.c_{rc}^{(u)}.b+A_s^{'}.\left(\frac{\varepsilon_{fb,rc}^{(u)}.\left(c_{rc}^{(u)}-d_s^{'}\right)}{\left(d_f-c_{rc}^{(u)}\right)}\right).E_s-A_s.f_{sy}-A_f.f_{fu}=0$$

$$\rightarrow\left(\frac{3.\varepsilon_c^{'}.\frac{\varepsilon_{fb,rc}^{(u)}.c_{rc}^{(u)}}{\left(d_f-c_{rc}^{(u)}\right)}-\left(\frac{\varepsilon_{fb,rc}^{(u)}.c_{rc}^{(u)}}{\left(d_f-c_{rc}^{(u)}\right)}\right)^2}{3.\varepsilon_c^{'2}}\right).f_c^{'}.c_{rc}^{(u)}.b+A_s^{'}.\left(\frac{\varepsilon_{fb,rc}^{(u)}.\left(c_{rc}^{(u)}-d_s^{'}\right)}{\left(d_f-c_{rc}^{(u)}\right)}\right).E_s=A_s.f_{sy}+A_f.f_{fu}$$

$$\rightarrow\left(\frac{3.\varepsilon_c^{'}.\varepsilon_{fb,rc}^{(u)}.c_{rc}^{(u)}.\left(d_f-c_{rc}^{(u)}\right)-(\varepsilon_{fb,rc}^{(u)}.c_{rc}^{(u)})^2}{3.\varepsilon_c^{'2}.\left(d_f-c_{rc}^{(u)}\right)^2}\right).f_c^{'}.c_{rc}^{(u)}.b+A_s^{'}.\left(\frac{\varepsilon_{fb,rc}^{(u)}.\left(c_{rc}^{(u)}-d_s^{'}\right)}{\left(d_f-c_{rc}^{(u)}\right)}\right).E_s=A_s.f_{sy}+A_f.f_{fu}$$

$$\rightarrow\frac{\left(3.\varepsilon_c^{'}.\varepsilon_{fb,rc}^{(u)}.c_{rc}^{(u)}.\left(d_f-c_{rc}^{(u)}\right)-(\varepsilon_{fb,rc}^{(u)}.c_{rc}^{(u)})^2\right).f_c^{'}.c_{rc}^{(u)}.b+A_s^{'}.E_s.3.\varepsilon_c^{'2}.\varepsilon_{fb,rc}^{(u)}.\left(c_{rc}^{(u)}-d_s^{'}\right).\left(d_f-c_{rc}^{(u)}\right)}{3.\varepsilon_c^{'2}.\left(d_f-c_{rc}^{(u)}\right)^2}=A_s.f_{sy}+A_f.f_{fu}$$

$$\rightarrow\varepsilon_{fb,rc}^{(u)}.f_c^{'}.b.\left(3.\varepsilon_c^{'}+\varepsilon_{fb,rc}^{(u)}\right).c_{rc}^{(u)3}+3.\varepsilon_c^{'}.\left(\varepsilon_{fb,rc}^{(u)}.(\varepsilon_c^{'}.E_s.A_s^{'}-f_c^{'}.b.d_f)+\varepsilon_c^{'}.\left(A_f.f_{fu}+A_s.f_{sy}\right)\right).c_{rc}^{(u)2}$$
$$-3.\varepsilon_c^{'2}.\left(\varepsilon_{fb,rc}^{(u)}.E_s.A_s^{'}.\left(d_f+d_s^{'}\right)+2.d_f.\left(A_f.f_{fu}+A_s.f_{sy}\right)\right).c_{rc}^{(u)}+3.\varepsilon_c^{'2}.d_f.\left(\varepsilon_{fb,rc}^{(u)}.E_s.A_s^{'}.d_s^{'}+d_f.\left(A_f.f_{fu}+A_s.f_{sy}\right)\right)=0 \tag{A19)-b}$$

References

ABAQUS. (2011). Abaqus Analysis User's Manual.

Abdelatif, A., Owen, J., and Hussein, M. (2014). Modelling the Prestress Transfer in Pre-tensioned Concrete Elements. *Finite Elements in Analysis and Design,* 94: 47-63.

ACI-318-05. (2005). Building Code Requirements for Structural Concrete. *American Concrete Institute (ACI) Committee 318*.

ACI-318-08. (2008). Building Code Requirements for Structural Concrete. *American Concrete Institute (ACI) Committee 318*.

ACI-440.1R. (2001). Guide for the Design and Construction of Concrete Reinforced with FRP Bars, *American Concrete Institute (ACI) Committee 440*.

ACI-440.1R. (2006). Guide for the Design and Construction of Structural Concrete Reinforced with FRP Bars. *American Concrete Institute (ACI) Committee 440.*

ACI-440.2R. (2008). Guide for the Design and Construction of Externally Bonded FRP Systems for Strengthening Concrete Structures. *American Concrete Institute (ACI) Committee 440.*

Akmaluddin, P. (2012). Effective Moment of Inertia Approach for Predicting Deflection of Concrete Beams Reinforced with Twisted Bamboo Cable. *International Journal of Civil & Environmental Engineering (IJCEE),* 12(3): 6-13.

Al-Mahmoud, F., Castel, A., Francois, R., and Tourneur, C. (2009). Strengthening of RC Members with Near-Surface-Mounted CFRP Rods. *Composite Structures,* 91.

Al-Mahmoud, F., Castel, A., Francois, R., and Tourneur, C. (2010). RC Beams Strengthened with NSM CFRP Rods and Modeling of Peeling-off Failure. *Composite Structures,* 92.

Alwis, W. (1990). Trilinear Moment-Curvature Relationship for Reinforced Concrete Beams. *ACI Structural Journal*, 8.

Badawi, M., and Soudki, K. (2009). Flexural Strengthening of RC Beams with Prestressed NSM CFRP Rods- Experimental and Analytical Investigation. *Construction and Building Materials*, 3292-3300.

Badawi, M., Wahab, N., and Soudki, K. (2010). Evaluation of the Transfer Length of Prestressed Near Surface Mounted CFRP Rods in Concrete. *Construction and Building Materials*, 25: 1474-1479.

Barros, J. (2009). Pre-Stress Technique for the Flexural Strengthening with NSM-CFRP Strips. *9th International Symposium on Fiber Reinforced Polymer Reinforcement for Concrete Structures*, Sydney, Australia.

Barros, J., and Dalfre, G. (2013). A Model for the Prediction of the Behaviour of Countinuous RC Slabs Flexurally Strengthened with CFRP Systems. *11th International Symposium on Fiber Reinforced Polymer Reinforcement for Concrete Structures,* Guimaraes, Portugal.

Barros, J., and Fortes, A. (2005). Flexural Strengthening of Concrete Beams with CFRP Laminates Bonded into Slits. *Cement and Concrete Composites,* 27(4) p: 471-480.

Barros, J., and Kotynia, R. (2008). Possibilities and Challenges of NSM for the Flexural Strengthening of RC Structures. *4th International Conference on FRP Composites in Civil Engineering* Zurich, Switzerland.

Barros, J., Costa, I., and Gouveia, A. (2011). CFRP Flexural and Shear Strengthening Technique for RC Beams: Experimental and Numerical Research. *Advance in Structural Engineering,* 14(3.).

Barros, J., Dias, S., and Lima, J. (2007). Efficacy of CFRP-based Techniques for the Flexural and Shear Strengthening of Concrete Beams. *Cement and Concrete Composites,* 29(3).

Barros, J., Perrone, M., and Aprile, A. (2008a). Hybrid CFRP-Based Strengthening Technique to Increase the Flexural Resistance and Concrete Confinement of RC Columns Submitted to Axial and Cyclic Lateral Loading. *Conference on Challenge for Civil Construction*. Porto, Portugal.

Barros, J., Varma, R., Sena-Cruz, J., and Azevedo, A. (2008b). Near Surface Mounted CFRP Strips for the Flexural Strengthening of RC Columns - Experimental and Numerical Study. *Engineering Structures,* 30(12): 3412-3425.

Bianco, V. (2008). Shear Strengthening of RC Beams by Means of NSM CFRP Strips: Experimental Evidence and Analytical Modeling. *PhD Thesis, Sapienza University of Rome*, Italy.

Bianco, V., Monti, G., and Barros, J. (2014). Design Formula to Evalute the NSM FRP Strips Shear Strength Contribution to a RC Beam. *Composite Part B: Engineering,* 56: 960-971.

Bonaldo, E., Barros, J., and Lourenço, P. (2008). Efficient strengthening technique to increase the flexural resistance of existing RC slabs. *Composites for Construction Journal (ASCE)*, 12(2), 149-159.

CAN/CSA-S6-00. (2000). Canadian Highway Bridge Design Code. Toronto, Canada.

Casadei, P., Galati, N., Boschetto, G., Tan, K., Nanni, A., and Galecki, G. (2006). Strengthening of Impacted Prestressed Concrete Bridge I-Girder Using Prestressed Near Surface Mounted C-FRP Bars. *2nd International Congress*, *Federation Internationale du Beton (fib),* Italy,.

CEB-FIP. (2011). Model Code 2010. Final draft, *Federation Internationale du Beton (fib).*

CEB-FIP. (1993). Comite Euro-International du Beton, 213/214.

Chen, J., Teng, J. (2001). Anchorage Strength Models for FRP and Steel Plates Bonded to Concrete. *Journal of Structural Engineering (ASCE)*, 127(7).

Choi, H. (2008). Flexural Behaviour of Partially Bonded CFRP Strengthened Concrete T-Beams. *PhD thesis, University of Waterloo,* CANADA.

Choi, H., West, J. and Soudki, K. (2011a). Partially Bonded Near-Surface-Mounted CFRP Bars for Strengthened Concrete T-beams. *Construction and Building Materials,* 25: 2441–2449.

Choi, H., West, J., and Soudki, K. (2008). Analysis of the Flexural Behavior of Partially Bonded FRP Strengthened Concrete Beams. *Journal of Composites for construction (ASCE),* 12(4.).

Choi, H., West, J., and Soudki, K. (2011b). Effect of Partial Unbonding on Prestressed Near-Surface-Mounted CFRP-Strengthened Concrete T-Beams. *Journal of Composites for construction (ASCE),* 15(1.).

Costa, I., and Barros, J. (2009a). Design a System to Apply Prestressed CFRP Laminate According to the NSM Technique for the Flexural Strengthening of RC Elements. Technical Report No: 09DEC/E-29, *University of Minho*.

Costa, I., and Barros, J. (2012). Design and Development of Hydraulic-Electro-Mechanical System to Apply Pre-Stressed CFRP Laminates According to the NSM Technique in Laboratory Conditions. Technical Report No: 12-DEC/E12, *University of Minho*, pp:59.

Costa, I., and Barros, J. (2009b). Flexural and Shear Strengthening of RC Beams with Composite Materials- The Influence of Cutting Steel Stirupps to Install CFRP Strips. *Cement & Concrete Composites,* 32: 544-553.

Dai, J., Ueda, T., and Sato, Y. (2005). Development of the Nonlinear Bond Stress-Slip Model of Fiber Reinforced Plastics Sheet-Concrete Interfaces with a Simple Method. J*ournal of Composites for Construction (ASCE)*, 9(1).

Dalfre, G., and Barros, J. (2011). Flexural Strengthening of RC Continuous Slab Strips Using NSM CFRP Laminates. *Advance in Structural Engineering,* 14(6.).

De Lorenzis, L., and Teng, J. (2007). Near-Surface Mounted FRP Reinforcement: an Emerging Technique for Structural Strengthening. *Composite Part B: Engineering,* 39(2): 119-149.

Dias, S., and Barros, J. (2009). Performance of Reinforced Concrete T-Beams Strengthened in Shear with NSM CFRP Laminates. *Engineering Structures,* 32: 373-384.

Dias, S., and Barros, J. (2010). Shear Strengthening of RC T-section Beams with Low Strength Concrete Using NSM CFRP Laminates. *Cement & Concrete Composites.*

Dias, S., and Barros, J. (2012a). Experimental Behaviour of RC Beams Shear Strengthened with NSM CFRP Laminates. *International Journal for Experimental Mechanics,* 48(1): 88-100.

Dias, S., and Barros, J. (2012b). Shear Strengthening of RC Beams with NSM CFRP Laminates: Experimental Research and Analytical Formulation. *Composite Structures* 99: 477-490.

El-Hacha, R., and Gaafar, M. (2011). Flexural Strengthening of Reinforced Concrete Beams Using Prestressed Near-Surface-Mounted CFRP Bars. *PCI Journal*.

El-Hacha, R., and Rizkalla, S. (2004). Near-Surface-Mounted Fiber-Reinforced Polymer Reinforcements for Flexural Strengthening of Concrete Structures. *ACI Structural Journal,* 101(5): 717-726.

El-Mihilmy, M., and Tedesco, W. (2000). Deflection of Reinforced Concrete Beams Strengthened with Fiber-Reiforced Polymer (FRP) Plates. *ACI Structural Journal,* 97(5): 8.

EN 1992-1-1., (2004). Design of Concrete Structures. Part 1-1: General Rules and Rules for Buildings. *European Committee for Standardization.*

Faella, C., Martinelli, E., and Nigro, E. (2003). Interface Behaviour in FRP Plates Bonded to Concrete: Experimental Tests and Theoretical Analyses. *Proceedings of Advanced Materials for Construction of Bridges, Buildings, and Other Structures III.*

Fernandes, P., Granja, J., Benedetti, A., Sena-Cruz, J., and Azenha, M. (2015). Quality Control and Monitoring of NSM CFRP System: E-modulus Evolution of Epoxy Adhesive and its Relation to the Pull-out Force. *Composite Part B: Engineering,* 75, pp:95-103.

Gao, B., Leung, C., Kim, J. (2004). Prediction of concrete cover separation failure for RC beams strengthened with CFRP strips. *Engineering Structures*, 27: 177-189.

Hajihashemi, A., Mostofinejad, D., and Azhari, M. (2011). Investigation of RC Beams Strengthened with Prestressed NSM CFRP Laminates. *Journal of Composites for Construction (ASCE),* 15(6.).

Hassan, T., and Rizkalla, S. (2003). Investigation of Bond in Concrete Structures Strengthened with Near Surface Mounted Carbon Fiber Reinforced Polymer Strips. *Journal of Composites for Construction (ASCE)*, 7(3).

Hawileh, A. (2011). Nonlinear Finite Element Modeling of RC Beams Strengthened with NSM FRP Rods. *Construction and Building Materials,* Doi: 10.1016/j.conbuildmat.2011.07.018.

He, X. (2010). Effect of Mechanical Properties of Adhesive on Stress Distributions in Structural Bonded Joints. *Proceedings of the World Congress on Engineering Vol II*. London, UK.

Hosseini, M., Dias, S., and Barros, J. (2013). Effectiveness of Prestressed NSM CFRP Laminates for the Strengthening of RC Slabs. *Composite Structures*, 111: pp:249-258.

ISIS-9 (2007). Prestressing Concrete Structures with Fibre Reinforced Polymers. Department of Civil Engineering, University of Calgary, *Canadian Network of Centres of Excellence,*14.

Jankowiak, T., and Lodigowski, T. (2005). Identification of Parameters of Concrete Damage Plasticity Constitutive Model. *Foundation of civil and environmental engineering,* (6.).

Jayaprakash, J., Pournasiri, E., Choong, K., Tan, C., and De'nan, F. (2011). External CFRP Repairing of Pretested Beams Reinforced Using Prestress Rebars. *Reinforced Plastics and Composites,* 30(20): 1753-1768.

Jo, B., Tae, G., and Kwon, B. (2004). Ductility Evaluation of Prestressed Concrete Beams with CFRP Tendons. *Reinforced Plastics and Composites,* 23:834.

Kalkan, I. (2010). Deflection Prediction for Reinforced Concrete Beams Throuth Different Effective Moment of Inertia Expressions. *International Journal of Engineering Research & Development,* 2(1.).

Kmiecik, P., and Kaminski, M. (2011). Modeling of Reinforced Concrete Structures and Composite Structures with Concrete Strength Degradation Taken into Consideration. *Archives of Civil and Mechanical Engineering*, Wroclaw University of Technology, Poland.

Mahmoud, Z., Rizkalla, S., and Zaghloul, E. (1999). Transfer and Development Length of Carbon Fiber Reinforced Polymers Prestressing Reinforcement. *ACI Structural Journal,* 96(4).

Malek, A., Saadatmanesh, H., and Ehsani, M. (1998). Prediction of Failure Load of RC beams Strengthened with FRP Plate Due to Stress Concentration at the Plate End. *ACI Structural Journal,* 95.

Mufti, A., Newhook, J., and Tadros, G. (1996). Deformability versus Ductility in Concrete Beams with FRP Reinforcement. *International conference of advanced composite materials in bridges and structures (ACMBS-2)*, 189-199.

Nordin, H., and Taljsten, B. (2006). Concrete Beams Strengthened with Prestressed Near Surface Mounted CFRP. *Journal of Composites for Construction,* 10(1): 60-68.

Omran, H., and El-Hacha, R. (2011). Nonlinear 3D Finite Element Modeling of RC Beams Strengthened with Prestressed NSM-CFRP Strips. *Construction and Building Materials*, 74-85.

Oudah, F., and El-Hacha, R. (2011a). Fatigue Behavior of RC Beams Strengthened with Prestressed NSM CFRP Rods. *Composite Structures,* 94: 1333-1342.

Oudah, F., and El-Hacha, R. (2011b). Ductility of Reinforced Concrete Beams Strengthened using Prestressed NSM CFRP Strips/Rebars- Analytical Study. *First Middle East Conference on Smart Monitoring*. Dubai, UAE.

Oudah, F., and El-Hacha, R. (2012). A New Ductility Model of Reinforced Concrete Beams Strengthened Using Fiber Reinforced Polymer Reinforcement. *Composite Part B: Engineering,* 43: 3338-3347.

Perrone, M., Barros, J., and Aprile A. (2009). A CFRP-Based Strengthening Technique to Increase the Flexural and Energy Dissipation Capacities of RC Columns. *Journal of Composites for Construction (ASCE),* 13 (5): 372-383.

Radfar, S., Foret, G., Saeedi, N., and Sab, K. (2012). Simulation of Concrete Cover Separation Failure in FRP Plated RC Beams. *Construction and Building Materials,* 73: 791-800.

Rajendra, K. (2012). Numerical Models for the Simulation of the Cyclic Behaviour of RC Structures Incorporating New Advanced Materials. *PhD Thesis, University of Minho,* Portugal.

Rasheed, H., Charkas, H., and Melhem, H. (2004). Simplified Nonlinear Analysis of Strengthened Concrete Beams based on a Rigorous Approach. *Journal of Structural Engineering (ASCE),* 130(7.).

Russell, B., and Burns, N. (1993). Design Guidlines for Transfer, Development and Bebonding of Large Diameter Seven Wire Strands in Pretensioned Concrete Girders. *University of Texas*. Report No. 1210-5F.

Saqan, E., and Rasheed, H. (2010). Simplified Nonlinear Analysis to Compute Neutral Axis Depth in Prestressed Concrete Regtangular Beams. *Journal of the Franklin Institute,* 348: 1588-1604.

Sena-cruz, J., and Barros, J. (2004). Modeling of Bond between Near Surface Mounted CFRP Laminate Strips and Concrete. *Computers and Structures*, 1513-1521.

Seracino, R., Saifulnaz, M., and Oehlers, D. (2007). Generic Debonding Resistance of EB and NSM Plate-to-Concrete Joints. *Journal of Composites for construction (ASCE),* 11(1.).

Sharaky, I. (2013). A Study of the Bond and Flexural Behaviour of Reinforced Concrete Elements Strengthened with Near Surface Mounted (NSM) FRP Reinforcement. *PhD Thesis.*, *University of Girona*, Spain.

Sharaky, I., Torres, L., Comas, J., and Barris, C. (2014). Flexural Response of Reinforced Concrete (RC) Beams Strengthened with Near Surface Mounted (NSM) Fibre Reinforced Polymer (FRP) Bars. *Composite Structures,* 109.

Tasnimi, A., and Rezazadeh, M. (2012). Experimental and Numerical Study of Strengthened Single Storey Brick Building under Torsional Moment. *International Journal of Civil Engineering*, 10(3).

Teng, J., Smith, S., Yao, J., and Chen, J. (2003). Intermediate Crack-induced Debonding in RC Beams and Slabs. *Construction and Building Materials,* 17: 447-462.

Toutanji, H., Han, M., and Ghorbel, E. (2012). Interfacial Bond Strength Characteristics of FRP and RC Substrate. *Journal of Composites for Construction (ASCE)*, 16(1).

Wu, Z., Yang, S., and Zheng, J. (2005). An Analytical Model For Rectangular RC Beams Reinforced with Prestressed CFRP Plates. *30th Conference on our World in Concrete & Structures*.

Xiong, G., Jiang, X., Liu, J., and Chen, L. (2007). A Way for Preventing Tension Delamination of Concrete Cover in Midspan of FRP Strengthened Beams. *Construction and Building Materials,* 21: 402–408.

Xue, W., Tan, Y., and Zeng, L. (2009). Flexural Response Predictions of Reinforced Concrete Beam Strengthened with Prestressed CFRP plates. *Composite Structures,* 92: 612-622.